Annual Report 2014

Physik-Department

Lehrstuhl für Funktionelle Materialien
mit dem
Fachgebiet Physik Weicher Materie

Technische Universität München

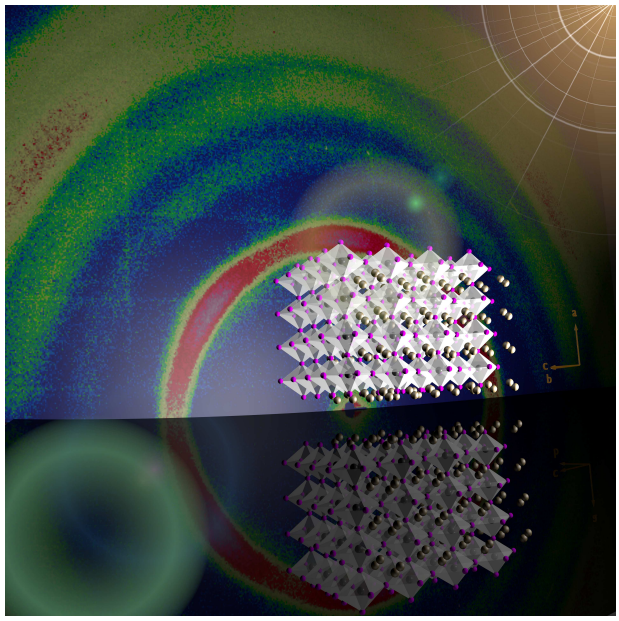

Prof. Dr. Winfried Petry
Chair of Functional Materials
Physik-Department

Deputy chairman for Prof. Dr. Winfried Petry:
Prof. Dr. Peter Müller-Buschbaum

Prof. Dr. Christine M. Papadakis
Soft Matter Physics Group

Physik-Department
Technische Universität München
James-Franck-Straße 1
85748 Garching

Secretaries: Marion Waletzki
Susanna Fink

Tel.: +49(0)89 289 12452
Fax: +49(0)89 289 12473

Email: peter.mueller-buschbaum@ph.tum.de
papadakis@tum.de
marion.waletzki@ph.tum.de
susanna.fink@ph.tum.de
http://www.functmat.ph.tum.de
http://www.softmatter.ph.tum.de

Editor: Dr. Martine Philipp

Cover-page picture:

2D GIWAXS data show highly oriented crystal grains of $MAPbI_3$ on a flat substrate, a hybrid perovskite that is used in photovoltaics and consists of organic methylammonium (MA, gold) incorporated within an inorganic lattice of iodide (purple) and lead (grey).

1 Preface

It is a great pleasure to present in the name of the staff of the Chair of Functional Materials the annual report for the year 2014. It provides an overview of our teaching, research, and development activities. Our research activities are focused on functional materials and cover a broad range from soft matter physics to developments in methods and instrumentation. We examine the fundamental physics of material properties using mainly scattering methods (neutrons, x-ray and light scattering). The general goal of our research is to explain the functional characteristics of soft condensed matter from the knowledge of the molecular dynamics and nanostructure.

In 2014, the chair activities covered the areas of water-based polymer systems, thin polymer films, polymer films for application in photovoltaics, polymer-hybrid systems, dynamics, and methodological and instrumental developments. The activities in the fields of polymer films for application in photovoltaics and polymer-hybrid systems have increased even further. With 'TUM.solar' the keylab in the network of the Bavarian Collaborative Research Project 'Solar Technologies go Hybrid' (SolTec) headed by Prof. Müller-Buschbaum evolved very fruitfully and successfully reached the second funding period. It bundles the research activities in the field of solar energy conversion and storage at TUM. The partnership with the Dielectrics Group at the National Technical University of Athens, Greece, funded by Deutscher Akademischer Austausch Dienst was started. Moreover, Prof. Papadakis edited together with Prof. Andreas Schönhals a special issue in 'The Colloid and Polymer Science' to the honor of Prof. Friedrich Kremer, University of Leipzig.

The in-house experiments available in the laboratories of the chair were supplemented by the lively activities at numerous large scale facilities, comprising synchrotron radiation and neutron scattering experiments. The instruments in the X-ray laboratory were further complemented with an additional SAXS/WAXS instrument, which broadened our capacities for small and wide angle scattering. With the addition of instruments to measure the spectral intensity distribution and for impedance spectroscopy, more and new experimental options have been added to our facilities.

In 2014, the Chair of Functional Materials comprised 11 fellows, 38 PhD students, 29 master students, 20 bachelor students, 6 student assistants and 10 administrative and technical staff members. 6 PhD theses were accomplished; moreover, 13 master theses as well as 20 bachelor theses were finished. As all the years before, we had the pleasure to host several guests from abroad, which stimulated a lively and inspiring scientific atmosphere.

In general, all members of the chair were very active at conferences and workshops, participating with both talks and posters. Moreover, important conferences were organized by members of the chair: During the '23rd Congress and General Assembly of the International Union of Crystallography' Prof. Papadakis and Prof. Müller-Buschbaum both organized independent micro-symposia having invited world-famous speakers. The Munich research reactor Heinz Maier-Leibnitz (MLZ) celebrated 10 years of operation which was organized by Prof. Petry, and the MLZ successfully passed its review in 2014. Again, two Edgar-Lüscher seminars were organized, this year on the subjects 'Umwelt- und Geophysik' and 'Die Energiewende'. The 4th Colloquium of the Munich School of Engineering 'Energy in motion' took place in Garching. Moreover, a kick-off meeting between TUM and CEA, to initiate bi-lateral projects in the area of renewable energies, was organized. The first German-Greek Workshop 'Structural methods for the investigation of responsive soft matter' was held in Garching. For the chair, a very important event this year was the summer school in Bergheim (Obertauern) in Austria - in the wonderful scenery of the Austrian Alps, all members of the chair gave talks on general subjects from the field of polymer physics. Everybody enjoyed the extensive discussions in combination with a

fascinating landscape a lot!
Regarding teaching activities of the chair, we offered general physics lectures for the TUM elite engineers in the Munich School of Engineering (MSE) (Müller-Buschbaum) and advances physics for teachers for vocational schools (Papadakis). Specialized lectures comprised 'Polymer physics' and 'Nanostructured soft materials'. Prof. Papadakis acted again as a deputy women's representative of the Physics Department. Moreover, Prof. Müller-Buschbaum headed the activities in the 'Network Renewable Energies (NRG)' in the MSE.
As a service to the community, Prof. Papadakis acted as Regional Editor for 'The Colloid and Polymer Science', and Prof. Müller-Buschbaum served as Associate Editor for 'ACS Applied Materials and Interfaces'.
This annual report comprises a selection of the different research topics and projects carried out in the individual groups of the chair. It highlights the dedicated and successful research activities and collaborations with other groups and large scale facilities. We wish all chair members a fruitful continuation and a very successful year 2015.

Peter Müller-Buschbaum and Christine M. Papadakis February 2015

Contents

2 Water based polymer systems

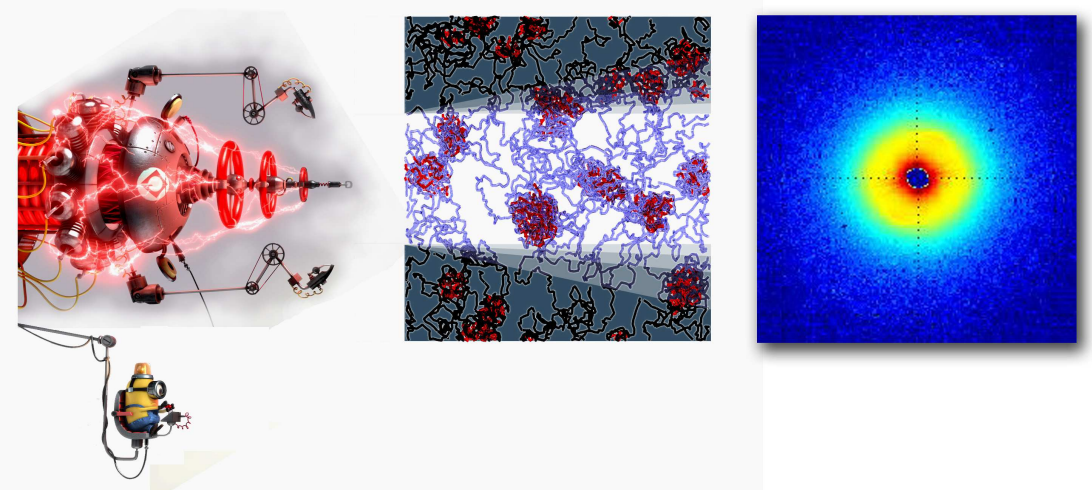

2.1 The aggregation kinetics of a PS-*b*-PNIPAM solution in pure water and water/methanol mixture - a TR-SANS study

K. Kyriakos, M. Philipp, C. H. Lin, M. Dyakonova, N. Vishnevetskaya, A. Zaccone[1], I. Grillo[2], A. Miasnikova[3], A. Laschewsky[3,4], P. Müller-Buschbaum, C. M. Papadakis

[1] Theorie weicher Materie, TU München, Garching, Germany
[2] ILL, Grenoble, France
[3] Universität Potsdam, Potsdam-Golm, Germany
[4] Fraunhofer Institut für Angewandte Polymerforschung, Potsdam Golm, Germany

The stability of colloidal particles consisting of responsive matter is of importance for the design of smart materials. Among them, systems that contain poly(N-isopropyl acrylamide) (PNIPAM) as the thermoresponsive part are of special interest. Their ability to strongly vary their physical properties in a response to small temperature changes is of great use. Recently the behavior of PNIPAM in mixed solvents of water and methanol has attracted strong interest. Despite the fact that PNIPAM is soluble in both water and methanol in ambient conditions, it fails to dissolve in mixtures of these solvents at certain compositions. This phenomenon is called *cononsolvency* and its origin is still under debate [1].

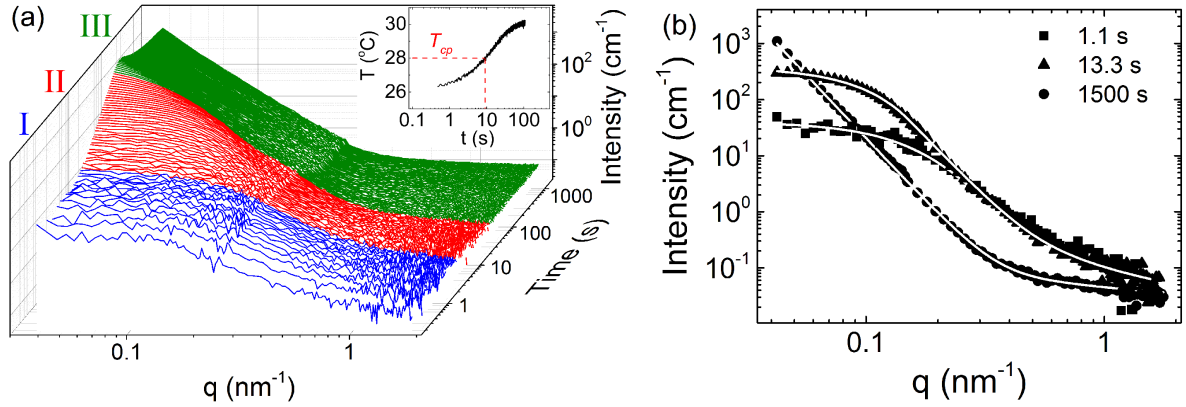

Figure 2.1: (a) TR-SANS curves for a solution of P(S-d_8)$_{11}$-*b*-PNIPAM$_{431}$ in D_2O:*d*-MeOD 95:5 mol.% for the temperature jump from 25 °C to 30 °C. The inset presents the temperature profile obtained ex-situ. (b) Representative fits (white solid lines) of selected curves from the three different regimes.

Here, we report on time-resolved small-angle neutron scattering (TR-SANS) experiments on solutions of a micelle forming P(S-d_8)$_{11}$-*b*-PNIPAM$_{431}$ (PS stands for polystyrene) diblock copolymer in D_2O and in a D_2O:*d*-MeOD 95:5 mol.% mixture upon temperature jumps. The solutions were heated rapidly from T_{cp}-3 K to T_{cp}+2 K by using a modified stopped flow instrument Biologic SFM-300 (in D_2O T_{cp}=30 °C and in D_2O:*d*-MeOD T_{cp}=28 °C). The concentration of the polymer was 30 mg/ml. The TR-SANS experiments were performed at the high-flux SANS instrument D22, at ILL, Grenoble, France.

Fig. 2.1a shows representative SANS curves for the sample dissolved in D_2O:*d*-MeOD. Three regimes are distinguished. Regime I (below T_{cp}) reflects swollen micelles. The presence of methanol does not affect the micellar structure of the system. As soon as T_{cp} is reached the micelles collapse and associate to form larger aggregates, which are described in regime II. This is reflected by the systematic increase of the forward scattering with time. Eventually the aggregate radius exceeds the resolution limit of the set up, and regime III begins, being characterized by very strong forward scattering.

For the different regimes, we use different structural models to account for the different states of the system. Fig. 2.1b compiles representative fits for the solution in D_2O:*d*-MeOD. Below T_{cp} a form factor that describes core-shell micelles is used together with an Ornstein-Zernicke term to account for density fluctuations within the swollen micellar shell. The latter has a characteristic length scale of ∼1.5 nm. The former gives the behavior of the radius of the micelle r_{mic} as a function of time (see Figs. 2.2a and b). We observe in both cases that r_{mic} increases slightly as T_{cp} is approached. This increase is stronger in the case of D_2O:*d*-MeOD. Above T_{cp} the size of the formed aggregates is described by the generalized Guinier-Porod model. With time the size of the aggregates increases, as expected. Different initial values are obtained, namely 5.7 nm for D_2O and 15.6 nm for D_2O:*d*-MeOD. This difference highlights the acceleration of the aggregation induced by the presence of *d*-MeOD. In regime III the curves are modelled by a modified Porod law. From regimes II and III, we extract information about the surface properties of the aggregates from the Porod exponent α. In both cases, α increases from values > 4 to ~ 5.6. From this, we conclude a concentration gradient along the surface normal of the aggregates appears; i.e. the surface becomes more polymer-rich with time. The aggregation process of the

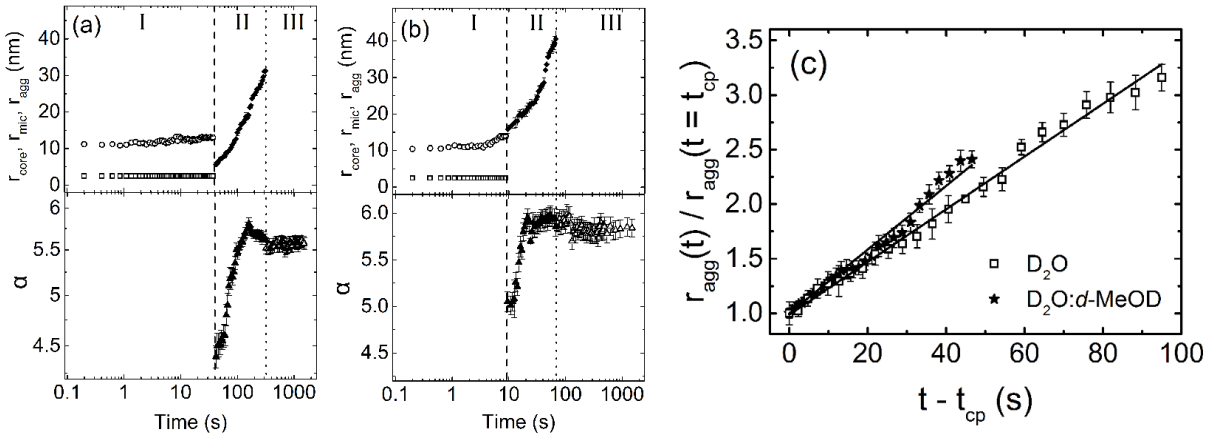

Figure 2.2: Results of the fits of the structural models for (a) D_2O and (b) D_2O:*d*-MeOD. In both cases, the dashed line marks the time when T_{cp} was reached and the dotted one the transition from the regime II to regime III. (c) Normalized aggregate radius as a function of the reduced time. t_{cp} is the time when T_{cp} is reached. The solid lines show the fits of the reversible association model [2] on our data.

two systems is analysed by the reversible association model [2], which describes the data well (Fig. 2.2c). From this model, we can extract information on the influence of the methanol on the colloidal stability of the dispersion.
To summarize, we study the influence of methanol on the kinetics of aggregation of a dispersion of themoresponsive particles upon a temperature jump. TR-SANS offers a tool to follow the process at a mesoscopic length scale. Moreover we use the reversible association model to characterize the influence of methanol on the kinetics of the aggregation.

The project was supported by DFG within the priority program SPP1259 "Intelligente Hydrogele" (Pa771/4).

[1] K. Kyriakos, M. Philipp, J. Adelsberger, S. Jaksch, A. Berezkin, D. M Lugo, W. Richtering, I. Grillo, A. Miasnikova, A. Laschewsky, P. Müller-Buschbaum, C. M. Papadakis, *Macromolecules* **47**, 6867 (2014)

[2] A. Zaccone, J. J. Crassous, B. Béri, M. Ballauff, *Phys. Rev. Lett* **107**, 168303 (2011)

2.2 Initial stages of swelling of thin polymer films sorbing a good solvent

M. Philipp, V. Körstgens, G. Santoro[1], S. V. Roth[1], P. Müller-Buschbaum
[1] DESY, Hamburg, Germany

The uptake or release of low-molecular species by polymer films and polymer-based composite films is essential for many applications, for instance in the field of sensors, actuators, and stimuli-responsive drug carriers [1]. Polymer films that sorb penetrants and thereby swell can undergo phase transformations. The swelling of polymers often interferes with the glass transition, segregation or crystal melting. These complex processes are codetermined by the physicochemical interactions of the penetrant at the surface and within the bulk of the polymer, and the number density of the penetrant's molecules in the vicinity of the surface of the film. Further important issues are the structural homogeneity and the elastic properties of the polymer film, as well as its amorphous or semi-crystalline nature. Within thin films, geometrical confinement of the macromolecular chains and their interactions at internal surfaces also influence the mobility of the polymer chains and thus the swelling capability of the film. Due to the above-mentioned phenomena, the diffusion behavior of low-molecular species within polymer films usually deviates significantly from classical Fickian diffusion.

Mostly the controlled uptake or release of gases, but not of liquids, by thin stimuli-responsive polymer films is studied in a quantitative manner, even though many of the above-mentioned applications involve the diffusion of liquids into films. The structural changes induced in thin polymer films by good solvents have so far not been investigated at all. Environmentally responsive polymers are of high technological and scientific relevance as the polymer-solvent interactions can easily be tuned in a wide range by slightest variations of adjustable parameters, like temperature, the pH value, or the ionic strength [2]. The responsible phenomenon is a demixing phase transition [2]. The uptake of low-molecular species and the rich swelling behavior of responsive polymers can be systematically varied with smallest changes in solicitation. However, due to experimental reasons, the physicochemical interactions of stimuli-responsive polymers have only been widely investigated for micellar systems, hydrogels and brushes, but much less for thin films [1, 3].

We contribute to this topic by studying for the first time the initial stages of structural changes provoked within a thin thermo-responsive polymer film, which sorbs a good solvent. The classical thermo-responsive polymer poly(N-isopropylacrylamide) (PNIPAM) is spin-coated on hydrophilized glass substrates. According to X-ray reflectivity, the as-spun, glass-supported PNIPAM films have a thickness of 50 nm. Such a film was exposed at room temperature to liquid water, which is under these conditions a good solvent for PNIPAM. A custom-built microfluidics device was used for the investigations, in order to guarantee well-defined conditions for the sorption of liquid water by the PNIPAM film. The in-situ microfluidics investigations were combined with grazing incidence small angle X-ray scattering (GISAXS) at the MiNaXS beamline P03 of the synchrotron source PETRA III of DESY, Hamburg [4]. The high brilliance of this source allows for resolving the structural changes, in height as well as laterally within the bulk and at the surface of the PNIPAM film, on the time scale of seconds. Another prerequisite for the investigation is the use of a micro-focused X-ray beam, which footprint can exactly be positioned on the film beneath the micro-fluidics channel.

A representative set of detector cuts, i.e. along the q_z-direction at q_y=0 nm^{-1}, of the 2D GISAXS patterns is presented in Fig. 2.3a) during the initial stages of sorption and swelling of the thin PNIPAM film at room temperature [5]. The intensity modulations of the detector cuts are determined by the partially correlated bottom and top interfaces of the PNIPAM film, as well as by the waveguide property for X-rays of the thin film. Quantitative information about the sorption and swelling kinetics is extracted from the GISAXS dataset by modelling the patterns using the software package FitGISAXS.

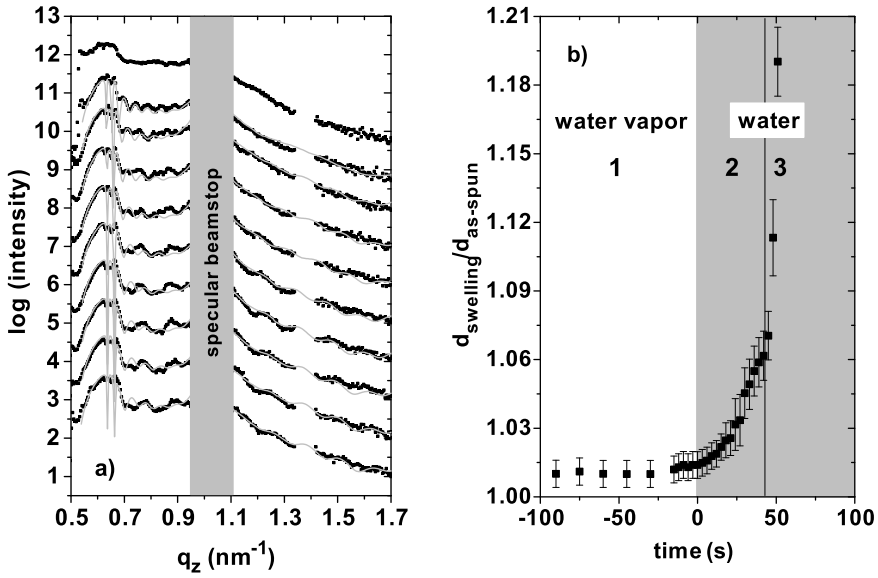

Figure 2.3:
a) Representative set of measured detector cuts (black squares and corresponding modelled intensities (grey lines) during water uptake of the PNIPAM film, first from water (-150, -90, -30 s) and subsequently from liquid water (0, 15, 30, 36, 45, 51, 54 s). For clarity, the curves are vertically shifted. b) Normalized increase in film thickness during uptake of under-saturated vapor (step 1) and subsequently liquid water (steps 2 and 3) by the PNIPAM film.

A three-step process, regarding the evolution of thickness and surface reorganization of the film, is observed during sorption of water by the glass-supported PNIPAM film and its initial stages of swelling (Fig. 2.3b)). During the sorption of water molecules from under-saturated vapor, mainly free volumes of the polymer are filled. In the second step, characterized by significant swelling, the top layer of the film becomes gel-like and its swelling is thus enabled. In the third step, reduced cohesion forces within the devitrified film probably trigger a much faster swelling process.
This investigation evidences the potential of related and extended studies for clarifying major scientifically and technologically relevant questions regarding the structural changes of thin films exposed to liquid penetrants.

[1] M. A. Cole, N. H. Voelcker, H. Thissen, H. J. Griesser, *Biomaterials* **30**, 1827-1850 (2009)

[2] M. Philipp, U. Müller, R. Aleksandrova, R. Sanctuary, P. Müller-Buschbaum, J. K. Krüger, *Soft Matter* **9**, 9887-9896 (2013)

[3] M. Koenig, D. Magerl, M. Philipp, K.-J. Eichhorn, M. Müller, P. Müller-Buschbaum, M. Stamm, P. Uhlmann, *RSC Advances* **4**, 17579-17586 (2014)

[4] V. Körstgens, M. Philipp, D. Magerl, M. A. Niedermeier, G. Santoro, S. V. Roth, P. Müller-Buschbaum, *RSC Advances* **4**, 1476-1479 (2014)

[5] M. Philipp, V. Körstgens, D. Magerl, C. Heller, Y. Yao, W. Wang, G. Santoro, S. V. Roth, P. Müller-Buschbaum, *submitted*

2.3 The collapse and aggregation of thermoresponsive poly(2-oxazoline) gradient copolymers: A time-resolved SANS study

S. Jaksch, A. Schulz[1], K. Kyriakos, J. Zhang, I. Grillo[2], R. Jordan[1], C. M. Papadakis

[1] Professur für Makromolekulare Chemie, Department Chemie, TU Dresden, Germany

[2] Institut Laue-Langevin, Grenoble, France

Thermoresponsive polymers in aqueous solution respond reversibly to small temperature stimuli by strong changes in their solubility and chain conformation, i.e. they show lower critical solution temperature (LCST) behavior. Thus, they have received increased attention as smart materials, e.g. for biomedical applications. Theoretical predictions for the collapse transition at the cloud point have been made for equilibrium conditions and have put forward the cooperativity of hydrogen bonding to the polymer as an important parameter for the nature of the transition. Time-resolved small-angle neutron scattering (TR-SANS) may provide detailed structural information. Thermoresponsive poly(alkyl-2-oxazoline)s with ethyl, *iso*- or *n*-propyl side groups (POx, Fig. 2.4) are well suited because they show a very sharp collapse transition in aqueous solution and nearly no hysteresis. This is attributed to the fact that it can only act as an acceptor when forming hydrogen bonds. The focus of the present investigation is on the influence of few hydrophobic moieties, which may alter the collapse behavior.

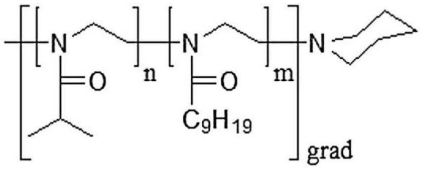

Figure 2.4: Structure of P[*i*PrOx$_n$NOx$_m$]$_{grad}$ copolymers.

We present here an investigation of aqueous solutions of poly[(2-*iso*-propyl-2-oxazoline)$_{48}$-(2-*n*-nonyl-2-oxazoline)$_2$]$_{grad}$ (P[*i*PrOx$_{48}$NOx$_2$]$_{grad}$). In our recent SANS study [1], we found that immediately above the cloud point, small aggregates (formed already below the cloud point) form, and only at higher temperatures, large aggregates are present in significant number. The question arises, whether the small aggregates are stable with time, or whether large aggregates will appear at the expense of the small ones. To address this question, we have carried out TR-SANS investigations during temperature jumps across the cloud point. The target temperatures were chosen to be either in the intermediate regime, i.e. just above the cloud point, or in the high-temperature regime. This way, we were able to follow the changes in chain conformation as well as the aggregate formation as a function of time. The results reveal the influence of the amount of hydrophobic moieties and the target temperature on the aggregation behavior [2].
SANS experiments were performed at instrument D22 at ILL in Grenoble. Rapid temperature changes were enabled by a modified Biologic SFM-300 [3]. The sample solution was equilibrated at the start temperature in the reservoir while the cuvette in the neutron beam was preheated to the target temperature in a custom-made sample holder. The sample was injected into the cuvette, whereby it heated up to the target temperature, and data acquisition was started simultaneously. The accumulation time was 3-30 s. Each temperature jump was repeated at least twice, and the resulting SANS curves were averaged. The neutron wavelength was $\lambda = 8.0$ Å and the sample-detector distances (SDD) 4.0 m and 14.0 m. The resulting 2D images were azimuthally averaged, corrected for background scattering as well as the detector sensitivity and brought to absolute units. The curves were modeled by a form factor of small fractals [4], giving the size of the single chain, ξ, and its fractal dimension, D, which is related to the Flory exponent ν, describing the chain conformation, by $\nu = 3/(D + 2)$. Forward scattering was modeled using a Porod law.

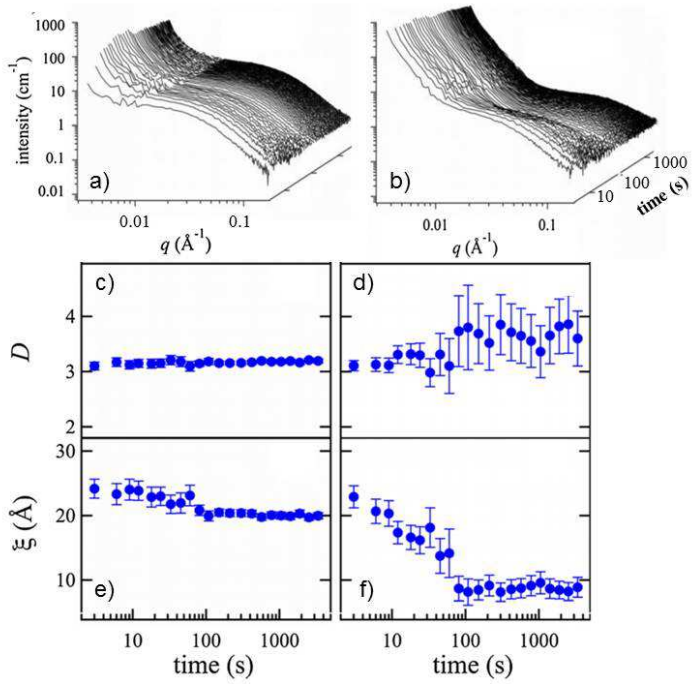

Figure 2.5:
TR-SANS curves of P[*i*PrOx$_{48}$NOx$_2$]$_{grad}$ in D_2O taken during the temperature jumps. Start temperature 23.0 °C. Target temperature 27.0 °C (a) and 30.0 °C (b). Corresponding fitting parameters: fractal dimension, D (c,d) and fractal size, ξ (e,f).

Figure 2.5a and b shows the SANS curves taken during the temperature jumps into the intermediate and the high-temperature regime. Initially, the slope of the forward scattering increases; afterwards, it stays constant. The cloud point at 24.5 °C is reached immediately after injection, and the temperature becomes stable at the target value after ca 100 s. The results of the fits are shown in Fig. 2.5c-f. For the jump into the intermediate regime, the fractal dimension, D, is constant at 3.1-3.2, which corresponds to a Flory exponent $\nu = 0.58$-0.59, i.e. the solvent is good. The size ξ is initially 24.2 ± 1.5 Å, i.e. a relatively high value. Thus, P[*i*PrOx$_{48}$NOx$_2$]$_{grad}$ forms small aggregates already below the cloud point because of intermolecular bridging by the hydrophobic *n*-nonyl groups of the NOx monomers. ξ decreases to 19.3 ± 0.7 Å during the first 126 s, which reflects the collapse of these small aggregates. For the temperature jump into the high-temperature regime, the decay at $q > 0.02$ Å^{-1} changes shape during the first 100 s. Afterwards, no more changes are observed. The fractal dimension D is constant at 3.1 ± 0.1 during the first 30 s, then it increases and reaches 3.5 ± 0.7 110 s after the injection, i.e. ν decreases from 0.59 ± 0.01 to 0.54 ± 0.07. The initially good solvent thus becomes slightly worse, but not yet a theta solvent. ξ decreases from 23 ± 2 Å to 8 ± 2 Å 110 s after the injection, i.e. the small aggregates collapse. This means that the final solvent quality is worse and the collapse is stronger than for the jump into the intermediate regime, as expected.
The present results confirm that the gradient copolymers form small aggregates already below the CP. Moreover, the intermediate regime found in our previous work is stable.
This project is supported by DFG (Pa771/6-2).

[1] S. Jaksch, A. Schulz, K. Kyriakos, J. Zhang, I. Grillo, V. Pipich, R. Jordan, C.M. Papadakis, *Colloid Polym. Sci* **292**, 2412 (2014)

[2] S. Salzinger, S. Huber, S. Jaksch, P. Busch, R. Jordan, C. M. Papadakis, *Colloid Polym. Sci.* **290**, 385 (2012)

[3] J. Adelsberger, E. Metwalli, A. Diethert, I. Grillo, A.M. Bivigou-Koumba, A. Laschewsky, P. Müller-Buschbaum. C.M. Papadakis, *Macromol. Rapid Commun.* **33**, 254 (2012)

[4] J. Teixeira, *J. Appl. Crystallogr.* **21**, 781 (1988)

2.4 Cononsolvency in PNIPAM aqueous solutions - A time resolved SANS study

K. Kyriakos, M. Philipp, J. Adelsberger, S. Jaksch, A. V. Berezkin, I. Grillo[1], A. Miasnikova[2], A. Laschewsky[2,3], P. Müller-Buschbaum, C. M. Papadakis

[1] ILL, Grenoble, France

[2] Universität Potsdam, Potsdam-Golm, Germany

[3] Fraunhofer Institut für Angewandte Polymerforschung, Potsdam Golm, Germany

Among thermoresponsive polymers, poly(N-isopropyl acrylamide) (PNIPAM) occupies a prominent place. Its lower critical solution temperature (LCST) in aqueous solution lies at 32 °C, making PNIPAM an excellent candidate for numerous applications. Recently, the behavior of PNIPAM in mixed solvents of water (H_2O) and short chain alcohols (e.g. methanol) has attracted strong interest [1]. Even though methanol is good solvent for PNIPAM, their mixture is a worse solvent. This phenomenon is termed *cononsolvency* and results in a strong decrease of the cloud point (T_{cp}) upon increasing the amount of methanol. The discussion regarding the molecular origin of the phenomenon until now has not lead to conclusive results.
Here we report on time-resolved small-angle neutron scattering (TR-SANS) experiments on aqueous solutions of PNIPAM homopolymers and micelle forming PS_{14}-*b*-$PNIPAM_{310}$ diblock copolymers (PS stands for polystyrene) upon rapid addition of *d*-MeOD [2]. We focus on the influence of the methanol volume fractions on the aggregation process of the collapsed, hydrophobic chains or micelles for PNIPAM and PS-*b*-PNIPAM, respectively. To this end, *d*-MeOD was added to aqueous (in D_2O) polymer solutions of an initial polymer concentration of 20 mg/ml; at 10 %, 15 % and 20 % vol. of *d*-MeOD by using a stopped-flow instrument (Biologic SFM-300). TR-SANS experiments, performed at the high flux instrument D22 in ILL, Grenoble, allowed the study of the kinetics of the aggregation process. Two sample-to-detector distances of 4.0 m and 14.4 m were selected, that together with a wavelength of λ = 0.8 nm resulted in a q range from 0.03 to 2 nm^{-1}. In Fig. 2.6a, representative SANS curves of PNIPAM homopolymer for a mixing

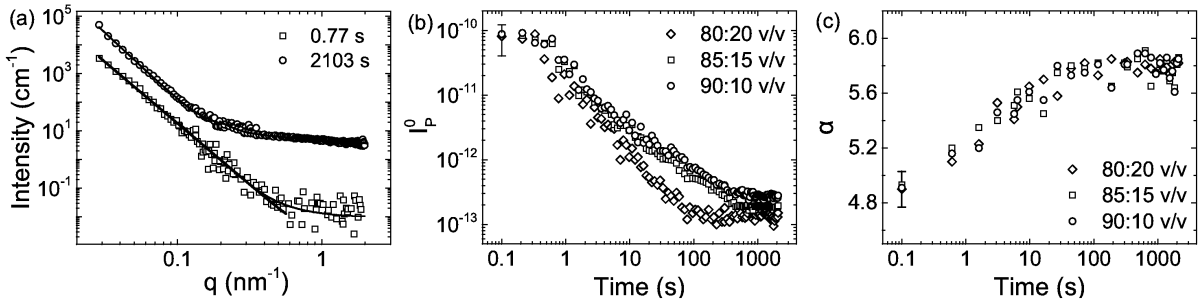

Figure 2.6: (a) Representative SANS curves of PNIPAM homopolymer for 80:20 v/v D_2O:*d*-MeOD for selected time frames (open symbols). The lines are fitting curves to the open symbols. For clarity the curve at 2103 s were shifted vertically by a factor of 10^3. (b) Porod intensity I_P^0 and (c) Porod exponent α for all mixing ratios are presented as a function of time.

ratio 80:20 v/v of D_2O:*d*-MeOD are shown. Already from the beginning, the curves are dominated by very strong forward scattering; i.e. large aggregates are formed. In the high q-regime a small contribution is present, reflecting density fluctuations within the aggregates, presumably due to trapped solvent molecules. To account for these contributions, a combination of the Porod law and an Ornstein-Zernicke term is used. With time, we observe the decrease of the Porod intensity I_P^0 (Fig. 2.6b), in other words the decrease of their specific surface which can be explained through the increase of their size. The rate of this increase depends on the *d*-MeOD

content. The Porod exponent (α) (Fig. 2.6c) has an initial value of 4.8 and increases to 5.8 until 100 s after mixing, reflecting the formation and the further evolution of a SLD gradient along the surface normal; i.e the interfaces become sharper.
Fig. 2.7a shows representative SANS curves of PS_{14}-*b*-$PNIPAM_{310}$ for a mixing ratio 80:20 v/v of D_2O:*d*-MeOD. The first curves decay smoothly. After ca. 15 s, a minimum appears at $q \sim 0.15$ nm^{-1} and moves to lower q values with time. For the first curves, a generalized Guinier-Porod model and for the later stages a model describing spheres with a Gaussian size distribution is used. The aggregation pathway depends on the amount of *d*-MeOD (Fig. 2.7b). For all three solutions, small aggregates are present from the beginning and grow with time. At the last stage, they enter a kinetically frozen regime which hinders the further increase, thus they remain stable at values 44 - 49 nm, depending on the system. The evolution of the radii is captured by two different models. For the first 20 s, the diffusion-limited coalescence model (DLC) is applied [3], whereas, for later times, a logarithmic coalescence model fits well [2]. Both models quantify the observation that, the addition of higher amounts of *d*-MeOD leads to an earlier onset of the aggregate radius on the one hand, and on the other hand leads to larger final aggregate radius. The impact of the methanol on the water structure that mediates the interaction between the aggregates may be at the origin of this dependence. Summarizing, we report here on a study

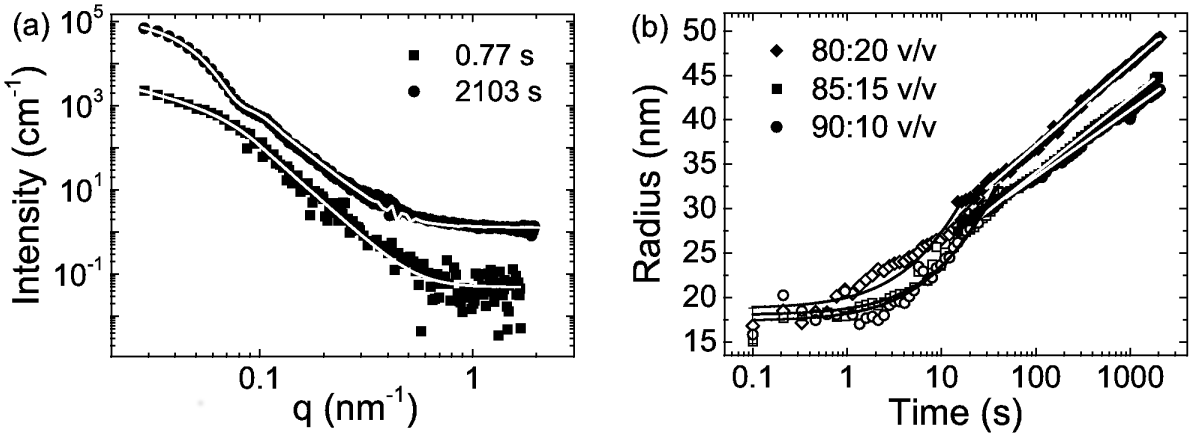

Figure 2.7: (a) Representative SANS curves of PS-*b*-PNIPAM for a mixing ratio D_2O:*d*-MeOD of 80:20 v/v for selected time frames. The lines are fitting curves. For clarity, the curve at 2103 s was shifted vertically by a factor of 100. (b) Aggregate radii as a function of time for the three mixing ratios. The lines present the fits of the two models: solid black lines for the DLC model and solid white lines for logarithmic coalescence. See text for details.

of the aggregation process that is triggered by the addition of *d*-MeOD to aqueous solutions of PNIPAM and PS-*b*-PNIPAM. The two systems exhibit different aggregation processes; larger aggregates are formed in the case of PNIPAM. For PS-*b*-PNIPAM, we follow the formation of aggregates that consist of several collapsed micelles and we use different models to describe their growth.
The project was supported by DFG within the priority program SPP1259 "Intelligente Hydrogele" (Pa771/4).

[1] C. Scherzinger, A. Schwarz, A. Bardow, K. Leonhard, W. Richtering, *Curr. Opin. Colloid Interface Sci.* **19**, 84 (2014)

[2] K. Kyriakos, M. Philipp, J. Adelsberger, S. Jaksch, A. Berezkin, D. M Lugo, W. Richtering, I. Grillo, A. Miasnikova, A. Laschewsky, P. Müller-Buschbaum, C. M. Papadakis, *Macromolecules* **47**, 6867 (2014)

[3] R. Stepanyan, J. G. J. L. Lebouille, J. J. M. Slot, R. Tuinier, M. A. Cohen Stuart, *Phys. Rev. Lett.* **109**, 138301 (2012)

2.5 Aggregation behavior of doubly thermo-responsive poly(sulfobetaine-*b*-(N-isopropylmethacrylamide) diblock copolymers

N. Vishnevetskaya, V. Hildebrand[1], M. Philipp, A. Laschewsky[12], P. Müller-Buschbaum, C. M. Papadakis

[1] Institute of Chemistry, University of Potsdam, Germany
[2] Fraunhofer Institut für Angewandte Polymerforschung, Potsdam-Golm, Germany

Thermoresponsive polymers are a class of "smart" materials that have attracted much scientific interest. Poly(N-isopropylmethacrylamide), (PNIPMAM), shows a sharp collapse transition at ca. 42 °C, i.e. lower critical solution temperature behavior (LCST). It is very attractive to combine this LCST switching behavior with another stimuli-responsiveness, such as an upper critical solution temperature (UCST) behavior [1,2]. The latter is encountered in poly(sulfobetaine)s (PSB), which undergo a phase transition from a collapsed dehydrated state to a swollen hydrated state at ca. 42 °C, in contrast to PNIPMAM. A diblock copolymer P(SB-*b*-NIPMAM) exhibits double thermo-responsive behavior in water. PSB is a permanently zwitterionic polymer [1], and its UCST can be tuned by adding small amounts of electrolyte [3,4]. This special feature of PSB will affect the phase transition temperatures of P(SB-*b*-NIPMAM) as it is shown on Fig. 2.8.

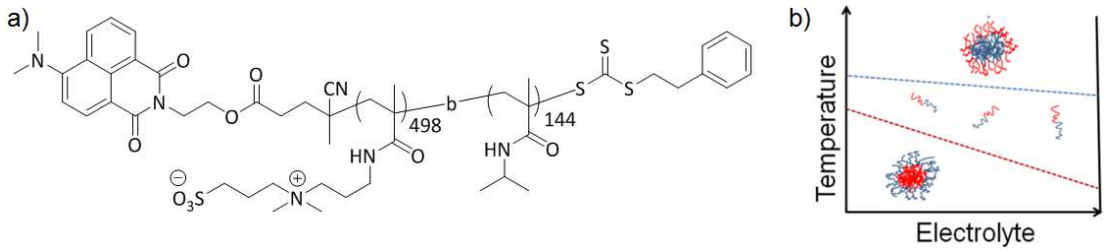

Figure 2.8:
a) Chemical structure of P(SB-*b*-NIPMAM). b) Expected structures (three possible phases in water): micelles with PNIPAM shell and PSB core or vice versa and unimers in intermediate temperature range, with changes in UCST and LCST transitions caused by the addition of an electrolyte.

Using turbidimetry, we have identified the phase transition temperatures for 5 wt.-% of the P(SB-*b*-NIPMAM) in D2O at 29.2 °C and 50.7 °C, which are presumably due to the aggregation of the PSB (UCST) and PNIPMAM (LCST), respectively, and in 0.006 M solution of NaCl in D2O at 30.7 °C and 48.1 °C which illustrates the salt-in effect that leads to the behavior sketched in Fig. 2.8b).
The aggregation behavior of P(SB-b-NIPMAM) diblock copolymer (164 500 g/mol) and homopolymers PNIPMAM (15 500 g/mol) and PSB (184 300 g/mol) in aqueous solution with dual stimuli (temperature and electrolyte) is studied by temperature-resolved small-angle neutron scattering (SANS) (Fig. 2.9a)). SANS results revealed that the aggregation of P(SB-b-NIPMAM) in D2O occurs above 54 °C and below 32 °C, and that the structure depends on the length of the blocks. The scattering from P(SB-b-NIPMAM) is best described by a product of the form factor of polydisperse spheres below 54 °C or by core-shell cylinders above, respectively, in dependence on the hydrophobicity of the blocks, with a hard-sphere structure factor, and an Ornstein-Zernicke (OZ) and a Porod term, describing the inner polymer structure and large aggregates at low and high q-values respectively (Fig. 2.9a)). The corresponding structures presented in Fig. 2.9b). The different form factors are due to the difference of the blocks length in the diblock copolymer: above 50 °C, the micelles consist of a hydrophobic PNIPMAM core and a hydrophilic PSB shell. Since the PSB block is more than three times longer than

the PMIPMAM block, the micelles are cylindrical at high temperatures. In the intermediate temperature range, a decrease of the micellar radius is observed. The salt-induced structural changes are weak both for block copolymers (Fig. 2.9c)) and for homopolymers. The SANS curves from homopolymers PNIPMAM and PSB could be fitted with the same model, but with form factor of polydisperse spheres only.

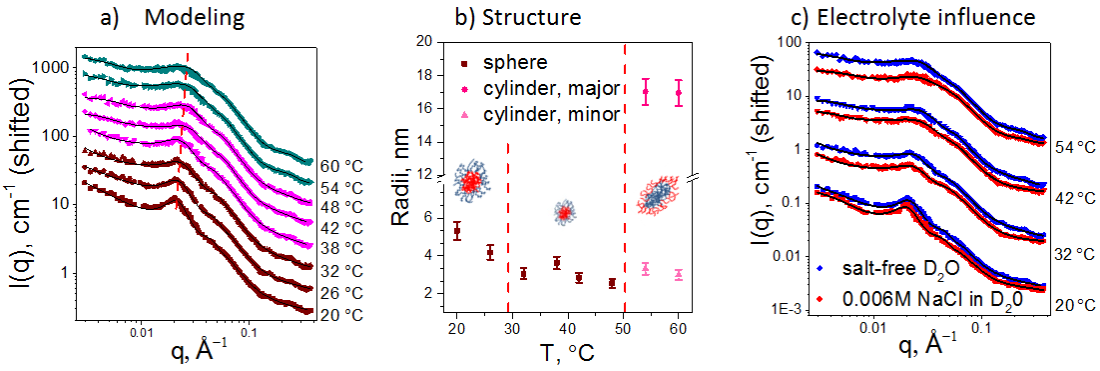

Figure 2.9:
Temperature-resolved SANS curves from 5 wt.-% P(SB-*b*-NIPMAM) solutions in log(Int) vs. log(q) representation a), the corresponding structures b) and comparison of the data obtained with and without salt (NaCl) c) in the sample solutions.

Using small-angle X-ray scattering (SAXS), we have observed that the conditions of the samples preparation have only minor impact on the kinetics of phase transition.

The aggregation behavior modulated by dual stimuli (temperature and electrolyte concentration) is studied by temperature-resolved small-angle X-ray and neutron scattering (SAXS, SANS). Aggregation of P(SB-*b*-NIPMAM) in deuterated water was found to occur above LCST and below UCST. The structures formed depended markedly on the blocks lengths, whereas the salt-induced structural changes were only minor.
The work is funded by the DFG (Pa771/14-1).

[1] M. Arotçaréna, B. Heise, S. Ishaya, A. Laschewsky, *J. Am. Chem. Soc.* **124**, 3787 (2002)

[2] M. Mertoglu, S. Garnier, A. Laschewsky, K. Skrabania, J. Storsberg, *Polymer* **46**, 7726 (2005)

[3] M. B. Huglin, M.A. Radwan, *Polym. Int.* **26**, 97 (1991)

[4] P. Köberle, A. Laschewsky, T. D. Lomax, *Makromol. Chem., Rapid Commun.* **12**, 427 (1991)

2.6 Stimuli-responsive polyampholyte hydrogels - influence of charge asymmetry and ionic strength

M. A. Dyakonova, M. T. Popescu[1], K. Kyriakos, S. Jaksch[2], C. Tsitsilianis[1], C. M. Papadakis

[1] Department of Chemical Engineering, University of Patras, Greece
[2] MLZ, Garching, Germany

Hydrogels from polyampholytes display very strong variations of their mechanical properties in dependence on the charge asymmetry (controlled by the pH value) and ionic strength and the polymer concentration, among others. Elucidating the underlying structural changes may promote the understanding of the mechanical properties.

We have investigated the structural properties of stimuli-responsive hydrogels from triblock polyampholytes. These consist of negatively charged poly(acrylic acid), PAA, and positively charged poly(2-vinylpyridine), P2VP. Their charge density varies with pH value, and the uncharged monomers are hydrophobic. Moreover, instead of P2VP, chemically quaternized P2VP, QP2VP, was used which is highly positively charged, independently of pH. More specifically, we have chosen PAA_{109}-*b*-$P2VP_{819}$-*b*-PAA_{109} in D_2O at pD 3 and PAA_{109}-*b*-$QP2VP_{819}$-*b*-PAA_{109} in D_2O at pD 5, focusing on the influence of the ionic strength on the morphology. The transition behavior depends on the response of each block on pH variation: For PAA, the lower the pH, the lower the fraction of charges. In contrast, P2VP is positively charged at low pH, whereas at high pH, the fraction of charges decreases. Therefore, in presence of both kind of charges on both blocks, rather stiff networks form due to the electrostatic interaction between the two blocks [1]. The charge asymmetry is high in PAA_{109}-*b*-$QP2VP_{819}$-*b*-PAA_{109} at pD 5, which is expected to lead to a high cross-linking connectivity and to the formation of a highly dynamic network. In contrast, in PAA_{109}-*b*-$P2VP_{819}$-*b*-PAA_{109} at pD 3, the charge asymmetry is lower, and the hydrophobic effect becomes the prevailing factor, determining the morphology in the system.

In Fig. 2.10a, steady-state shear viscosity measurements of 30 mg/ml solutions of PAA_{109}-*b*-$P2VP_{819}$-*b*-PAA_{109} at pD 3 with varying ionic strength are presented. For the salt-free solution and at low NaCl concentrations (0.15 M, 0.3 M), the value of low shear viscosity reaches 10^5 Pa·s, suggesting the formation of a rigid network. This corroborates with previous studies, which have shown that, at this pD, a strong physical network with a high cross-link functionality is formed [1]. For a hydrogel with 0.5 M of NaCl, the low shear viscosity is one order of magnitude lower, revealing a diminished number of junction points and a decrease in the degree of cross-linking, i.e. a weaker network. At all salt concentrations, the sudden drop of viscosity indicates a rupture of the transient network. These findings can be explained as follows: Counter-ion condensation on the P2VP blocks induces their collapse, hindering the bridging between the micelles and thus lowering the network connectivity. Gels with a lower content of NaCl maintain their rigidity up to a higher critical stress value (90 Pa) than the ones at higher salt contents (0.3 and 0.5 M, 40 Pa). This rather moderate change is due to a rather high charge density of both blocks, which cannot be fully screened, leading to a tearing of a fraction of junctions only.

Small-angle neutron scattering (SANS) curves of PAA_{109}-*b*-$P2VP_{819}$-*b*-PAA_{109} at pD 3 and of PAA_{109}-*b*-$QP2VP_{819}$-*b*-PAA_{109} at pD 5 at different NaCl concentrations are presented in Fig. 2.10b,c. These feature a broad maximum with some shoulders which are more pronounced in the latter system and which, for both systems, gradually vanish with increasing NaCl concentration. The model fitting for salt-free solutions has shown that both hydrogels consist of core-shell particles, connected by stretched protonated P2VP chains [2]. The core is a complex formed

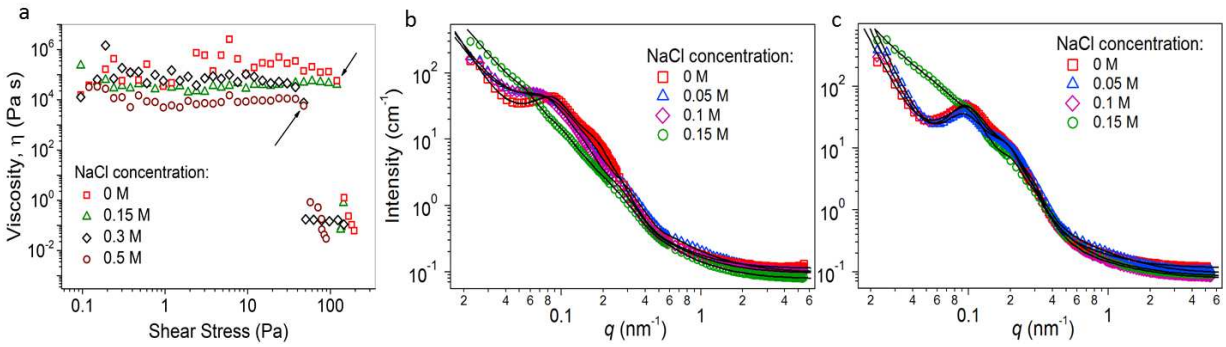

Figure 2.10:
(a) Steady-state shear viscosity of 30 mg/ml PAA_{109}-*b*-$P2VP_{819}$-*b*-PAA_{109} polymer solutions at pD 3 at different NaCl concentrations as indicated in the graph. The arrows mark the critical stress values. SANS curves of solutions of PAA_{109}-*b*-$QP2VP_{819}$-*b*-PAA_{109} at pD 5 (b) and PAA_{109}-*b*-$P2VP_{819}$-*b*-PAA_{109} at pD 3 (c) at a concentration of 30 mg/ml at and 26°C with different NaCl concentrations. The solid lines are the models fits.

by oppositely charged blocks of PAA and P2VP, whereas the shell consists of protonated P2VP moieties. Whereas the salt-free solutions of these two hydrogels show similar behavior, the response of the systems on addition of NaCl differs slightly. In PAA_{109}-*b*-$QP2VP_{819}$-*b*-PAA_{109}, it leads to conformational changes, namely the transition from core-shell to niform spheres which further collapse, moreover large aggregates form which are accompanied by small particles. The size of the aggregates increases with NaCl concentration. This continuous growth is induced by an increasing hydrophobicity due to neutralization of the blocks. The distance between the particles in the network increases accordingly, preventing contacts between identically charged particles. The hydrogel from PAA_{109}-*b*-$P2VP_{819}$-*b*-PAA_{109} maintains its original conformation upon higher amount of added salt (0.15 M, Fig. 2.10c), due to the presence of additional hydrophobic compartments from P2VP blocks, which make the gel more rigid. Thus, salt ions, associating with charged units are not able to disrupt these junctions fully. The aggregate radius changes only after addition of 0.15 M of NaCl. Accordingly, the distance between the micelles is unchanged. This high network stability may arise from a higher hydrophobicity in the system due to the presence of hydrophobic units along the P2VP chain, which are incorporated inside the core or distributed along the bridging chains, making the system more resistant to ionic strength variation.

This project was supported by DAAD in the framework of the IKYDA program.

[1] N. Stavrouli, T. Aurby, C. Tsitsilianis, *Polymer* **49**, 1249 (2008)

[2] M. A. Dyakonova, N. Stavrouli, M. T. Popescu, K. Kyriakos, I. Grillo, M. Philipp, S. Jaksch, C. Tsitsilianis, C. M. Papadakis, *Macromolecules* **47**, 7561 (2014)

2.7 Crystallization and mesophase formation of bottle brush copolymers with poly(propylene oxide)-*b*-poly(ethylene oxide) side chains

C. Psylla, K. Kyriakos, J. Zhao[1], S. Pispas[1], S. Kripotou[2], A. Kyritsis[2], C. M. Papadakis

[1] Theoretical and Physical Chemistry Institute, National Hellenic Research Foundation, Athens, Greece

[2] Physics Department, National Technical University of Athens, Athens, Greece

Graft copolymers have a number of potential applications related to the multibranched molecular architecture. Recently, novel molecular architectures have been synthesized, where PPO-*b*-PEO (PPO and PEO stand for poly(propylene oxide) and poly(ethylene oxide), respectively) diblock copolymers are grafted on a poly(*p*-hydroxystyrene) (PHOS) backbone with high grafting densities [1]. Both, the length and composition of the side chains were varied. Moreover, by inverting the sequence of the monomer addition, two different molecular structures were achieved, with either PPO or PEO linked directly to the backbone. However, the phase behavior of these bottlebrush copolymers, especially the crystallization of PEO, is poorly understood. We report here on small- and wide-angle X-ray scattering experiments (SAXS and WAXS) on bottle brush systems of various architectures and molecular compositions, focusing on the crystallization and the microphase separation.

Samples with different PEO volume fractions and different sequences of PEO and PPO segments in the side chains were investigated. To investigate the crystal structure and the mesoscopic structure, WAXS and SAXS experiments were carried out using the instrument Ganesha 300XL with a wavelength $\lambda = 1.54$ Å and the sample-detector-distances of 101 and 401 mm. The samples were mounted in holders between mica sheets. They were heated to 80 °C or 100 °C and were after 5 min cooled to -80 °C with a cooling rate of -10 K/min. The measurements were taken during stepwise heating with equilibration times of 5 min after each step of 5-10 K. The measuring times were 10-30 min. Lorentz functions were fitted to the peaks in the SAXS curves to determine their positions.

We focus here on a sample with PPO near the PHOS backbone and PEO at the end of the side chains. The PEO weight fraction is 62.5 %. Figure 2.11a displays the WAXS curves in dependence on temperature. The (120) and (032) diffraction peaks from PEO are observed at low temperatures. Their intensity above the amorphous halo decreases with temperature, and they vanish above 10 °C, i.e. the PEO crystallites melt at 15 ± 5 °C. This is in accordance with the melting point of 6 °C determined using differential scanning calorimetry. The SAXS curves (Fig. 2.11b) show a strong reflection at $q \sim 0.05$ Å^{-1} up to -40 °C. Above this temperature, the peak moves first to lower q values, but, above 0 °C, it moves abruptly to lower q values and becomes much weaker. A higher order reflection is present at temperatures up to 0 °C at ca. 0.08 Å^{-1} which is indicative of the morphology.

The resulting peak positions and widths are shown in Fig. 2.12. The repeat distance of the mesoscopic structure increases abruptly between -40 and -20 °C from ca. 65 Å to ca. 140-150 Å, and then decreases above 0 °C to ca. 110 Å (Fig. 2.12a). The ratio of the positions of the second and the first order peak is given in Fig. 2.12b. It is close to the one expected for a hexagonal structure ($\sqrt{3}$) below -40 °C, then increases to ca. 1.88, i.e. a value slightly lower than the one expected for a lamellar structure (2). Above this temperature, the morphology cannot be determined unambiguously, since no higher order reflection is present.

We conclude that, in this sample, crystallization initially takes place in the hexagonal morphology. Due to the high fraction of PEO, the matrix presumably consists of crystallizing PEO and the cylinders of amorphous PPO. Above -40 °C, the crystallites break out and form lamellae before the sample goes through the order-to-disorder transition at ca. 5 °C.

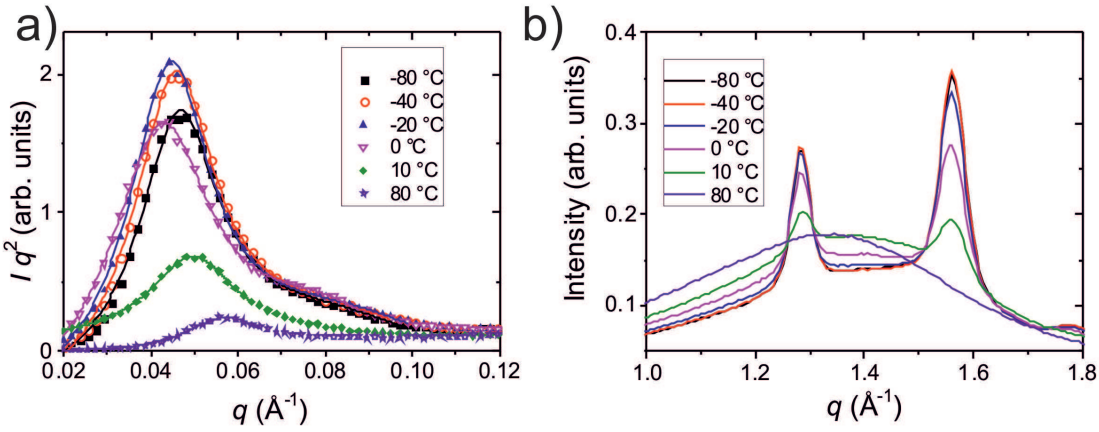

Figure 2.11: Representative SAXS (a) and WAXS curves (b) in dependence on temperature.

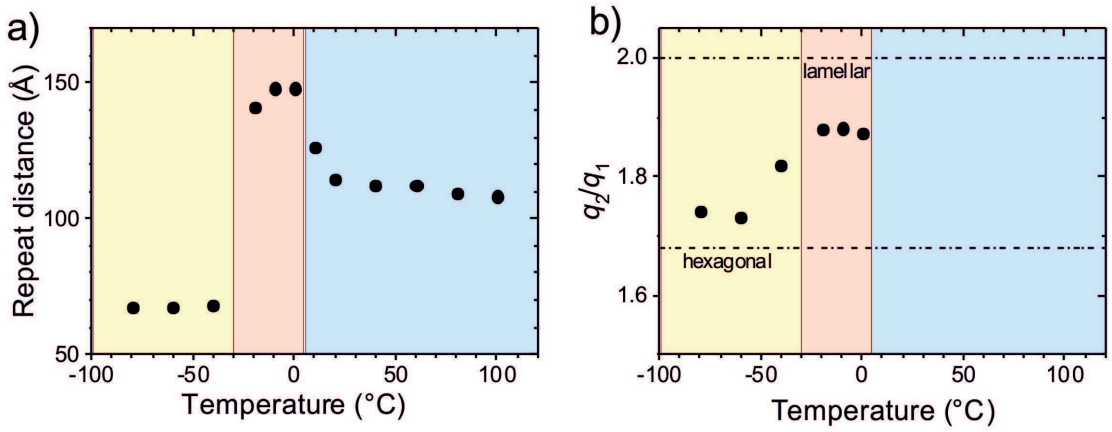

Figure 2.12: Results from model fitting to the SAXS curves. (a) Repeat distances, (b) ratio of positions of the second and the first order peak.

The mesostructure and the crystallization behavior of bulk samples of bottle brush block copolymers depend strongly on the polymer architecture, i.e. the sequence of PEO and PPO in the side chains as well as on the composition. Depending on these parameters, we have identified confined, unconfined and break-out crystallization.

[1] J. Zhao, G. Mountrichas, G. Zhang, S. Pispas, *Macromolecules* **43**, 1771 (2010)

2.8 Networks from amphiphilic star block copolymers

X. Zhang, K. Kyriakos, M. Rikkou-Kalourkoti[1], E. N. Kitiri[1], C. Patrickios[1], C. M. Papadakis

[1] Department of Chemistry, University of Cyprus, Nicosia, Cyprus

Polymer networks are an important type of polymeric materials in which all polymer chains are interconnected with each other. As the synthesis of most polymer networks involves simultaneous polymerization and cross-linking, the structure of the networks is usually poorly controlled, with a very broad distribution of chain lengths between cross-linkers. The successful synthesis of a new type of double network (DN) gel has recently been reported [1], with the expectation that these feature well-defined mesoscopic structure and promising macroscopic mechanical properties.

This study emphasizes the characterization of the above-mentioned DN gels which are based on a first amphiphilic polymethacrylate conetwork (ACPN) and a second polyacrylamide network (Fig. 2.13). The first ACPN network is composed of interconnected star-like copolymers of 2-(dimethylamino) ethyl methacrylate (DMAEMA, hydrophilic ionisable monomer) and 2-ethylhexyl methacrylate (EHMA, hydrophobic monomer) or lauryl methacylate (LauMA, second hydrophobic monomer). (Fig. 2.13)

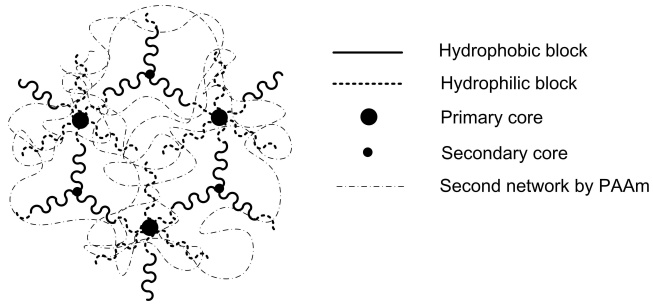

Figure 2.13: Schematic of the amphiphilic double network gel

We investigate the microphase separation of the first networks, the second network and the DNs. Using small angle X-ray scattering (SAXS), we characterize their morphology in dependence on hydrophobic block lengths ($N_B = 10$, 20 or 30) and different hydrophobic monomers (EHMA or LauMA). All the polymeric network samples are swollen with deionized water for 24 h, and then the SAXS experiments are carried out at room temperature. Subsequently, the scattering patterns are azimuthally integrated, resulting in SAXS curves where the scattering intensity I is plotted versus the momentum transfer q (Fig. 2.14.)

To obtain the size of the hydrophobic domains, the SAXS curves are modeled by a form factor of core-shell micelles [2], the core of which describes densely packed hydrophobic domains and the shell of the micelle corresponds to swollen hydrophilic chains around the hydrophobic domains. The average distance between the hydrophobic domains is obtained using the hard-sphere structure factor [3-4] which describes the interaction between the domains.

For all the conetworks with long hydrophobic blocks (*i.e.* $N_B \geq 20$), a pronounced correlation peak is present, meaning that these conetworks microphase-separated strongly and mesoscopic structures are formed. Moreover, the observed core dimensions are found to be strongly dependent on the N_B values for both the EHMA and the LauMA systems. We attribute this to

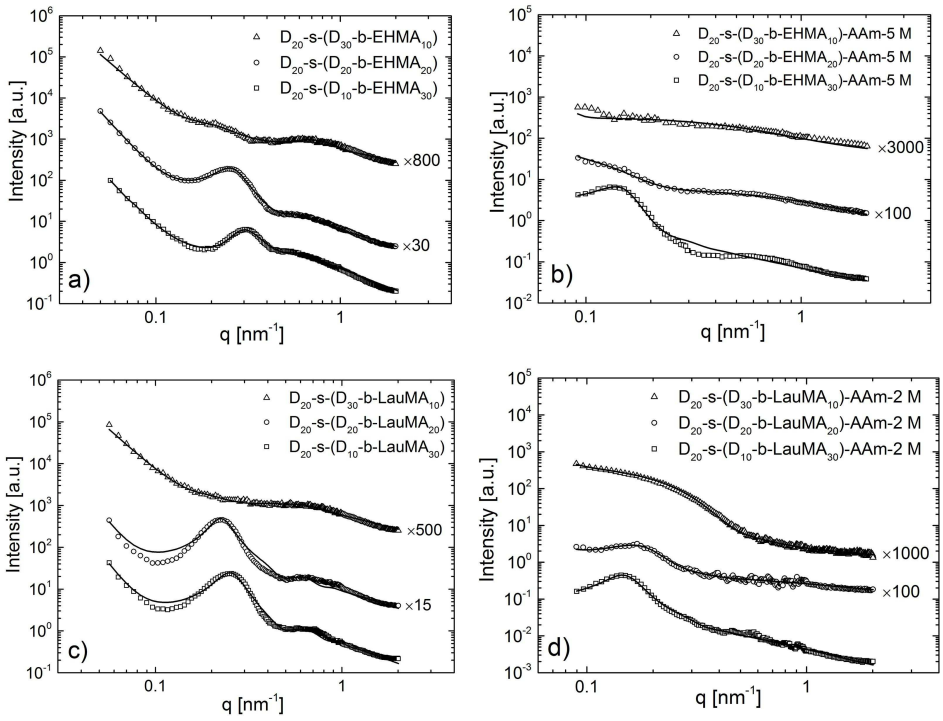

Figure 2.14:
SAXS profile of (a) single network with EHMA monomer; (b) double network with EHMA monomer; (c) single network with LauMA monomer and (d) double network with LauMA monomer.

the merging of several cores to larger domains for medium and long hydrophobic blocks (*i.e.* $N_B = 20$ and 30).

For the DN systems, reduced correlations between hydrophobic domains are observed. For the DN EHMA system, a correlation is present only in the case of the longest hydrophobic block (*i.e.* $N_B = 30$), meaning that the presence of the second PAAm network has a negative impact on the well-defined structures. Meanwhile, the average domain size of the DNs is much larger than those found in single networks for system with the same N_B value, which is possibly due to the penetration of PAAm chains into the hydrophobic domains. Moreover, the hydrophobic domains are distributed further from each other, due to the volume that is occupied by PAAm chains in between the domains.

To summarize, the micro-phase separation and resulting mesoscopic structures of the amphiphilic conetworks are successfully observed using SAXS and quantitatively analyzed by modeling of the SAXS curves.

[1] M. Vamvakaki, C. S. Patrickios, *Chem. Mater.* **14** 1630-1638 (2002)

[2] P. Bartlett, R. H. Ottewil, *J. Chem. Phys.* **96** 3306 (1992)

[3] J. K. Percus, G. J. Yevick, *Phys. Rev.* **110** 1 (1958)

[4] D. J. Kinning, E. L. Thomas, *Macromolecules* **17** 1712 (1984)

3 Thin polymer films

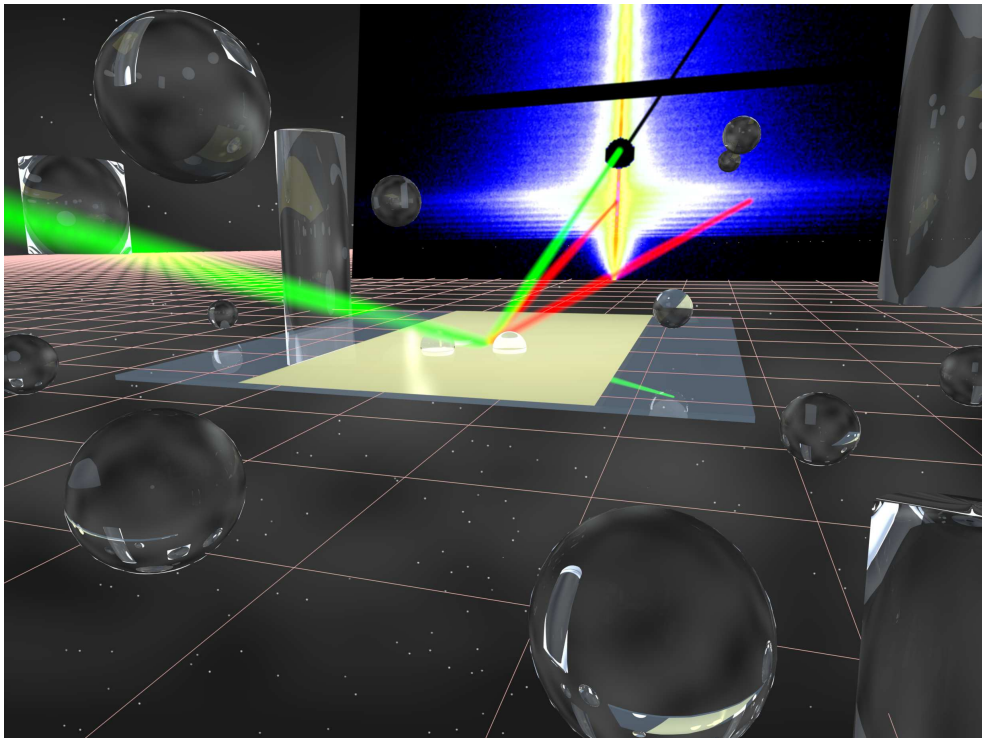

3.1 Structure and dynamics of asymmetric poly(styrene-*b*-1,4-isoprene) diblock copolymer under 1D and 2D nanoconfinement

W. K. Kipnusu[1], M. M. Elmahdy[1], E. U. Mapesa[1] , W. Böhlmann[2], J. Zhang[2], D.-M. Smilgies[3], C. M. Papadakis, and F. Kremer[1]

[1] Institute of Experimental Physics I, Leipzig University, Germany
[2] Institute of Experimental Physics II, Leipzig University, Germany
[3] CHESS, Cornell University, Ithaca, NY, USA

From both technological and fundamental view points, studies of structure and dynamics of confined block copolymers (BCPs) is of great interest. Owing to their self-assembly to form nano-scale domains, they are now at the cutting edge of nanotechnology. They currently find applications in many fields which include but not limited to; data storage media, biosensors, drug delivery, plasmonics, anti–reflection coating, nanophotonics, infiltration membranes, opto-electronics and nanopatterning. In almost all of these applications, BCPs are constrained within nano-scale spaces of different dimensions. The question of how dimensionality of nanoconfinement affects the morphologies and the dynamical properties such as glass transition temperature of BCPs therefore become weighty. In this work the impact of 1–and 2–dimensional (2D) confinement on the structure and dynamics of asymmetric poly(styrene-*b*-1,4-isoprene) P(S-*b*-I) diblock copolymer is investigated by a combination of Scanning Electron Microscopy (SEM), Atomic Force Microscopy (AFM), Grazing–Incidence Small–Angle X–ray Scattering (GISAXS), and Broadband Dielectric Spectroscopy (BDS). 1D confinement is achieved by spin coating the P(S-*b*-I) to form nanometric thin films on silicon substrates, while in the 2D confinement, the copolymer is infiltrated into cylindrical anodized aluminum oxide (AAO) nanopores. Figure 3.1 shows the SEM and GISAXS results for the sample confined in AAO pores and in thin films respectively.

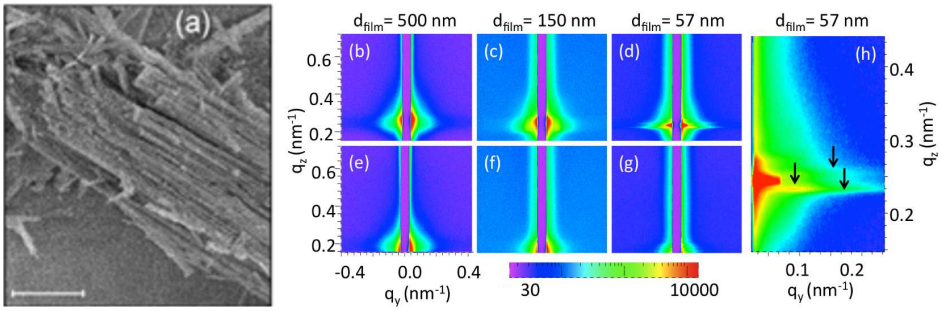

Figure 3.1:
SEM micrograph of P(S-*b*-I) nanorods after removing AAO template having an average pore diameter of 150 nm. Scale bar: 2μm (a). 2D GISAXS images for the samples having film thicknesses of 500 nm (b, e), 150 nm (c, f) and 57 nm (d, g and h). (b, c, d, and h) represent images taken at $\alpha_i = 0.14°$ while (e, f, and g) were taken at $\alpha_i = 0.08°$. Except (h), all the images have the same q_y and q_z scales as shown in (e). (h) is an enlargement of a section in (d) within the q_y and q_z ranges depicted in the axis. The arrows in (g) indicate the DBRs of P(S-*b*-I) while the very high intensity region is due to the specularly reflected beam. The intensity scale is shown at the bottom of (f) and (g).

The morphology of P(S-*b*-I) contained in AAO matrix having mean pore sizes of 150 nm as revealed by SEM (Fig. 1a) shows exposed copolymer nanorods after dissolution of the confining matrix. The GISAXS results shown in Fig. 3.1, represent images taken at two incident angles, namely $\alpha_i = 0.14°$ and $\alpha_i = 0.08°$. The former which is between the critical angles of total external reflection of P(S-*b*-I) ($\alpha_{pc} = 0.11°$) and that of Si substrate ($\alpha_{Si} = 0.16°$) allows the X–rays

to penetrate the entire film thickness, hence enabling detection of the inner film structures while the latter probes the region near the film surface because $\alpha_i < \alpha_{cp}$. The intensity in all images mostly extends along the q_y–axis. A zoomed image of Fig. 3.1 (d) shown in Fig. 3.1 (h) point to the possible existence of out–of–plane diffuse Bragg rods (DBRs) at higher q_y values in addition to the first–order out–of–plane DBRs at $q_y \approx 0.1\text{nm}^{-1}$ as indicated by the vertical arrows. This arrangement is akin to that of standing cylinders. We can therefore conclude that samples of P(S-*b*-I) ($f_{PI} = 0.73$) spin cast on Silicon wafers with native oxide layer and annealed at 423 K in high vacuum (10^{-6} mbar) feature standing cylinders when the film thickness is approximately above 50 nm. The AFM results (not shown) shows that reducing the films thickness to ~ 30 nm results to mainly lying cylinders.

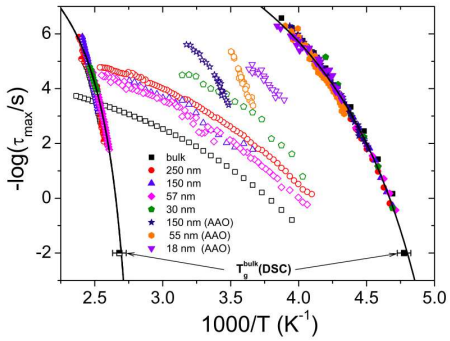

Figure 3.2:
Activation plot of the relaxation rates corresponding to the segmental mode of the isoprene blocks (filled symbols), normal mode of the isoprene blocks (open symbols) and segmental mode of the styrene blocks (half-filled symbols) for the sample in the bulk state, and when confined in thin films and in AAO nanopores with film thickness and pore sizes as indicated in the legend. Bulk PI and PS-homopolymers with M_w = 55000 (PI–55) and 58900 (PS–58) gram/mol, respectively are included for comparison (squares). The bulk Tg values of PI and PS determined by DSC at a scanning rate of 10 K/min are also shown. The solid lines are VFT fits to the experimental data.

Molecular dynamics under 1D and 2D geometrical constraints have been studied by BDS. The segmental relaxation of isoprene and styrene blocks and the chain dynamics due to fluctuation of the end-to end vector in isoprene blocks are observed. Fig. 3.2 shows that all the data from different film thicknesses and pore sizes for the segmental/structural relaxation of either styrene (higher T) or isoprene blocks (lower T) collapse to a single curve regardless of the dimensionality and the finite-sizes of confining geometries utilized in this study. This data follows Vogel,Fulcher Tammann (VFT) type of thermal activation. The lines in Fig. 3.2 represent the fit of the data by the VFT equation. The T_g, which is the temperature at which $\tau = 100$ s directly coincides within experimental accuracy with that of bulk homopolymers determined calorimetrically. Therefore confinement of asymmetric P(S-*b*-I) in 1D (d_{film} = (250–30 nm)) and in 2D(d_{pore} = (150 –18 nm)) has no impact on the T_g of the respective blocks. However, the chain dynamics of the isoprene blocks is affected by both the size and dimensionality of confinement. This is attributed to the osmotic constraints and the interaction of the chains with the substrate. This project is funded by SFB/102 and DFG (Pa771/10-1).

[1] W. K. Kipnusu, M. M. Elmahdy, E. U. Mapesa, J. Zhang, W. Böhlmann, D.-M. Smilgies, C. M. Papadakis, F. Kremer, *ACS Appl Mater Inter*, accepted, DOI: 10.1021/am506848s

3.2 Simulations of solvent vapor annealing of cylinder-forming block copolymer films

A. V. Berezkin, D. Posselt[1], I. I. Potemkin[2], C. M. Papadakis

[1] Roskilde University, IMFUFA, Denmark

[2] Physics Department, Lomonosov Moscow State University, Russia

Ordered block copolymer films are promising as functional templates for block copolymer lithography, molecular biology, colloid science etc. For many of these applications, domains in the film need to have both, long-range order and a properly controlled orientation. To remove dislocations and expand the correlation length of the domain ordering in copolymer films, solvent vapor annealing (SVA) is widely used. In this method, the copolymer film, being exposed to the vapor of a solvent, swells up to certain controlled degree, and then dries at a controlled rate. The main effect of SVA is related to the decay of the glass transition temperature of polymers upon swelling, which facilitates relaxation of the domain structure towards the equilibrium morphology. However, also the final structure and the domain orientation are strongly influenced by the conditions of SVA, among them the solvent evaporation rate and the polymer-solvent interactions. To clarify the general mechanism of SVA, we simulated drying of thin films of asymmetric cylinder-forming A-*block*-B copolymers.

The simulations are performed using dissipative particle dynamics (DPD) [1, 2], a coarse-grained molecular simulation technique, which reproduces both the long-range Navier-Stokes hydrodynamics and the Flory-Huggins theory. The Flory-Huggins parameter (χ_{ij}) for two molecular moieties or components is related to the repulsion parameter a_{ij} of DPD particles i and j via the equation

$$\chi_{ij} = \frac{(0.306 \pm 0.003)(a_{ij} - 25)}{1 + 3.9N^{-0.51}},$$

where N is the number of statistical segments (particles) in the polymer molecule.

The simulation proceeds in a rectangular periodic box of size $l_x \times l_y \times l_z = 50 \times 50 \times 70$, as shown in Fig. 3.3a, containing initially three components: copolymers of length $N = 20$ with block lengths $N_A = 5$ and $N_B = 15$, solvent (S-particles) and gas (G-particles). At the bottom of the box, the homogeneous copolymer/solvent mixture with an initial volume fraction of solvent, ϕ_{S0}, is located, while the space above the film is filled with a mixture of S and G particles at the ratio 1:3. The bottom and upper sides of the box are impenetrable for all particles and non-selective to A and B blocks.

During the molecular dynamics simulation, all molecules are able to diffuse, but the solvent particles being found at a distance larger or equal to a height δ above the film surface (i.e. in the gas phase) are irreversibly transformed into gas particles to simulate solvent vapor dilution by the solvent-free gas flow. As the result, the film dries due to gradual removal of solvent. The final film thickness, h_0, was varied in a range from 5 to 30 particle sizes (r_c), but in equilibrium, perpendicular cylindrical domains are stable only at $h_0 = 5$, while at larger thicknesses, the cylinders prefer to be parallel to the substrate. Our simulations revealed a wide range of conditions, where SVA stabilizes perpendicular and well-ordered cylinders even in thick films with $h_0 = 30$.

Moreover, we found a mechanism of domain ordering that notably distinguishes from those observed in recent mean-field calculations with dynamic density functional theory [3]. Our simulations also start with swollen disordered films. Upon the solvent evaporation the

film stays disordered up to a certain moment. When the degree of swelling drops below $h(t)/h_0 = 1.25$, a hexagonal ordering of spherical domains starts near the interface. Then the spheres are transformed into perpendicular hexagonally packed cylinders.

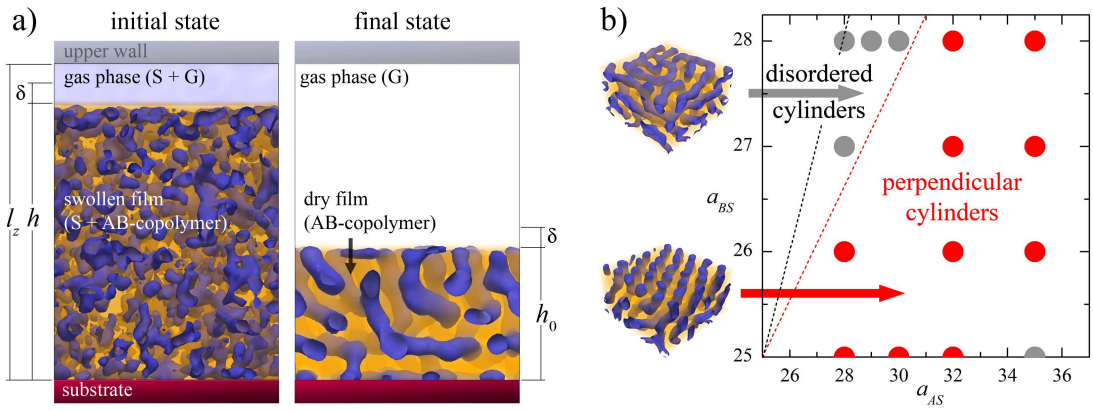

Figure 3.3:
Scheme of the simulation box a) and effect of polymer-solvent interactions on the domain ordering. Black dashes show the non-selective solvent conditions ($a_{AS} = a_{BS}$) b).

We have shown that the fast solvent evaporation is a necessary but not sufficient condition for perpendicular alignment of cylinders. Another necessary condition is the disorder-to-order transition during the solvent evaporation step. This can be attained when the initial solvent concentration is in the range $0.2 \leq \phi_{S0} \leq 0.5$ and at moderate block segregation with a repulsion parameter $a_{AB} = 35$. Additionally at weak segregation ($a_{AB} = 30$) or at too strong block segregation ($a_{AB} \geq 40$), the films stay disordered after SVA because the driving force of microphase separation is too weak or because the relaxation of microdomain structure is too slow, respectively. It was found that the perpendicular cylinder alignment also requires a certain solvent selectivity for the long block or a slightly elevated physical adsorption of this block at the free film interface. This is probably necessary to compensate entropy-driven adsorption of short blocks at the film surfaces, revealed by recent systematic theoretical studies of confined block copolymer films. The region of polymer-solvent repulsion parameters resulting in ordered perpendicular cylinders is shown in Fig. 3.3b.

The vertical alignment of domain interfaces in a gradient of solvent concentration may be driven by the gradient of interdomain surface tension, and can be explained by Gibbs-Marangoni effect. Preceding simulations have already demonstrated, thar similar effects can be observed non only in copolymeric films, but also in simple mixtures of homopolymers [4].

[1] P. Espanol, P. B. Warren, *Europhys. Lett.* **30**, 191 (1995)

[2] R. D. Groot, P. B. Warren, *J. Chem. Phys.* **107**, 4423 (1997)

[3] S. P. Paradiso, K. T. Delaney, C. J. García-Cervera, H. D. Ceniceros, G. H. Fredrickson, *ACS Macro Lett.* **3**, 16 (2014)

[4] G. A. Buxton, N. Clarke, *Europhys. Lett.* **78**, 56006(5) (2007)

3.3 Complex nanostructure induced by micro-phase separation in thin films

J. Zhang, K. Kyriakos, S. Jaksch, J. Perlich[1], D. Posselt[2], D.-M. Smilgies[3], C. M. Papadakis

[1] DESY, Hamburg, Germany
[2] Roskilde University, IMFUFA, Denmark
[3] Cornell University, Ithaca, NY, USA

Nanostructures obtained from self-assembly of block copolymers have attracted much attention due to their simple and cost-effective characteristics with many promising applications in nanotechnology, such as ultrahigh-density data storage media, molecular sieves, dielectric reflectors, and sensors. Although self-assembly of block copolymers offer a rich variety of periodic nanoscale patterns, and researchers have succeeded in finding conditions that lead to very long range order of the domains, there are still major challenges to manipulate the self-assembly process to realize these promising applications, such as creating a specific structure.
Binary blends of diblock copolymers exhibit both, micro- and macrophase separation, and offer the possibility to create thin films with complex structures. In the bulk, they form macroscopic domains which are either rich in long diblock copolymers and thus form thick lamellae or rich in short diblock copolymers which form thin lamellae, provided the molar masses are sufficiently different [1]. The reason is that the short diblock copolymers form a brush at the interfaces of the lamellae formed by the long diblock copolymers which results in inhomogeneous stretching of the long diblock copolymers and thus a loss of entropy. For a sufficiently high volume fraction of short diblock copolymers, a certain fraction forms separate domains which form thin lamellae. In thin film geometry, the macrodomains may be separated laterally or along the film normal, for instance. Moreover, the interactions at the film interfaces may have an influence on the phase behavior.
In the present work, we investigate binary blends of compositionally symmetric poly(styrene-*b*-butadiene) (P(S-*b*-B)) diblock copolymers having molar masses of 215.8 kg/mol $(\text{P(S-}b\text{-B)})_\alpha$ and 28 kg/mol $(\text{P(S-}b\text{-B)})_\beta$ [3]. In thin film geometry, the high and the low molar mass copolymers form perpendicular or parallel lamellae, respectively [2]. Macrophase separation has been observed in the bulk for volume fractions of the low molar mass diblock copolymer, $\phi_\beta = 0.3 - 0.7$ [1].

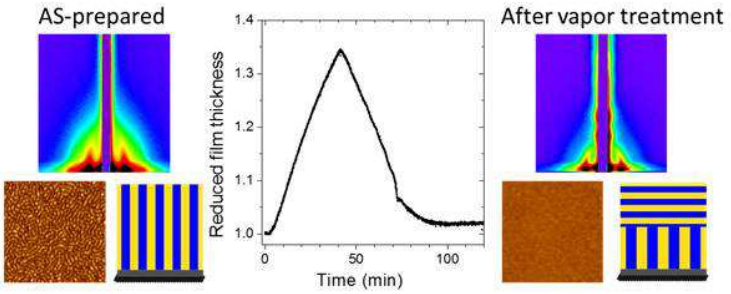

Figure 3.4:
2D GISAXS maps and AFM images of a thin film from a blend with $\phi_\beta = 0.7$ together with schematic side views of the structures. Left: as-prepared film, right: solvent-vapor annealed film. In the center, the film thickness profile during SVA is shown.

Thin films having different mixing ratios were prepared by spin coating of silicon wafers. The film thicknesses were 190 ± 5 nm. The thin film morphologies were studied by means of grazing-incidence small-angle X-ray scattering (GISAXS) at BW4, HASYLAB at DESY, and at beamline

D1, CHESS at Cornell University. The incident angles were chosen above and below the critical angle of total external reflection, i.e. the signal is either averaged over the entire film thickness or it is surface-sensitive, respectively. The surface textures were investigated using atomic force microscopy (AFM). Solvent vapor annealing (SVA) was carried out using a home-made cell. Swelling was accomplished by letting cyclohexane vapor flow through the sample cell for 35 min. Drying of the film was performed over 55 min by increasing the flow of dry N_2 gas and by simultaneously decreasing the flow of CHX vapor to 0.
Figure 3.4 shows the 2D GISAXS map of a binary blend thin film with $\phi_\beta = 0.7$. It displays Bragg rods (BRs) which means that the film predominantly features perpendicular lamellae. This lamellar structure is corroborated by the AFM image shown in the bottom left of Fig. refpapadakis14-rep2-fig1. Interestingly, the film is not laterally macrophase-separated, as is expected from the bulk phase behavior. GISAXS maps measured at different locations are indistinguishable, i.e. no macroscopic inhomogeneities are present. Similar behavior is found for thin films with $\phi_\beta = 0 - 0.7$. At higher ϕ_β values $(0.9 - 1)$, parallel lamellae are observed instead.

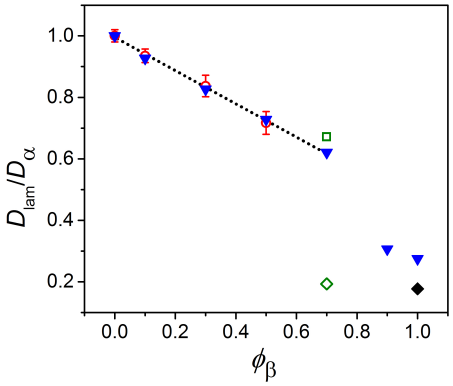

Figure 3.5:
Reduced lamellar thickness in dependence on ϕ_β. D_α denotes the lamellar thickness of the pure long diblock copolymer. Solid triangles: from GISAXS, open circles: from AFM, both from perpendicular lamellae before SVA. The dotted line indicates the linear decrease. Solid diamond: from GISAXS before SVA, parallel lamellae. Values after SVA are given as an open square (perpendicular lamellae) and as an open diamond (parallel lamellae).

The lamellar thicknesses, D_{lam}, were obtained from the q_y position of the Bragg rods (Fig. 3.5). An intriguing result is that D_{lam} decreases linearly for $\phi_\beta = 0.1 - 0.7$. This is a great advantage for nanofabrication applications using diblock copolymer thin films as a template, because the periodicity of the nanostructure can simply be tailored by mixing two diblock copolymers instead of having to use *de novo* synthesized diblock copolymers with the appropriate molar mass.
To induce the expected macrophase separation, the thin film with $\phi_\beta = 0.7$ was subjected to SVA, resulting in the film thickness profile shown in the center of Fig. 3.5. The GISAXS map of the annealed film displays not only BRs, but also diffuse Bragg sheets (DBSs) which are due to parallel lamellae (Fig. 3.5 on the right). The AFM image is featureless (Fig. 3.4 on the right), and in the surface-sensitive GISAXS experiment, the BRs are not present. An analysis of the lamellar thicknesses corresponding to the BRs and the DBSs shows that perpendicular lamellae rich in long diblock copolymers are present near the substrate, whereas parallel lamellae rich in short diblock copolymers form near the film surface.
We conclude that, during the fast spin-coating process, macrophase separation is hindered, presumably because it requires long-range mass transport. SVA enables the expected macrophase separation, resulting in complex structures with macrophase separation along the film normal.
This project is funded by DFG (Pa771/10-1).

[1] C. M. Papadakis, K. Mortensen, D. Posselt, *Eur. Phys. J. B* **4**, 325 (1998).

[2] P. Busch, D. Posselt, D.-M. Smilgies, M. Rauscher, C. M. Papadakis, *Macromolecules* **40**, 630 (2007).

[3] J. Zhang, D. Posselt, D.-M. Smilgies, J. Perlich, K. Kyriakos, S. Jaksch, C. M. Papadakis, *Macromol. Rapid Commun.* **35**, 1622 (2014)

3.4 A small-angle X-ray scattering study of liquid crystals having propylene carbonate units

A. Eisele[1], K. Kyriakos, K. Raftopoulos, C. M. Papadakis, B. Rieger[1]

[1] WACKER-Lehrstuhl für Makromolekulare Chemie, TU München, Garching, Germany

Liquid crystals have gained remarkable attraction because of their anisotropic properties. Besides their use in displays and information storage devices, they can be used as solid electrolytes in Li-Ion batteries. Nanosegregation which leads to the formation of nanoscale ion pathways may enhance ionic conductivity [1].

In the study of liquid crystals, small- and wide-angle X-ray scattering (SAXS/WAXS) are useful tools to probe crystalline and mesoscopic structures, e.g. the packing and the orientation of the molecules in the liquid crystalline state [2].

For our X-ray studies, we have chosen a liquid crystalline molecule with a perfluorinated aromatic ring as mesogenic core and a cyclic carbonate moiety. The length of the alkyl chain is C_{10} (Fig. 3.6a). Cyclic carbonates have a high dipole moment, so they enhance nanosegregation and the formation of a liquid crystalline state.

To measure the structural changes, the samples were placed between thin mica sheets (∼5-7 μm). They were heated above the isotropization temperatures and then cooled down with a rate of -10 K/min. Sample-detector-distances (SDD) of 101 mm (WAXS) and 401 mm (SAXS) were used, resulting in a q-range of 0.01 to 2.5 $Å^{-1}$ (q is the momentum transfer). The 2D images obtained were azimuthally averaged. The layer spacing was determined from a Lorentzian fit to the first-order Bragg reflection and Bragg's law, $d = 2\pi/q_0$.

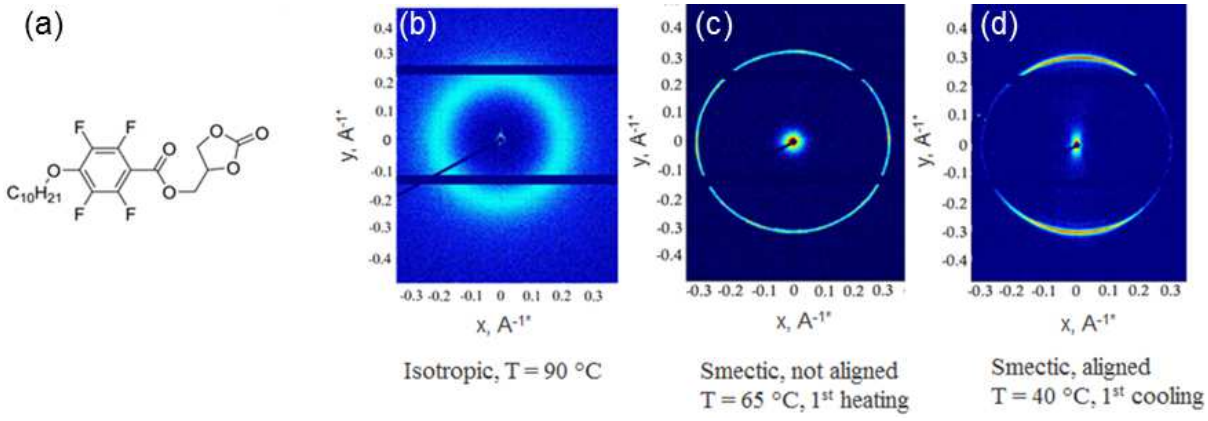

Figure 3.6: We present the (a) chemical structure of the investigated molecule and (b-d) 2D SAXS patterns of the liquid crystalline molecules; i.e. (b) Isotropic state at 90 °C, (c) smectic phase not aligned during 1^{st} heating, (d) aligned in smectic A phase upon cooling from the isotropic temperature. The horizontal stripes of lower intensity are due to the blind regions of the detector.

Figs. 3.6 (b-d) show the 2D SAXS images of the molecule at different temperatures. In the isotropic phase, the 2D SAXS profile exhibits a blurred ring (Fig. 3.6b). This is an indication that the molecules do not have a preferred orientation. When cooled from the isotropic melt, the 2D SAXS pattern shows an inhomogeneous intensity distribution of the diffraction rings along the y-axis (Fig. 3.6d). The sharpness of the ring is an indication for a strongly preferred orientation and an alignment in a smectic phase. This observation was confirmed by polarized optical microscopy, where a fan-shaped texture could be seen. For the non-aligned samples the diffraction rings are homogeneous (Fig. 3.6c). To show the influence of the lithium salt concentration

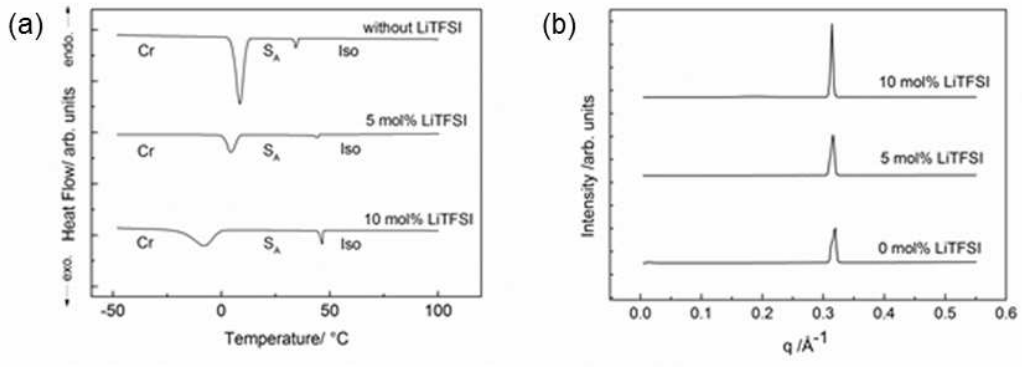

Figure 3.7: (a) DSC heat flow traces of the mixtures with different amounts of LiTFSI recorded during 1^{st} cooling cycle. (b) SAXS curves for the mixtures with different amounts of LiTFSI.

on the molecular packing and the thermal behavior of the molecules, SAXS measurements and differential scanning calorimetry (DSC) with various amounts of Li salt were performed. As Li salt, LiTFSI (lithium bis(trifluoro-methanesulfonyl)-imide) was chosen. The investigated mixtures have a monotropic liquid crystalline phase, i.e. the formation of a liquid crystalline phase is only observed during cooling from the isotropic melt. The cooling scans show that increasing amounts of LiTFSI broaden the temperature range of the mesophase from a range of 25.8 °C without LiTFSI up to a range of 55.6 °C with 10 mol% LiTFSI (Fig. 3.7a). This is an indication that the Li-salt is incorporated into the polar parts of the molecule. The incorporation of the salt enhances phase segregation as it makes the polar parts even more polar.
From the SAXS curves, we calculate the average layer distance. Without LiTFSI, the substance has an intermolecular layer distance of 19.6 Å. Increasing amounts of Li-salt increases the intermolecular distance to 20.1 Å for the mixture with 10 mol% LiTFSI (Fig. 3.7b).
From the layer spacing and the length of the molecule (l = 24.7 Å), the d/l ratio was determined. The d/l ratio gives an indication about the packing structure of the molecules. A d/l ratio $<$ 1 points to a strongly interdigitated monolayer. The Li-salt mixtures exhibit a d/l ratio of 0.79 without LiTFSI and 0.81 with 5% and 10% of LiTFSI, respectively. Hence, the molecules align in an interdigitated smectic monolayer.
The study was carried out with molecules with varying length of the alkyl chain and different aromatic cores. The SAXS experiments demonstrate the spontaneous alignment in a smectic phase when the substances are cooled from the isotropic melt and that fluorination of the aromatic core enhances the alignment in a smectic phase [3].
Combining the results of the SAXS and the ionic conductivity measurements, we expect to get a deeper insight into the conductivity mechanism of liquid crystalline electrolytes.

Funding from Consortium für elektrochemische Industrie der Wacker Chemie AG is gratefully acknowledged.

[1] K. Hoshino, K. Kanie, T. Ohtake, T. Mukai, M. Yoshizawa, S. Ujiie, H. Ohno, T. Kato, *Macromol. Chem. Phys.* **203**, 1547 (2002)

[2] A. de Vries, *Mol. Cryst. Liq. Cryst.* **131**, 125 (1985)

[3] A. Eisele, K. Kyriakos, R. Bhandary, M. Schönhoff, C. M. Papadakis, B. Rieger, *J. Mater. Chem. A* **3**, 2942 (2015)

3.5 Optical properties of the low band gap polymers PBDTT-FTTE and PBT7

F. C. Löhrer, S. Guo, P. Müller-Buschbaum

Organic photovoltaics are gaining impact as a feasible alternative to conventional silicon solar cells. Using polymers as active material has several potential advantages, for instance reduced production costs and an increased device flexibility. A prominent example is poly(3-hexylthiophene) (P3HT), which has been diligently investigated in the last years. However, efficiencies of solar cells based on P3HT stay far below those of competing inorganic solar cells. In order to enhance the solar cell performance, recent research efforts focus on identifying new, low band gap polymers. This has led to the development of high-efficiency materials such as poly[[4,8-bis[(2-ethylhexyl)oxy]benzo[1,2-b:4,5-b']dithiophene-2,6-diyl][3-fluoro-2-[(2-ethylhexyl)carbonyl]thieno[3,4-b]thiophenediyl]] (PTB7) with solar cell efficiencies close to 10 %. [1] PTB7 belongs to a group of push-pull copolymers based on benzo[1,2-b:4,5-b0]dithiophene (BDT) and thieno[3,4-b]thiophene (TT) units called PBDTTTs. These polymers have low band gaps and therefore show an increase in the absorption of light. Functional groups can be introduced in order to increase the efficiency even further. A high degree of fluorination shows favorable effects on the solar cell performance, as observed recently. [2] Additionally, exchanging oxygen with thiophene units in PTB7 leads to a high efficiency polymer called poly[4,8-bis(5-(2-ethylhexyl)thiophen-2-yl)benzo[1,2-b:4,5-b']dithiophene-2,6-diyl-alt-(4-(2-ethylhexyl)-3-fluorothieno[3,4-b]thiophene-2-carboxylate] (PBDTT-FTTE) with a reduced highest occupied molecular orbital (HOMO) and therefor an even lower band gap. Reported record efficiencies for PBDTT-FTTE based solar cells broke the important barrier of 10 %. [3]
In order to acquire a better understanding of the underlying fundamental mechanisms in different PBDTTT polymers, we investigate two of their most promising examples, namely PTB7 and PBDTT-FTTE, regarding their optical and morphological properties. Figure 3.8 shows the structures of the respective monomer units, with carbon atoms depicted in white, oxygen in red, sulfur in yellow and fluorine atoms in magenta.

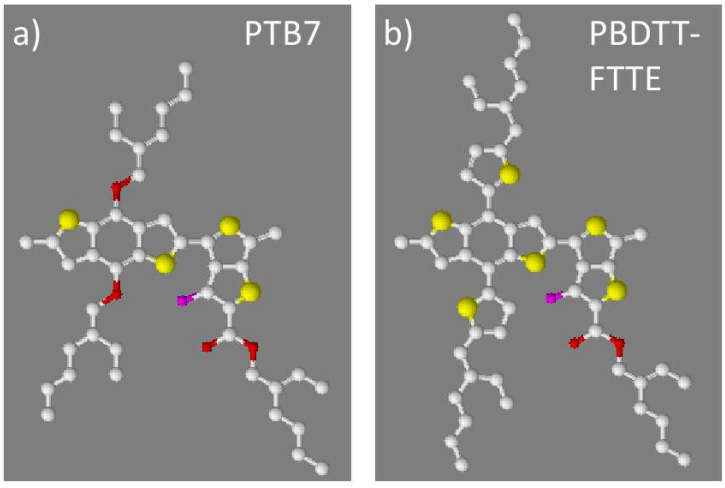

Figure 3.8:
Chemical structures of monomer units of PTB7 and PBDTT-FTTE with carbon (white), oxygen (red), sulfur (yellow) and fluorine atoms (magenta)

For solar cell application, the respective polymers are mixed with the high-efficiency electron acceptor [6,6]-phenyl C_{71}-butyric acid methyl ester ($PC_{70}BM$) using solvents such as 1,2-dichlorobenzene (oDCB). Thin films are prepared out of solution via spin coating. UV-vis absorption measurements performed on thin films of varying PBDTT-FTTE / $PC_{70}BM$ mixtures are shown in figure 3.9. The absorption values are normalized to the absorption maximum around 710 nm. Pure PBDTT-FTTE exhibits pronounced peaks at about 320 nm, 640 nm and 710 nm. [3] Mixing with $PC_{70}BM$ leads to an additional absorption at 480 nm typical for the fullerene. [4] The absorption peak positions of the mixtures are in good accordance with earlier measurements by Liao et al.. [3]

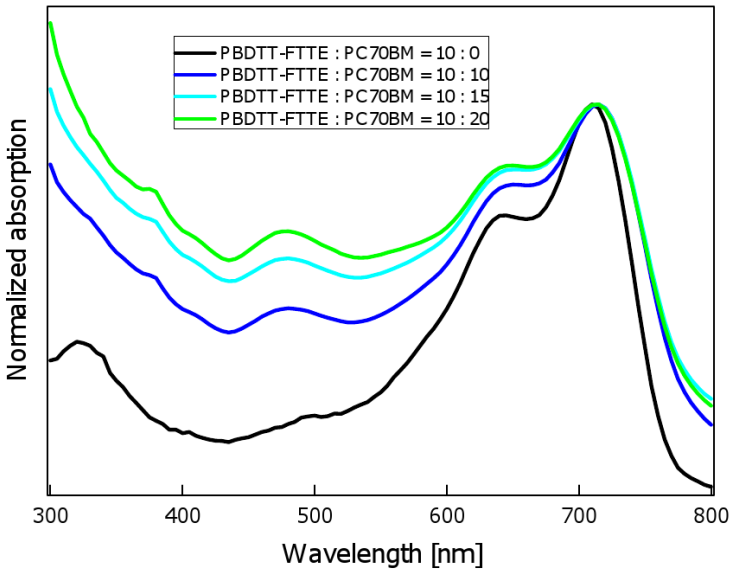

Figure 3.9:
UV-visible absorption spectra of thin films of mixtures of PBDTT-FTTE with $PC_{70}BM$, normalized to the highest absorption at the intensity maximum around 710 nm

A deeper look into the absorption spectra of thin films varying the thin film composition based on PBDTT-FTTE and PTB7 is ongoing. These findings will be compared to the ones already established concerning P3HT. Future morphology studies will apply characterization techniques including optical and atomic force microscopy, X-ray reflectometry and diffraction as well as GIWAXS/GISAXS. First exploratory solar cells have been built and will be further examined with respect to the dependence of the power conversion efficiency on parameters such as the active layer composition and morphology.

[1] Z. C. He , C. M. Zhong, S. J. Su, M. Xu, H. B. Wu, Y. Cao, *Nat. Photonics* **6**, 591 (2012)

[2] S. Guo, J. Ning, V. Körstgens, Y. Yao, E. M. Herzig, S. V. Roth, P. Müller-Buschbaum, *Adv. Energy Mater.* (2014)

[3] S.-H. Liao, H.-J. Jhuo, P.-N. Yeh, Y.-S. Cheng, Y.-L. Li, Y.-H. Lee, S. Sharma, S.-A. Chen, *Sci. Rep.* **4**, 6813 (2014)

[4] Y. He, Y. L, *Phys. Chem. Chem. Phys.* **13**, 1970-1983 (2011)

3.6 Enhanced interchain coupling in co-solvent modified PEDOT:PSS polymeric electrodes

C. M. Palumbiny, F. Liu[1], T. P. Russell[1], A. Hexemer[2], C. Wang[2], P. Müller-Buschbaum[2]

[1] University of Massachusetts Amherst, Amherst, USA
[2] ALS, LBNL, Berkeley, USA

Since the invention of organic electronics, thin films of organic semiconducting polymers have attracted immense interest amongst researchers. The possibility of realizing thin film devices with outstanding properties, such as flexibility, light weight, low cost and easy up-scaling, opens a market for these electronic devices. Strong focus in research lies within the thin films preparation, e.g. up-scalable printing together with a profound understanding of the device performances. In this context, morphological investigations lead to a better understanding of the complex material behavior of polymeric thin films.
To this day, most investigations are performed on laboratory-based techniques such as spin-coating. One of the greatest advantages of organic electronics over classical Si-based electronics however, is the possibility of roll-to roll fabrication. It is important to keep in mind that depending on the deposition method used, the inner film morphology and thereby the material behavior is changed.[1]
In order to realize the goal of flexible devices and scaling in roll to roll processes, material which are stable upon bending are desired. In the field of organic electronics the commonly used transparent electrode is indium tin oxide (ITO). Due to its brittleness, this material has been shown to lead to a decrease in device performance upon bending. Therefore, there is a strong need for replacing ITO as an electrode. Poly(3,4-ethylenedioxythiophene):poly(styrenesulfonate)(PEDOT:PSS) is one of the most promising candidates in this context. Conveniently, PEDOT:PSS is already implemented as a hole injection layer in standard electronic devices such as organic solar cells or organic light emitting diodes. Further, PEDOT:PSS can be modified via secondary doping to increase its conductivity from $\sim 0.1\ S/cm$ to $\sim 1000\ S/cm$, reaching the level of ITO conductivity ($\sim 3000\ S/cm$).[1]

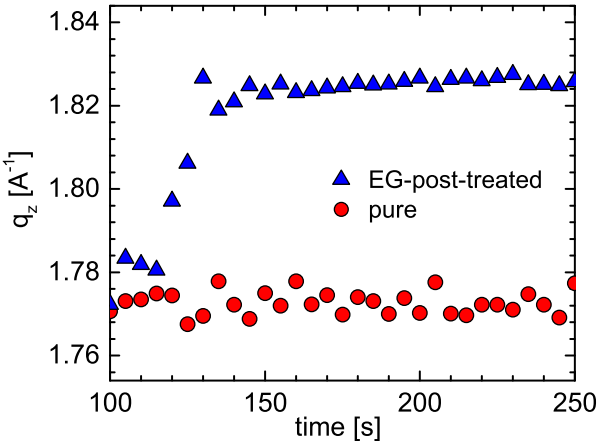

Figure 3.10:
Time evolution of the $\pi - \pi$ stacking distance of PEDOT molecules in pure and EG-post-treated films. The increase seen with EG-post-treatment relates to a decrease in $\pi - \pi$ stacking distance and hence an increased interchain coupling.

In this work, printed PEDOT:PSS films were characterized using grazing incidence wide angle X-ray scattering.[2] We investigate the film evolution in terms of nanomorphology and crystallinity in-situ during the printing process. The PEDOT:PSS polymer mixture is printed from

water-based solution at $50\ ^{\circ}C$. With the evaporation of water from the thin film, PEDOT crystallization is observed resulting in a scattering signal originating from the $\pi - \pi$ stacking of the PEDOT molecules. This scattering signal is centered at $1.77\ \mathring{A}^{-1}$, which is related to a $\pi - \pi$ stacking distance of $3.6\ \mathring{A}$ as shown in Fig. 3.10. After an annealing step of 10 min at $140\ ^{\circ}C$ the PEDOT:PSS thin film was post-treated with the co-solvent additive ethylene glycol (EG) by printing the solvent onto the PEDOT:PSS film at an elevated temperature of $95\ ^{\circ}C$. Upon the EG-post-treatment, the scattering signal is shifted from $1.77\ \mathring{A}^{-1}$ to $1.83\ \mathring{A}^{-1}$ which is related to a shift of the $\pi - \pi$ stacking distance from $3.6\ \mathring{A}$ to $3.4\ \mathring{A}$. The decrease of $\pi - \pi$ stacking distance leads to an increase of the interchain coupling between PEDOT molecules as shown in Fig. 3.10.[3]
Besides the decrease of $\pi - \pi$ stacking distance between PEDOT molecules in the PEDOT:PSS system upon EG-post-treatment, changes in the scattering from PSS molecules are observed. As depicted in Fig. 3.11, the scattering position of the PSS molecules is increased from $1.24\ \mathring{A}^{-1}$ to $1.29\ \mathring{A}^{-1}$ with EG-post-treatment of the film. This increase in the scattering position is related to a decrease in the $\pi - \pi$ stacking distance of PSS molecules from $0.51\ \mathring{A}$ to $0.49\ \mathring{A}$.[3]

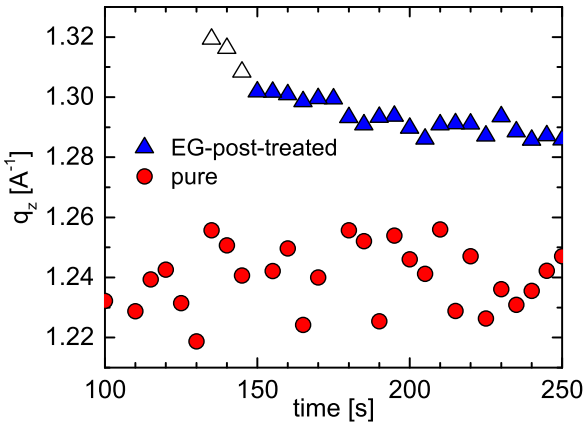

Figure 3.11:
Time evolution of the $\pi - \pi$ stacking distance of PSS molecules in pure and EG-post-treated films. The larger scattering distance with EG-post-treatment relates to smaller $\pi - \pi$ stacking distance and hence an increased interchain coupling, similar to the the trend observed for PEDOT $\pi - \pi$ stacking.

In summary, we could show that the use of the co-solvent additive EG in PEDOT:PSS systems leads to a decrease in $\pi - \pi$ stacking distance of PEDOT as well as PSS molecules. Since PEDOT is the conductive part of the polymer mixture, the decrease in its $\pi - \pi$ stacking distance and thereby the increase in interchain coupling of the PEDOT molecules, leads to the enhancement in conductivity of co-solvent modified PEDOT:PSS thin films.

[1] C. M. Palumbiny, C. Heller, C. J. Schaffer, V. Körstgens, G. Santoro, S. V. Roth, P. Müller-Buschbaum, *J. Phys. Chem. C* **118**, 13598 (2014)

[2] P. Müller-Buschbaum, *Adv. Mater.* **26**, 7692 (2014)

[3] C. M. Palumbiny, F. Liu, T. P. Russell, A. Hexemer, C. Wang, P. Müller-Buschbaum, *submitted*

3.7 Grazing incidence resonant small angle x-ray scattering (GI-RSAXS) of conducting polymers

M. Coric[1], N. Saxena, J. Wernecke[2], S. Langner[2], M. Krumrey[2], P. Müller-Buschbaum and E. M. Herzig[1]

[1] MSE, Garching, Germany
[2] BESSY, Berlin, Germany

In recent time organic photovoltaics has emerged to a very interesting and largely investigated scientific field. With its broad and tunable absorption spectra combined in thin films of hundred of nanometers, it has the potential to be integrated in a vast variety of applications. These facts combined with cheap production costs that are realistic in the future, present organic photovoltaics as a good alternative to conventional silicon solar cells. Despite these advantages there are still some challenges that have to be tackled. Although in the last year new records for efficiencies for organic solar cells were achieved above 10% [1] in the lab, the over all performance of OPV cannot yet compete with silicon based solar cells.

One crucial issue is the morphology of the film, meaning the inner composition of the organic materials within the solar cell. As the excitons have only a limited diffusion path until they recombine, pathways have to be created within the inner morphology that guarantee direct percolation pathways for the charges to the respective electrodes to extract them. Such paths are only guaranteed if the inner composition is well distributed. But yet the understanding of how these mechanisms work is not quite understood especially how to induce a certain morphology that is more favorable for the use in organic solar cells.

In this work a ternary system is investigated, consisting of two polymers and a fullerene. One of the polymers is non-conducting. This third component is used to influence the morphology, investigating to which extent an additional component can influence it. Investigation of the structural changes are quite difficult. An advanced and sophisticated method are scattering experiments done at synchrotrons. In the last few years the use of X-ray for investigation of morphological structure of polymeric thin films in photovoltaic has increased. So far mostly hard x-ray around 10 keV are used to probe the samples. The disadvantage of using hard x-rays when looking at polymers is that the scattering contrast is low and therefore the different components are difficult to distinguish from each other.

Another approach that is pursued in this work is choosing x-ray energies that are near the absorption edges of certain elements that are part of the investigated polymers. Using x-rays at energies around the absorption edge excites electrons from a ground state to a higher state. Within this state the incoming x-rays are more "sensitive" to the excited electrons. This increases the scattering contrast making it easier to distinguish between the different components of the blend within the active film of the organic solar cell. A very common element in organic compounds is carbon. Through tuning the energy of the x-ray beam around the carbon 1s absorption edge, it is possible to differentiate each polymer and offering a greater insight into film morphology and the distribution of each component within the blend [2].

For example in figure 3.12 horizontal cuts from 2D scattering patterns of the same sample are shown, measured at higher energies (black) and at the absorption edge of one element that is part of one of the polymers (red). The red datapoints in figure 3.12 show a distinct peak around $q_y \approx 0.01\,\mathrm{nm}^{-1}$. Comparing the black data points, that correspond to the same sample as the red datapoints just for a higher energy, such a peak is not visible. As the investigated sample

is the same for both energies the distinct peak arising for the measurements at the absorption edge is the result of a higher contrast between two components. This finding allows another differentiate view on the morphological investigation of polymeric blends enabling a even more detailed prediction of the inner composition of the components.

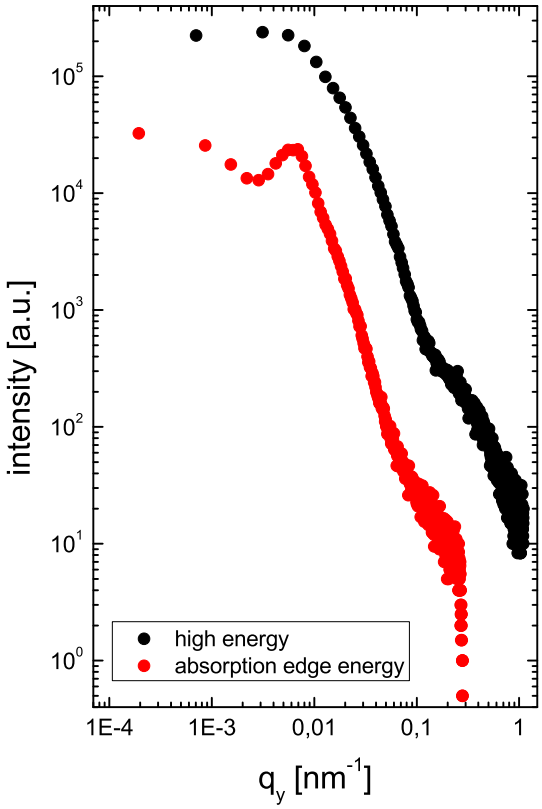

Figure 3.12:
Horizontal cuts out of the 2D scattering patterns of the same sample measured for two different energies. The black datapoints correspond to the higher energy and the red datapoints to an energy near an absorption edge of one certain element. At around $q_y \approx 0.01\,\mathrm{nm}^{-1}$ a distinct peak is visible in the red datapoints. As the peak is not present in the black datapoints, one can conclude that due to a higher scattering contrast that arises with the measurement at the absorption edge, resonant GISAXS offers a more sensitive way for investigation of morphological changes through additives.

Summarizing, using x-ray energies at the absorption edge in combination with the sophisticated technique of gracing incidence small angle x-ray scattering (GISAXS) offers an advanced method for morphological investigations [3]. It enables a higher scattering contrast between the components, offering the possibility to distinguish the different materials from each other. This again allows a more differentiate view on the material distribution within the blend.

[1] M. A. Green, K. Emery, Y. Hishikawa, W. Warta, E. D. Dunlop, *Progress om Photovoltaics: Research and Applications* **22**, 701-710 (2014)

[2] C. Wang, D. H. Lee, A. Hexemer, M. I. Kim, W. Zhao, H. Hasegawa, H. Ade, T. P. Russell, *Nano Letters* **11**, 3906-3911 (2011)

[3] M.A. Ruderer, C. Wang, E. Schaible, A. Hexemer, T. Xu, P. Müller-Buschbaum, *Macromolecules* **46**, 4491-4501 (2013)

4 Polymer films for applications in photovoltaics

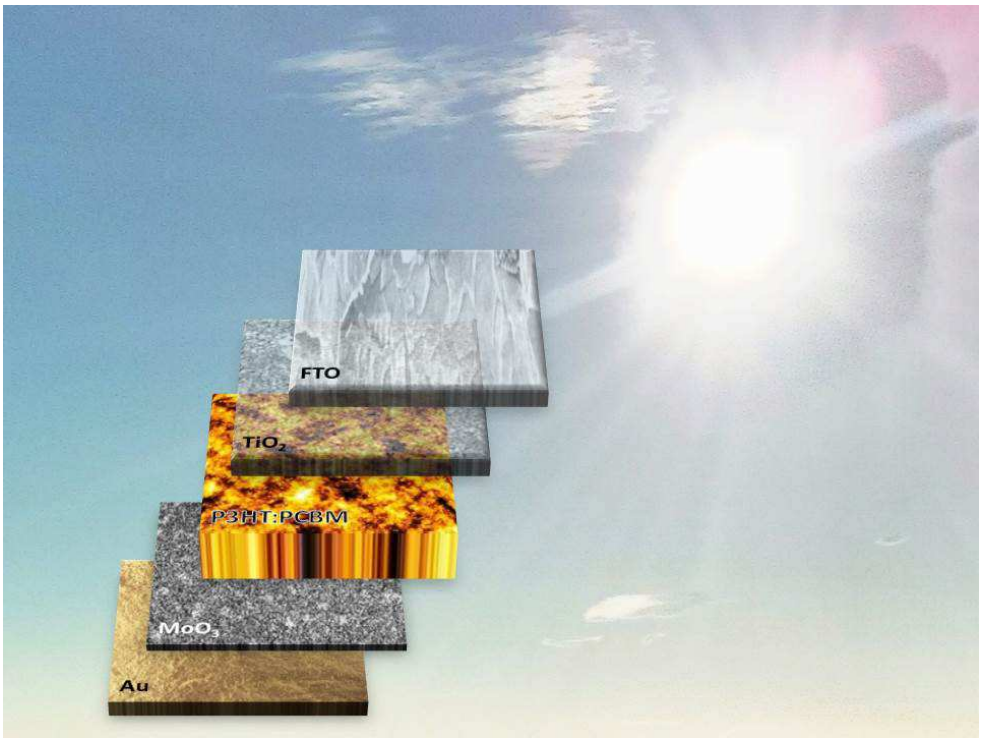

4.1 On the morphology of PCPDTBT:$PC_{71}BM$ blend thin films for organic photovoltaics

C. J. Schaffer, J. Schlipf, B. Su, E. D. Indari, S. Bernstorff[1], P. Müller-Buschbaum

[1] Elettra-Sincrotrone Trieste, Basovizza, Italy

Organic solar cells provide a highly versatile framework for future photovoltaic energy conversion due to their numerous advantages as compared to conventional solar cells. These advantages contain not only mechanical flexibility and the resulting ability to be manufactured on a large scale by printing or spray coating techniques, but also a stylistic variability allowing even for semitransparent solar cells applicable in window glasses.
In the case of so-called polymer-fullerene bulk heterojunction solar cells, the power conversion process takes place within the active layer, which is fabricated from a mature polymer:fullerene solution by an adequate coating technique such as spin coating, printing or spray coating. During evaporation of the solvent, micro phase separation occurs and causes pure interpenetrating polymer and fullerene domains with sizes on a nanometer scale which ideally matches the exciton diffusion length for efficient charge carrier separation. It has been shown that the morphology of these domain networks essentially influences the power conversion characteristics of the solar cell [1,2]. A convenient pathway towards high efficiencies of polymer based organic photovoltaics is the use of solvent additives for tuning the nanometer scale morphology of the blend layer. Using this method, efficiencies approaching 10% [3] have been reported. However, the exact mechanism of how solvent additives influence the active layer morphology of the specific polymer:fullerene systems is not fully understood. Further, it is not yet clear how the active layer stability is affected by the use of solvent additives.
Using grazing incidence small angle X-ray scattering (GISAXS) we investigate the lateral nanomorphology of PCPDTBT:$PC_{71}BM$ blend thin films processed with and without using 1,8-octanedithiol (ODT). Emission and absorption spectroscopy in the UV and visible range complement the morphological investigations. For this purpose, PCPDTBT:$PC_{71}BM$ films with blend ratios of 1:1.5, 1:2.0 and 1:2.7 are prepared with and without use of 3% vol. ODT as solvent additive and investigated by the methods mentioned above.

Figure 4.1a) shows exemplary GISAXS raw patterns of thin films (1:2.7) with and without ODT. All GISAXS data are obtained at the Austrian SAXS beamline at Elettra, Trieste with a sample-detector distance of 2.05 m and a X-ray energy of 8.0 keV. For a more detailed evaluation, horizontal line cuts at the Yoneda region of the polymer are taken and fitted as shown in Fig. 4.1b). This analysis reveals that the use of ODT doubles the domain sizes on a length scale of a few up to several ten nanometers in all probed polymer:fullerene ratios. We ascribe this domain growth to an enhanced micro phase separation caused by ODT. This hypothesis is further supported by UV/Vis measurements. A representative UV/Vis absorption spectrum of the two films with a polymer:fullerene ratio of 1:2.7 with (blue) and without ODT (green) is shown in Fig. 4.1c). Hereby, the absorption peak at around 800 nm appears only in the films where ODT was used and indicates enhanced polymer crystallinity. All these findings can contribute to the improved efficiency by using ODT as reported by Peet et al. [4]. Meanwhile, first experiments suggest that the morphology of films processed with ODT might not be stable with time. Further investigation on this instability is yet due.

Concluding, we found that ODT enhances micro phase separation in PCPDTBT:$PC_{71}BM$ blend films, giving rise to improved power conversion properties of corresponding solar cells. The mentioned instability of the films with use of ODT, however, raises further questions. In order to evaluate solvent additives as a meaningful pathway for enhancing OPV performance,

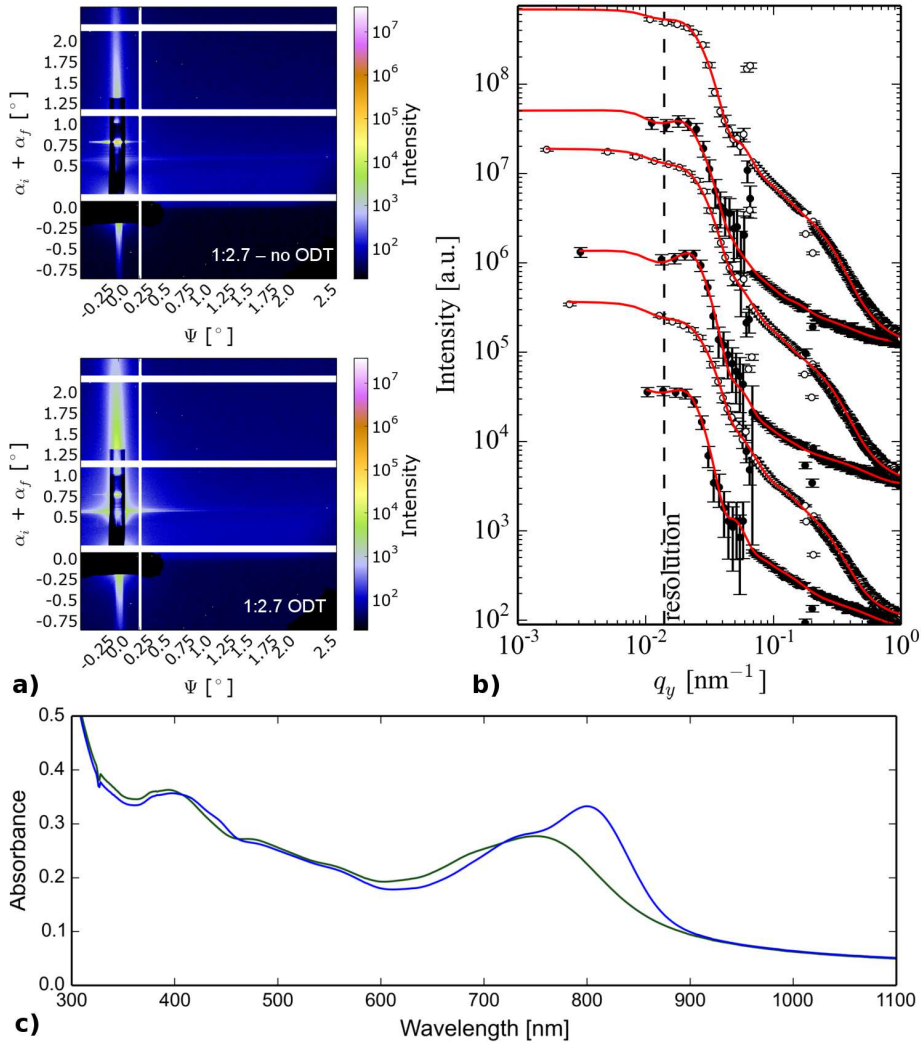

Figure 4.1:
GISAXS and UV/Vis data. a) Exemplary raw GISAXS data of films with a polymer:fullerene ratio of 1:2.7 without (upper) and with (lower) ODT. b) Horizontal line cuts and fitting curves of all three polymer:fullerene ratios 1:1.5, 1:2.0, and 1:2.7 (from bottom to top). Open symbols refer to films where ODT was used, full symbols refer to films without solvent additive. c) Representative UV/Vis Absorption spectra of films with a 1:2.7 ratio without (green) and with (blue) ODT.

it might be necessary to have additional ways of structure stabilization to counterbalance the degradation effect.

[1] M. A. Ruderer, S. Guo, R. Meier, H. Chiang, V. Körstgens, J. Wiedersich, J. Perlich, S. V. Roth, P. Müller-Buschbaum, *Adv. Funct. Mater.*, **21**, 3382-3391 (2011)

[2] C. J. Schaffer, C. M. Palumbiny, M. A. Niedermeier, C. Jendrzejewski, G. Santoro, S. V. Roth, P. Müller-Buschbaum, *Adv. Mater.* **25**, 6760 - 6764 (2013)

[3] Z. He, C. Zhong, S. Su, M. Xu, H. Wu, Y. Cao, *Nat. Photon.*, **6**, 591-595 (2012)

[4] J. Peet, J. Y. Kim, N. E. Coates, W. L. Ma, D. Moses, A. J. Heeger, G. C. Bazan, *Nat. Mater.*, **6**, 497-500 (2007)

4.2 Improved performance of organic solar cells from a quantum point of view

D. Moseguí González, V. Körstgens, Y. Yao, L. Song, G. Santoro[1], S. V. Roth[1], P. Müller-Buschbaum

[1] DESY, Hamburg, Germany

Over the past years organic photovoltaics has received an increasing interest due to their flexibility, semi-transparency, lightweigth, and their potentially low production costs. Recently, organic solar cells have reached power conversion efficiencies over 10 %, setting themselves as a real low-cost alternative to their expensive inorganic counterparts in many daily life applications.

One cornerstone for the performance of organic solar cells is the morphology of the active layer. Since the introduction of the bulk heterojunction (BHJ) morphology by Heeger and coworkers almost two decades ago [1], many approaches towards optimized morphologies were reported. Morphology optimization turns out to be crucial for the device performance, since its typical length scales and arrangement will mainly determine the exciton splitting efficiency within the device, as well as the quality of charge transport. As a consequence, many research groups have aimed for controlling the morphology through various procedures, such as introduction of solvent additives, nanostructuring or different thermal and/or solvent annealing protocols.

However, one recent approach that starts gaining interest within the OPV community, and that finds its origins in the OLED technology, regards the extension of the exciton lifetime within the device, given the difficulty to tune the device morphology at such intimate scales. Such procedures rely on the increased rate of intersystem crossing for the photogenerated excitons, which can bias the average spin-state of the excitons within the device towards the triplet state. Thereby, the efficiency of the exciton radiative recombination mechanism is lowered, resulting in an increased average lifetime and, hence, in longer exciton diffusion lengths.

We report a novel approach in which this effect was closely investigated on a system consisting of the famous donor-acceptor pair on poly(3-hexylthiophene):[6,6]-phenyl-C60-butyric acid methyl ester (P3HT:PCBM) doped with Fe_3O_4 nanoparticles [2]. The strong spin-orbit coupling provided to the system by the doping nanoparticles relaxes the spin selection rule and thereby increases the rate of intersystem crossing.

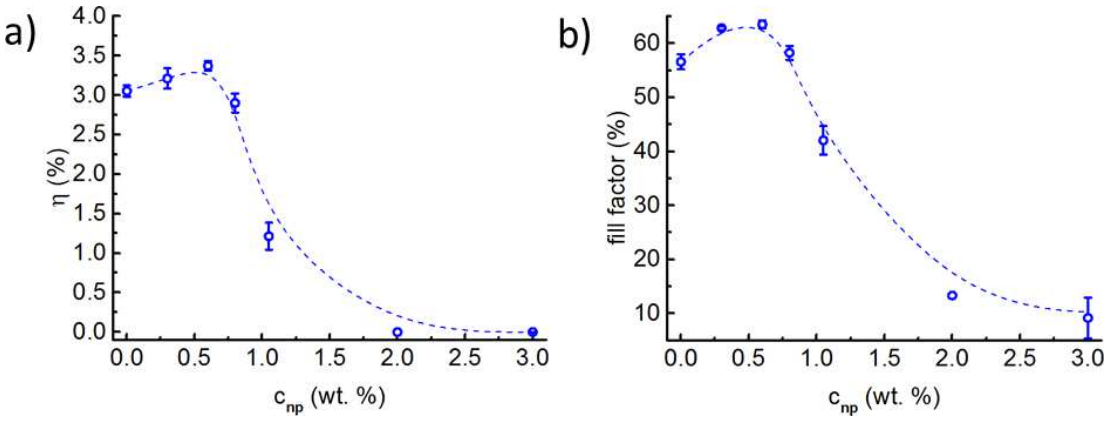

Figure 4.2:
a) Evolution of the efficiency of solar cells as a function of mass percentage of iron oxide nanoparticles. The range between 0.3 % and 1.0% shows the most efficient performance. b) Corresponding trend of the fill factor associated to the solar cells doped with different concentrations of iron oxide nanoparticles. Dashed lines are guides to the eye [2].

Figure 4.2 shows the evolution in device performance and fill factor for the doped solar cells as a function of the nanoparticle concentration. A maximum in performance is found at low doping

levels (under 1 wt.%). Such doping level provides an 11 % improvement in performance with respect to the non-doped sample and a 12 % increase in fill factor. The reasons for this improvement are investigated in detail. After an investigation of the morphology evolution provided by means of grazing incidence small angle x-ray scattering (GISAXS), the morphology evolution throughout the differently doped samples is found to be too small for being appointed as responsible for the improved device performance. Moreover, the evolution of the morphology does not follow any trend that correlates with that of the solar cell performance.
Once the morphology changes are discarded as origin of the improved power conversion efficiency, a spectral response investigation featuring photoluminescence measurements pointed out the possible origin of the improvement. For the doping causing highest device performance, the total photoluminescence signal shows a minimum, indicating an increased quenching and therefore reduced recombination. This observation is in agreement with the increased fill factor presented in Fig. 4.2b). Moreover, subsequent fluorescence and phosphorescence measurements with a time resolution of 10 μs showed an increased delayed to prompt fluorescence ratio with respect to non-doped samples (see Fig. 4.3a)). By fitting the corresponding signal decay, a lower decay ratio was found for the region of enhanced device efficiency, which correlates with a longer average exciton lifetime. Figure 4.3b) depicts the calculated exciton lifetime as a function of the doping concentration, showing a maximum in the region of low doping, thereby showing an excellent agreement with the theoretical framework expected for such a system.

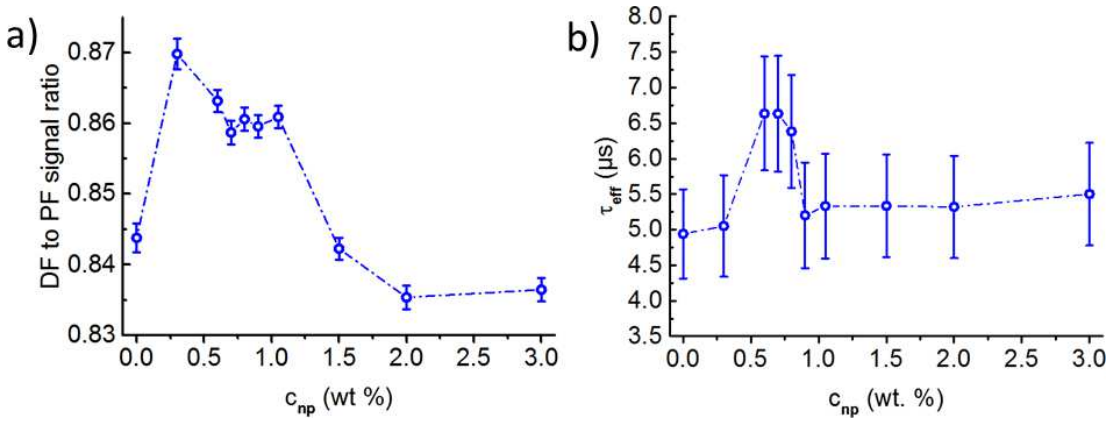

Figure 4.3:
a) Ratio of delayed fluorescence (DF) to prompt fluorescence (PF) and effective exciton lifetime τ_{eff} plotted versus the concentration of Fe_3O_4 nanoparticles. The dashed lines are guides to the eye [2].

Crystallinity investigations done by grazing incidence wide angle x-ray scattering (GIWAXS) on the same system yield a very likely insight on the origin of the worsened performance of the devices for high doping regime.

[1] G. Yu, J. Gao, J. C. Hummelen, F. Wudl, A. J. Heeger, *Science*, **270**, 1789 (1995)

[2] D. Moseguí González, V. Körstgens, Y. Yao, L. Song, G. Santoro, S. V. Roth, P. Müller-Buschbaum, *Adv. Energ. Mat.*, doi: 10.1002/aenm.201401770

4.3 Morphology investigation during functional stack assembling of P3HT:PCBM inverted solar cells

W. Wang, S. Pröller[1], M. A. Niedermeier, V. Körstgens, M. Philipp, B. Su, D. Moseguí González, S. Yu[2,3], S. V. Roth[2], P. Müller-Buschbaum

[1] MSE, Garching, Germany
[2] DESY, Hamburg, Germany
[3] KTH, Stockholm, Sweden

Poly(3-hexylthiophene-2,5-diyl) (P3HT) and phenyl-C61-butyric acid methyl ester (PCBM) are the typical donor and acceptor materials for organic bulk heterojunction (BHJ) solar cells. As is known, the improvement of power conversion efficiency (PCE) can be achieved by tuning the morphology between the P3HT and PCBM phase in the active layer [1]. Alternatively, an inverted geometry has also been applied in P3HT:PCBM BHJ solar cells to achieve higher PCE values [2]. However, the fundamental understanding of enhanced PCE is still unknown, especially from the perspective of the active layer morphology. Moreover, the evolution of the morphologies during the complex functional stack assembling is of great interest as well.
For this purpose, both standard and inverted P3HT:PCBM BHJ solar cells, are fabricated and examined with current-voltage (I-V) characterization and external quantum efficiency (EQE) measurements. Moreover, the gradual evolution of the inner morphology is tracked by grazing incidence small angle X-ray scattering (GISAXS) during the functional stacks assembling. The different samples from the functional stack assembly are denoted with S1 to S7. S1 denotes the fluorine-doped tin oxide (FTO)/glass substrate. The samples originating after the titanium dioxide (TiO_2) deposition and after the subsequent titanium tetrachloride bath treatment are named as S2 and S3, respectively. Afterwards, the P3HT:PCBM active layer is deposited via spin coating (denoted S4). Spraying coating of PEDOT:PSS as blocking layer is the next step (denoted S5). Finally, the gold contacts are deposited (denoted S6) and the full device is subjected to thermal annealing (denoted S7).

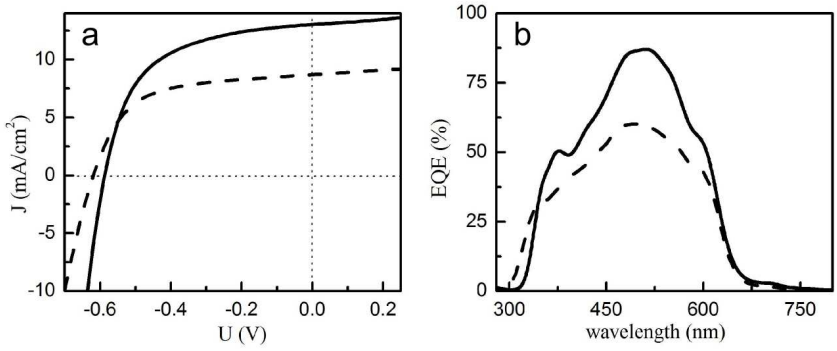

Figure 4.4:
a) I-V curves under illumination and b) EQE data of P3HT:PCBM BHJ solar cells with standard geometry (dashed lines) and inverted geometry (solid lines).

Fig. 4.4a presents the I-V curves of standard and inverted solar cells under solar illumination (with AM 1.5 spectrum). The photovoltaic performance of each solar cell is characterized by short circuit current (J_{sc}), open circuit voltage (V_{oc}), fill factor (FF) and PCE. It is notable that the inverted solar cells show much higher J_{sc} values (13.1 $\pm$ 0.3 mA/cm^2) as compared to those of standard solar cells (8.9 $\pm$ 0.2 mA/cm^2). The V_{oc} values (0.58 $\pm$ 0.01 V for inverted solar cell and 0.62 $\pm$ 0.01 V for standard solar cell) and FF values (55.9 $\pm$ 0.7% for inverted solar cell and 57.4 $\pm$ 1.3% for standard solar cell) exhibit no very significant differences. In total, the PCE

values of inverted solar cells are improved from 3.13 $\pm$ 0.1% to 4.23 $\pm$ 0.1%, mainly due to the enhanced J_{sc}. Additionally, EQE measurements are carried out and shown in Fig. 4.4b. Both devices show typical EQE curves for P3HT:PCBM active layer devices. However, for inverted solar cells, much higher EQE values are observed in the range from 350 nm to 800 nm. The J_{sc} values calculated from the EQE curves confirm that the inverted solar cells have much higher currents as compared with standard solar cells. This observation is in agreement with the direct comparison of the J_{sc} values obtained from the I-V measurements. Additionally, much lower EQE values are observed below 350 nm for inverted solar cells, which might be due to the light absorption of the TiO_2 hole-blocking layer.

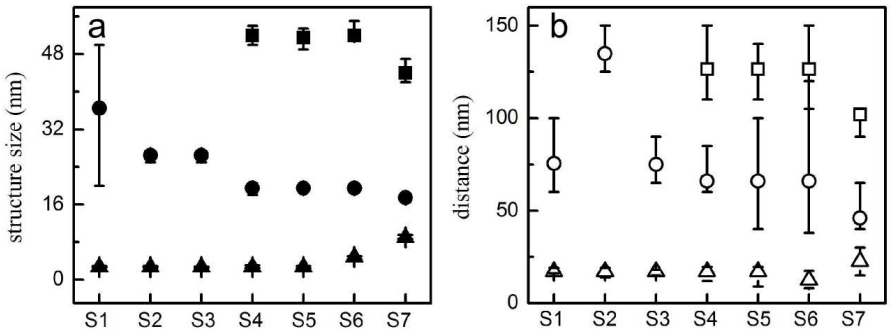

Figure 4.5:
Structure sizes a) and distances b) obtained from the fitting of horizontal line cuts of the 2D GISAXS data. The FTO (S1) and TiO_2 (S2 and S3) are fitted with two structures, whereas for P3HT (S4 to S7) three structures are found.

Furthermore, the gradual evolution of the inner morphology is probed by GISAXS measurements. The structure sizes and distances are extracted from fitting of the horizontal line cuts of the 2D GISAXS data (Fig. 4.5). According to the position where horizontal line cuts are performed, the structure information is dominated by FTO (S1), TiO_2 (S2 and S3) and P3HT (from S4 to S7). The FTO owns two structures (2.7 nm and 36.5 nm). It is notable that this small structure of 2.7 nm is replicated by TiO_2 (S2 and S3) and further by P3HT (S4 and S5). Afterwards, the structure size of P3HT increases to 4.8 nm after gold contact deposition (S6) and further increased to 9 nm after thermal annealing (S7). The 9 nm P3HT structure size contributes to the more efficient exciton dissociation since this structure size well matches exciton dissociation length in polymer. Oppositely, the other two structure sizes of P3HT (S7) are decreased from 19.5 nm to 17.5 nm and from 52 nm to 44 nm, which are much smaller than that in a standard P3HT:PCBM solar cell (around 65nm [3]). Therefore, it is concluded that the higher J_{sc} and PCE values of inverted P3HT:PCBM solar cells are attributed to the smaller structure sizes in the active layer as compared to a standard geometry.
In summary, the PCE of inverted P3HT:PCBM solar cells can be improved to 4.23 $\pm$ 0.1% as compared to a standard geometry with PCE of 3.13 $\pm$ 0.1%, which is mainly attributed to an increased value of J_{sc}. Through GISAXS investigation, it is concluded that the higher performance of inverted solar cell is due to the small domain sizes in the active layer.

[1] P. Westacott, J. R. Tumbleston, S. Shoaee, S. Fearn, J. H. Bannock, J. B. Gilchrist, S. Heutz, J. deMello, M. Heeney, H. Ade, J. Durrant, D. S. McPhail, *Energy Environ. Sci.* **6**, 2756-2764 (2013)

[2] Z. He, C. Zhong, S. Su, M. Xu, H. Wu, Y. Cao, *Nature Photon.* **6**, 591-595 (2012)

[3] S. Guo, M. A. Ruderer, M. Rawolle, V. Körstgens, C. Birkenstock, J. Perlich, P. Müller-Buschbaum, *ACS Appl. Mater. Interfaces* **5**, 8581-8590 (2013)

4.4 Efficiency enhancement of polymer solar cells introduced by alcohol solvent treatment

S. Guo, B. Cao, W. Wang, J.-F. Moulin[1], P. Müller-Buschbaum

[1] MLZ, Garching, Germany

To date, the highest power conversion efficiency (PCE) of polymer solar cells in a single junction device has reached 10% , above which commercial application is feasible [1]. In order to further enhance the device performance of bulk heterojunction (BHJ) polymer solar cells using the low bandgap copolymers based on thieno[3,4-b]thiophene-alt-benzodithiophene units (PTB7) and [6,6]-phenyl-C71-butyric acid methyl ester ($PC_{71}BM$), environmentally friendly solvent treatment with four different alcohols have been applied in the present work. Besides the most commonly used methanol treatment, other alcohols such as ethanol, 2-propanol, and 1-butanol also improve the device performance to certain extents as compared to the untreated solar cells. The surface structure modification of the polymer BHJ films after solvent treatments and the modification of inner film morphology are probed by the combination of atomic force microscopy (AFM) and advanced time of flight-grazing incidence small angle neutron scattering (TOF-GISANS) measurements.

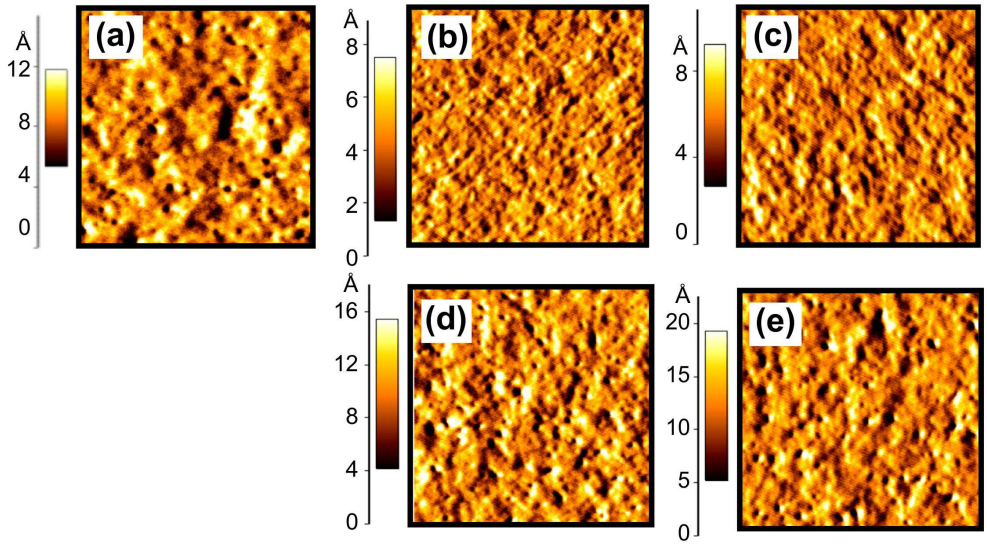

Figure 4.6:
AFM error images of PTB7:$PC_{71}BM$ solar cells with different solvent treatments: (a) reference solar cell , (b) with methanol treatment, (c) with ethanol treatment, (d) with 2-propanol treatment, and (e) with 1-butanol treatment. The scan size for all images is $2 \times 2\ \mu m^2$.

In Fig. 4.6, AFM error images for all investigated samples are shown. A phase-separated morphology is observed in general for all preparation procedures, but clearly different images are found depending on sample treatment: A phase separation structure with coarsened domains is formed for pristine PTB7:$PC_{71}BM$ films as observed in Fig. 4.6(a), whereas fibrillar features with smaller structures are generally observed for all films with solvent treatment of different alcohols. Amongst all, the smallest structure sizes on film surface are obtained from methanol treated films, which is in good agreement with previous investigations by Wang et al. [2]. Such smallest structure size is suggested to be correlated with the highest solar cell efficiency of 6% found for the methanol treatment.
In Fig. 4.7(a-l), an exemplary presentation of 2D scattering data of butanol treated PTB7:$PC_{71}BM$ film with increasing wavelength obtained simultaneously in the TOF-GISANS measurement are

presented. To further analyze the 2D GISANS data, horizontal line cuts at the Yoneda peak position and a simplified model for fitting the corresponding line cuts are used. In this model, spherical-shaped scattering objects distributed over a one dimensional paracrystal lattice within the frame of the distorted-wave Born approximation (DWBA) are assumed to determine the most prominent in-plane length scales [3].

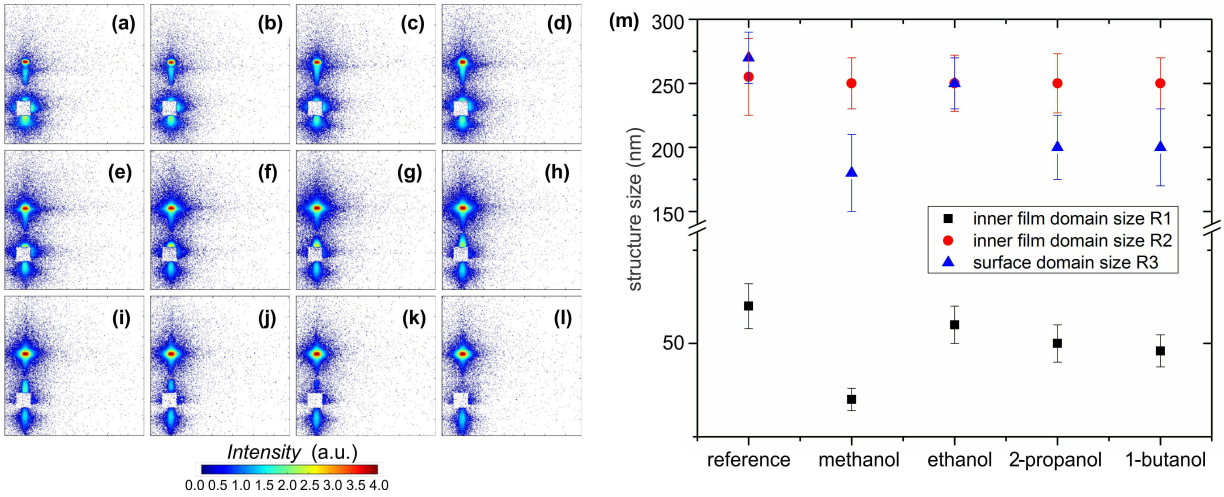

Figure 4.7:
A series of 2D scattering data (a-l) of butanol treated PTB7:PC_{71}BM film with increasing wavelength obtained simultaneously in the TOF-GISANS measurement, and (m) the most prominent structural features of PTB7:PC_{71}BM films without and with solvent treatment as extracted from TOF-GISANS: Two inner film domain sizes R1 (black squares), R2 (red circles), and one surface domain size R3 (blue triangle).

In Fig. 4.7(m), the most prominent structural features of the PTB7:PC_{71}BM BHJ active layers, without and with alcohol solvent treatment (methanol, ethanol, 2-propanol, and 1-butanol), are plotted. For both, the pristine and solvent-treated PTB7:PC_{71}BM BHJ films, the large inner domain sizes R2 of about 250 nm remain rather constant. The surface domain sizes R3 are in a similar order. For all solvent-treated films an overall size decrease of R2 and R3 is found, and the smallest domain size is again observed for methanol-treated films, agreeing with previous features of AFM error images. In contrast more pronounced changes are observed for the smallest inner domain size R1, which evolves from (70±6 nm) for the pristine PTB7:PC_{71}BM BHJ films to smaller sizes in general for all solvent treated PTB7:PC_{71}BM BHJ films. Furthermore, the one after methanol treatment exhibits the smallest inner lateral structures (35±3 nm), which is likely associated with the improved short-circuit current J_{sc} and FF values.
In summary, it is suggested that the enhanced device performance introduced by the alcohol treatments is correlated to the reconstruction of the inner film structures and the modified energy levels at the interfaces between the BHJ layer and the aluminum electrode, evident by the enhanced J_{sc} and open-circuit voltage V_{oc} of the I-V curves (not shown here) [4].

[1] M. A. Green, K. Emery, Y. Hishikawa, W. Warta, E. D. Dunlop, *Prog. Photovolt: Res. Appl.* **22**, 1 (2014)

[2] Y. Wang, Y. Liu, S. Chen, R. Peng, Z. Ge, *Chem. Mater.* **25**, 3196 (2013)

[3] S. Guo, J. Ning, V. Körstgens, Y. Yao, E. M. Herzig, S. V. Roth, P. Müller-Buschbaum, *Adv. Energy Mater.* DOI: 10.1002/aenm.201401315.

[4] S. Guo, B. Cao, W. Wang, J.-F. Moulin, P. Müller-Buschbaum, *ACS Appl. Mater. Interfaces* submitted, (2014)

4.5 In-situ morphology investigations of printed photoactive layers for application in organic solar cells

S. Pröller[1], F. Liu[2], C. Zhu[3], P. Müller-Buschbaum, T. P. Russell[2], A. Hexemer[3], E. M. Herzig[1]

[1] MSE, Garching, Germany
[2] University of Massachusetts Amherst, Amherst, USA
[3] ALS, Berkeley, USA

Organic solar cells are a promising alternative to silicon based inorganic modules. Latter ones require a more material for the same absorption and a high energy input for the production of the solar cell modules making them not as environmentally friendly as photovoltaic should be. Organic solar cells on the other hand exhibit the advantage of being a highly absorptive material reducing the needed amount of material. Furthermore, a key advantage of organic photoactive layers is the processability out of solution. Using this property opens the opportunity to produce the active layer of the solar cell via printing methods and allows for up-scaling to industrially-oriented scales which is not the case for laboratory techniques like spin coating. Thus, roll-to-roll processing on flexible substrates is the goal of production techniques for organic solar cells. A huge variety of printing and coating techniques can be used to reach this goal, among others knife coating, slot-die coating, screen printing or spray coating. [1]
However, the inner morphology has an enormous impact on the charge transport and therefore on the device performance. [2] Tuning and influencing the assembling of the materials in the organic thin film is still challenging and a better knowledge of the structure determining parameters is of utmost importance. Useful techniques for investigating the inner morphology of a thin organic active layer are grazing incidence wide and small angle X-ray scattering GIWAXS and GISAXS, respectively. [3,4] While there are investigations on the development of nanoscale morphology in polymer:fullerene photoactive layers during solvent casting [5], not much is known about the equivalent development in printed systems.

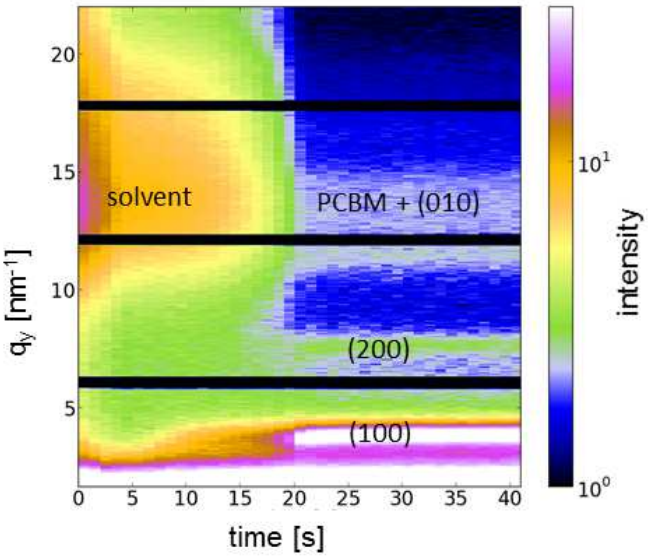

Figure 4.8:
Development of the scattering intensity with time for a q-range of 1.5 to 22.5 nm^{-1} in GIWAXS, clearly showing the evolution of a scattering of the (100) P3HT peak at 3.9 nm^{-1}as well as the appearance of the PCBM and (010) peak after attenuation of the solvent signal.

We performed in-situ GIWAXS and GISAXS measurements on slot-die printed standard photoactive blends of poly(3-hexylthiophene-2,5-diyl) and phenyl-C61-butyric acid methyl ester (P3HT:PCBM). The experiments were performed at the Advanced Light Source (ALS) at the Lawrence Berkeley National Laboratory in Berkeley, California, USA. Figure 4.8 shows

an 2-dimensional color plots of the time dependence of the scattering intensities on typical length scales obtained with GIWAXS. The pattern shows initially a strong scattering signal at $q_y \approx 14$ nm^{-1}, which can be attributed to the evaporating solvent. With the decrease of the solvent signal, the characteristic (100) signal of the P3HT backbone spacing appears at $q_y \approx 3.9$ nm^{-1}. Additionally contributions of the (200) and (010) signals can be seen after evaporation of solvent. This development clearly shows the crystallization of the P3HT. Furthermore, similarly as the (010) peak, contributions of the PCBM can clearly be seen.
To identify the orientation of the polymer crystals and its development sector integrals of the GIWAXS patterns were performed in both, vertical (Fig. 4.9 a) and horizontal (Fig. 4.9 b) direction. Figure 4.9 shows exemplarily the time evolution of the sector integrals for the most important time stages. The development of the characteristic (100), (200), (300) and (010) P3HT peaks can be followed. The strong pronunciation of the (100) peak in vertical (Fig. 4.9 a) and the (010) peak in horizontal (Fig. 4.9 b) direction clearly shows the predominant edge-on orientation of the polymer crystals.

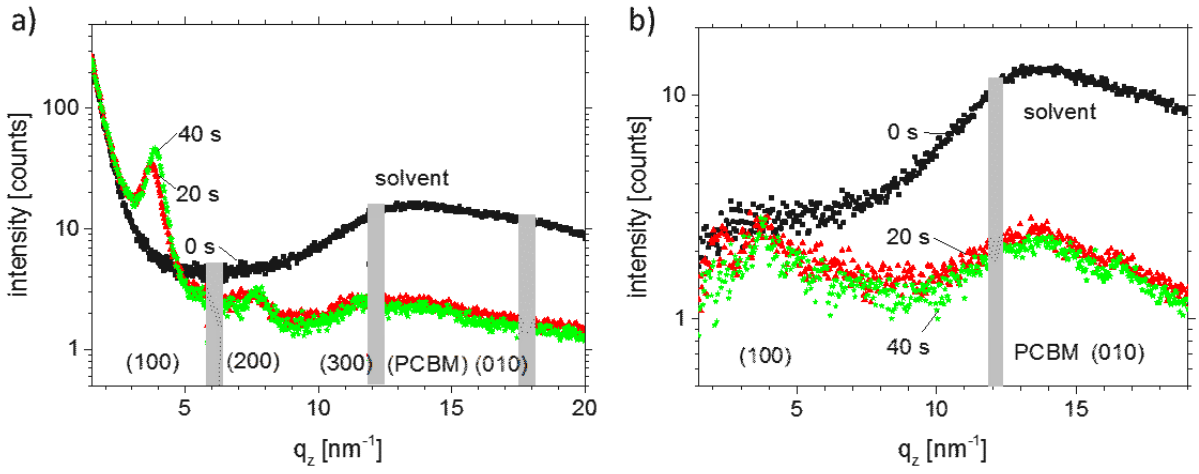

Figure 4.9:
Time development of the a) vertical and b) horizontal scattering intensities. The evolution of the P3HT:PCBM scattering peaks can clearly be followed. The (100) intensity in vertical direction is much more pronounced than in horizontal direction indicating a predominant edge-on orientation of the polymer lamellae.

The performed experiments give an insight into the crystallization kinetics of a slot-die coated P3HT:PCBM active layer. Quantitatively analyzing these results will provide the possibility to picture the crystallization process and we will be able to provide a model of the crystal growth. This knowledge is important for further influencing the inner nanoscale morphology in printed films to optimize the device performance of organic solar cells in an up-scalable technique.

[1] R. R. Søndergaard, M. Hösel, F. C. Krebs, *J. Polym. Sci. B Polym. Phys.* **51**, 16-34 (2013)

[2] R. Noriega, J. Rivnay, K. Vandewal, F. P. V. Koch, N. Stingelin, P. Smith, M. F. Toney, A. Salleo, *Nat. Mater.* **12**, 1038-1044 (2013)

[3] P. Müller-Buschbaum, *Adv. Mater.* **26**, 7692–7709 (2014)

[4] W. Wang, S. Pröller, M. A. Niedermeier, V. Körstgens, M. Philipp, B. Su, D. Moseguí González, S. Yu, S. V. Roth, P. Müller-Buschbaum, *ACS Appl. Mater. Interfaces*, doi: 10.1021/am5067749

[5] T. Wang, A. D. F. Dunbar, P. A. Staniec, A. J. Pearson, P. E. Hopkinson, J. E. MacDonald, S. Lilliu, C. Pizzey, N. J. Terrill, A. M. Donald, A. J. Ryan, R. A. L. Jones, D. G. Lidzey, *Soft Matter* **6**, 4128-4134 (2010)

4.6 Degradation in printed polymer:fullerene thin films as active layers for organic photovoltaic devices

J. R. Stockhausen, C. J. Schaffer, P. Müller-Buschbaum

Clean and renewable energy sources gain more and more importance. Among them, solar energy has the largest growth potential. In comparison to conventional silicon solar cells, organic photovoltaics (OPVs) offer several advantages, like cheap and energy-saving production or the possibility to produce flexible, transparent and portable solar cells. Nevertheless, their efficiency is still below that of conventional solar cells. Up to now, OPVs reached a maximum efficiency of over 10 % for the champion solar cells in laboratory device scale [1]. However, a further increase in device efficiency might be realistic due to the ongoing improvement in tailoring the applied polymer materials.Beside the overall efficiency another disadvantage of OPVs is the device degradation, which lowers the efficiency with time. In comparison to silicon solar cells significant fast degradation occurs. Hence, the lifetime needs to be prolonged, so that a profitable large-scale production becomes feasible. Therefore, a detailed understanding of the degradation mechanisms is necessary. The possibility of printing OPVs enables a large-scale fabrication, e.g. by roll-to-roll-print fabrication, in contrast to techniques such as spin-coating. So far, a lot of research has been focusing on OPVs produced by spin-coating techniques. Less research was addressing printed films. The morphology of the active layer will likely be affected by the preparation process, e. g. printed and spin-coated films will have different morphologies. As a consequence, it is not clear how the method of film application affects the aging behavior.

Figure 4.10:
The picture shows the example of the glass plates that was imprinted with a P3HT:PCBM active layer in the shim mask slot dye coating machine. The printed film appears in carmine color.

In the present investigation, we address UV light induced aging of PCPDTBT:PC71BM and P3HT:PCBM active layers, printed with a home-made positive shim mask slot dye coater. This printing machine was constructed by S. -Günther in the context of his master thesis. More informations about the working principle and the manual can be found in his thesis [2]. We investigate the influence of the applied production technique on the morphology of the active layer in comparison to that of spin- or spray-coated active layers. Changes in the morphology of the films due to accelerated aging are investigated by means of atomic force microscopy (AFM), X-ray reflectivity (XRR) and UV/Visible light spectroscopy (UV/Vis). So far, films and solar cells, based on P3HT could be successfully printed and displayed efficiencies up to 3.14 % [2]. Furthermore, the printing of cells with an active layer consisting of PCPDTBT:PC71BM, will be conducted.

Figure 4.10 shows one example of a printed P3HT:PCBM film. The P3HT:PCBM active layer is printed on a glass substrate with a PEDOT:PSS layer, which is the common blocking layer in standard device configuration. As it can be seen in Fig. 4.10, the film that appears red, is printed homogeneously onto the sample plate.

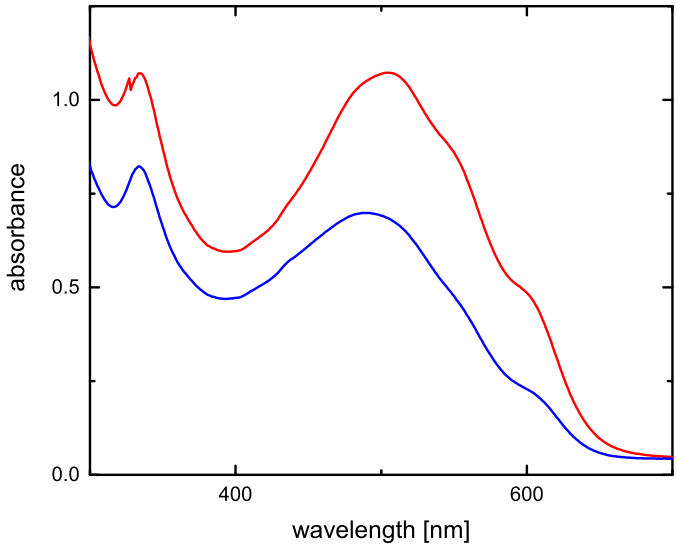

Figure 4.11:
Comparison between the absorbance spectrum of the printed (blue line) and the annealed (red line) active layer. Annealing changes the absorbance to higher values.

To investigate the influence of thermal annealing on the absorbance of the active layer, the printed film is probed with UV/Vis spectroscopy after the printing process. This is done without and with a thermal annealing. During the annealing process, the sample is put onto a heating plate. The heat induces structural changes in the active layer, so that the crystalline order of the polymers is enhanced. As it can be seen in Fig. 4.11, the absorbance is much higher after annealing than before. Moreover, the characteristic features in the spectrum, which are assigned to vibrations in P3HT have established. This increase in absorbance as well as the characteristic absorbance features arises from the fact that the crystallinity enhances during the annealing process. This higher crystallinity leads to a better conductivity and absorbance. As a consequence, a higher efficiency in the solar cell can be reached. The absorbance of the printed P3HT:PCBM active layer is higher than that of the absorbance typically measured for spin-coated P3HT:PCBM active layers. The simple reason for that is the difference in film thickness. The thickness measurements are performed by a surface profilometer and reveale an average film thickness of the active layer of 200 nm. This value is higher than the thicknesses of the active layers, which are observed on spin-coated samples. These are normally in the range of 80-100 nm. In the ongoing experiments, the changes of the absorbance data as function of time are followed. The printed and spin-coated films are exposed to a well-controlled dose of UV light. From the comparison of both aging series, it will be easy to address potential differences in the degradation.

[1] Chen, Jing-De, C. Cui, Y.-Q. Li, L. Zhou, Q.-D. Ou, C. Li, Y. Li, J.-X. Tang, *Adv. Mater.* doi:10.1002/adma.20140453581 (2014)

[2] S. Günther, master thesis, Physik-Department TU München (2014)

4.7 Solvent tuning of aqueous processed P3P6T/WS-C_{60} thin films for OPV applications

N. Hohn, D. Moseguí González, P. Müller-Buschbaum

Among the renewable green energy sources organic photovoltaics (OPV) represents a promising bet to overcome foreseeable future energy supply shortages. The advantage of low cost and large scale processability causes an increasing amount of scientific interest. Nevertheless, common production routines in OPV fabrication still imply the use of a high amount of toxic organic solvents.
To reduce the amount of environmental unfriendly solvents in organic solar cell (OSC) production routines, the water soluble, hole conducting polymer poly[3-(potassium-6-hexanoate)thiophene- 2,5-diyl] (P3P6T) is further investigated. In combination with an electron accepting, water soluble C_{60}-malonic acid (WS-C_{60}) derivative, both materials can be employed to manufacture an organic active layer for application in OSCs.
Initial steps for this system include the optimization of solubility parameters as well as a study upon different deposition methods. Within this frame, solubility limits for the electron acceptor WS-C_{60} are tested.

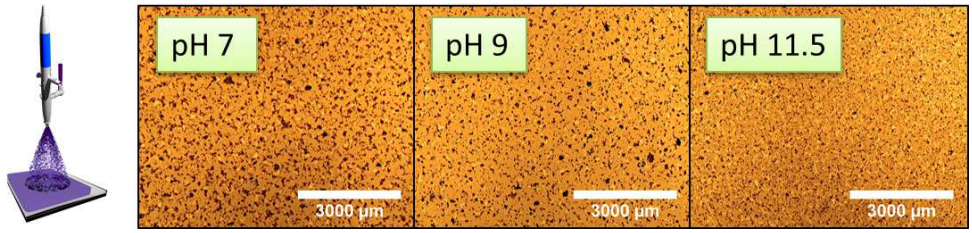

Figure 4.12:
Optical microscope images of spray-coated WS-C_{60} samples with increasing pH values as indicated in the insets

To overcome these limitations, thin films of WS-C_{60} are spray coated out of solutions of decreased concentration. This is an advantage over the commonly used spin coating technique, as film thicknesses at the order of 100 nm require a minimum concentration of 5 mg/ml. The spray coating technique, hence, allows to reduce the concentration and consequently enhancing the solubility of the WS-C_{60} in the solution. The result of spray coating at low concentrations for different pH values is depicted in Fig. 4.12. The increased amount of polar OH-groups for higher pH value solutions improves the solubility of the WS-C_{60} due to its polar, hydrophilic side groups. The images show a decrease in the population of large scale fullerene clusters ($> 2000\,\mu\mathrm{m}^2$). The analysis yields that with increasing pH value the population of these clusters is decreased to $< 20\,\%$ of the value for pH 7.
Solvent doping is found as another promising way to enhance the solubility of WS-C_{60} for spin coating deposition at higher concentrations. To address the polar, hydrophilic blocks of the fullerene sidechains, doping is performed with N,N-dimethylformamide (DMF). Due to the high polarity of this solvent compared to deionized water solvent-sidechain coupling is enhanced.
In order to analyze the effect of doping with regard to application in OPV, bilayer films of WS-C_{60}, spin coated for different DMF concentrations of up to $60\,\mathrm{vol.\%}$, and spray coated P3P6T have been fabricated. The films act as active layers in an OSC. An estimation of the impact upon the conductivity of solar cells is obtained from x-ray diffraction (XRD) measurements. The obtained XRD images are exposed in Fig. 4.13.

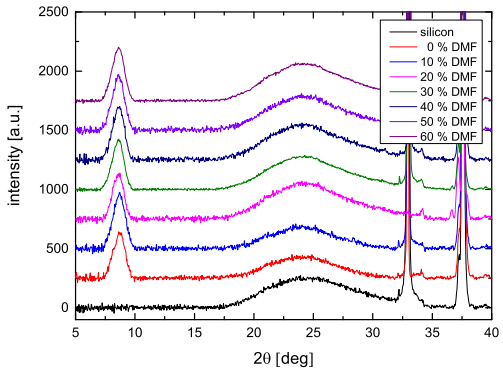

Figure 4.13: XRD data of bilayered films of WS-C_60/P3P6T with increasing DMF content as indicated.

Unlike findings of Thalluri et al. [1], which state P3P6T to be amorphous, the peak at $8.6\,^\circ$ is assumed to be the crystalline phase contribution of P3P6T, as the peak does not appear for the bare substrate and corresponds to distances in the nm regime. Comparison with different literature yields similar positions for the (100) crystal plane of P3P6T . The corresponding lattice spacing of around 1.1 nm is found to be smaller than values obtained for the structural similar P3HT [2]. For further analysis of the impact of the solvent doping, the peaks are fitted with Gaussian functions. According to the Scherrer equation the crystallite sizes are determined and the outcome is plotted against the DMF concentration (Fig. 4.14).
As a result the crystallite size is found to be maximal for DMF concentrations of around $20\,\mathrm{vol.\%}$. The trends found are in good agreement with measurements of OSCs for different DMF concentrations, which exhibit a boost in performance for DMF doping around $20\,\mathrm{vol.\%}$.

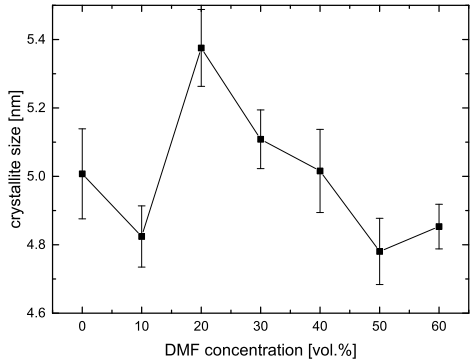

Figure 4.14: DMF doping impact upon the crystallite size of P3P6T

Altogether, the XRD measurements yield promising information to explain structural changes upon solvent doping. This information facilitates the optimization of the exposed systems and provides helpful explanations for the behavior in solvent tuned OSCs.

[1] G. Thalluri, J. Bolsée, A. Gadisa, M. Parchine, T. Boonen, J. D'Haen, A. Boyukbayram, J. Vandenbergh, T. Cleij, L. Lutsen, D. Vanderzande, J. Manca, *Solar Energy Materials and Solar Cells* **95**, 3262-3268 (2011)

[2] N. Kayunkid, S. Uttiya, M. Brinkmann, *Macromolecules*, **43**, 4961–4967 (2010)

4.8 Investigation of a third component addition on organic solar cells

R. M. Torrademé, S. Guo, B. Cao, W. Wang, P. Müller-Buschbaum

One of the biggest challenges in this century is the energy transition from fossil fuels to more environmentally friendly energy sources. Given its broad availability and amount, solar energy is considered as one of the most promising renewable energy sources. The use of photovoltaics offers a clean and renewable way to produce electricity. So far, inorganic photovoltaics cells made of silicon is the most common solar technology due to its high efficiency (25.6% [1]), however a huge amount of energy for the fabrication is still required. To overcome this limitation, a new generation of solar cells based on organic compounds is expected to change the worldwide concept of solar energy. Among the advantages of plastic solar cells, flexibility and potentially low cost are the most remarkable properties. Bulk-heterojunction (BHJs) organic solar cells consist of a two-component thin film sandwiched between two electrodes. Typically, the active layer of such thin films is a self-assembled mixture of a low band gap polymer and a fullerene, which provides a wide absorption range and a proper morphology for the light conversion process.
Among all the strategies taken in order to improve the device morphology and the electric properties, the addition of a third component to the standard binary blend is one of the most promising methods. Two ternary candidates, a non-fluorinated copolymer based on thieno[3,4-b]thiophene (PTB7-F00), previously studied in binary blends [2], and poly(3-hexylthiophen) (P3HT), are mixed with the active layer of poly(4,8-bis[(2-ethylhexyl)oxy]benzo[1,2-b:4,5-b]dithiophene-2,6-diyl3-fluoro-2-[(2-ethylhexyl)carbonyl]thieno[3,4-b]thiophenediyl):[6,6]-phenyl-C71-butyric acid methyl ester (PTB7:$PC_{70}BM$) using chlorobenzene (CB) as solvent and 3% in volume of 1,8-diiodoctane (DIO) as organic additive.
The optical and electronic properties of the ternary films are investigated with UV-Vis spectroscopy and photoluminiscence.

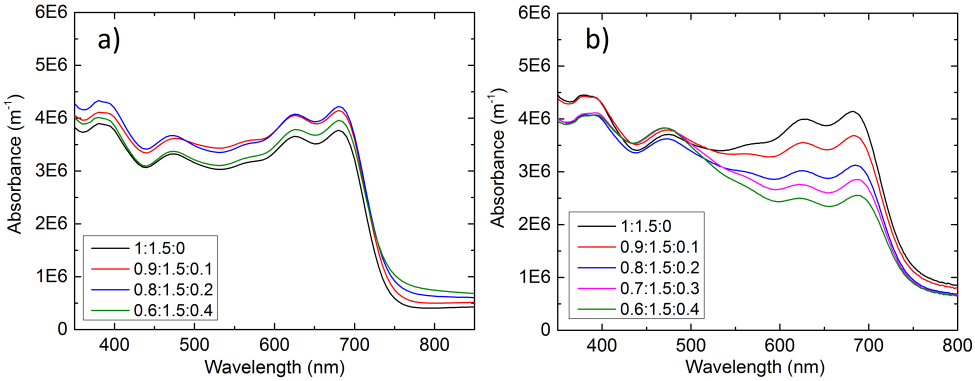

Figure 4.15:
UV-Vis absorbance for the ternary system PTB7:$PC_{70}BM$:PTB7-F00 (a) and PTB7:$PC_{70}BM$:P3HT (b). The different curves correspond to different concentrations of the third component. The legend in the graph represents the ratio of each component: polymer, fullerene, third component.

For the present investigation, different concentrations (0%, 10%, 20%, 30% and 40% wt%) of the third component are added while keeping the polymer-fullerene ratio constant at 1:1.5.
In the absorbance spectra of the standard blend, PTB7:$PC_{70}BM$, the high energy region corresponds to the absorbance range of the fullerene while the prominent peaks between 650 nm and 750 nm are determined by the bandgap of PTB7. As the non-fluorinated third component, PTB7-F00, is added the overall absorbance signal increases with respect to the standard binary blend

(Fig. 4.15a). The most prominent improvement is found when PTB7-F00 is added in concentrations of 10% and 20%. However, in the case of the ternary system with P3HT, the absorbance intensity of the PTB7 peak decreases as the amount of the low band gap polymer decreases (Fig. 4.15b). The absorbance signal of the fullerene region is increased due to the fact that P3HT has its bandgap in the same range [3].

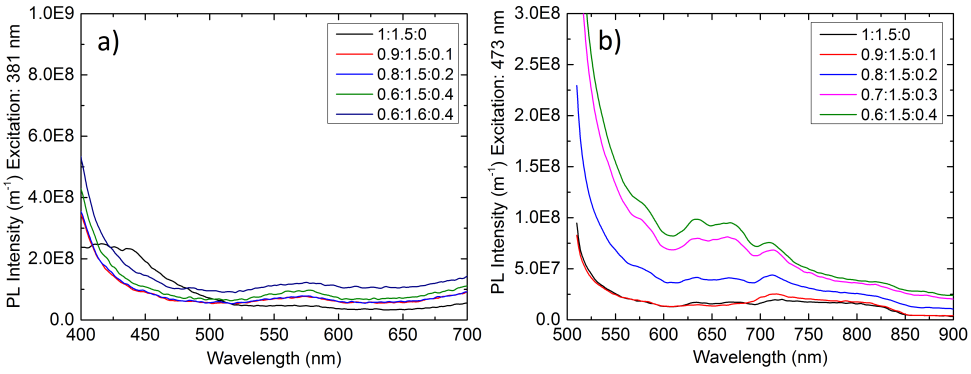

Figure 4.16:
Photoluminiscence signal for the ternary system PTB7:PC_{70}BM:PTB7-F00 (a) and PTB7:PC_{70}BM:P3HT (b) with varying concentration of the third component. The legend in the graph represents the ratio of each component, polymer, fullerene, third component.

Regarding the photoluminiscence emission, the PTB7 based ternary system (Fig. 4.16a) shows an overall lower signal when compared with the PTB7:PC_{70}BM:P3HT blend (Fig. 4.16b). In the other ternary system, the addition of the third component, PTB7-F00, increases slightly the intensity of the emitted light, although the values stay low. In contrast, the signal of the second ternary blend increases with increasing amount of P3HT, leading to higher recombination rates. In conclusion, the addition of a second low band gap polymer to the blend PTB7:PC_{70}BM leads to changes in both absorbance signal and recombination rates. For the PTB7 based ternary system the absorbance spectra shows notable increment for low concentrations of PTB7-F00 with respect to the standard blend, PTB7:PC_{70}BM, reaching its maximum when the third component is added with a concentration of 20%. Regarding the photoluminiscence signal of the same system, the emitted light also increases with the addition of the third component, although this increment is relative moderate when compared with the standard blend emission spectra. The system with an addition of 20% of PTB7-F00 shows again the lowest recombination rate after the standard system, PTB7:PC_{70}BM. In the case of P3HT, the absorbance intensity decreases as the amount of the third component is increased. In terms of photoluminiscence emission, the signal increases as a function of concentration of P3HT, indicating more recombination with increasing concentration of the third component.

[1] K. Masuko, M. Shigematsu, T. Hashiguchi, D. Fujishima, M. Kai, N. Yoshimura, T. Yamaguchi, Y. Ichihashi, T. Mishima, N. Matsubara, T. Yamanishi,T. Takahama, M. Taguchi, E. Maruyama, S. Okamoto, *IEEE Journal of Photovoltaics* **4**, 1433-1435 (2014)

[2] G. Zhao, Y. He, Y. Li, *Adv. Mat.* **22**, 4355–4358 (2010)

[3] S. Guo, J. Ning, V. Körstgens, Y.Yao, E.M. Herzig, S. Roth, P. Müller-Buschbaum, *Adv. Energy Mater.* (2014) DOI: 10.1002/aenm.201401315

4.9 Breath figure porous layer for organic solar cell applications

A. Hassan, V. Körstgens, P. Müller-Buschbaum

Organic solar cells become more and more competitive with conventional silicon based solar cell technology concerning efficiencies. In other fields organic solar cells are already superior as they offer light weight properties, mechanical flexibility and potential low cost production. As for conventional solar cells the application of additional optical coatings may enhance the usability of the devices. Bulk heterojunction (BHJ) organic solar cells processed out of poly(3-hexylthiophene-2, 5-diyl) (P3HT):phenyl-C61-butyric acid methyl ester (PCBM) are among the most investigated systems in organic photovoltaics [1]. We investigate such BHJ organic solar cells with P3HT:PCBM out of 1,2 dichlorobenzene with an additional functional layer of a porous breath figure structure with aspired antireflection properties. The application of breath figure porous structures as an anti-reflection coating has been shown previously by Park and Kim for infrared wavelengths [2].
To prepare typical honey-comb structures as particular patterned thin films with a 2D or 3D array of pores, the so called breath figures or moist casting methods have been established [3]. A number of different realizations of moisture casting have been reported to get nano- and microporous thin films. Examples include drop casting, solution casting and spin coating under high humidity conditions. The polymer we used to fabricate breath figure porous structure is a statistical copolymer consisting of methylacrylate and ethyl methacrylate. This transparent polyacrylate shows high stability against degradation by UV light and has shown its applicability as optical coating [4]. Porous structured thin films are prepared using the polyacrylate out of chloroform. Different amount of methanol is added to a polymer solution with 100 mg/ml of polyacrylate in chloroform. Glass substrates are used after hot acid bath and plasma cleaning process. The spin coating rotational speed was 1000 rpm for 60 seconds. Humidity is applied by using humidity flask instrument with a flexible tube in such a way that the rotational center of the sample is exposed to a flow of humid air during the spin coating process. Depending on the amount of methanol, which is not a solvent for polyacrylate, the sizes and the distribution of pores significantly differs. For a volume ratio V(methanol):V(chloroform) of 1:10, the porous structure is not homogeneous (Fig. 4.17a). With a volume ratio of 1:5 large pores with an average pore size of 5.2 $\pm$ 1.8 μm are homogeneously distributed (Fig. 4.17b). Increasing the quantity of the methanol in the solution further, leads to even larger structures caused by dewetting as shown in Fig. 4.17c.

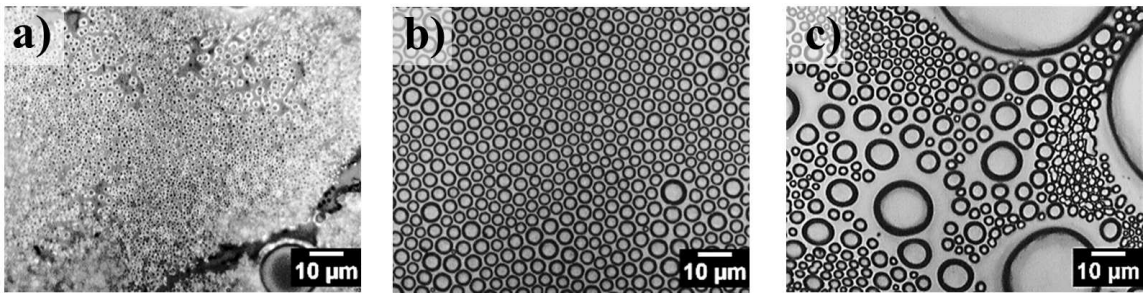

Figure 4.17:
Porous structured polyacrylate thin films out of chloroform with methanol as solvent additive with a solvent volume ratio V(methanol):V(chloroform) of a) 1:10 b) 2:10 and c) 3:10.

To analyze the effect of such porous thin films on organic solar cells, samples are prepared on the glass-ITO (indium tin oxide) substrate after cleaning them with organic solvents and

plasma cleaning. The PEDOT:PSS (poly(3,4-ethylenedioxythiophene) polystyrene sulfonate) is annealed at 150 °C for 10 minutes after spin coating for 60 s at 3000 rpm rotational speed. Then P3HT:PCBM solution, which has been stirred overnight, is spin coated on the electron blocking layer for 30 s at 2000 rpm rotational speed. After evaporating the layer of aluminum at vacuum conditions the breath figure porous layer is spin coated on the back side of the active layer giving the total stack of layers as sketched in Fig. 4.18a. For the porous layer a polyacrylate concentration of 5 mg/ ml was chosen with a solvent volume ratio V(methanol):V(chloroform) of 1:50.

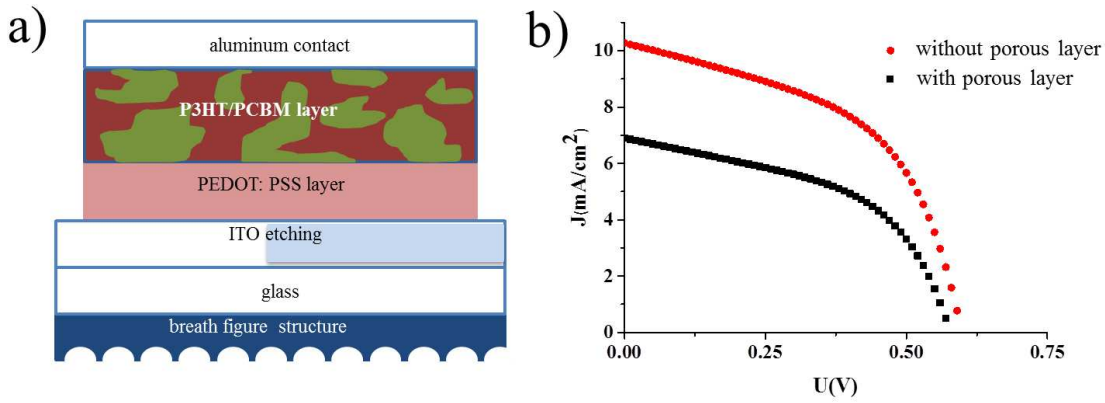

Figure 4.18:
a) Scheme of P3HT:PCMB based BHJ solar cell with breath figure porous structured layer and b) current density - voltage curve of the solar cell with and without breath figure layer.

The current density - voltage curves in Fig. 4.18b clearly demonstrate that the functionality of the solar cells is preserved with a reduced efficiency after adding the coating with the breath figure procedure. The power conversion efficiency of the reference solar without porous layer is 3.1%, whereas with the breath figure layer only 2.0% is achieved. The short circuit current, open circuit voltage and fill factor of the reference solar cell are 10.27 mA/cm^2, 0.598 V and 50.7%, respectively. In contrast, for the solar cell with porous layer these values are reduced to 7.08 mA/cm^2, 0.577 V and 49.8%, respectively. The decreased short circuit current for the solar cell with a breath figure layer clearly indicates a reduced transmission of light into the active layer. In ongoing investigations the porous layer is optimized towards higher transmission while preserving the anti-reflection properties. The aim is to achieve efficiencies very close to the one for solar cell without additional coating, whereas an advantage of the coated solar cells is expected at an inclined incidence of light.

[1] S. Guo, M. A. Ruderer, M. Rawolle, V. Körstgens, C. Birkenstock, J. Perlich, P. Müller-Buschbaum, *Appl. Mater. Interfaces* **5**, 8581-8590 (2013)

[2] M. S. Park, J. K. Kim, *Langmuir* **21**, 11404-11408 (2005)

[3] L. Heng, B. Wang, M. Li, Y. Zhang, L. Jiang, *Materials* **6**, 460-482 (2013)

[4] V. Körstgens, C.-C. Hsu, D. Paneque, J. Wiedersich, P. Müller-Buschbaum, *Appl. Phys. Lett.* **9**3, 041916 (2008)

4.10 Conjugated diblock copolymer-fullerene bulk heterojunction system for organic photovoltaic applications

R. Wang[1], H. Frielinghaus[1], P. Müller-Buschbaum

[1] JCNS at MLZ, Garching, Germany

Organic photovoltaics attract worldwide research interest due to its potential for low-cost fabrication processing, lightweight and flexible applications. In order to achieve an optimum energy conversion efficiency an interpenetrating bulk heterojunction (BHJ) network is needed, which has a nanoscale morphology on the order of the exciton diffusion length. The interpenetrating network provides larger interface area for exciton dissociation as well. Diblock copolymers are very promising for achieving well controlled nanoscale morphologies, because of the well-ordered micro-phase separation structures which they can form. In the present work we focus on a diblock copolymer with a polythiophene and with a polystyrene block. We blend this diblock copolymer P3HT-b-PS with the fullerene derivative PCBM. The resulting active layer is investigated by applying grazing incidence x-ray diffraction (GI-XRD) combined with optical electronic characterization.
All blend films are prepared by spin coating on pre-cleaned silicon substrates. Five different blend ratios are investigated. As shown in Fig. 4.19, a surface structure is achieved for all blend films, which is uniform on micrometer scale. An irregular domain structure occurs if the amount of PCBM in the system is increased. At a blend ratio of 2:1 PCBM-depleted areas arise, which reflects the nucleation of PCBM crystals and the diffusion of PCBM molecules to these crystals. For the films with a blend ratio 1:2 aggregates are elongated and showed branched macroscopic flower-like crystals. This originates from the miscibility limit of PCBM. At this blend ratio, PCBM aggregates already appear in the pre-casted solution and grow along with the thermal annealing treatment.

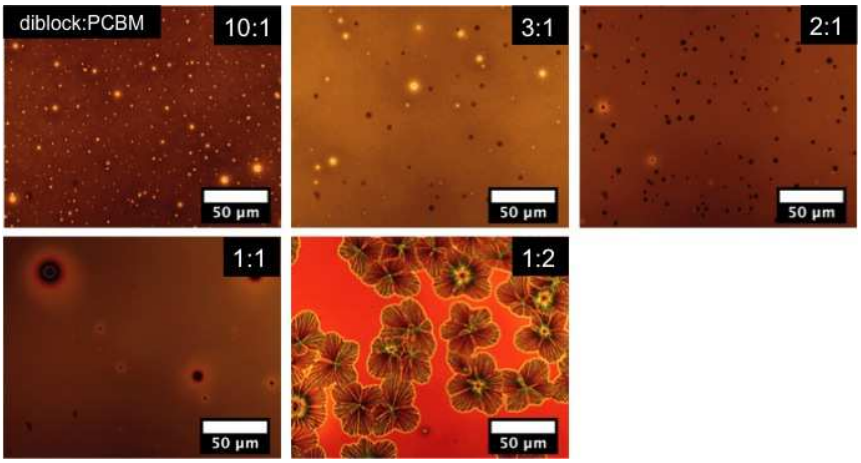

Figure 4.19:
Optical microscope images of diblock copolymer-PCBM blend films with different blend ratios as indicated.

The wavelength-dependent absorbance spectra of annealed P3HT-b-PS:PCBM films with five different blend ratios are shown in Fig. 4.20. The absorption peak at around 335 nm is attributed to PCBM, whereas the features above 400 nm are induced by P3HT. The distinct vibrational excitation peaks at 550 and 605 nm reflect the crystalline P3HT phases and vanish with increasing PCBM content, which means that the crystallinity of P3HT is disturbed by PCBM addition [1]. This is emphasized by the blue shift of the P3HT main absorbance peak, because the PCBM

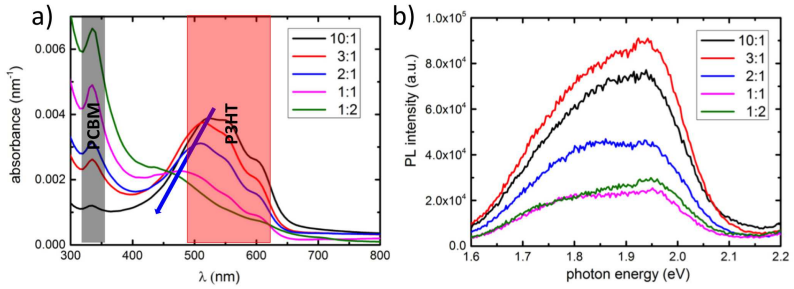

Figure 4.20:
a) Wavelength dependent absorbance spectra and b) photoluminescence (PL) measurements of annealed P3HT-b-PS:PCBM films with five different blend ratios as indicated.

molecules not only disrupt the P3HT π-π stacking, but also decrease the conjugation length of the P3HT chains.
Photoluminescence (PL) spectroscopy shows the PL intensity of the exciton radiative decay within the pure P3HT. As shown in Fig. 4.20 b), PL intensity is originating from both, P3HT (bandgap around 1.9 eV) and PCBM (bandgap around 1.7 eV). Apart from the blend ratios of 3:1 and 1:2, an increased quenching of the PL is found for increasing PCBM content. It is known that photoluminescence of P3HT is sensitive to the degree of chain order. A higher PL intensity can result either from an increased disordered of the P3HT chains or from repulsive forces between the different crystals [2].

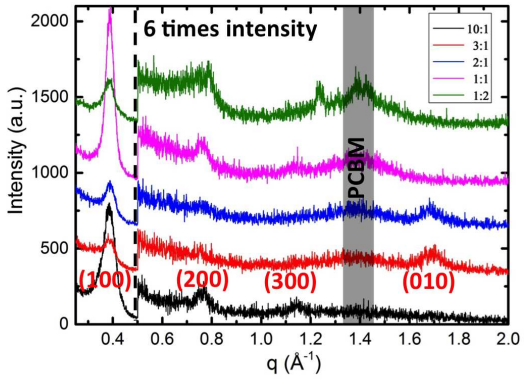

Figure 4.21:
GI-XRD patterns of P3HT-b-PS:PCBM blend films with five different blend ratios as indicated.

In the XRD data (Fig. 4.21) the (100) reflection of P3HT, located at 0.38 $\AA^{-1}$, and related higher orders (200) and (300), locate at 0.76 and 1.15 $\AA^{-1}$, are seen. These results are in good agreement with literature [3]. In spite of (100) orientation and the higher order of (h00) families, another two reflections can be recognized, the P3HT (010) orientation at 1.72 $\AA^{-1}$ appears for the blend ratio 3:1 and the diffraction peak of PCBM at 1.4 $\AA^{-1}$. Consequently, the total P3HT order in the films is disturbed when more PCBM has been added into the system, and thus corroborating the PL results. Further data analysis obtained from small angel neutron scattering experiment is undergoing.

[1] M. A. Ruderer, R. Meier, L. Porcar, R. Cubitt, P. Müller-Buschbaum, *J. Phys. Chem. Lett.* **3**, 683-688 (2012)

[2] S. S. v. Bavel, M. Bärenklau, G. d. With, H. Hoppe, J. Loos, *Adv. Funct. Mater.* **20**, 1458-1463 (2010)

[3] Z. Sun, K. Xiao, J. K. Keum, X. Yu, K. Hong, J. Browning, I. N. Ivanov, J. Chen, J. Alonzo, D. Li, B. G. Sumpter, E. A. Payzant, C. M. Rouleau, D. B. Geohegan, *Adv. Mater.* **23**, 5529-5535 (2011)

4.11 The influence of hole blocking layer on inverted P3HT:PCBM solar cells

E. Barabino, W. Wang, P. Müller-Buschbaum

Organic photovoltaic devices are likely approaching the comparable efficiency to traditional silicon based solar cells and promise low-cost and ease roll-to-roll printing production. In bulk heterojunction morphology a conjugated polymer (electron donor) and a fullerene derivative (acceptor) are blended together forming the active layer. In a standard solar cell (sSC), the back transparent electrode collects the positive charge carriers and the top electrode collects the negative charge carriers. In an alternative device geometry, the so-called inverted solar cell (iSC) the charges are collected in the opposite way. In comparison to the sSC the iSC provides a longer lifetime stability under ambient conditions, which is one of the main issues regarding organic solar cells. In devices employing such architecture, the active layer is sandwiched between two charge blocking layers (BL), resulting in the following cell architecture: back electrode/hole blocking layer (HBL)/active layer/electron blocking layer (EBL)/top electrode. In the present work we investigate the influence of two different HBLs: titanium dioxide (TiO_2) [1] and zinc oxide (ZnO) [2]. The surface structure of these layers is explored via scanning electron microscopy (SEM) and the solar cells performances is studied via J-V characterization and external quantum efficiency (EQE) measurements.
To prepare the zinc oxide layer, first 1 ml of a 100 mg/ml zinc acetate dehydrate solution in 2-methoxyethanol is ultrasonicated for 15 min. Then 30 μl of diethanolamide is added to this solution. The final solution is stirred for 5 min and spin coated at 1500 rpm for 30 s onto pre-cleaned silicon substrate for SEM measurements and onto the back electrode for solar cells. Finally the samples are placed in the furnace and calcinated up to 400 ^{o}C for 30 min with rate of 350 ^{o}C/h.

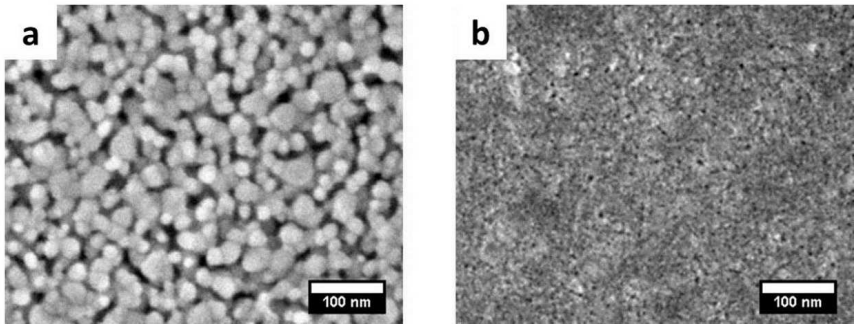

Figure 4.22: SEM images of a) zinc oxide and b) titanium dioxide blocking layers in top view.

The titania layer has been prepared starting from two solutions. The first one contains ethanol, titanium IV butoxide and diethylamine in a volume ratio $V_{ethanol} : V_{titanium} : V_{diethylamine}$ = 0.71 : 0.23: 0.06 for a total volume of 3.685 ml. The second solution contains ethanol and deionized H_2O in a volume ratio $V_{ethanol} : V_{H_2O}$ = 0.965 : 0.035 for a total volume of 1.295 ml, which is added drop wise to the first solution. Then, the resulting titania sol is kept stirring for 24 hours before spin coating at 2000 rpm for 60 s onto pre-cleaned silicon substrate for SEM examination, and onto the back electrode for solar cells preparation. The samples are then calcinated in a furnace up to 450 ^{o}C for 2 hours using the rate of 375 ^{o}C/h. Afterwards, the samples are treated with a titanium tetrachloride ($TiCl_4$) bath: once immerged in 50 ml deionized H_2O, 1 ml of 2M $TiCl_4$ is drop wised above at a temperature of 70 ^{o}C. A second calcination is performed up to 500 ^{o}C for 30 min using the rate of 600 ^{o}C/h.
The ZnO layer (Fig. 4.22 a) shows well defined grains uniformly clustered, resulting in a highly rough surface. While the titanium dioxide layer (Fig. 4.22 b) is much more compact and has a

significantly smaller surface roughness.
In order to understand the influence of these two HBLs on solar cell performances, a batch of devices has been prepared. The titania and ZnO layers are deposited onto fluorine tin oxide (FTO) substrates separately. The active layers are spin coated at 2000 rpm for 30 s, using a solution of poly(3-hexylthiophene-2,5-diyl) (P3HT) and phenyl-C61-butyric acid methyl ester (PCBM) with the concentration of 24 mg/ml and the ratio of 1:1 in chlorobenzene. Afterwards, the samples are annealed for 10 min at 140 ^{o}C in nitrogen filled glove box. Subsequently, thin films of molybdenum oxide (MoO_3) performing as EBL are deposited by the thermal evaporation set up. The EBL has the purpose of minimizing the recombination of electrons and holes at the top electrode building up an energy barrier for the electrons. The optimum thickness of the MoO_3 layer is around 10 nm [3]. For this experiment, the MoO_3 layer is formed by thermal evaporation at a pressure of $3 \cdot 10^{-5}$ mbar, keeping the deposition rate around 0.2 Å/s and the current around 120 A. The gold contacts are deposited as top electrode to complete the devices.

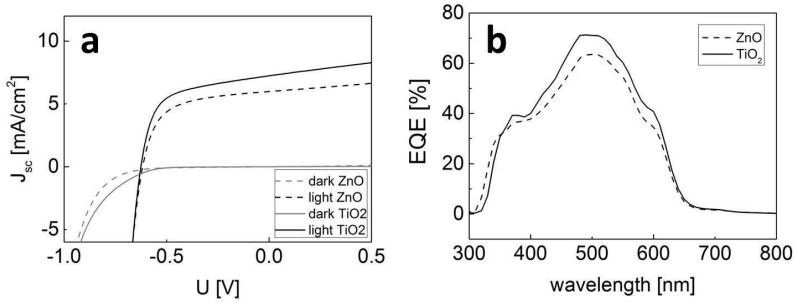

Figure 4.23:
a) J-V curves of best performing pixels for iSC with ZnO (dashed lines) and TiO_2 (solid line) HBLs in dark condition (gray) and under illumination (black). b) EQE data of best performing pixels for the devices with ZnO (dashed lines) and TiO_2 (solid line) HBLs.

EQE and J-V measurements have been performed on iSC with ZnO and TiO_2 HBL, separately. The J-V curves under simulated 1000 W/m^2 at 1.5 AM illumination show that the solar cells with TiO_2 HBL reach higher efficiency values. The best performing devices (in brackets the average over all the tested devices is given) exhibit short circuit current densities J_{sc}) = 7.24 (6.44) mA/cm^2, open circuit voltages V_{oc}) = -0.63 (-0.61) V, fill factors (FF) = 60.25 (54.88) % and efficiencies (η) = 2.73 (2.16) %. For comparison to the devices with ZnO HBL perform less well with J_{sc} = 5.99 (5.71) mA/cm^2, V_{oc} = -0.62 (-0.59) V, FF = 59.72 (54.04) % and η = 2.21 (1.84) %.
The EQE curves depict the percentage of electrons extracted from the solar cells in dependence of the wavelength of the incident electromagnetic radiation. In Fig. 4.23 the EQE curve at short wavelengths (300 - 350 nm) shows higher response for the cell with ZnO HBL compared as compared to the one with titania layer, which is attributed to the theoretical lower band gap for zinc oxide (3.3 eV) than titania (anatase phase 3.2 eV). However, it is clear that device with TiO_2 HBL exhibits overall higher EQE values in agreement with the higher J_{sc} values obtained from J-V characterization. It is concluded that the solar cells with TiO_2 HBL perform better than that with ZnO layer, which is probably due to the more compact layer morphology that lead to less recombination of charge carriers at the back electrode.

[1] M. A. Niedermeier, I. Groß, P. Müller-Buschbaum, *J. Mater. Chem. A* **1**, **43**, 13399-13403 (2013)

[2] K. Sarkar, E. V. Braden, S. Pogorzalek, S. Yu, S. V. Roth, P. Müller-Buschbaum, *Chem. Sus. Chem.* **7**, **8**, 2140-2145 (2014)

[3] A. Ng, X. Liu, C. H. To, A. B. Djurijsio, J. A. Zapien, W. K. Chan, *ACS Appl. Mater. Inter.* **5**, 4247-4259 (2013)

4.12 Influence of selective solvent additive on photovoltaic devices based on P3HT:PCBM blend

J. F. Martínez Grisales, E. M. Herzig[1], P. Müller-Buschbaum

[1] MSE, TUM, Garching, Germany

The use of selective solvent additives with high boiling point such as 1,8-diiodooctane have been shown to be beneficial for the performance of organic photovoltaics based on P3HT:PCBM blends, boosting efficiencies from 3.4% to 5.1% [1]. These solvent additives work by inducing aggregates already in solution and hence promoting a phase separation in solution and in drying films. These effects have been shown to have an impact on the conductivity and the morphology on thin films. However, the drying time is increased due to the slow evaporation rate [2] making the fabrication process much more extensive. Cyclohexanone (CHX) is used as a candidate to replace such substances with a boiling point much lower than the conventional selective solvents but still with the desired higher boiling point than the solvent host, retaining so the desired effects with lower drying times. The effects of CHX were studied using different techniques such as UV-Vis spectroscopy and Grazing Incident Wide Angle Scattering (GIWAXS).

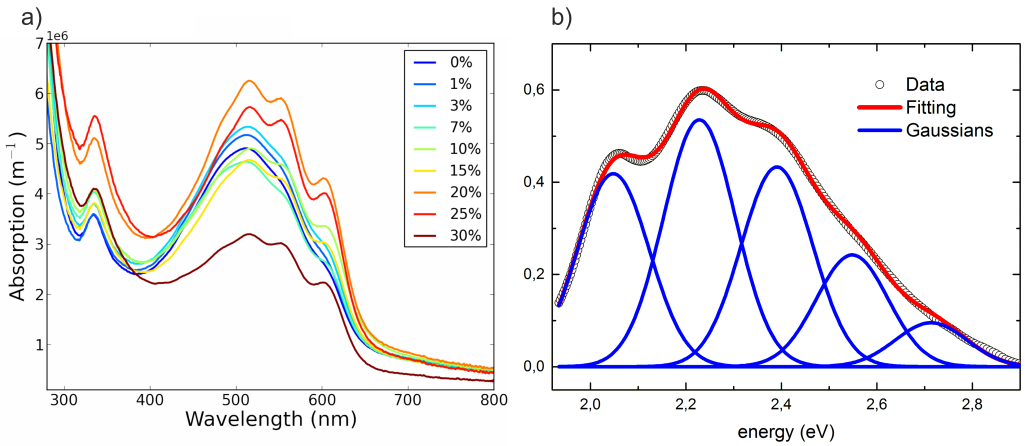

Figure 4.24:
Absorption spectra normalized to the maximum of P3HT for the different samples a) and fitting procedure to calculate the exciton bandwidth b).

To study the effect of CHX on the morphology the absorption curves were fitted and the exciton bandwidth was calculated. This parameter gives information on the energetic difference between minimum and maximum in the band conformed by the LUMO. This change is due to a tilt of the transition dipole (located along the molecular plane) with respect to the $\pi - \pi$ stacking direction [3]. This gives direct indication of how well aligned the backbone is throughout the whole molecule, which is important in the process of charge transportation. The development of the shoulders is a physical evidence of backbone alignment and therefore reduced exciton bandwidth. This is an important condition for good alignment of $\pi - \pi$ stacking for the polymer crystals. It seems to be however a loss of the P3HT absorption with increasing amount of CHX. This is evident by the increase of the PCBM absorption peak when the data is normalized to the maximum of P3HT absorption.
To measure the effect of the selective solvent on solar cell devices, samples were made using an inverted architecture and illuminated under 1.5AM conditions. The fill factor increases for the low amount of CHX in solution for the small amounts. For the higher amounts, a small

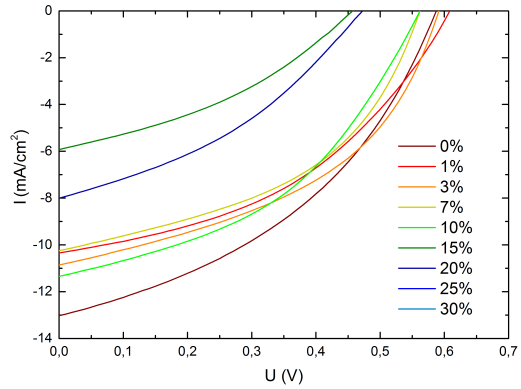

Figure 4.25:
I-V curves for photovoltaic devices using P3HT:PCBM blend. The percentage shown in the figure represents the volume percentage of CHX in the solution, from where the BHJ active layer films where produced. The area of the inset graph shows the different behaviour of the devices with the different contents of CHX in the quadrant where power output is possible.

deviation from the diode behaviour is observed in the negative bias, which may be related to germinative recombination [4]. There seems to be a maximum for the volume percentage of CHX in solution, where beyond this the devices presented short-circuits which may be induced due to the size of crystals. To understand the physical background behind this increase of PCE,

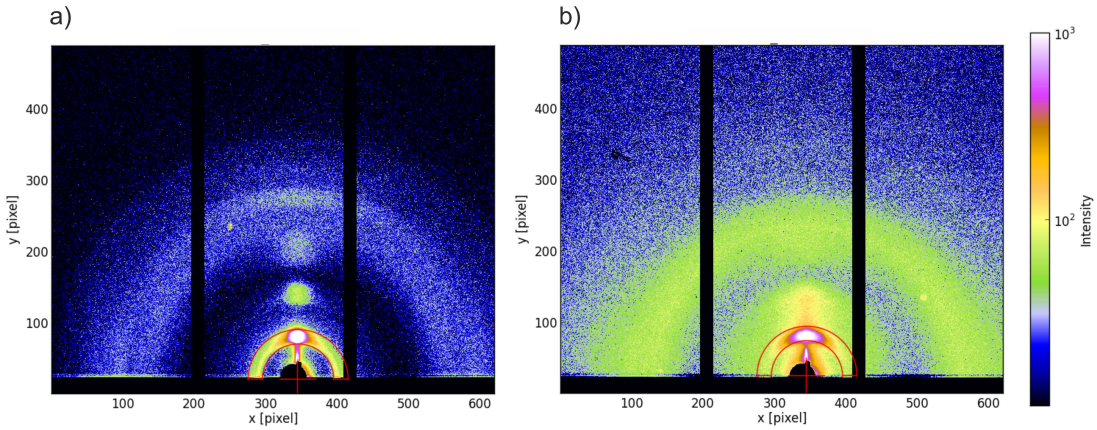

Figure 4.26:
Comparison between GIWAXS images of annealed samples without CHX treatment (0%) a) and with the highest content tested (30%) b). In both images a tube cut is shown around the typical distance of the 100 peak corresponding to the lamellar spacing, to emphasize the different configuration arisen from the solvent additive treatment.

GIWAXS measurements were done on treated thin films. These are prepared on glass and on a layer of TiO_2 to mimic the conditions of such layer in a solar cell. For first inspection raw GIWAXS images from 0 and 30% of CHX are used. Better ordering is observed for the untreated sample in comparison to the high scattering of the 30% sample, which may be responsible for the linear behaviour of solar cells with this CHX content.

[1] J. K. Lee, W. L. Ma, C. J. Brabec, J. Yuen, J. S. Moon, J. Y. Kim, K. Lee, G. C. Bazan, A .J. Heeger, *J. Am. Chem. Soc.* **17**, 3619-3623 (2008)

[2] X. Liu, S. Huettner, Z. Rong, M. Sommer, R. H. Friend, *Adv. Mater.* **24**, 669–674 (2012)

[3] R. Totoki, T. Aoki-Matsumoto, K. Mizuno, *JOL* **112**, 308-311 (2005)

[4] C. Groves, *Energy Environ. Sci.*, **6**, 3202-3217 (2013)

5 Polymer-hybrid systems

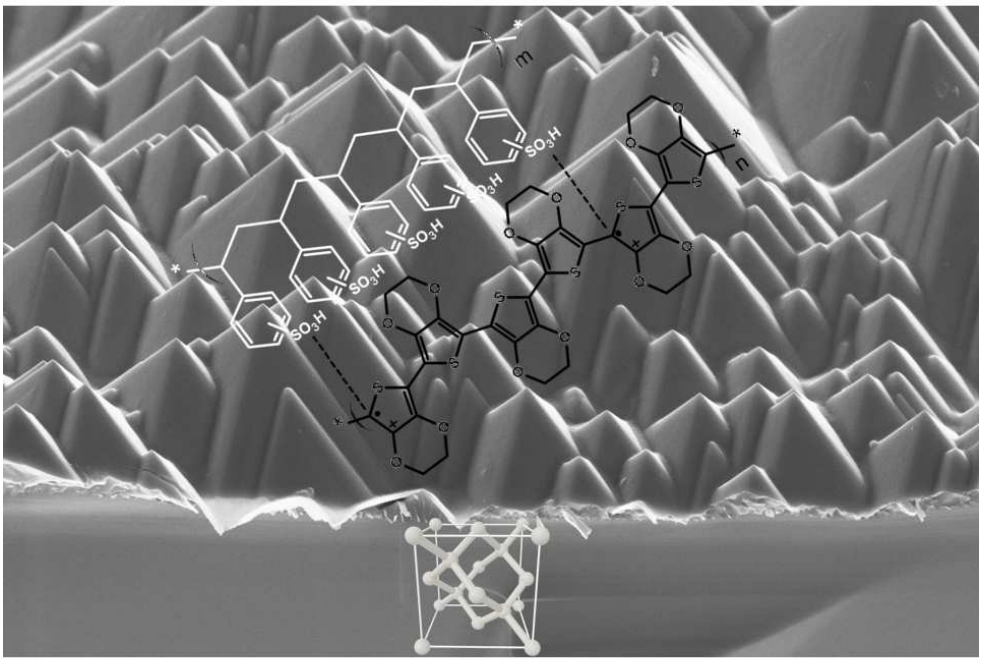

5.1 Morphology investigation of diblock copolymer-maghemite nanoparticle hybrid thin films fabricated via self-assembly

Y. Yao, E. Metwalli, J.-F. Moulin[1], B. Su, P. Müller-Buschbaum

[1] MLZ, Garching, Germany

The alignment of maghemite (γ-Fe_2O_3) nanoparticles (NPs) in poly (styrene-d8-*block*-n-butyl methacrylate) P(Sd-*b*-BMA) diblock copolymer (DBC) thin films via a wet chemical self-assembly method is investigated towards the preparation of highly ordered diblock copolymer-maghemite nanoparticle hybrid thin films. This film preparation is motivated by great interests of fabricating hybrid nanocomposites for wide potential applications in functional nano-devices [1,2]. The surface and depth-dependent nanomorphologies of the hybrid films are characterized with scanning electron microscopy (SEM) and time-of-flight grazing incidence small angle neutron scattering (TOF-GISANS), respectively, as a function of the NP concentration. The employed maghemite NPs were selectively deposited in the PSd domains of the DBC via a micro phase separation process due to the surface modification of the NPs with PS chains.
The solutions containing DBC and NPs are prepared with toluene as a solvent, and the concentration of polymer is set to a fix value of 12.4 mg/mL to achieve the desired film thickness, while the weight ratio of NPs vs. DBC in the resulting film is varied (0, 0.1, 0.5, 1, 3, 7, and 15 wt%). The hybrid films are prepared by spin coating on Si substrates, which are pre-cleaned in an acid solution. The acid cleaning procedures of Si substrate and spin coating parameters are describe elsewhere in detail [1]. To reach an equilibrium of the morphology, the as-prepared hybrid films are heated at 160 °C for 5 h.

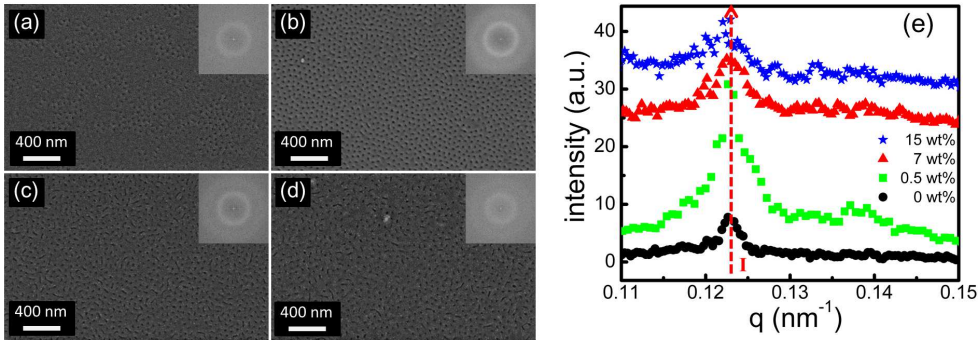

Figure 5.1:
SEM micrographs of selected hybrid films with incorporation of different NP concentrations: (a) 0, (b) 0.5, (c) 7, and (d) 15 wt%. Upright insets are the corresponding FFT patterns. (e) Power spectral density (PSD) functions with different NP concentrations.

It is observed (Fig. 5.1a-d), that at a low NP concentration of 0.5 wt%, the NPs are well selectively dispersed in its preferred PSd domains and swell up these domains, which also enhances the structural order. However, at higher NP concentrations, the cylindrical PSd domains begin to expand anisotropically, which results in the increase of interfacial curvature. In (Fig. 5.1e, PSD functions are shown, which are obtained from azimuthally integration of the intensity distribution in the FFT patterns. A quantitative result extracted from the PSD shows the lateral distance of inter domain of the DBC is 58±2 nm, irrespective of the NP concentration.
As seen in Fig. 5.2c, the experimentally observed Yoneda peak positions match the theoretical critical angle of the polymer PSd at short wavelengths, which indicates a PSd enrichment layer at the polymer/substrate interface. Such enrichment layer results in a morphological transition to a perforated lamella. In Fig. 5.2d, a well prominent peak located at large q_y values remains in an unchanged position irrespective of the NP concentrations. The fit results of the peak show

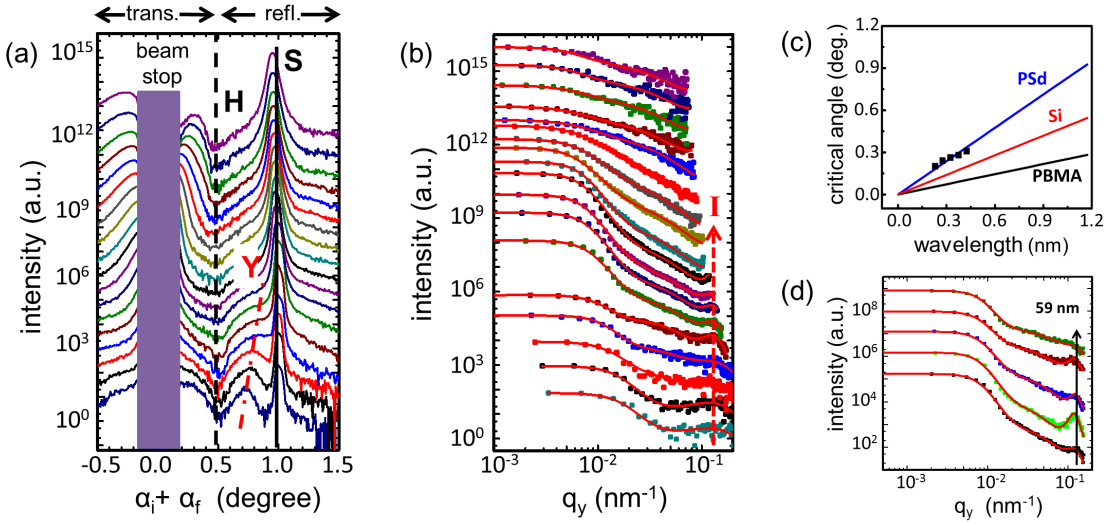

Figure 5.2:
(a) Vertical line cuts of the 2D GISANS data for the pure DBC film as a function of the detector angle (α_i+α_f). The sample horizon (H), the Yoneda peak (Y), and the specular peak (S) are emphasized with lines. (b) The horizontal line cuts as a function of the lateral scattering vector component q_y are shown together with the fits (red solid lines). The red dashed line I is guiding the eye to the determined peak position. (c) Theoretical critical angle positions (solid lines) of the involved materials for the pure DBC film as a function of the wavelength. The squares show the experimentally observed Yoneda peak positions. (d) Selected horizontal line cuts (solid squares) of the 2D TOF-GISANS data at a wavelength of 0.475 nm and corresponding fits (red lines) of the hybrid films at different NP concentrations from bottom to top: 0, 0.5, 1, 7, and 15 wt%.

the value of the inter-domain spacing is constant at 59±1 nm as well. Thus, the results of the TOF-GISANS data complement the observations from the SEM.

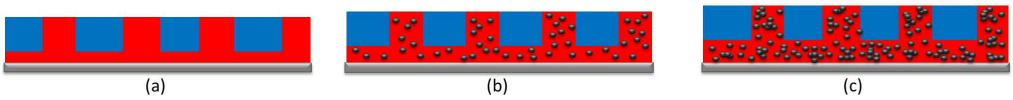

Figure 5.3:
Sketch of the cross-section of (a) pure DBC film, (b) low, and (c) high NP concentrations hybrid films. The PSd domain, PBMA domain maghemite NPs and Si substrate are marked in red, blue, black, and grey, respectively.

In summary, the morphological transition upon NP addition is illustrated in Fig. 5.3. The resulting thin hybrid films show a perforated lamella with a PSd enrichment layer containing NPs at the substrate/film interface. The incorporation of the NPs within the DBC thin films enhances the micro-phase separation process and results in highly oriented, well ordered nanostructured hybrid films at low NP concentrations. Whereas, at higher NP concentrations, the NPs form large NP-aggregates and large sized metal oxide clusters dominate the morphology. Furthermore, the film thickness is increased prominently due to a large volume of NPs deposited into the PSd enrichment layer.

[1] Y. Yao, E. Metwalli, J.-F. Moulin, B. Su, M. Opel, P. Müller-Buschbaum, *ACS Appl. Mater. Interfaces* **6**, 18152 (2014)

[2] E. Metwalli, J.-F. Moulin, J. Perlich, W. Wang, A. Dietert, S. V. Roth, P. Müller-Buschbaum, *Langmuir* **25**, 11815 (2009)

5.2 Magnetic field guided hybrid films of diblock copolymer and iron oxide nanoparticles

S. Xia, E. Metwalli, Y. Yao, P. Müller-Buschbaum

Hybrid nanocomposites based on a block copolymer matrix and embedded inorganic nanoparticles have attracted great interest because of the potential of tailoring their properties for numerous potential applications [1-2]. For preparing hybrid polymer films, solution casting is one of the most important methods, which is frequently used in this field. In order to obtain polymer films added with nanoparticles, solution casting was adopted during the preparation process. Materials used include the diblock copolymer poly(styrene-*b*-methyl methacrylate), denoted P(S-*b*-MMA), maghemite ($\gamma-Fe_2O_3$) nanoparticles and toluene as solvent. The copolymer has a number average molecular weight of 218 kg/mol with a polydispersity of 1.18, and the weight fraction of PS is 0.15. The nanoparticles are coated with polystyrene chains. The mean diameter of the nanoparticles is 10 nm and the weight ratio of nanoparticles in toluene solution is 2 wt%.

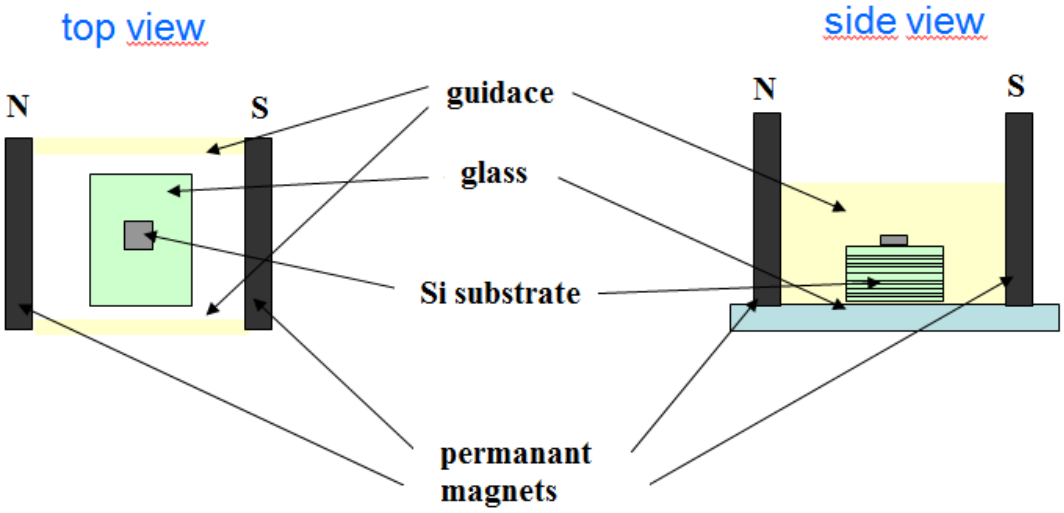

Figure 5.4: Sketch of solution casting set-up with applied magnetic field.

Silicon substrates (Si 100, n-type, Silchem) are immersed into an acid cleaning bath (200 mL of H_2SO_4, 70 mL of H_2O_2, and 130 mL of deionized water) at 80 ^oC for 15 min followed by strong rinsing with deionized water and subsequent drying with N_2 gas. Different nanoparticle-polymer solutions are prepared by using toluene as solvent and having a fixed polymer concentration of 10 mg/mL. The weight ratio of maghemite nanoparticles with respect to the polymer P(S-*b*-MMA) is varied: 0, 0.5 and 1.0 wt%. Diblock copolymer films containing magnetic nanoparticles are produced by solution casting on the Si substrates placed horizontally with a laser alignment, while applying an external magnetic field oriented parallel to the sample surface. To obtain solid films, the casting procedure lasted 24 h. Fig. 5.4 shows the casting set-up with the direction of the applied magnetic field.
The resulting hybrid films are characterized by optical microscopy (OM). The optical micrographs shown in Fig. 5.5 and Fig. 5.6 display the submicrometer- and micrometer-sized wire-shape nanoparticle aggregated formed on the film surface. No phase separation is discovered from Fig. 5.5 a-b, because the films are made at ambient conditions and no annealing or magnetic field have been applied after of during the formation of the polymer films. Random iron oxide nanoparticles and aggregates of nanoparticles can be observed in Fig. 5.5 b, which is due

to the polystyrene coating of the nanoparticles. This coating enables a well dispersion of the nanoparticles inside the PS domains and lowers the attraction for each other towards aggregation. Obviously wire-shape strips are found in Fig. 5.5 c-d and Fig. 5.6. The lines of nanoparticles orient well along the direction of the external magnetic field, and the width and density of the metal-oxide wires increase with the increment of nanoparticle concentration. Higher nanoparticle concentrations will contribute to an improvement of the overall hybrid polymer system.

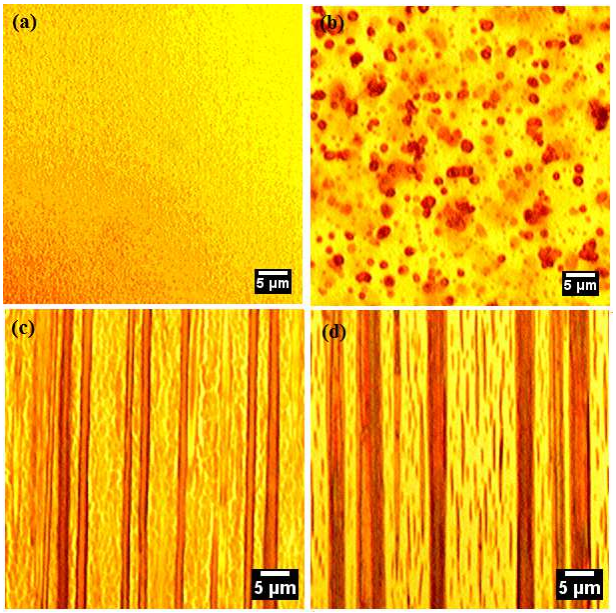

Figure 5.5:
Optical microscopy images of the polymer films with and without metal-oxide nanoparticles under or without magnetic field: (a) pure film, (b) 0.5 wt% nanoparticle concentration, (c) 0.5 wt% nanoparticle concentration with applied magnetic field, (d) 1.0 wt% nanoparticle concentration with applied magnetic field.

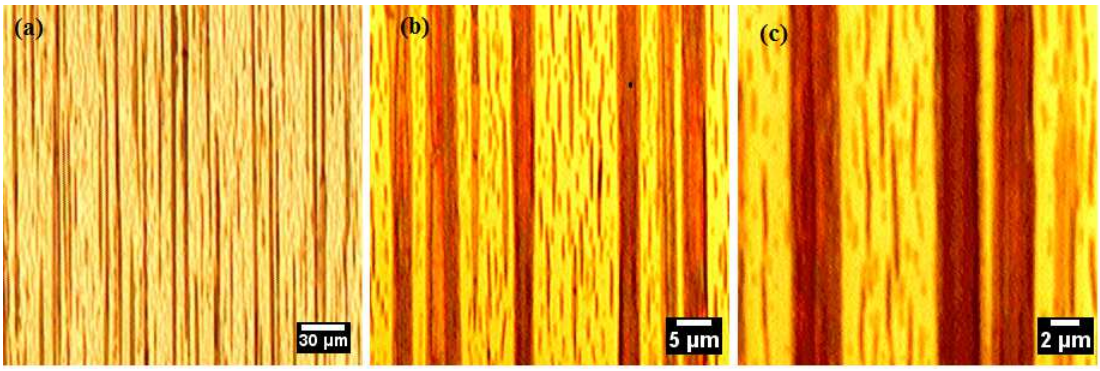

Figure 5.6:
Optical microscopy images of the polymer films under different magnifications, the nanoparticle concentration is 1.0 wt%.

[1] Y. Yao, E. Metwalli, J.-F. Moulin, B. Su, M. Opel, P. Müller-Buschbaum, *ACS Appl. Mater. Interfaces* **6**, 18152-18162 (2014)

[2] Y. Yao, E. Metwalli, M. A. Niedermeier, M. Opel, C. Lin, J. Ning, J. Perlich, S. V. Roth, P. Müller-Buschbaum, *ACS Appl. Mater. Interfaces* **6**, 5244-5254 (2014)

5.3 Polarized neutron reflectivity study of metal oxide-polymer nanocomposite films

E. Metwalli, M. Bahr, Y. Yao, A. Koustsioumpas[1], P. Müller-Buschbaum

[1] MLZ, Garching, Germany

Doping metal oxide nanoparticles (NPs) into block copolymers produces hybrid materials with novel thermal, mechanical, electric, optical, or magnetic properties, which enable many interesting applications such as catalysis, solar cell, sensors, target drug delivery, and magnetic storage devices. Diblock copolymers (DBCs) are promising materials for the manufacturing of diverse nanoscale ordered structures via a low cost, high efficient self-assembly method [1-5]. The poly(styrene-d8-block-n-butyl methacrylate) DBC denoted PSd-b-PBMA, with the total number average molecular weight of 298 kg/mol, the weight fraction of PSd of 0.53 and polydispersity M_w/M_n = 1.18 was used. On the basis of the theoretical phase diagram of DBCs, a lamella morphology is expected for the bare PSd-b-PBMA bulk sample. Polystyrene (PS) coated 10 nm sized maghemite NPs ($\gamma-Fe_2O_3$) are used in the current investigation.
The polymer solution of 100 mg/mL was prepared at room temperature and mixed with the appropriate amount of nanoparticle solution. The weight ratio of PS-coated maghemite NPs with respect to the polymer PSd-b-PBMA was 5 wt%. The hybrid films are produced by spin coating on pre-cleaned Si substrates. The as-prepared hybrid films are further annealed at 150 °C for 14 hours for establishing the morphology. Polarized neutron reflectometry (PNR) experiments are performed at the MARIA instrument of the JCNS at MLZ.

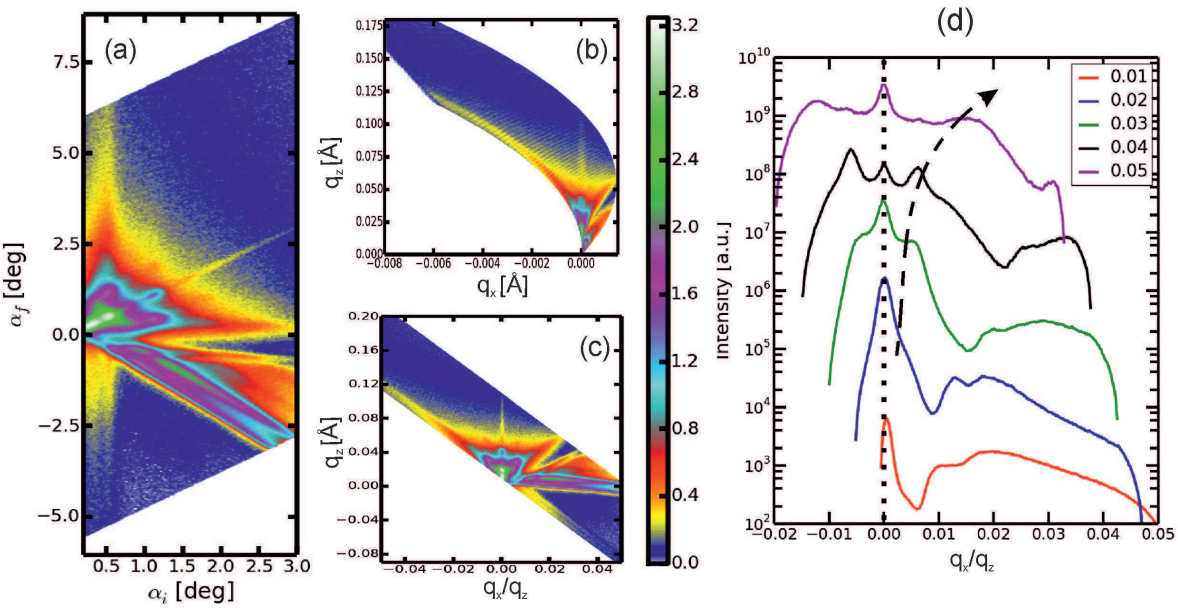

Figure 5.7:
(a) Measured 2D intensity maps for the metal oxide-polymer nanocomposite with 5 wt% NPs in angular presentation and in (b) reciprocal space presentation (q_x, q_z map). This representation suffers from a squeeze of the q_x component at small q_z values. (c) Alternative presentation using a normalization with respect to q_z resolves this problem. (d) Line cuts from the q_x, q_z map at different q_z positions showing the off-specular scattering as a function of q_x (transverse scans).

A collimated neutron beam (λ = 6 Å) impinges on the sample at an angle θ_i while the specular ($\theta_i = \theta_f$) and off-specular scattering is collected on a 2D position sensitive detector (pixel size of 2 x 3 mm^2). Polarized neutron reflectivity (PNR) data of the investigated sample (5 wt% NPs)

are measured at 10 K under an external applied magnetic field of 600 mT. The PNR data are further collected after removing the magnetic field to probe possible magnetic correlations at remanence. Fig. 5.7 shows the 2D intensity data of the PNR measurement in different representations. From Fig. 5.7 high off-specular intensity is observed at $q_x \neq 0$.

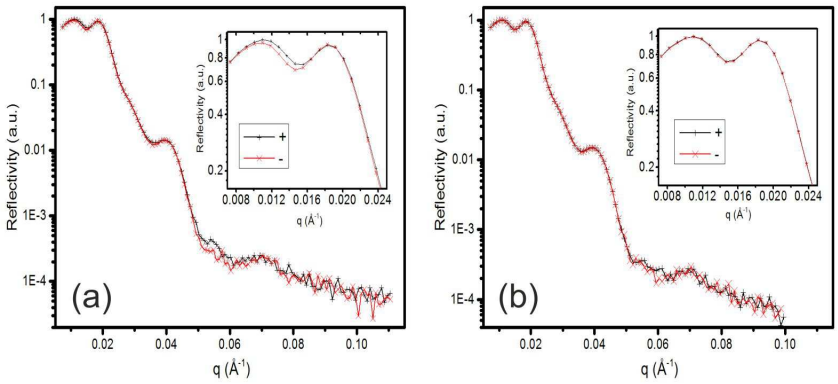

Figure 5.8:
PNR data measured at 10 K with the sample (a) at the saturation magnetization (600 mT) and (b) at remanence. The reflectivity profiles are shown for two different polarization orientations.

Two symmetric high-intensity scattering Yoneda wings mirrored around the specular (q_x = 0) reflection are visible in Fig. 5.7c. The off-specular intensity is due to both, the surface and interfacial roughness as well as nanoparticles dispersion in the nano-composite film. The specular reflectivity data (q_x = 0) are extracted from the 2D intensity maps as a function of the incident momentum transfer normal to the surface ($q_z = 4\pi \sin\theta_i / \lambda$). At an external magnetic field of 600 mT, variations between the reflected intensities (Fig. 5.8) for neuron with positive and negative spin projection onto the magnetization direction are indicative of a magnetization component either parallel or perpendicular to the neutron polarization. In contrast, upon removing the external magnetic field the reflectivity profiles coincidence, indicating a complete demagnetization of the sample at remanence.
Thus, the PNR data reveal strong evidence that the particles are highly confined within the lamella morphology of the DBC, while laterally highly dispersed within the PS layers as indicated from the strong off-specular reflection. This experiment proves success to probe magnetization correlations of small NP size dispersed within layered polymer structure where long-range competing random interactions dominate.

[1] E. Metwalli, V. Körstgens, K. Schlage, R. Meier, G. Kaune, A. Buffet, S. Couet, S. V. Roth, R. Röhlsberger, P. Müller-Buschbaum, *Langmuir* **29**, 6331-6340 (2013)

[2] E. Metwalli, I. Krisch, I. Markovits, M. Rawolle, M. A. Ruderer, S. Guo, S. Wyrzgol, A. Jentys, J. Perlich, J. A. Lercher, P. Müller-Buschbaum, *Chem. Phys. Chem.* **15**, 2236-2239 (2014)

[3] X. Xia, E. Metwalli, M. A. Ruderer, V. Körstgens, P. Busch, P. Böni, P. Müller-Buschbaum, *J. Phys.: Condens. Matt.* **23**, 254203 (2011)

[4] Y. Yao, E. Metwalli, J.-F. Moulin, B. Su, M. Opel, P. Müller-Buschbaum, *ACS Appl. Mater. Interfaces* **6**, 18152-18162 (2014)

[5] Y. Yao, E. Metwalli, M. A. Niedermeier, M Opel, C. Lin, J. Ning, J. Perlich, S. V. Roth, P. Müller-Buschbaum, *ACS Appl. Mater. Interfaces* **6**, 5244-5254 (2014)

5.4 Nanocomposites composed of HEUR polymer and magnetite iron oxide nanoparticles: structure and magnetic response of the hydrogel and dried state

A. Campanella [1], H. Frielinghaus [1], P. Müller-Buschbaum

[1] MLZ, Garching, Germany

Nanocomposite materials have attracted much attention because of their novel physical properties, which promise potential use in future applications. For instance, magnetic nanocomposites have a potential use in electronics. For such systems, often magnetic nanoparticles, e. g. magnetite (Fe_3O_4) or maghemite (γ-Fe_2O_3) nanoparticles, are dispersed in a polymeric phase, so that the final systems shows novel magnetic properties.
A novel type of nanocomposite composed of hydrophobically modified ethoxylated urethane (HEUR) polymer and coated magnetite nanoparticles is investigated in the present study. Because of its ability to connect hydrophobic domains through the two hydrophobic end groups in an otherwise aqueous phase, the HEUR polymer is often called telechelic polymer [1]. A sketch is shown in Fig. 5.9.

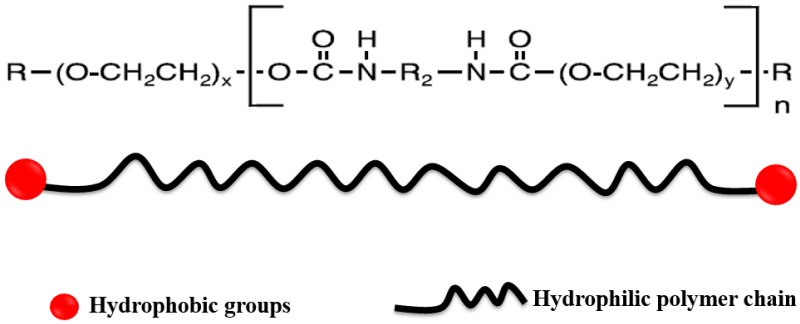

Figure 5.9: Chemical structure and sketch of the telechelic polymer (HEUR) under investigation

For the nanocomposite preparation we synthetized two different kinds of coated magnetite nanoparticles, which differ in their coating: One type of nanoparticles is hydrophobic due to an oleic acid and oleylamine coating. The second type of nanoparticles is hydrophilic, because it exhibits the cationic surfactant C18TAB as an additional layer to the oleic acid and oleylamine coating [2,3]. A sketch of types of the nanoparticles is displayed in Fig. 5.10.
In the first step we characterize the structure of the polymer network formed in the hydrogel and compare this to that in the dried state. For this purpose, small angle neutron scattering (SANS) measurements are carried out. The SANS measurements are performed at KWS-1 at the MLZ using a neutron wavelength of 4.7 Å ($\pm 5\%$). The hydrogel samples are measured in D_2O as solvent in order to avoid recording the high incoherent scattering of H_2O.
We analyzed 8 telechelic polymer solutions at increasing concentration: 0.46 wt %, 0.92 wt %, 1.38 wt %, 1.84 wt %, 5 wt %, 10 wt %, 15 wt % and 25 wt %. Based on the change of the correlation peak positions Q_{max} in the SANS data with increasing the polymer concentration, we can state that the HEUR polymer network is patch-wise dense in 3-dimensional space. In a second step, the structure of the nanocomposites as hydrogels with either magnetic nanoparticles is analyzed separately using SANS as well. We analyze the 2 different kind of hydrogels at different magnetic nanoparticles loading, i.e. from 0.23 wt % up to 3 wt %. In the SANS data we observe an increase of the domain spacing d of the polymer network, which is related to the distance between the hydrophobic domains of the HEUR polymer network. From the comparison between the SANS patterns of hydrogels containing hydrophobic magnetic nanoparticles and the hydrogels containing hydrophilic magnetic nanoparticles, we can observe a stronger influence

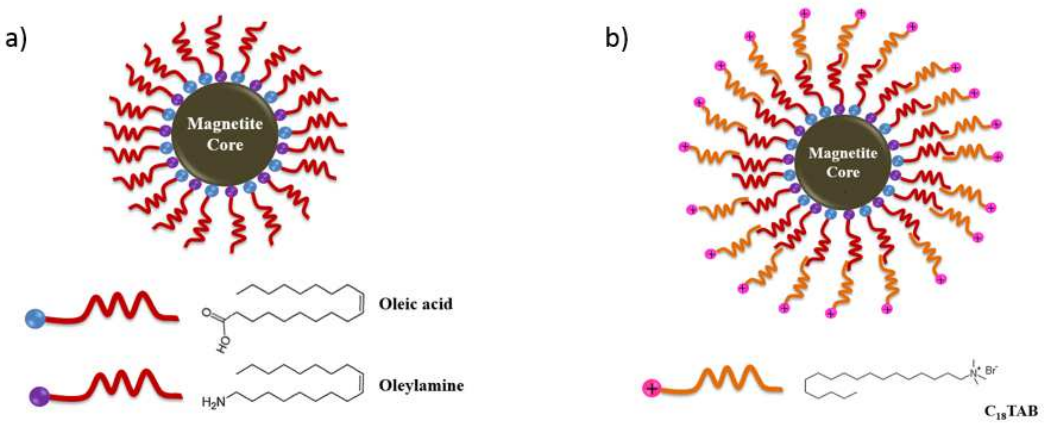

Figure 5.10:
a) Sketch of the magnetic nanoparticles with hydrophobic coating and b) with hydrophilic coating

of the hydrophobic magnetic nanoparticles on the domain spacing of the HEUR polymer network than with the hydrophilic ones. This is due to the different interactions occurring between the polymer molecules and the two different kinds of magnetic nanoparticles. The hydrophobic nanoparticles interact preferably with the hydrophobic end-groups of the telechelic polymer and most probably they are embedded in the hydrophobic domains of the polymer network. On the other hand, the hydrophilic nanoparticles interact mainly with the polar backbones of the polymer molecules and with the solvent. Therefore, the influence of the hydrophilic nanoparticles on the hydrophobic domains of the polymer network is not that important.
We also prepare the nanocomposite systems containing hydrophobic magnetic nanoparticles as thin dry films. On these dry films we perform magnetic response measurements. We observe a high magnetic response which matches a superparamagnetic behavior, as expected from the small nanoparticle size. Such superparamagnetic behavior is very useful in several applications, since it allows to change the magnetization without losses [4]. An interesting application of this novel type of nanocomposites could be electromagnetic wave absorbers. Since the performance of these devices depends on microwave absorption properties we would like to perform dielectric and magnetic spectroscopy measurements on the hydrogels and dry films in the future.

[1] A. N. Semenov, I. A. Nyrkova, M. E. Cates, *Macromolecules* **28**, 7879-7885 (1995)

[2] L. Wang, J. Luo, Q. Fan, M. Suzuki, I. S. Suzuki, M. H. Engelhard, Y. Lin, N. Kim, J. Q. Wang, C. J. Zhong *J. Phys. Chem.* **109**, 21593-21601 (2005)

[3] S. Sun, H. Zeng, D. B. Robinson, S. Rauox, P. M. Rice, S. X. Wang, G. Li, *J. Am. Chem. Soc.* **126**, 273-279 (2004)

[4] Z. Guo, S. Park, T. Hahn, S. Wei, M. Moldovan, A. B. Karki, D. P. Young, *J. Appl. Phys.* **43**, 09M511 (2007)

5.5 Polymer metal oxide hybrid materials

M. Bahr, E. Metwalli, P. Müller-Buschbaum

Metal oxide-polymer nanocomposites are novel materials due to their unique electrical, optical and magnetic properties [1-3]. Thin films of metal oxide-polymer nanocomposites can also be prepared for many potential applications including sensors and memory devices. In such composites diblock copolymers are the matrix of choice for providing the desired arrangement of the metal oxide, since they develop nanostructures via micro-phase separation and self-assembly processes. Due to the high metal selectivity to one block of the block copolymer, well ordered metal oxide nanopatterns within the polymer matrix can be achieved. We use the diblock copolymer poly(styrene-*b*-methylmethacrylate) (PS-*b*-PMMA), which forms a lamellar structure, as a matrix and a cobalt salt based on a 2,2′ bipyridine ring ($C_{10}H_8Cl_2CoN_2$) as a precursor for the metal oxide. Bulk samples are prepared with different Co/PMMA molar ratios (R_{mol}). The structural evolution of the bulk samples is investigated as a function of temperature using in situ small-angle x-ray scattering (SAXS). In an initial experiment we study the morphology transformation of the as cast film. Samples are prepared at room temperature and heated up to 205°C. A lamellar structure seems to develop during the progressive heating steps (see figure 5.11) as indicated from the emerging scattering peaks, which exhibit a ratio of the corresponding q-position q*/q = 3. The observed broad scattering peaks indicate the transformation of a non-equilibrium morphology, which has to be expected since an as cast sample was studied. Moreover, the cobalt salt is transformed into cobalt oxide.

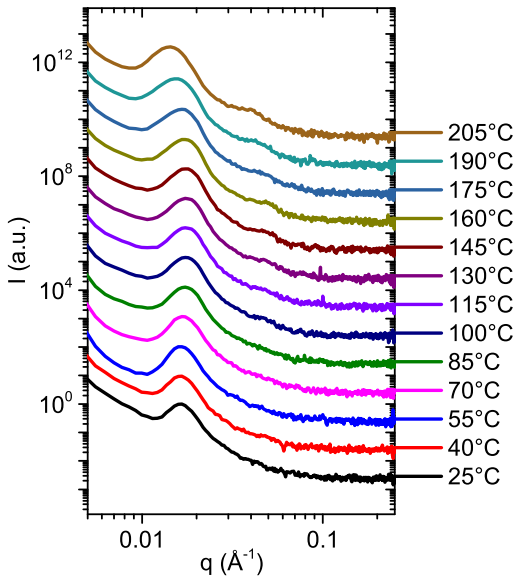

Figure 5.11:
SAXS data measured in situ during heating up the as cast sample PS-*b*-PMMA with cobalt salt (R_{mol}=0.025). The curves are shifted along the y axis for clarity of the presentation.

For getting equilibrated samples, they have to be heated up for longer times to temperatures well above the glass transition temperature, but below the order-to-disorder temperature. Thus, after the first heating-up and cooling-down series of the hybrid samples they are further heated up a second time and measured again. Figure 5.12 shows the 2D SAXS data for the hybrid materials annealed at 150°C for different time. The extracted SAXS profiles are plotted in figure 5.13. The development of further scattering peaks following q*/q= 1,2,3,4,5 is seen upon heating for 65 hours. The results indicate that the sample is in a more equilibrated state after heat annealing for longer times. Heating above the order-to-disorder temperature erases the micro-phase separation because the two block become miscible and no phase separation occurs. From a less

ordered structure or even unordered structure no characteristic scattering features arise.

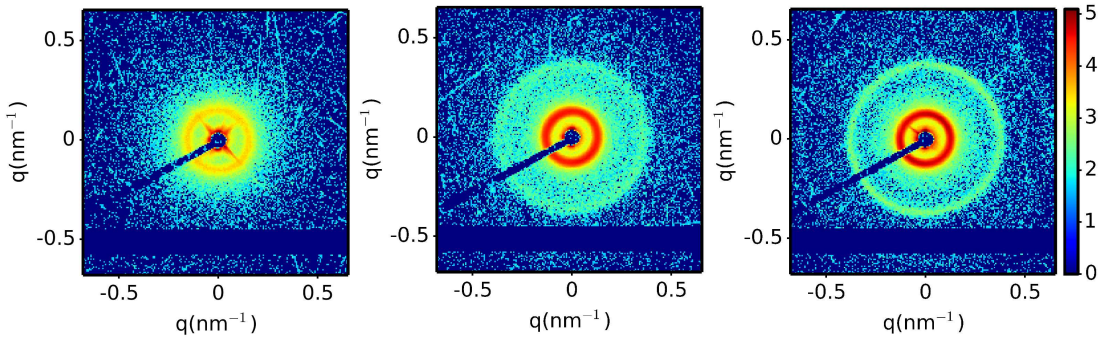

Figure 5.12:
2D SAXS data of hybrid samples of the PS-*b*-PMMA block copolymer and the cobalt salt thermally post-treated at 150°C for 0 h, 15 h and 65 h annealing time (from left to right).

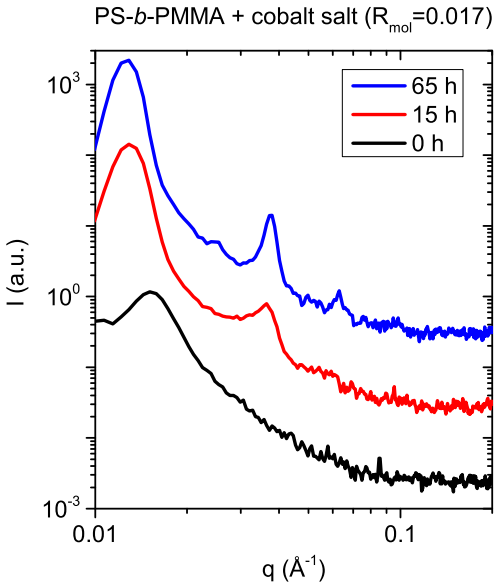

Figure 5.13:
SAXS profiles of hybrid samples of the (PS-*b*-PMMA) block copolymer and the cobalt salt thermally post-treated at 150°C for different annealing time as indicated. The curves are shifted along the y axis for clarity of the presentation.

Bulk samples with different molar ratios have been prepared. Upon increasing the metal salt content the lamellar spacing tends to continuously decrease. This observation is consistent with the assumption that the cobalt selectively adsorbs to the PMMA domains. The MMA monomers order around the metal oxide. Due to more metal oxide in the matrix, the chain tends to be in a more compact format and this leads to a pronounced decrease of the polymer domain dimensions (data not shown). Further investigations have to be done with thin films of these metal oxide-polymer nanocomposites, such as AFM and SEM measurements for analyzing the structure. FTIR and UV-Vis can be used to investigate the oxidation of the cobalt and if there is a change during the sample preparation and the heating measurements. Magnetic measurements will be added to consider the hybrid film for future applications.

[1] Y. Yao, E. Metwalli, J.-F. Moulin, B. Su, M. Opel, P. Müller-Buschbaum, *ACS Appl. Mater. Interfaces* **6**, 18152-18162 (2014)

[2] E. Metwalli, I. Krisch, I. Markovits, M. Rawolle, M.A. Ruderer, S. Guo, S. Wyrzgol, A. Jentys, J. Perlich, J.A. Lercher, P. Müller-Buschbaum, *Chem. Phys. Chem.* **15**, 2236-2239 (2014)

[3] Y. Yao, E. Metwalli, M.A. Niedermeier, M. Opel, C. Lin, J. Ning, J. Perlich, S.V. Roth, P. Müller-Buschbaum, *ACS Appl. Mater. Interfaces* **6**, 5244-5254 (2014)

5.6 Hybrid thermoelectrics based on a polymer nanoparticle composite

N. Saxena, A. Greppmair[1], M. Coric[2], J. Wernecke[3], S. Marggraf[3], E. M. Herzig[2], M. S. Brandt[1], P. Müller-Buschbaum

[1] WSI, TU München, München,Germany
[2] MSE, TU München, München,Germany
[3] PTB, BESSY II, Berlin, Germany

In recent years, global concern of climate change has led to dramatically increased interest in research on renewable energies. In daily processes, e.g. upon combustion of fossil fuels in car engines, heat is generated which dissipates into the environment without being used further. Also about half of the solar spectrum comprises infrared radiation, which cannot be used by conventional solar cells. Therefore, it is feasible to develop technologies which utilize this kind of low-quality waste heat. Thermoelectrics transform temperature gradients into electrical voltages by letting charge carriers flow from the hot to the cold side of the material. The conversion efficiency is dependent on both the thermal and electrical conductivity (κ and σ, respectively), and also a material property called the Seebeck coefficient S which is the ratio of the generated voltage and the corresponding temperature difference. These quantities are combined in the dimensionless so-called figure of merit ZT, seen in Formula 5.1.

$$ZT = \frac{\sigma S^2}{\kappa} T \tag{5.1}$$

One major bottleneck for the increase of the ZT is the interdependence of these three quantities. In 1993 Dresselhaus *et al.* proposed an increase of efficiencies upon confinement of the material to nanoscale [1]. Following this, researchers synthesized highly efficient nanostructured semiconducting heavy metal chalcogenides such as Bi_2Te_3 or PbTe. Unfortunately, the high cost in energy and money for obtaining and processing the raw materials into thermoelectrics has impeded their large-scale application. Also these devices are operated at high temperatures (above 200 °C), and are therefore not usable for many daily life applications.
Thus, we want to circumvent the limitations imposed by pure inorganic materials, and use a hybrid composite of conducting polymers and inorganic nanoparticles. In our case, the polymer blend PEDOT:PSS is used as the electrically conducting scaffold, while the silicon nanoparticles

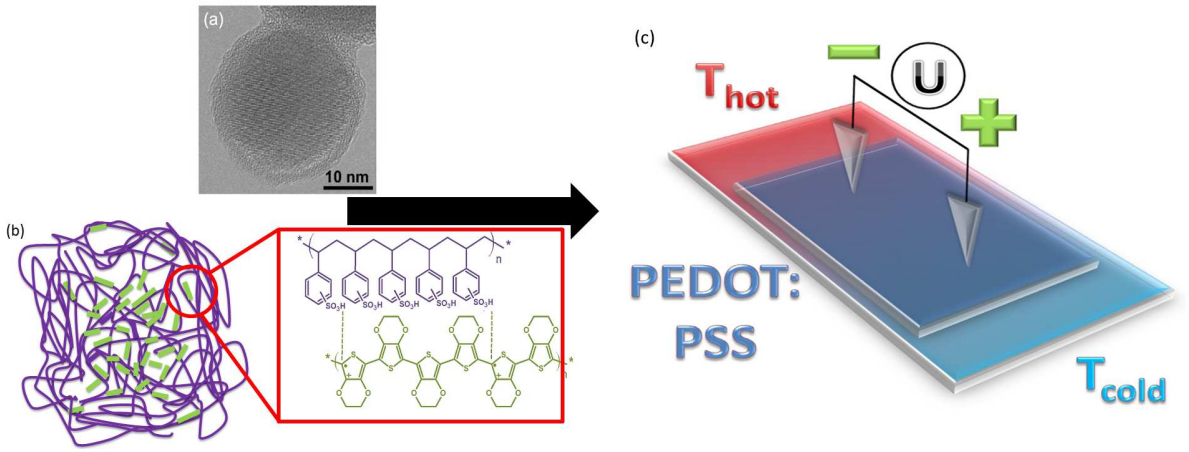

Figure 5.14: (a) Transmission electron micrograph of a silicon nanoparticle (Si-NP) [2] (b) conducting polymer blend PEDOT:PSS (green: PEDOT, purple: PSS) (c) measurement setup for thermopower with temperature gradient.

(Si-NPs), as the inorganic component, act as scattering centers for heat within the material. We prepare thin films by means of standard preparation techniques, in this case spin-coating and aim to investigate the morphological changes upon introduction of Si-NPs into the polymer film with grazing incidence small angle x-ray scattering (GISAXS) and correlate them to the macroscopically measurable properties such as thermal conductivity and thermopower.
Figure 5.14 (a) shows transmission electron microscope images of the Si-NPS used in this work, with the crystalline silicon core and the amorphous silicon oxide shell clearly visible. The conducting hydrophobic component of the polymer blend poly(3,4-ethylenedioxythiophene (PEDOT, indicated by bars) and its water-soluble insulating counterpart polystyrenesulfonate (PSS, indicated by curvy lines) are shown in Figure 5.14 (b). The setup for thermovoltage measurements, which involves a heating stage allowing for the generation of a temperature gradient along the thermoelectric film resting on a glass substrate, is shown in Figure 5.14 (c). Research over the past few years showed that the electrical conductivity of PEDOT:PSS can be increased to levels of about 1000 S/cm by secondary doping with high-boiling point solvents such as glycerine or ethylene glycol. Palumbiny *et al.* assigned this increase in conductivity to the breakdown and the higher packing density of PEDOT domains, as well as removal of insulating PSS [2].

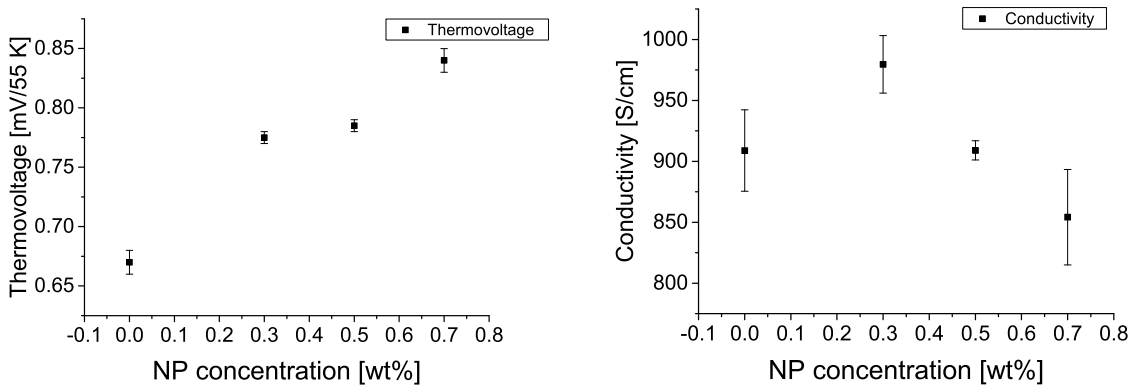

Figure 5.15: Left: Dependence of thermovoltage on NP concentration, right: dependence of electrical conductivity on NP concentration.

Based on a 7 wt% stock solution of Si-NPs in EtOH we prepare dilutions in pure EtOH (0.1 wt%, 0.3 wt%, 0.5 wt%, 0.7 wt%). As can be seen in the left graph in Figure 5.15, a linear increase of the thermovoltage with increasing NP concentration in the dilution is observable. In contrast, regarding the electrical conductivity, no such linear relation is visible. In order to get better insight into the morphological changes of PEDOT:PSS induced by the presence of the Si-NPs, we performed GISAXS measurements under resonant conditions at the BESSY II beamline in Berlin. By choosing appropriate wavelengths, we can selectively enhance or neglect contributions to scattering coming from certain atoms or functional groups. With this, we are able to determine the lateral distribution of the Si-NPs, and discern their influence on their above mentioned findings.

[1] L. D. Hicks, M. S. Dresselhaus, *Phys. Rev. B*, **47**, 16631 (1993)

[2] A. Stegner, *Shallow dopants in nanostructured and in isotopically engineered silicon*, TUM (2010)

[3] C. M. Palumbiny, C. Heller, C. J. Schaffer, V. Körstgens, G. Santoro, S. V. Roth, P. Müller-Buschbaum, *J. Phys. Chem. C.* **118**, 13598 (2014)

5.7 Real time observation of gold nanoparticles growth on polymer nanotemplates

E. Metwalli, Y. Yao, M. Schwartzkopf[1], S. V. Roth[1], P. Müller-Buschbaum

[1] DESY, Hamburg, Germany

Nanoparticles (NPs) are important for many technological applications, including catalysis, recording media, thin film technology, optoelectronic, magnetic sensors, anti-bacterial surfaces, and biological imaging. The properties of the NPs are related to their size and shape. Physical sputtering of metal on chemically or energetically different surfaces can result in the formation of different NP sizes and shapes. Therefore, the growth kinetics of metal NP on solid supports has crucial consequences on the structure and physical properties of the prepared active hybrid surfaces. Gold metal deposition on polymer templates is generally a powerful way for achieving various kinds of metal nano-patterns [1-5]. In order to understand the effect of polymer chemistry and morphology on the metal growth kinetics, in situ real-time grazing incidence small-angle x-ray scattering (GISAXS) is employed.

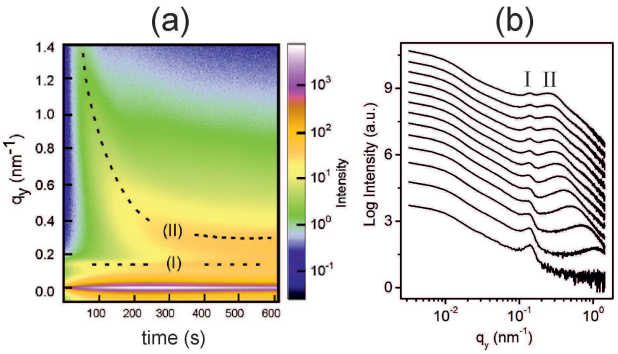

Figure 5.16:
a) Mapping of the horizontal line cuts (q_y) collected from 0.1 s time-resolved 2d GISAXS data. Intensity peak related to polymer template (I) and metal (II) are indicated. b) GISAXS q_y profiles of the metal-hybrid film upon real time continuous Au deposition on the polymer template. The horizontal line cuts are presented for deposition times from 0 s up to 600 s in steps of 50 s.

The real time GISAXS technique systematically monitors the growth behavior of the metal NPs and provides details on the geometric structure of metal NPs. A diblock copolymer film with a cylindrical microphase separation structure (polystyrene-block-polybutadiene, PS-b-PB with molecular weight M_w = 104.7 kg/mol and f_{ps} = 0.32) was prepared by spin coating out of solution. A highly automated sputtering equipment (HASE) is used for the in situ GISAXS measurement [6]. The main sputtering chamber is evacuated down by a two-stage turbo molecular pump that brings the chamber into a base pressure of 1.5 x 10^{-8} mbar. Then, the deposition is performed at an argon pressure of 1.1 x 10^{-2} mbar. Gold in its atomic phase is deposited on the polymer template. A sputtering rate of 1.44 $\pm$ 0.09 nm/min is employed and 2d GISAXS data are simultaneously acquired during the gold sputtering time. The in situ GISAXS measurements are carried out at beamline P03 of PETRAIII storage ring at DESY, Hamburg. We have collected 6000 frames using a Pilatus 1M detector in 600 s (10 frames per s) using a micro-focused X-ray beam with a beam size of 31 μm x 19 μm (horizontal x vertical) with a wavelength λ = (96.0 $\pm$ 0.2) pm, incidence angle of 0.452° and sample to detector distance D = 3518 mm. Quantitative information of the growing metal particle size and sized distribution are gained by performing horizontal line cuts of the 2d GISAXS data at an average value of the Yoneda peaks of the materials involved. From the q_y line cuts (Fig. 5.16b) two characteristic peaks are identified: The polymer peak (I) and the metal peak (II). A single characteristic peak (0.141 nm^{-1}) is initially observed for the metal-free polymer template. As seen from Fig. 5.16b, the position of the peak related to the polymer (I) stays at a fixed q_y position (0.141 nm^{-1}) with increasing deposition time. In contrast, the metal characteristic peak (II) shifts from high q_y values to low q_y values upon progressive metal load (Fig. 5.16b, from bottom to top). Using the DPDAK software, all scattering peaks in the 6000 frames are fitted (example fit is in the inset in Fig. 5.17a). The evolution of the scattering peaks is represented in reciprocal space in Fig. 5.17a. These reciprocal space data show an increase of the corresponding real space distance between the metal

particles with increasing sputter time (Fig. 5.17b). It reveals a continuous particle coalescence forming large particle sizes. At a metal load of about 4.4 nm, the latter peaks (II) levels off at a q_y value (0.281 nm^{-1}). At this metal load, a quasi-uniform metal layer on top of the polymer film can be assumed.

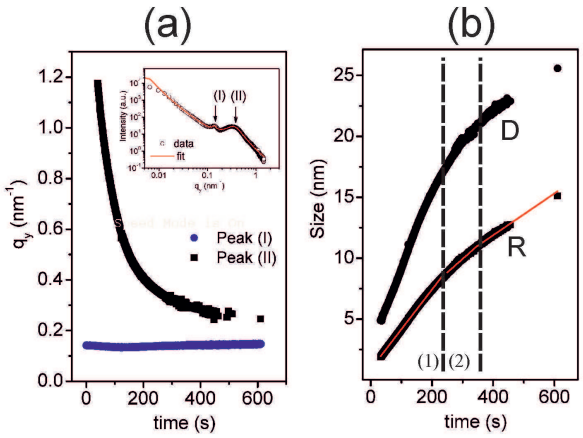

Figure 5.17:
The q_y values of the position of peak (I) and peak (II) as a function of time, obtained by fitting of individual horizontal line cuts. The inset shows an individual fit of the frame number 3000. b) The real space inter-particle distance D and the metal particle radius (R).

The overall experiment indicates that as the metal atoms arrive at the polymer surface, they migrate on the surface and when two of them are near neighbors, they form a stable nucleus and remain on the surface. With increasing the gold metal upload on or in the polymer film, many random nucleation sites are formed. When the distance between the two neighboring islands is less than the diffusion length of the atoms in the polymer matrix, the density of nuclei reaches saturation. After that, all arriving adatoms are captured by the islands either directly or after diffusion along the substrate surface to minimize their energy. The diffusion of gold NPs in the polystyrene domains may explain the fast aggregation on the PS domains and the high selectivity of gold on the PS block. This diffusion is mainly determined by the metal-polymer interaction, which depends mainly on the chemistry, stiffness, and surface topography of the films.

[1] E. Metwalli, V. Körstgens, K. Schlage, R. Meier, G. Kaune, A. Buffet, S. Couet, S. V. Roth, R. Röhlsberger, P. Müller-Buschbaum, *Langmuir* **29**, 6331-6340 (2013)

[2] E. Metwalli, J.F. Moulin, J. Perlich, W. Wang, A. Diethert, S.V. Roth, P. Müller-Buschbaum, *Langmuir* **25**, 11815 (2009)

[3] M. Schwartzkopf, A. Buffet, V. Körstgens, E. Metwalli, K. Schlage, G. Benecke, J. Perlich, M. Rawolle, A. Rothkirch, B. Heidmann, G. Herzog, P. Müller-Buschbaum, R. Röhlsberger, R. Gehrke, N. Stribeck, S.V. Roth, *Nanoscale* **5**, 5053 (2013)

[4] E. Metwalli, I. Krisch, I. Markovits, M. Rawolle, M. A. Ruderer, S. Guo, S. Wyrzgol, A. Jentys, J. Perlich, J. A. Lercher, P. Müller-Buschbaum, *Chem. Phys. Chem.* **15**, 2236-2239 (2014)

[5] Y. Yao, E. Metwalli, M. A. Niedermeier, M Opel, C. Lin, J. Ning, J. Perlich, S. V. Roth, P. Müller-Buschbaum, *ACS Appl. Mater. Interfaces* **6**, 5244-5254 (2014)

[6] R. Dohrmann, S. Botta, A. Buffet, G. Santoro, K. Schlage, M. Schwartzkopf, S. Bommel, J. F. H. Risch, R. Mannweiler, S. Brunner, E. Metwalli, P. Müller-Buschbaum, S. V. Roth, *Rev. Sci. Instrum.* **84**, 043901 (2013)

5.8 In situ growth study of gold nano domains on P3HT films

B. Su, W. Liu, Y. Yao, G. Santoro[1], S. V. Roth[1], P. Müller-Buschbaum

[1] DESY, Hamburg, Germany

Hybrid solar cells and solid-state dye sensitized solar cells (ssDSSC) have been studied to a large extend in recent years, since they can combine the advantages of low cost and chemical stability of inorganic materials and easy processing of the organic materials. Poly(3-hexylthiophene) (P3HT) is widely used in hybrid solar cells as a sensitizer and hole conductor, due to its high hole mobility and light absorption. In addition, the interface of P3HT and the cathode layer plays an important role in photo-induced charge separation, where the holes are inject to the cathode. A commonly used material for the cathode layer is gold, since it has a proper work function for hybrid solar cells. In the present study, we use in-situ grazing incidence small angle x-ray scattering (in situ GISAXS) to characterize the morphology evolution of gold films on a P3HT layer [1].
A silicon wafer (100) is used as a substrate for the P3HT film. To redefine the native oxide layer and remove the organic traces from the silicon wafer, silicon is put into the acid bath (54 ml DI water, 84 ml H_2O_2 and 198 ml H_2SO_4) for 15 min at 80 °C. The P3HT was purchased from Rieke, and used without any further purification. P3HT is dissolved in anhydrous chlorobenzene at 70 °C and stirred for 1 hour. In the final solution the weight ratio of P3HT is 3 wt%. In order to measure the UV-Vis spectrum, the P3HT films are deposited on glass substrates as well. For the P3HT layer deposition we use spin coating. The parameters of rotation speed and spinning time are 2000 rpm and 40 s, respectively.

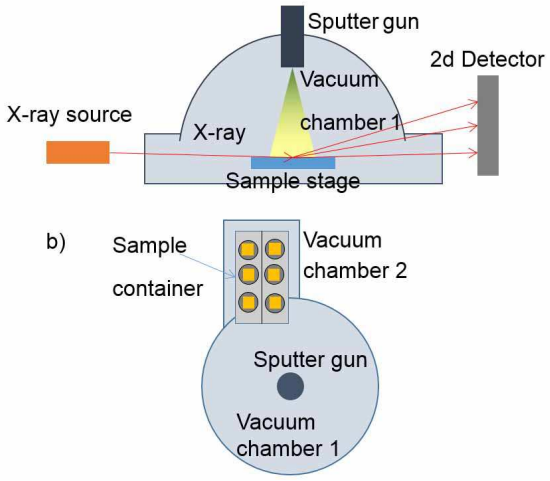

Figure 5.18:
Schematic illustration of the experimental setup for the in situ GISAXS investigation of a gold layer growth on a P3HT film. In the chamber, argon plasma is used to sputter the gold atoms from the target to the P3HT film. The x-ray beam enters and exits the chamber through two beryllium windows. The scattering signal is detected by a two-dimensional detector.

We follow the real-time gold film growth with in situ GISAXS measurements performed at the beamline P03 at PETRA III (DESY). Fig. 5.18 shows a simplified illustration of the applied sputter chamber, named Highly Automated Sputter Equipment (HASE). A x-ray wavelength of 0.957 nm, corresponding to an x-ray energy of 13 keV is used. The beam size of 28 μm x 15 μm, an incident angle of 0.5°, exposure times of 0.095 s, and exposure periods of 0.1 s are chosen. Gold films are sputtered at a pressure of 1.55 $\times 10^{-2}$ mbar, using a sputtering power of 200 W, and a sputtering time of 1220 s. Fig. 5.19 shows the 2D GISAXS data after 5 s, 25 s, 50 s, 100

s, 150 s and 200 s sputtering time. For further analysis horizontal line cuts and vertical line cuts of the 2D GISAXS data are selected at a position of the P3HT Yoneda peak and at $q_z = 0$, respectively. For a quantitative analysis of the lateral gold film structure, the horizontal line cuts are fitted with a Lorenzian function with the software DPDAK [2] and the related fitting parameters are extracted. Since the side peak positions change with time, the fitting process is divided in several intervals with different fitting ranges from 30 s until 2000 s. The peak position and corresponding Full Width Half Maximum (FWHM) are considered for further analysis. From Fig. 5.19 b) it can be seen that the inter-nanostructure distance increases with increasing sputtering time. In contrast, the increase rate decreases with the sputtering time. Moreover, at the beginning of the sputtering, the high FWHM indicates that the gold film is inhomogeneous. Later, the decrease of the FWHM shows that the system becomes more and more homogeneous. According to this growth tendency, the growth process can be divided into several regions. A similar tendence of different growth regimes was reported by Kaune et al. in earlier works on the gold sputter deposition on poly(N-vinylcarbazole) (PVK) [3]. Kaune et al. identified four steps, each dominated by a characteristic kinetic process: nucleation, lateral growth, coarsening, and vertical growth.

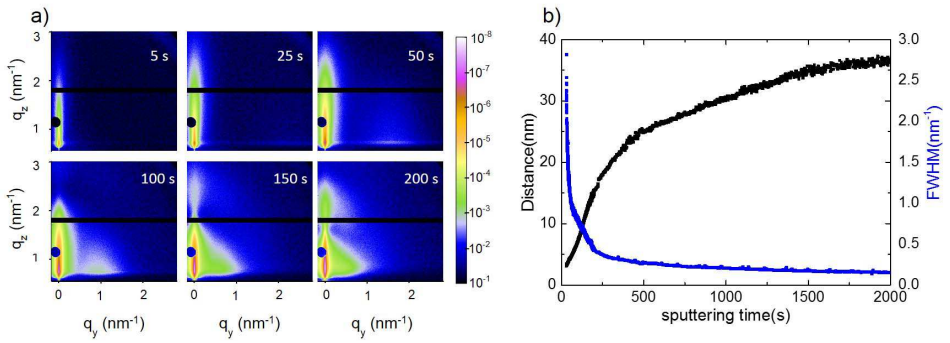

Figure 5.19:
In situ GISAXS results: a) Selected 2D GISAXS data after different sputtering times of 5 s, 25 s, 50 s, 100 s, 150 s and 200 s, respectively. b) Evolution of the lateral correlation distance as a function of sputtering time.

In conclusion, the in situ GISAXS characterization provides information of the lateral and vertical structure evolution regarding the inter-nanostructure of the gold particles during sputtering. The size of the gold nanostructure shows the tendency that it increases rapidly at the beginning of sputtering then reaches to an equilibrium state. The sizes of the gold particles are broadly distributed at the beginning, but they become more homogenous after 500 s. The result indicates gold particles are quite small and inhomogeneous at the start of sputtering, but the small particle could diffuse to neighbors then merge to large particles with increasing the time. Finally, these particles' size could reach to an equilibrium value. Thus at the end of sputtering, the gold cathode layer consists of a densely packed assembly of gold nanoparticles.

[1] E. Metwalli, S. Couet, K. Schlage, R. Rohlsberger, V. Körstgens, M. Ruderer, W. Wang, G. Kaune, S. V. Roth, P. Müller-Buschbaum, *Langmuir*, **24**, 4265-4272 (2008)

[2] G. Benecke, W. Wagermaier, C. H. Li, M. Schwartzkopf, G. Flucke, R. Hoerth, I. Zizak, M. Burghammer, E. Metwalli, P. Müller-Buschbaum, M. Trebbin, S. Förster, O. Paris, S. V. Roth, P. Fratzl, *J. Appl. Crystallogr.*, **47**, 1797-1803 (2014)

[3] G. Kaune, M. A. Ruderer, E. Metwalli, W. Wang, S. Couet, K. Schlage, R. Röhlsberger, S. V. Roth, P. Müller-Buschbaum, *ACS Appl. Mater. Interfaces*, **1**, 353-360 (2009)

5.9 Growth of silver layers on nanostructured surfaces

V. Körstgens, S. Bernstorff[1], P. Müller-Buschbaum

[1] Elettra-Sincrotrone Trieste, Basovizza, Italy

We prepared composite films with colloidal particles on a substrate decorated with silver. A two-step process is applied, were first metal ions adhere to the surface of colloidal particles and in a second step metal ions are reduced to the metallic state. By choosing the suitable reducing agent and adjusting the concentration the size and distribution of the metal nanoparticles decorating the colloids can be controlled [1]. We developed a method, in which the decoration of colloids is not performed in suspension, but with structured substrates. A layer of colloidal spheres is attached to a glass substrate via a thin coating of polyethyleneimine (PEI). These films are the source material for the metal decoration process. With this method we achieved the production of hierarchical structures with metallic nanoparticles distributed on the surface of spherical nanoparticles attached to a surface. Apart from these well-defined strawberry-like composite particles, it is also possible to achieve a closed layer of silver on a nanostructured surface in a one step process constituting a silver mirror reaction. An aqueous solution containing silver ions and a reduction agent is applied in a custom-built reaction vessel. In the reaction vessel several samples of glass slides coated with SiO_2 nanospheres of 142 nm diameter are exposed to the reactive solution under gentle stirring conditions. In Fig. 5.20 the achieved silver coatings

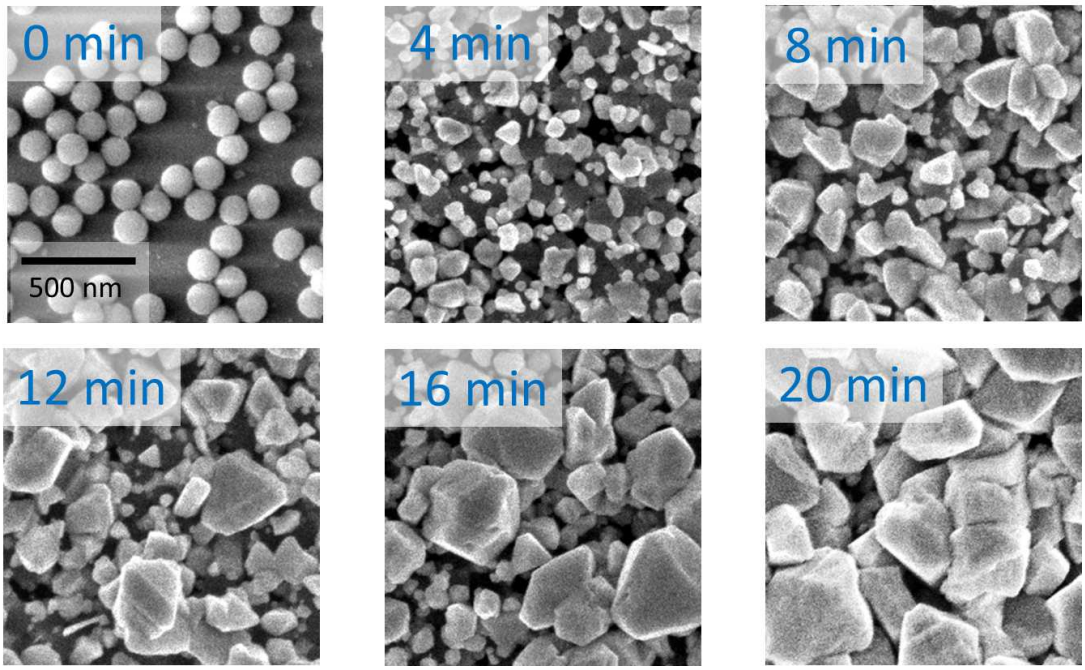

Figure 5.20:
SEM images of silver-coated nanostructured surface with different reaction times. "0 min" denotes the nanostructured initial film with SiO_2 nanospheres, the scale bar in the corresponding image is valid for all images shown. Note that silica nanospheres appear bright in the initial sample, but darker with changing contrast conditions, when electric conducting silver particles are grown on the surface with increasing reaction time.

on a glass substrate coated with SiO_2 nanospheres is shown for different reaction times. The initial nanostructured film is denoted "0 min" in Fig. 5.20. The SiO_2 nanospheres are dispersed on the surface as a single layer establishing a structured surface. Samples have been immersed for different times in the reactive solution. After 4 minutes angular silver particles are attached

to the surface with sizes in the range of the SiO_2 nanoparticles. Note that silica nanospheres appear bright in the initial sample, but much darker with the changing contrast conditions, when silver particles are grown on the surface. With increasing reaction time the growth of initially attached silver particles can be followed up to sizes of approximately 500 nm after 20 minutes.

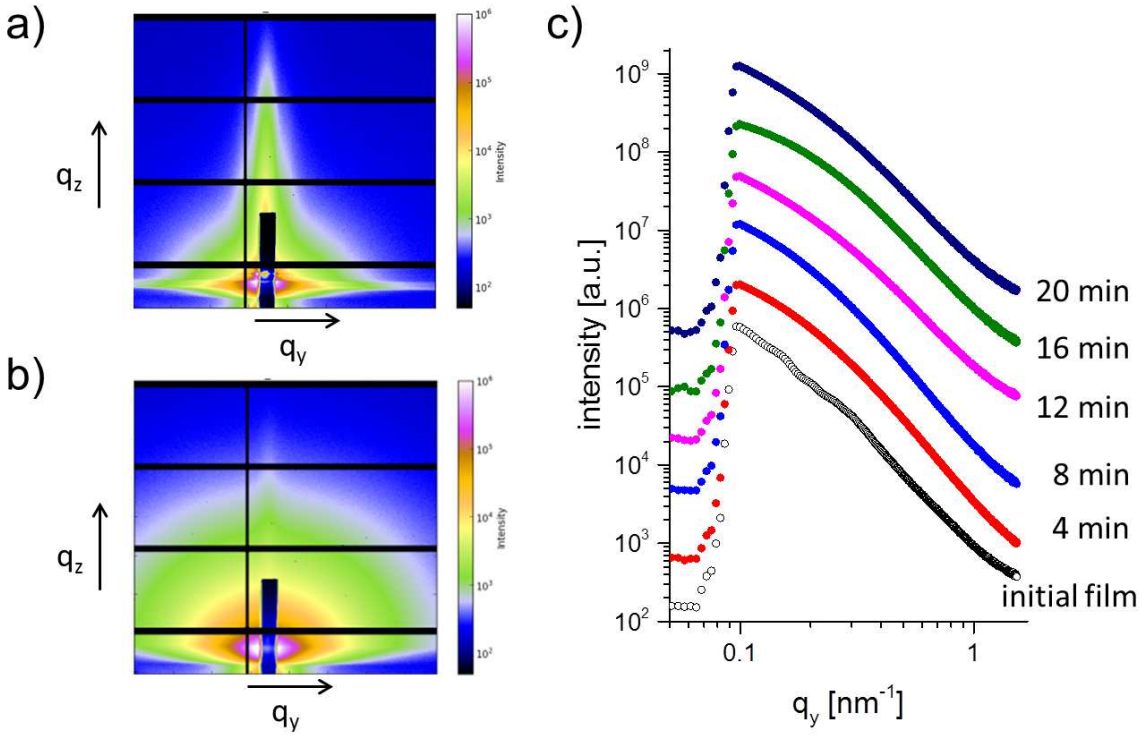

Figure 5.21:
a) 2D GISAXS data for a) a PEI coated glass substrate with SiO_2 spheres of 142 nm diameter and b) after one step coating and growth process with silver for 4 min in the reaction chamber. c) Horizontal line cuts of the 2D GISAXS data measured for the initial film and after different times in the reaction chamber. The curves are shifted along the y axis for clarity of the presentation.

We investigated the composite films with GISAXS at an energy of 8 keV with a sample-to-detector distance of 1992 mm and a Pilatus 1M Detector with 172 μm x 172 μm pixel size at the Austrian SAXS beamline of the Elettra synchrotron in Italy. The 2D GISAXS data of the initial film and the film after 4 minutes reaction time are shown in Fig. 5.21a and Fig. 5.21b, respectively. From the horizontal line cuts we are able to resolve the structure of the base colloidal layer (bottom black curves of Fig. 5.21c; form factor oscillations from spheres) for the initial films. For the films after metal decoration with increasing time from bottom to top in Fig. 5.21c, the structure of the base layer of SiO_2 spheres can hardly be resolved due to the dominating scattering of the silver particles. It has to be noted that for the presented data here, the correction for the semi-transparent beamstop in the low-q region is not performed yet. Further data analyzing of the GISAXS data and the GIWAXS information simultaneously obtained with a Pilatus 100 K detector will give a more detailed description on the morphology of the investigated composite materials.

[1] J. Zhang, J. Liu, S. Wang, P. Zhan, Z. Wang, N. Ming, *Adv. Funct. Mater.* **14**, 1089-1096 (2004)

5.10 In-situ growth of titania thin films by spray deposition

H. Caller, B. Su., V. Körstgens, S. V. Roth[1], P. Müller-Buschbaum

[1] DESY, Hamburg, Germany

The high demand on optoelectronics devices, in particular solar cells in the energy sector, has motivated an intense research to solve the problems of efficiency, costs and large scale production of thin films. Titania is widely used due to its chemical stability and semiconductor properties. In next generation solar cells, nanoporous titania layers are used for electron transport and for directing the dye layer. Spray deposition is a widely used coating method for the deposition of films at large scale. Moreover, spray coating is a deposition method which operates at low cost of the materials and equipment involved in the fabrication compared to vacuum environments and high voltage set-ups for another deposition techniques. The fabrication of titania thin films by spray deposition involves the preparation of a sol-gel, which allows to control the assembling of a nanostructure by variations of the solvent, precursor and polymer weight fraction. A study of the influence of the coating parameters on the morphology of the titania films leads to a better understanding of the mechanisms involved in the deposition process. In particular, foam-like nanostructures are morphologies of high interest because of features such as a large surface area for dye adsorption and a percolating network structure, which provides routes for the charge carrier transport. Those features are of importance in optoelectronics and particularly in photovaltaics [1]. In-situ grazing incidence small-angle X-ray scattering allowes us to study the morphology evolution of the film during spray deposition. The experiment was carried out at the PETRA III storage ring in DESY, Hamburg. The spray equipment consisted of a commercial airbrush gun with a nozzle of 2 mm diameter. The distance of substrate-to-nozzle was set to 16 cm. The substrate was heated up to $50°C$. A sol-gel was prepared with 105.45 mg of P(S-b-EO), 6.1434 ml of 1,4-dioxane, 56.79 μL of HCl and 351.96 μL of TTIP. The solution was stirred for 45 minutes. The sol-gel of titania was deposited with a nitrogen gas stream at a pressure of 1 bar. The spray coating consisted of a deposition in five steps with intervals of 10 seconds before starting a new spraying step. Each spraying step lasts for 5 seconds. In order to acquire detailed information of the spray deposition, we analyze the scattering data for each deposition step and drying step.

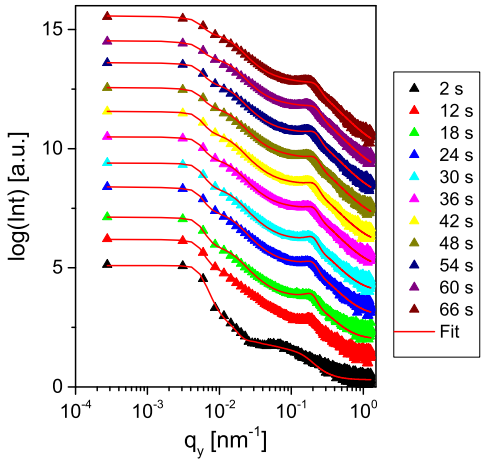

Figure 5.22:
Horizontal line cuts from the 2D GISAXS data for each deposition step and drying interval are show together with their fitting curves.

From the 2D GISAXS data horizontal line cuts are selected and fitted to obtain information about characteristic sizes. In this case we can observe two important features in the curves. At high q_y values, that is around $0.5nm^{-1}$, we can observe a small peak in the curves which is attached to the appearance of a nanostructure in the sample [2]. This fact allows us to model our nanostructure in order to extract the length scales of the sample. We model the characteristic structures in the sample as cylinders since our sol-gel provides a low degree of packing of the PS domains and the PEO domains form cylindrical structures to minimize its surface energy. The titania naoparticles are attached to the PEO domains and in part to the PS domains by Ti-O bonds. The fitting curves can be seen in the figure 5.22. We plot the radius of the PEO domains and its behavior over time which can be seen in figure 5.23. The squares represent the spraying steps and the diamonds represent the drying steps. The size of the pore radius decreases with time. This effect can be explained if we take in account the evaporation of the solvent during the drying cycle. Such evaporation results in a repacking of the domains of the diblock copolymer. We also plot the center-to-center separations between the PEO domains. We can notice a reduction on the separation distance. The contraction of the complex network of nanoparticles is also a result of the evaporation of the solvent, which turns into a repacking of the domains of the block copolymer.

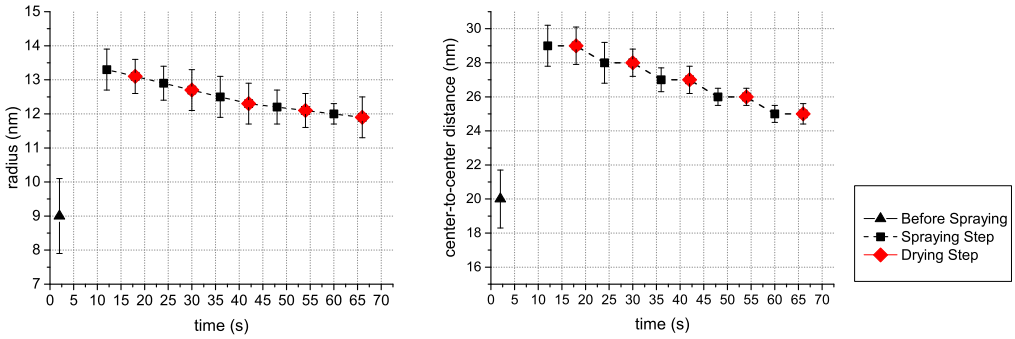

Figure 5.23: Radius and center-to-center distance of the PEO/TiO_2 domains as function of time.

[1] Y. Cheng, J. S. Gutmann, *J. Am. Chem. Soc.* **128**, 4658-4674 (2006)

[2] K. Sarkar, E. V. Braden, S. Pogorzalek, S. Yu, S. V. Roth, P. Müller-Buschbaum, *Chem. Sus. Chem.* **7**, 2140-2147 (2014)

5.11 Investigation of low-temperature processed titania films for application in flexible hybrid solar cells

T. Widmann, W. Wang, L. Song, P. Müller-Buschbaum

In recent years hybrid solar cells have attracted an increasing interest of researchers. Typically, they consist of a nanostructured inorganic semiconductor and a hole conducting polymer. With these components, it is possible to produce flexible solar cells which show many advantages. Most importantly, they can be produced on PET foils in large scale with a roll-to-roll process, making them light-weight and cheap. Due to its flexibility, solar bags for mobile charging of electronic devices and other applications become possible. However, only the polymer component is flexible, while the inorganic semiconductor may fail under mechanical stress. One attempt taken to improve its flexibility, is structuring the inorganic component as a sponge-like nanostructure, giving it sponge-like attributes. Titania is a typically used semiconductor in hybrid solar cells. However, for most production routines, a high temperature calcination step at minimum of 400 °C or even higher is required [1]. As flexible substrates such as PET cannot stand such high temperature, the hybrid layer needs to be processed at low temperature below 150 °C. Additionally, the hybrid layer also needs to be tested on its mechanical stability under deformation. Therefore a bending-test is performed with a custom made bending-machine.

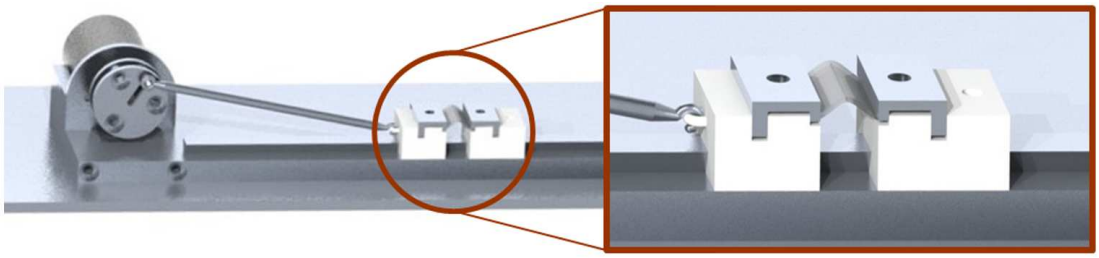

Figure 5.24:
Bending set-up used for the mechanical investigation of hybrid polymer/titania films. The aluminum plate on the left is driven by a motor and moves the aluminum rod in a cyclic motion back and forth. The connected Teflon block follows that motion and bends the PET film periodically. On the right side the PET is mounted in a fixed Teflon block.

For the production of the porous titania films a sol-gel synthesis in combination with microphase separation is used. Poly (styrene-block-ethylene oxide), denoted P(S-b-EO), an amphiphilic diblock copolymer, is used as the structure directing template and ethylene glycol-modified titanate (EGMT) as a titania precursor. By tuning the pH-value and the temperature of the sol-gel, different crystal phases of the titania can be achieved. For the preparation of the sol-gel, first of all P(S-b-EO) is dissolved in N,N-dimethylformamide (DMF) which is a good solvent for both polymer blocks. After stirring the solution for 30 min it is filtered with a 0.45 μm filter. Then HCl (37%) and EGMT are added and the solution is stirred again for 30 min and an additional 15 min at 90 °C. The weight ratio between the different constituents is W_{DMF} : $W_{P(S-b-EO)}$: W_{EGMT} : W_{HCL} = 20 : 1 : 1 : 2. Finally, the sol-gel is spin-coated (2000 rpm, 60 s) on pre-cleaned PET substrates and annealed at 90 °C for 30 min. The spin-coating and annealing process is repeated once in order to get a film thickness of around 200 nm suitable for hybrid solar cells. After careful investigation of different low-temperature extraction methods, it is found that UV-radiation for 20 h yields the best results. However, the PET turned brittle due to the UV irradiation, rendering a further mechanical stress test fruitless. Therefore, the P(S-b-EO) is extracted by placing the samples subsequently in a solvent bath of DMF for 10 min and chlorobenzene for one hour, baring the titania network without damaging the PET foil. Finally,

the titania layer is backfilled with the semiconducting polymer poly(3-hexyl-thiophene) (P3HT) to complete a functioning hybrid active layer for solar cells.
For the mechanical investigation of the films, a custom-made bending set-up is used as depicted in fig. 5.24. The films mounted between a fixed Teflon block on the right and a movable Teflon block on the left are periodically bent. The bending radius is set to 3.0 mm by adjusting the position of the aluminum rod in the long hole of the rotating plate on the left. The cycle speed is adjusted to 0.3 s^{-1} and the bending is performed for 0, 10, 100 ,1000 and 5000 times on separate samples. The four different bending series with different kinds of titania layers are performed. For the first series, the polymer template is not extracted yet. For the next one, the polymer template is partially removed by irradiation with oxygen plasma with 200 W for 30 min. The third series are performed on the completely extracted titania network and finally the fourth is performed on the titania network backfilled with P3HT. The SEM images after 1000 bending cycles for each series are shown in figure 5.25.

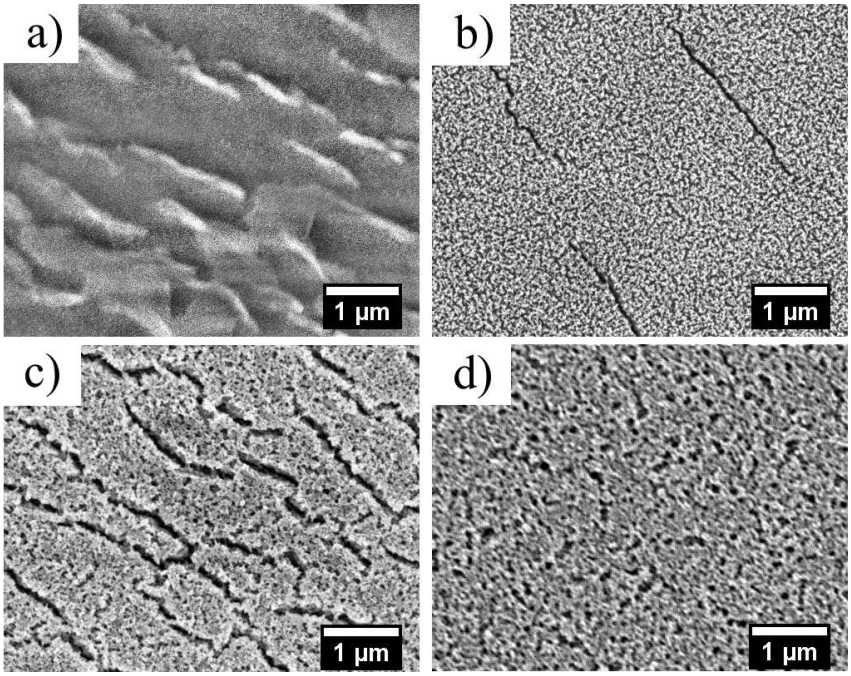

Figure 5.25:
SEM images after 1000 bending cycles of (a) the hybrid titania/P(S-b-EO) film, (b) the hybrid titania/P(S-b-EO) film treated with oxygen-plasma, (c) the completely extracted film treated with solvent baths in DMF and CB and (d) the film backfilled with P3HT. For the backfilled series, the P3HT was removed after the bending process in order to search for cracks.

For the used settings, the sponge-like titania nanostructure alone is not enough to inhibit the formation of cracks (see fig. 5.25 a), b) and c)). In case of the series on completely extracted titania films shown in fig. 5.25 c), the surface area covered by cracks was the largest. However, in combination with the backfilling of P3HT, no crack formation was observed (see fig. 5.25 d). It is concluded that backfilling P3HT in the titania sponge can highly improve the flexibility of the functional hybrid film. The forces on the titania structure could be more uniformly distributed, preventing overloading and failure.

[1] J. Weickert, R. B. Dunbar, H. C. Hesse, W. Wiedemann, L. Schmidt-Mende, *Adv. Mater.* **23**, 1810 - 1828 (2011)

5.12 Laser ablation in liquid for the generation of titania nanoparticles

V. Körstgens, S. Pröller[1], C. Mayr, H. Iglev[2], R. Kienberger[2], P. Müller-Buschbaum

[1] MSE, TU München, Garching, Germany
[2] LS Laser- und Röntgenphysik, TU München, Garching, Germany

One way to produce nanoparticles is the ablation of particles with a laser beam. This process can be carried out in a liquid environment. One of the main advantages of this technique is that nanoparticles of various compositions and morphologies can be produced in dispersion of a desired liquid [1]. We applied the laser ablation in water for the generation of titanium dioxide nanoparticle for the application in hybrid photovoltaics. The first approach we used for producing laser-ablated titania nanoparticles is illustrated in Fig. 5.26.

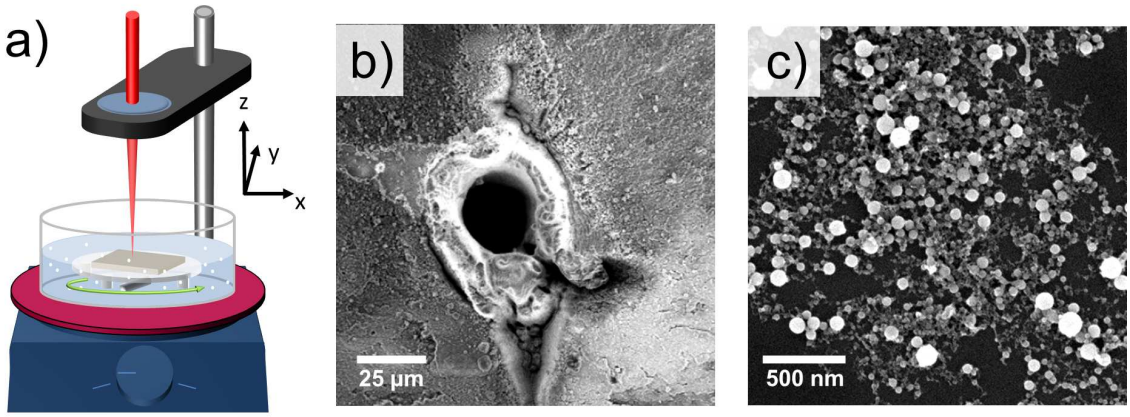

Figure 5.26:
a) Basic set-up of the laser ablation process for a solid titanium target in water. b) SEM image of a spot obtained by hitting a solid titanium target by the focused laser beam for 1 s in air. c) SEM images of nanoparticles achieved from laser ablation process in water with solid titanium target.

The processing of titania nanoparticles is carried out starting with a solid target (titanium foil, 0.89 mm thick, Alfa Aesar). The laser radiation is provided by a home-built titanium:sapphire laser system at the chair for laser and x-ray physics, delivering pulses at a central wavelength of 810 nm with pulse energy of 290 $\pm$ 20 μJ and a repetition rate of 1 kHz. The pulse duration was t_{pulse} of 270 $\pm$ 50 fs. The laser beam was focused in the sample via a fused silica lens (f = 100 mm) as shown in Fig. 5.26a. The beam diameter in the focal plane d_{laser} = 30.9 $\pm$ 0.2 μm was determined by a beam camera (BeamPro, Photon Inc.). The diameter of the focused laser beam can also be demonstrated by the ablation of the titanium target in air (Fig. 5.26b). The estimated pulse intensity in the focus of about 1.4 x 10^{13} W/cm^2 is much higher than the expected ablation threshold for titanium. After laser ablation processing of the titanium target in water a bluish suspension develops with nanoparticles of spherical shape with sizes in the range from 5 to 150 nm with an average diameter of 25 nm as observed with SEM (Fig. 5.26c).
A useful variation of the laser ablation technique is the change of the geometry of the solid target. A minimum of confinement of the plasma plume will be achieved with the ablation process of dispersed particles. The particles in suspension can transform in size, shape, phase and composition [1]. The basic set-up we used for the ablation of powder particles of titanium dioxide is given in Fig. 5.27a.

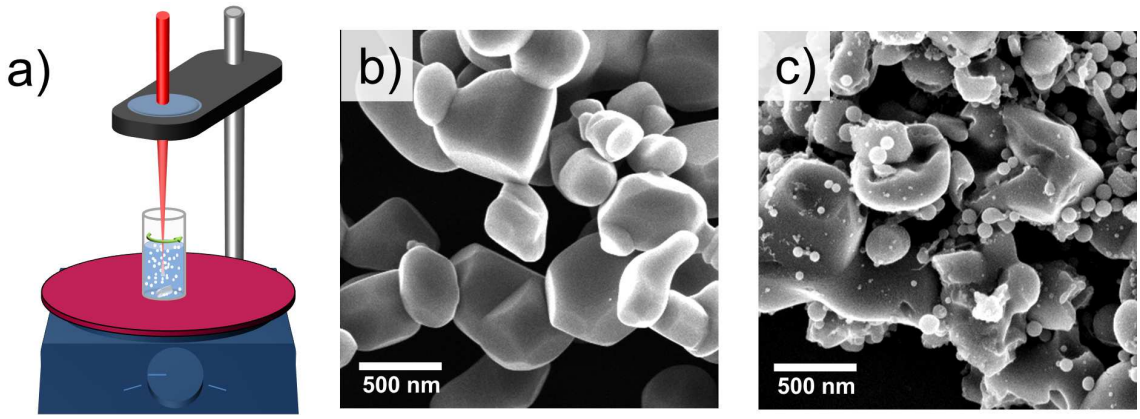

Figure 5.27:
a) Basic set-up of the laser ablation process for an aqueous suspension of titania particles. b) SEM image of the source titania powder and c) laser ablated material from titania powder.

We used titania powder (titanium(IV) oxide powder in a rutile phase, particle size < 5 μm, Sigma-Aldrich) in aqueous suspension as the source material for the laser ablation experiment. For the original titania powder a diameter of (750 ± 465) nm with very few particles > 3 μm is found by SEM analysis (Fig. 5.27b). After laser ablation of the material a mean value of 150 nm with a distinct size distribution is obtained from the SEM images (Fig. 5.27c).

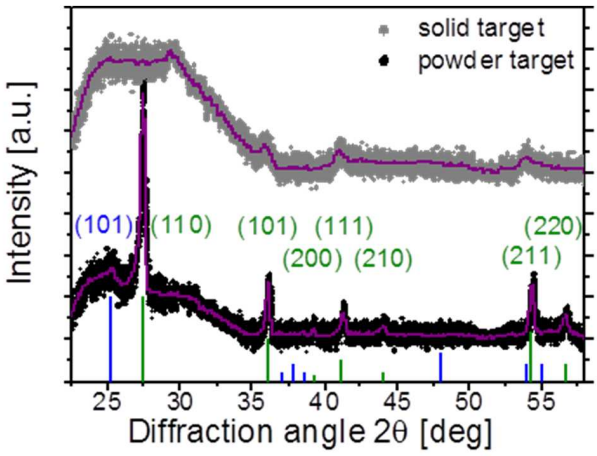

Figure 5.28:
XRD pattern of laser ablated TiO_2 from solid titanium and titania powder target. Theoretical positions of TiO_2 in anatase and rutile phase are plotted in green and blue, respectively.

The crystalline structure of the obtained titania nanoparticles is investigated with X-ray diffraction (XRD) as shown in Fig. 5.28. For the titania films, the main crystal phase is rutile. However, a certain amount of anatase phase can be found. For comparison, the source material for the laser ablation with suspended titania particles is mainly in its rutile phase. In general freshly prepared laser-ablated particles are positively charged giving the possibility to functionalize them with a polymer. We achieved the functionalization of the titanium dioxide with a water-soluble hole-conducting polymer. Application as the active layer in hybrid solar cells shows high fill factors and open circuit voltages underlining the potential of laser ablated titana nanoparticles in hybrid photovoltaics based on a production process free of organic solvents [2].

[1] H. Zheng, X.-W. Du, S.C. Singh, H. Zheng, S.A. Kulinich, S. Yang, J. He, W. Cai, *Adv. Funct. Mater.* **22**, 1333 (2012)

[2] V. Körstgens, S. Pröller, T. Buchmann, D. Mosegui Gonzalez, L. Song, Y. Yao, W. Wang, J. Werhahn, G. Santoro, S. V. Roth, H. Iglev, R. Kienberger, P. Müller-Buschbaum, *Nanoscale* **7**, 2900-2904 (2015)

5.13 Low temperature synthesis and structuring of mesoporous titania films

L. Song, T. Wang, A. Abdelsamie, V. Körstgens, C. Schaffer, S. Bernstorff[1], P. Müller-Buschbaum

[1] Elettra-Sincrotrone Trieste, Basovizza, Italy

Based on conducting polymers, fully organic solar cells and hybrid solar cells combining organic and inorganic materials have received great attention. Compared to fully organic solar cells, hybrid solar cells have combined advantages of both organic and inorganic components. Titania, a n-type semiconductor, has been intensively investigated as the electron-transporting material of hybrid solar cells over the last decades. For photovoltaic applications based on hybrid solar cells comprising titania, a high surface-to-volume ratio of the titania films is desirable since charge carrier generation occurs at the interface of titania and the organic hole-transporting material. Thus, the mesoporous titania structure is essential for the high efficiency of solar cells.
Titania nanostructures could be achieved via various routes, among which the sol-gel synthesis in combination with block copolymer assisted templating is very promising. In this approach, the morphologies of titania are controllable (ranging from form-like structure to worm-like aggregates by adjusting the reactant ratio in the sol-gel chemistry) and the mesopores can be tuned through the micro-phase separation of diblock copolymer induced by a so-called good-poor solvent pair. However, a high temperature calcination usually is required in the end to remove the polymer and crystallize the TiO_2. This high temperature step makes an application of lightweight and flexible solar cells impossible. For lightweight and flexible photovoltaic devices, the substrate for supporting the active layer usually is a transparent polymer thin foil such as a poly(ethylene terephthalate) (PET) foil, which cannot withstand high temperatures. Therefore, low temperature synthesis of titania nanostructures and polymer extraction methods need to be explored. In the present work, UV irradiation is chosen to extract the polymer matrix since the high energy of the UV light could break the polymer bonds.

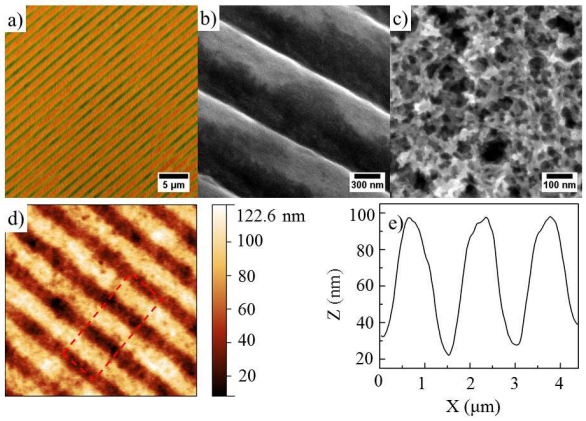

Figure 5.29:
a) Microscope image of imprinted titania/polymer composite film; b) cross-section view SEM image of imprinted titania/polymer composite film; c) plane-view SEM image and d) AFM image of imprinted titania flim after polymer extraction; e) height profile across the channels, as indicated in d) by the red rectangle.

Recently, hierarchical architectures of titania films from nanometer to micrometer length scales are of great interesting as they could provide higher photocatalytic and photovoltaic properties. Consequently, we fabricate TiO_2 superimposed structural order on multiple length scales via combining nanostructured titania films with micro-scale triangular structures. Specifically, the hierarchical structures are achieved via a combination of block copolymer assisted sol-gel processing with wet-imprinting. For the sol-gel, the amphiphilic block copolymer P(S-b-EO) is dissolved in a good solvent for both blocks, namely N,N-dimethylformamide (DMF), then filtered with a PTFE filter with a pore size of 0.45 um to get rid of the undissolved parts. Subsequently, a defined amount of the titania precursor, ethylene glycol-modified titanate (EGMT),

and hydrochloric acid (12mol L^{-1}) are mixed up in another cleaned glass vial. The EGMT/HCl mixture is transferred to an ultrasonic bath for 10 min to make EGMT hydrolysis. Afterwards, the polymer solution and EGMT/HCl mixture are mixed and stirred on a magnetic stirrer at a temperature of 90 °C for 15 min to improve the hydrolysis and to get a homogeneous solution. The HCl acts as selective solvent for the micro phase separation and as a catalyst for the sol-gel reaction here. Finally, the solution is spin-coated on silicon or glass substrates to form titania/polymer composite films. The presence of the polymer makes the composite films retain mechanical softness, which enable films to be embossed via wet imprinting. We choose a stamp with narrow channels (the cross section is a triangle) to pattern our composite films in micro-scale. The stamp is placed on the top of composite films and on its backside a force of 20 N is applied to ensure proper embossing of the superstructure. After drying overnight at 90 °C, the stamp is lift off and a micrometer-sized superstructured hybrid film is obtained. To get the titania nanostructure, UV irradiation is employed to remove the polymer matrix in the composite film. Fig. 5.29 a) shows the optical micrograph of the imprinted titania/polymer hybrid film. The channel-like structures indicate the successful transfer of the superstructures from the stamp. Fig. 5.29 b) shows cross-section scanning electron microscopy (SEM) images of the blend film at a higher resolution, from which triangle-shaped channel-like structures can be identified. After UV irradiation, the plane-view SEM image of an imprinted titania film is shown in Fig. 5.29 c). Foam-like nanostructures with pore size ranging from 10 nm to 50 nm are observed. Fig. 5.29 d) shows the AFM image of the imprinted sample after polymer extraction along with corresponding height profile. The AFM image shows that the triangle-shaped channel-like structures survive after polymer extraction and the channel depths are very homogeneous with an average depth of 80 nm.

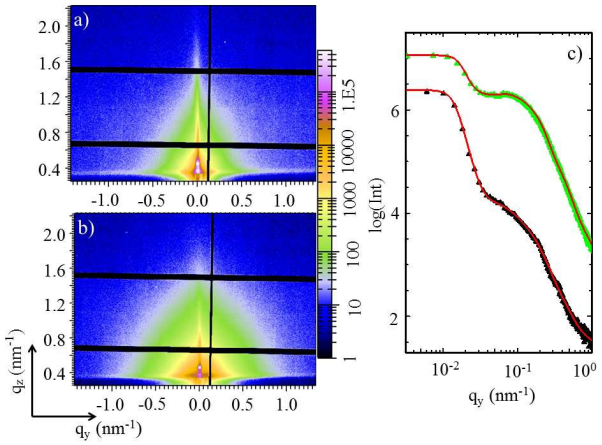

Figure 5.30:
2D GISAXS data of a) imprinted titania/polymer composite film and b) imprinted titania flim after polymer extraction. c) Horizontal line cuts from the 2 D GISAXS data of imprinted titania/polymer composite film (black solid triangles) and imprinted titania flim after polymer extraction (green solid triangles). The red lines represent the fits to the data. The curves are shifted along the y axis for clarity of the presentation.

To obtain information about the inner structures of the imprinted titania films, GISAXS measurements have been performed (Fig. 5.30 a) and b)). Horizontal line cuts of the 2D GISAXS data are implemented at the Yoneda position of TiO_2 (Fig. 5.30 c)). From the fits, characteristic lateral structures such as the radii of the scattering objects and their center-to-center distances are extracted. Both films exhibit two characteristic structure sizes. For the titania/polymer hybrid film, the small structure size is about 4.0 nm and the center-to-center distance is around 17 nm. The big structure size is approximately 8.0 nm and its center-to-center distance is around 42 nm. After polymer extraction, the titania structure collapses as the polymer matrix is removed. Consequently, the small structure and big structure increase slightly to around 4.6 nm and 9.1 nm, respectively. However, the center-to-center distances are relatively constant, showing 16.6 nm between the small structures and 40 nm between the big ones.

5.14 Investigating the morphology of planar $MAPbI_{3-x}Cl_x$ perovskite thin films

J. Schlipf, P. Docampo[1], T. Bein[1], P. Müller-Buschbaum

[1] Ludwig-Maximilians-Universität München, Department Chemie, München, Germany

The application of organo-metal halide perovskites as the absorbing layer in hybrid solar cells marks a paradigm shift in thin film photovoltaic research. Beginning in 2009 with the first application as substitute for the dye in a conventional DSSC setup on a mesoporous TiO_2 layer by Miyasaka and co-workers, recent findings report power conversion efficiencies exceeding 15 % for various different cell designs. Most prominent are the advances of Snaith and co-workers, namely the discoveries of intrinsic absorption (i.e. exciton dissociation at room temperature), exceptionally high open circuit voltages exceeding 1 V and ambipolar charge transport with equally high diffusion lengths for electrons and holes in the range of 100 nm to 1 μm that renders the application of planar cell designs possible [1][2].
Apart from these exceptional material properties, one of the most important advantages of this new class of hybrid thin film solar cells is the abundance and easy processability of the perovskite precursor materials which enables a preparation using solution based methods and thereby possibly cheap mass production in future. However, growing perovskite from a single solution incorporating all precursor materials requires precise tuning of their mixing ratio and processing conditions. While the film homogeneity and coverage suffers especially in planar cell designs where the crystallization is not directed by a mesoporous scaffold, Burschka et al. developed a sequential deposition technique to produce dense and homogeneous perovskite layers [3]. Soon afterwards, this technique was advanced further by Liu et al. and Docampo et al. to produce highly efficient planar solar cells with efficiencies over 15 % [4][5].

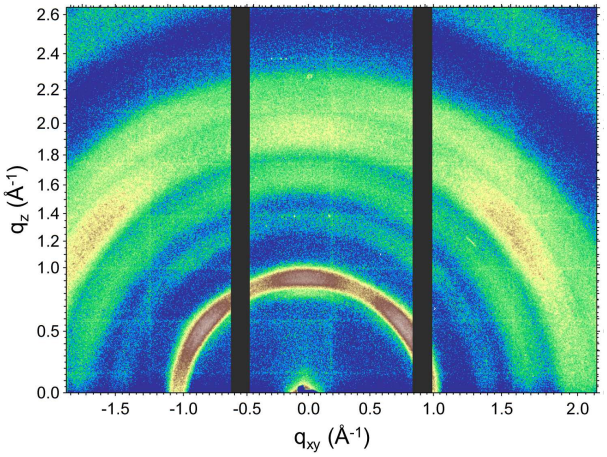

Figure 5.31:
2D scattering image of $MAPbI_{3-x}Cl_x$ perovskite on TiO_2 covered FTO substrate obtained with the Ganesha 300XL SAXS-WAXS. The prominent peaks indicate both a highly crystalline film and a preferential orientation of the crystallites in respect to the substrate.

We adopt the latter technique by Docampo et al. which is based on solution processing only: A saturated 1 M solution of PbI_2 in dimethylformamide (DMF) is spin-cast on a compact TiO_2 layer on fluorine-doped tin oxide (FTO) covered glass substrates, while it is crucial to keep both solution and substrate at an elevated temperature of 60°C and transfer the sample to a hot plate immediatly before the DMF is fully evaporated. The resulting deep-yellow PbI_2 thin film is clear and highly crystalline in a rhombohedral phase. The sample is immersed into a solution of methylamonium iodide (MAI) and MA chloride (MACl) in isopropyl alcohol, while the best solar cell performance was reported for 5 wt% MACl content in respect to MAI and 8 min bathing time [5].

A sample akin to the setup used in perovskite solar cells is investigated with grazing incidence wide angle X-ray scattering (GIWAXS) at the 'Ganesha 300XL SAXS-WAXS' of our chair. The 2D

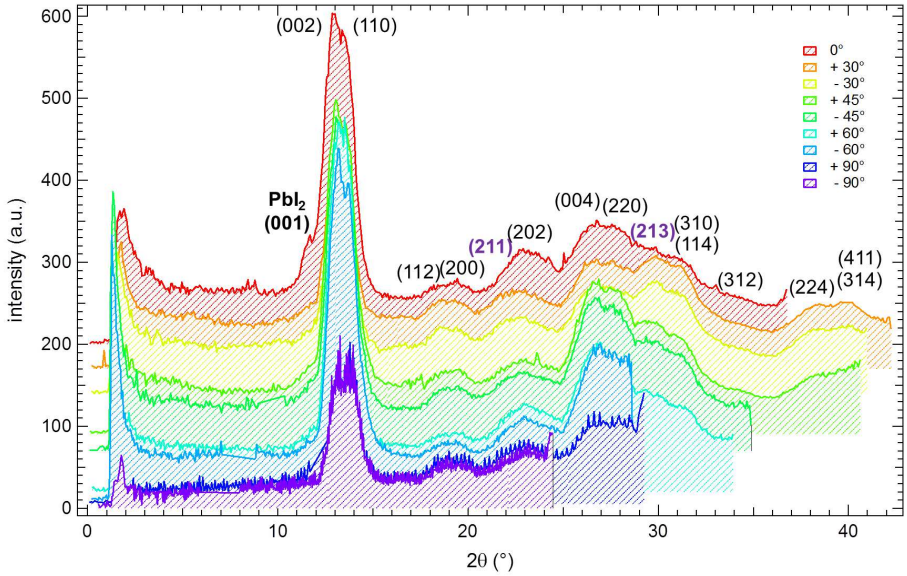

Figure 5.32:
Cake cuts integrated over 10° sectors for most important directions taken from the 2D image in Fig. 5.31, i.e. 0° (vertical), 30°, 45°, 60° and 90° (horizontal) are given in different colors and shifted in vertical direction for clarity, where + and - indicate right and left, respectively.

detector image is depicted in Fig. 5.31. It is already obvious from the defined peaks that the film at hand consists of well-oriented crystallites. Cake cuts are performed for various angles and integrated over a 10° sector and compared to X-ray diffractometry data from literature to identify the peaks (cf. Fig. 5.32). As already seen from the 2D image there is a preferential orientation of the (001) direction perpendicular and in an angle of 45° in respect to the substrate. As reported previously, $MAPbI_3$ perovskites form a tetragonal phase at room temperature, which is verified for this sample from the (211) and (213) peaks (purple). Therefore, the (002) is acompanied by an equally strong scattering from (110) planes. The high crystallinity is further supported by the prominent (004) and (220) peaks. It is worth mentioning that despite the bathing time of 8 min there is still a non-negligible amount of non-converted PbI_2 present in the sample, as is apparent from the peak around 12° for the vertical cut indicating preferentially oriented PbI_2 crystallites. In conclusion, these results show that a morphological investigation of organo-metal halide perovskites with GIWAXS is already feasible with lab-scale X-ray sources due to the high crystallinity of this class of materials. As crystal orientation is expected to have an important influence on charge transport properties this is directly linked to the performance of perovskite solar cells and thus makes morphological investigations crucial for further advancements in this field.

[1] M. M. Lee, J. Teuscher, T. Miyasaka, T. N. Murakami, H. J. Snaith, *Science* **338**, 643-647 (2012)

[2] S. D. Stranks, G. E. Eperon, G. Grancini, C. Menelaou, M. J. P. Alcocer, T. Leitjens, L. M. Herz, A. Petrozza, H. J. Snaith, *Science* **342**, 341-344 (2013)

[3] J. Burschka, N. Pellet, S.-J. Moon, R. Humphry-Baker, P Gao, M. K. Nazeeruddin, M. Grätzel, *Nature* **499**, 316-319 (2013)

[4] M. Liu, M. B. Johnston, H. J. Snaith, *Nature* **501**, 395-398 (2013)

[5] P. Docampo, F. Hanusch, S. D. Stranks, M. Döblinger, J. M. Feckl, M. Ehrensperger, N. K. Minar, M. B. Johnston, H. J. Snaith. T. Bein, *Adv. Energy Mater.* **43**, 1400355 (2014)

5.15 Investigating the structure of methylammonium lead iodide on glass substrates

L. Oesinghaus, J. Schlipf, P. Müller-Buschbaum

In 2009, Kojima *et al.* published the first article on the use of organometal halide perovskites in dye- sensitized solar cells (DSSC). Unfortunately, the liquid electrolyte used as hole transport material (HTM) rapidly dissolved the perovskite. This was solved by replacing the liquid electrolyte by a solid HTM, namely spiro-OMeTAD. In 2012, Lee *et al.* reported achieving a power conversion efficiency (PCE) of 7.8% using mesoporous TiO_2, and, surprisingly, an even higher PCE using non-conducting Al_2O_3 as a scaffold [1]. The high PCE of this configuration implied good ambipolar charge transport in $MAPbI_3$, which in turn implies the possibility of using it in a planar p-i-n heterojunction solar cell. In 2013, Liu *et al.* reported achieving a PCE of 15.4% for such a cell using a dual-source-evaporation deposition method [2]. Since then, efficiencies exceeding 15% have been reported in DSSC, meso-superstructured solar cell (MSSC) and planar solar cell architectures fabricated by a variety of different techniques, including solution-processing, printing or spraying. Thus, the PCEs of perovskite solar cells have leapfrogged those of other next generation solar cell types producible by solution-processing in just two years.
High efficiency in perovskite-SSCs was achieved by the application of a two-step sequential deposition method first introduced by Burschka *et al.* [3]. Instead of mixing precursor solutions before spin-coating, one precursor is spin-coated and the sample is then immersed in a solution of the other precursor. This method was extended to planar architectures by Liu *et al.* [4]. It leads to more crystalline and dense PbI_2 films as compared to the one-step deposition method using a mixed precursor solution.

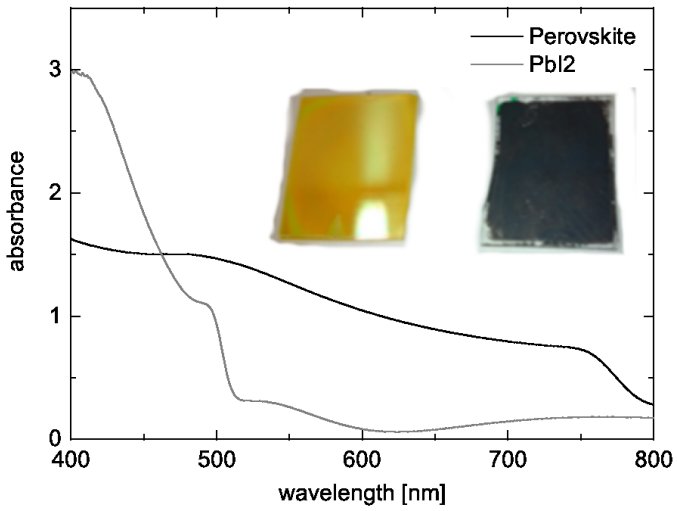

Figure 5.33:
UV/Vis measurement of $MAPbI_3$ and PbI_2 on glass. The insets show the photographs of the two films these curves were measured for.

With the goal of studying the properties of $MAPbI_3$ films, we deposited them on acid-cleaned glass using the method by Docampo *et al* [5]. Upon rinsing the sample in the solvent bath, almost the entire perovskite film dissolved. We attributed this to a lower film thickness of the PbI_2 and different surface properties of glass as compared to TiO_2. By reducing the immersion time in

the solution bath from 10 minutes to 1 minute and skipping the rinsing in the solvent bath, we could achieve an acceptable film coverage, though the films still looked inhomogeneous and optically dull, unlike the smooth and reflective films this method typically achieves on TiO_2. Both, a pure PbI_2 and a $MAPbI_3$ film, can be seen as insets in Fig. 5.33. Despite this, the $MAPbI_3$ films show strong absorption in the visible range, as can be seen in the UV/Vis curve in Fig. 5.33. The absorption shoulder at 500 nm typical for crystalline PbI_2 can be seen in the same graph. The high absorption of $MAPbI_3$ is critical to its good photovoltaic performance. An XRD measurement of the angular reflection in a $\theta/2\theta$ scan showing the characteristic Bragg reflections such as the (211) and (213) peaks associated with the tetragonal I4cm space group of $MAPbI_3$ can be seen in Fig. 5.34. The observed Bragg peaks are in good agreement with literature. Apart from the peaks originating from tetragonal $MAPbI_3$, we can identify several peaks from unconverted crystalline PbI_2 by comparing to the XRD picture obtained from pure PbI_2. This is due to the short immersion time in the solution bath necessary to achieve good coverage. Note also the much higher count rate for the unconverted PbI_2 in Fig. 5.34, which indicates a larger roughness of the $MAPbI_3$ film.
To study $MAPbI_3$ under growth conditions more similar to the one used in solar cells, but without disturbing features from other layers, we plan to apply a very thin film of TiO_2 to a glass substrate before spin-coating the PbI_2. This should also improve the adherence of the $MAPbI_3$ to the substrate, allowing for longer immersion times and thus more complete conversion of PbI_2.

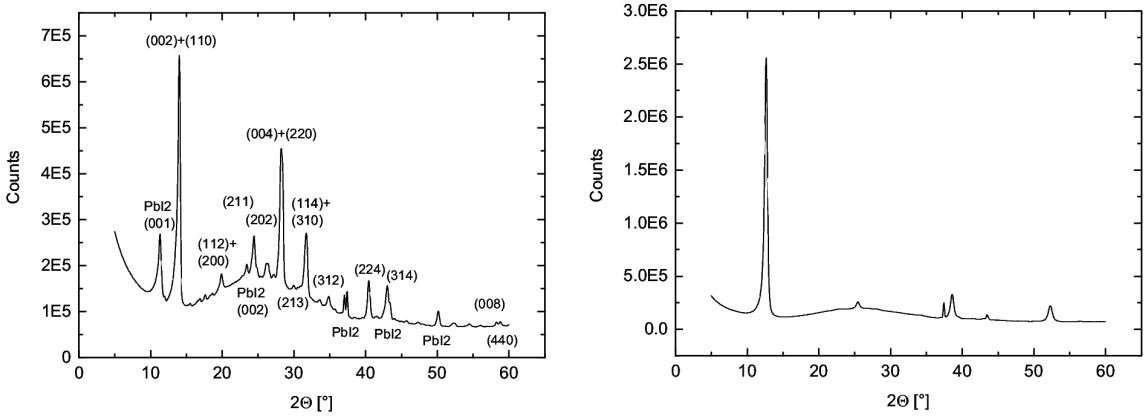

Figure 5.34: XRD measurements of $MAPbI_3$ (left) and pure PbI_2 (right) on glass.

[1] M. M. Lee, J. Teuscher, T. Miyasaka, T. N. Murakami, H. J. Snaith, *Science* **338**, 643-647 (2012)

[2] M. Liu, M. B. Johnston, H. J. Snaith, *Nature* **501**, 395–398 (2013)

[3] J. Burschka, N. Pellet, S.-J. Moon, R. Humphry-Gaker, P. Gao, M. K. Nazeeruddin, M. Grätzel, *Nature* **499**, 316-319 (2013)

[4] D. Liu, T. L. Kelly, *Nat. Phot.* **8**, 133 (2013)

[5] P. Docampo, F. C. Hanusch, S. D. Stranks, M. Döblinger, J. M. Feckl, M. Ehrensperger, N. K. Minar, M. B. Johnston, H. J. Snaith, T. Bein, *Adv. Energy Mater.* **4**, 1400355 (2014)

5.16 ZnO scattering layers for OLED applications

L. Biessmann, C. J. Schaffer, J. Schlipf, V. Körstgens, S. Bernstorff[1], P. Müller-Buschbaum

[1] Elettra-Sincrotrone Trieste, Basovizza, Italy

In the last years the efficiency and the life expectancy of organic light emitting diodes (OLEDs) reached values which make them suitable for industrial applications like display technology and room lighting. Mainly research was focused on the internal quantum efficiency to enhance the energy conversion of electrical power into light which makes the OLED much more efficient. By using phosphors it is possible to reach 100 % internal quantum efficiency, because the singlet as well as the triplet states are directed to the emitting triplet state [1]. However, the extraction of the photons out of the device is still a limiting factor, especially for white OLEDs. For conventional device architecture approximately 80 % of the generated photons are trapped in the organic and the substrate modes [2]. The combination of internal quantum efficiency and out-coupling efficiency gives the external quantum efficiency (EQE), which is a measure for the overall device efficiency. Hence, there is still a high potential for the enhancement of OLED efficiencies by increasing the extraction of photons.
There are several approaches to raise the photon extraction which are based on adding scattering centers into the device. Besides the direct structuring of the substrate surface, the attachment of a transparent layer on the substrate is a very promising approach. Such layers were produced by simply attaching nanoparticles on the substrate surface or attaching a polymer film included some nanoparticles [3]. However, beside these material systems nanostructures made from metal oxides are very promising because of their high stability and their high refractive index. The latter is important for including the scattering layer between the substrate and the ITO electrode as depicted in Fig. 5.35. Thus, the refractive index should adapt a value between the one of glass (n $= 1.5$) and ITO (n $= 1.8$) to reduce total reflection and additionally improve the out-coupling of photons. Obviously the material of the scattering layer has to be transparent for visible light as well. With an optical band gap of 3.3 eV and a refractive index of 2.0, zinc oxide (ZnO) is a very promising material for this purpose.

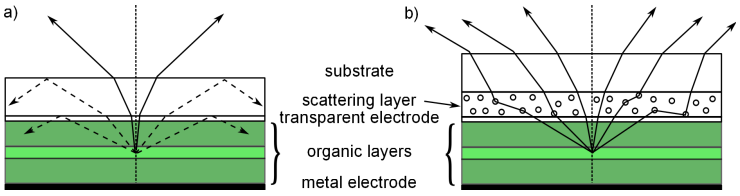

Figure 5.35:
Working principle of an additional scattering layer (b) in comparison to a standard device architecture of OLED (a). The illustrated light propagation shows the escaping modes as solid lines. The trapped modes are represented by dashed lines. In case of a scattering layer more modes are able to escape the device and thus the EQE is increased.

The working principle of the scattering layer is illustrated in Fig. 5.35. The photons are generated in the emitting part of the organic layers and are directed to the forward hemisphere of the OLED. The standard device architecture suffers from low photon extraction caused by trapped light due to substrate modes and total reflection on the high refractive ITO (transparent electrode) and lower refractive glass interface and glass to air interface, respectively.
An additional scattering layer positioned between the glass substrate and the transparent electrode yields two advantages. First, the high refractive metal oxide reduces total reflection caused

by the smaller jump of refractive indices. Second, the scattering centers of the layer yield a redirection of the generated light and suppress substrate modes. The combination of both effects can increase the light out-coupling of the device significantly.
In this work ZnO is used as scattering layer. For this purpose a structure giving diblock copolymer template is combined with sol-gel chemistry for tailoring the ZnO layer. We obtain thin ZnO films with a well-controlled nano- and micro-structure. In more detail, zinc acetate dihydrate (ZAD) is used as a precursor for ZnO, whereas poly(styrene-block-ethylene oxide), abbreviated as P(S-b-EO), is used as the structure giving template.
To achieve a suitable film thickness spray coating is chosen as the deposition technique for the prepared sol-gel. In first initial experiments pre-cleaned silicon substrates are used, replacing the common OLED substrates.
Depending on the composition of the prepared sol-gel the profile measurements of the films show average film thicknesses of 200 nm up to 900 nm combined with a high roughness. In order to investigate the inner film structure of the fabricated ZnO films grazing incidence small angle x-ray scattering (GISAXS) measurements are performed. All GISAXS data are obtained at the Austrian SAXS beamline at Elettra, Trieste with a X-ray energy of 8.0 keV. As results in Fig. 5.36 horizontal line cuts from the 2D GISAXS data are shown. Simultaneous measured GIWAXS data confirm the presence of ZnO in its wurtzite structure. In the GISAXS data, beside the resolution peak no pronounced peak is seen which originates from a broad variation of pore sizes in the films. Such broad variation of the pore sizes can be advantageous for application in the scattering layer since they serve as scattering centers for the generated photons with wavelengths in the order of the pore sizes.
From a fit to the horizontal line cuts more information about the pore sizes and pore size distribution will be obtained. In addition, real space measurements with SEM and AFM will be performed to complement the scattering data. As a next step the optical properties of porous ZnO structures will be investigated by UV-Vis spectroscopy.

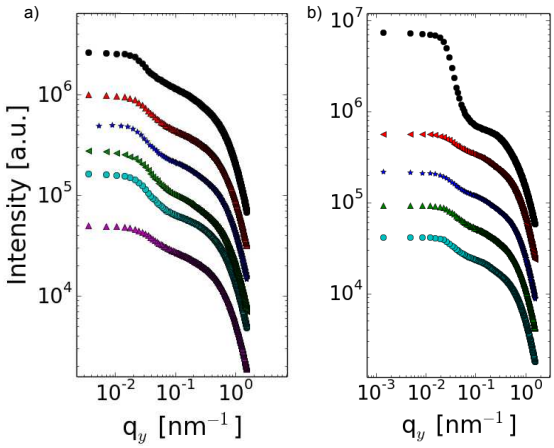

Figure 5.36:
Horizontal line cuts of the 2D GISAXS data for different ZnO layers cut at a fixed exit angle of $0.616°$. The sol-gel solution was prepared by using two different routes (a and b). The curves are shifted along the y axis for clarity of the presentation.

In conclusion, the fabrication of porous ZnO layers by using a structure giving diblock copolymer yields highly scattering thin films, which makes it to a suitable method for producing scattering layers. Furthermore, we are looking for possibilities for tailoring the scattering abilities by influencing the pore size of the ZnO structure.

[1] M. A. Baldo, D. F. O'Brien, Y. You, A. Shoustikov, S. Sibley, M. E. Thompson, S. R. Forrest, *Nature* **395**, 151-154 (1998)

[2] S. Reineke, F. Lindner, G. Schwartz, N. Seidler, K. Walzer, B. Lüssem, K. Leo, *Nature* **459**, 234-238 (2009)

[3] H.-W. Chang, Y. H. Kim, J. Lee, S. Hofmann, B. Lüssem, L. Müller-Meskamp, M. C. Gather, K. Leo, C.-C. Wu, *Organic Electronics* **15**, 1028-1034 (2014)

6 Dynamics

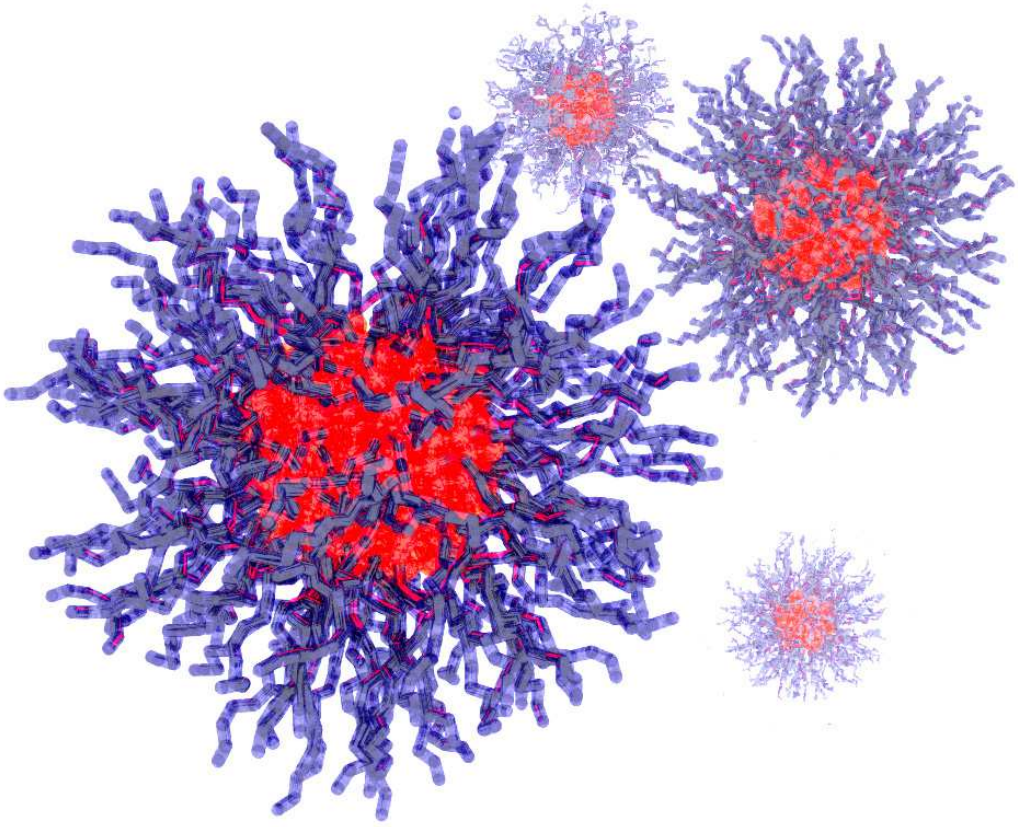

6.1 Hydrogen dynamics in $\beta-Mg(BH_4)_2$ in the picosecond time scale

L. Silvi, W. Lohstroh[1], E. Röhm, M. Fichtner[2]

[1] MLZ, Garching, Germany

[2] KIT, Karlsruhe, Germany

Metal borohydride have been object of intensive studies due to a quite promising hydrogen storage capacity. In this category, magnesium borohydride ($Mg(BH_4)_2$) is characterized by a gravimetric and volumetric storage density of 14.9 mass% H_2 and 90 kg/m^3. The decomposition temperature around 300 °C makes the material less suitable as a hydrogen storage compound, although it is interesting due to its gravimetric capacity.

Among the observed polymorphs of $Mg(BH_4)_2$ [1], a low-temperature α phase and a high-temperature β phase have been characterized. The low temperature phase, $\alpha-Mg(BH_4)_2$, is described by an hexagonal structure and a $P6_122$ symmetry. This polymorph is stable up to 490 K, when it transforms irreversibly into the β-phase. The latter has an orthorhombic $Fddd$ crystal structure symmetry, and it is metastable at room temperature.

Given the structure of $Mg(BH_4)_2$, the possible movements for the $[BH_4]^{-2}$ unit are long range translational diffusion, rotation around one specific unit axis, librations or vibrations of the unit itself. In this frame, the dynamics plays an important role, possibly driving the phase transition, and a deep understanding of it could clarify the various instability and decomposition processes in borohydrides [2][3]. Quasielastic neutron scattering (QENS) has been performed on β-magnesium borohydride using the isotope enriched ^{11}B, due to the high neutron absorption of the natural boron. For the measurements, approx. 164 mg of $\beta-Mg(BH_4)_2$ were mounted into an Aluminum flat cell, yielding a neutron transmission of 0.9. Quasielastic neutron scattering experiments have been performed at the cold time-of-flight spectrometer TOFTOF at the Heinz Maier-Leibnitz Zentrum in Munich, Germany. Two different wavelengths of the incoming neutrons were selected: the first $\lambda_1 = 2.5\,\AA$ yielding an energy resolution of $400\,\mu$eV (FWHM) of the elastic line, the second at $\lambda_2 = 6\,\AA$, with an energy resolution of $48\,\mu$eV (FWHM). The measurements were performed at temperatures ranging from 11 to 500 K. Due to the large hydrogen cross section, the experiment almost exclusively probes hydrogen dynamics. The scattering function for rotational motions can be written as a sum of a δ-function (mimicking the elastic line) and a series of Lorentzian $L_n(\Gamma_n, \omega)$:

$$S_{rot} = A_0(Q)\delta(\omega) + \sum_{n>0} A_n(Q) L_n(\Gamma_n, \omega), \tag{6.1}$$

where the half-width at the half-maximum (HWHM) Γ_n is related to the medium residence time τ between successive jumps and $\sum_{n>0} A_n(Q) = 1 - A_0(Q)$. The vibrational scattering function $S_{\text{vib}}(Q,\omega)$ can be written as a sum of an elastic and inelastic terms, $S_{\text{vib}}(Q,\omega) = f_Q\delta(\omega) + (1 - f_Q)$, where f_Q represent the Debye-Waller factor and it is related to the mean displacement square of a nucleus. The fraction of the elastically scattered neutrons

$$\text{EISF} = \frac{I_{el}(Q)}{I_{el}(Q) + I_{qel}(Q)} \tag{6.2}$$

is called Elastic Incoherent Structure Factor (EISF) which can be evaluated directly from the measured elastic and quasielastic integrated intensities, independent of any specific model. The functional dependence of the EISF on the momentum transfer Q reflects the spatial distribution of the hydrogen atoms in the long time average. The reorientational motions of the tetrahedra $[BH_4]$ could be described by rotations around symmetry axis, C_2 or C_3. In the case where the

motions are not separated the EISF is the product of the single EISF for vibration (Debye-Waller factor) and the $C_{2/3}$ rotations:

$$\text{EISF} = c + (1-c)\, f_Q A_0\,(Q) = c + \frac{1}{2}\,(1-c)\exp\left[-\frac{Q^2\langle u^2\rangle}{3}\right]\left[1 + j_0\left(\frac{2\sqrt{2}}{\sqrt{3}}\,Qr\right)\right] \tag{6.3}$$

where $j_0(x) = \sin(x)/x$ is the zeroth-order spherical Bessel function, $r = d_{\text{B–H}}$ is the bond length between B and H, c is the fraction of atoms that are not moving in the selected time scale. The measurements and the calculated EISF are are shown, respectively, in Figs. 6.1 and 6.2

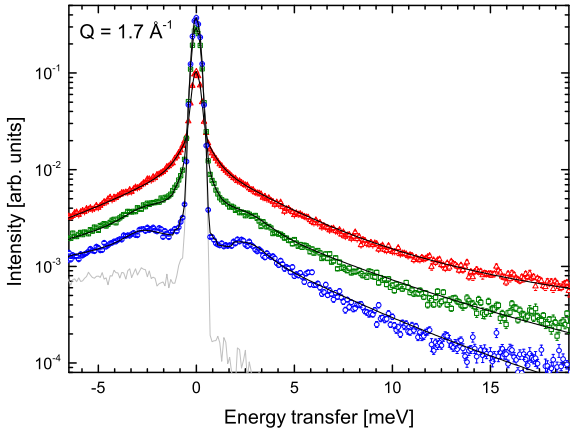

Figure 6.1:
$S(Q,\omega)$ at $2.5\mathring{A}$ of $\beta-Mg(BH_4)_2$ at 11, 100, 200 and 500 K. The black solid lines represent the fit of the data: (gray line) 11 K, (blue circle) 100 K, (green square) 200 K, (red triangle) 500 K.

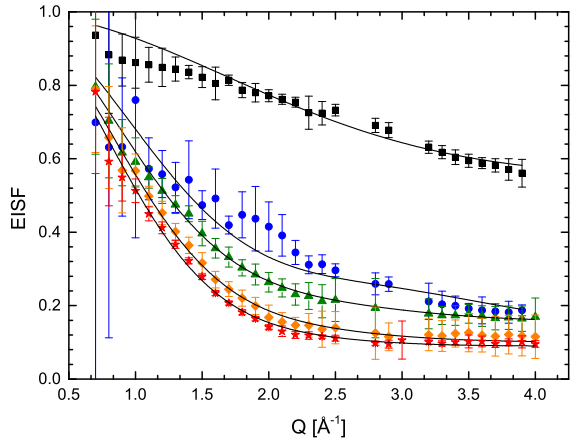

Figure 6.2:
Measured EISFs at $2.5\mathring{A}$ and the EISF model according to eq. 6.3 (solid lines): (black square) 100 K, (blue circle) 200 K, (green triangle) 300 K, (yellow rhombus) 400 K, (red star) 500 K.

In conclusion a QENS experiment has been performed on $\beta-Mg(BH_4)_2$ in two different time-scales in order to explore the hydrogen dynamics, and in particulr possible reorientations of the $[BH_4]$ units. The EISF is found to be dependent on the low energy vibrational motion. At a faster time-scale (10ps)a strong low energy inelastic contribution is visible for temperature under 200 K. Above 300 K the inelastic contribution is not any more visible and a transition from an undumped to an overdumped regime is also possible. This transition strongly affects the EISF, since vibrational and reorientational motions are not separable.

[1] Y. Jaroslav, B. Richter, T. R. Jensen, V. Dimitriev, D. Chernyshov, H. Hagemann, *Angew. Chem. Int. Ed.* **50**, 11162 (2011)

[2] N. Hanada, K. Chlopek, W. Lohstroh, M. Fichtner, *J. Mater. Chem.* **18**, 2611-2614 (2008)

[3] J. Yang, X. Zhang, J. Zheng, P. Song, X. Li, *Scripta Materialia* **3**, 225 - 228 (2011)

6.2 Kinetics and dynamics studied near the demixing transition of thermo-responsive solutions using temperature modulated optical refractometry

M. Philipp, R. Aleksandrova[1], U. Müller[1], M. Ostermeyer[2], P. Müller-Buschbaum, J. K. Krüger[1]

[1] Université du Luxembourg, Luxembourg
[2] Anton Paar OptoTec, Seelze, Germany

Slow kinetic and dynamical processes are characteristic for many phase transitions and glass transitions in soft condensed matter. This holds in particular true for the demixing transitions of the lower critical solution temperature (LCST) type of aqueous polymer solutions. The LCST-type phase diagram of polymer solutions is characterized by stable, metastable and instable regions, which are separated by the binodal and spinodal phase boundaries. The growth laws governing the segregation process of a homogeneous polymer solution into polymer-rich and solvent-rich domains have been much investigated. Of major scientific interest are the kinetics and dynamics related to macroscopic order parameter susceptibilities of the phase transition. The thermal expansion coefficient can be considered as the order parameter susceptibility for the LCST-type demixing transition of aqueous polymer solutions [1, 2]. However, to our knowledge, slow kinetic and dynamical processes are currently not accessible with state-of-the-art densitometers across the demixing transition of solutions.

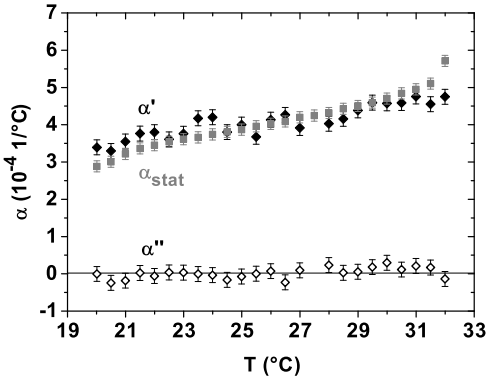

Figure 6.3:
TMOR investigation of the thermomechanical relaxation processes present at mHz frequencies within the homogeneous PNIPAM solution. Comparison of the complex thermal expansion coefficient, extracted from a TMOR dataset, and the static thermal expansion coefficient.

In order to access them indirectly, we have recently introduced temperature modulated optical refractometry (TMOR), in collaboration with the company Anton Paar [3]. This technique allows for investigating slow thermo-optical and thermo-mechanical relaxation processes within isotropic liquids and gels. The excitation frequency lies in the microhertz or the millihertz frequency range. If linear response theory is applicable, linearized irreversible thermodynamics permits to quantify the loss processes, which are induced by the temperature perturbation [4, 5]. Using the Lorentz-Lorenz relationship as a suitable relation between the refractive index and the mass density, thermo-mechanical relaxation processes become also accessible, determining the complex thermal expansion coefficient. As shown in Fig. 6.3, using TMOR we quantified the complex thermal expansion coefficient for the homogenous phase of an aqueous poly(N-isopropylacrylamide) (PNIPAM) solution [4]. The static thermal expansion coefficient of the solution was measured independently by densitometry. As the real part of the complex expansion coefficient equals to the static one and as the imaginary part is zero within the margin of error,

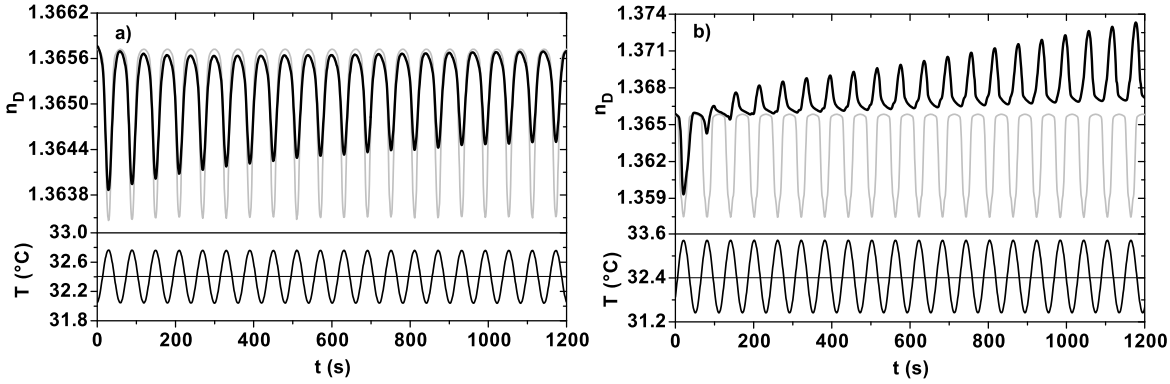

Figure 6.4:
TMOR investigation of the phase instability and the kinetic processes present at the demixing transition of a PNIPAM solution. Bottom panel: sinusoidal profile of the temperature perturbation applied at the demixing temperature of 32.4 ° C to the solution. Top panel: temporal response of the refractive index of the solution related to the sinusoidal switching of the demixing transition (black line). Grey line: expected evolution of the refractive index, in case that kinetic processes are absent. Amplitude of the temperature perturbation applied to the solution: a) 0.4 K, b) 1.1 K.

we conclude that slow thermo-mechanical relaxation processes are absent in the homogenous phase of the PNIPAM solution.
Furthermore, we utilized the TMOR technique for the first time to investigate systematically the phase instability and the kinetic processes near the demixing transition of the same PNIPAM solution [5]. As indicated in Fig. 6.4, the average temperature of the fresh PNIPAM solution was chosen to lie at its quasi-static demixing temperature. Employing increasing amplitudes of the sinusoidal temperature modulation lying in between 0.4 and 1.3 K, the adjacent phases were probed increasingly deeply. This temperature protocol implies a variation of the average temperature rate from approximately 1.6 to 5.2 K/min. As demonstrated in Fig. 6.4, the response of the refractive index of the PNIPAM solution to this temperature perturbation depends much on the chosen temperature amplitude or rate. For Fig. 6.4a), the observed stationary state corresponds to the one expected for quasi-static conditions. This means that kinetic processes are not relevant. For larger temperature rates, first over-heating and super-cooling become important. As indicated in Fig. 6.4b), non stationary states are easily achieved for higher amplitudes. We interpret this such that the repeated segregation and remixing does no longer occur in the metastable range, but that spinodal decomposition also comes into play. Our study demonstrates that TMOR is a smart technique to investigate the kinetics and dynamics of the thermal expansion coefficient, even across phase transitions within liquids and gels.

[1] M. Philipp, U. Müller, R. Aleksandrova, R. Sanctuary, P. Müller-Buschbaum, J. K. Krüger, *Soft Matter* **9**, 9887-9896 (2013)

[2] M. Philipp, K. Kyriakos, L. Silvi, W. Lohstroh, W. Petry, J. K. Krüger, C. M. Papadakis, P. Müller-Buschbaum, *J. Phys. Chem. B* **118**, 4253-4260 (2014)

[3] U. Müller, M. Philipp, M. Thomassey, R. Sanctuary, J. K. Krüger, *Thermochim. Acta* **555**, 17-22 (2013)

[4] M. Philipp, R. Aleksandrova, U. Müller, M. Ostermeyer, R. Sanctuary, P. Müller-Buschbaum, J. K. Krüger, *Soft Matter* **10**, 7297-7305 (2014)

[5] R. Aleksandrova, M. Philipp, U. Müller, R. Jiménez Riobóo, M. Ostermeyer, R. Sanctuary, P. Müller-Buschbaum, J. K. Krüger, *Langmuir* **30**, 11792-11801 (2014)

6.3 FTIR spectroscopy of molecular changes across the LCST transition in thermo-responsive polymers

A. Schulte[1], M. Futscher, M. Philipp, P. Müller-Buschbaum

[1] also at: University of Central Florida, Orlando, USA

Thermo-responsive polymers undergo a reversible coil-to-globule transition, after which the chains collapse and aggregate into bigger globules, in water above its lower critical solution temperature (LCST) [1]. Vibrational spectroscopic probes are sensitive to chemical bonding and micro-structural changes and complement small angle scattering techniques that are used to study morphology. To investigate molecular changes across the LCST transtion we employ Fourier-transform infrared (FTIR) spectroscopy. This technique provides a sensitive in-situ tool to monitor subtle molecular changes [2]. Poly(N-isopropyl acrylamide) (PNIPAM) exhibits a sharp demixing transition with an LCST near 32 ^{o}C globules that involves cooperative hydration changes along the polymer backbone. On the other hand, these are not expected to occur in the monomer.

The PNIPAM homopolymer (M_n = 20 - 25 kg/mol) and the NIPAM monomer were obtained form Sigma-Aldrich. Infrared spectra were acquired with a Bruker Equinox FTIR spectrometer equipped with a DTGS detector. The polymer and the monomer were dissolved in deionized water. For temperature dependent measurements the sample was sandwiched between two CaF_2 windows that were mounted in a copper holder to ensure temperature homogeneity. The sampler holder was mounted on a Cu block that was connected to a circulating bath thermostate. The temperature was measured on the sample holder with a Pt 100 thermometer and is accurate with 0.2 K. Per spectrum 128 scans were accumulated at a resolution of 2 cm^{-1}.

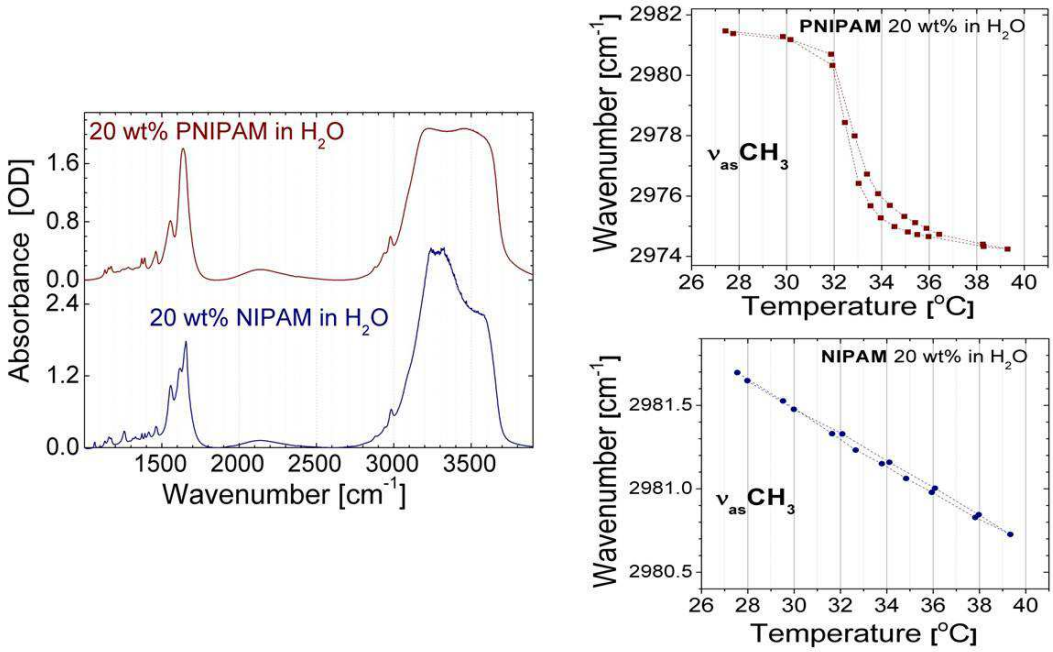

Figure 6.5:
Mid-infrared spectra of PNIPAM and its monomer NIPAM in aqueous solution (left). The panel on the right displays the peak frequencies of bands in the C-H spectral region as a function of temperature. Data from heating and cooling processes are shown. The dashed lines are guides to the eye

A comparison of the mid-infrared spectra of PNIPAM polymers and its monomer (NIPAM) is presented in Fig. 6.5. The broad band around 3,400 cm^{-1} is due to the O-H stretching vibration of water and not further considered here. The C–H stretching vibration bands occur in the range of 3,000–2,800 cm^{-1}. The intense bands in the range 1500 - 1750 cm^{-1} are attributed to the amide I and II vibrations. The amide modes involve contributions from several chemical groups (Amide I about 80% C=O stretching and 20% C-N stretching), Amide II (about 60% N-H bending and 40% C-H stretching).
The peak positions of the bands in the baseline corrected spectra were determined by deconvolution using Lorentzian line shapes. The peak frequencies of the asymmetric stretch vibration of the CH_3 groups ($\nu_{as}CH_3$) in the sidechains are displayed in Fig. 6.5. We observe a nearly discontinuous shift of the the peak frequencies in PNIPAM, whereas in NIPAM there is a continuous linear shift with temperature [3]. These findings are attributed to hydration changes in the amide group and cooperative interactions with bound water along the backbone chain.
Vibrational spectroscopic techniques provide a versatile approach to probe molecular interactions across the LCST transition for polymers with different chemical structure. These are of interest due to differences in the hydration behavior. For instance, the phase transition region may appear significantly broader. Initial studies reveal consistent changes in the temperature dependence of vibrational bands [4,5] in other thermo-responsive polymers.
This work has been financially supported by the DFG in the priority program SPP 1259 "Intellligente Hydrogele' (MU1487/8). A.S. thanks the University of Central Florida for research support.

[1] H. G. Schild, Prog Polym Sci 17:163-249, *Prog. Polym. Sci.* **17**, 163-249 (1992)

[2] B. Sun, Y. Lin, P. Wu, H. W. Siesler, *Macromol.* **41**, 1512-1520 (2008)

[3] M. Futscher, M. Philipp, P. Müller-Buschbaum, A. Schulte *DPG Frühjahrstagung* (2015)

[4] P. Spieler, B.S. Thesis, Physics Department, TU Munich (2014)

[5] P. Marzak, B.S. Thesis, Physics Department, TU Munich (2014)

6.4 Silicious chemical crosslinks in polyurethanes. Reduced microphase separation and slowing of dynamics

K. N. Raftopoulos[1], S. Koutsoumpis[2], M. Jancia[1], K. Kyriakos, E. Hebda[1], C. M. Papadakis, K. Pielichowski[1], P. Pissis[2]

[1] Cracow University of Technology, Kraków, Poland
[2] National Technical University of Athens, Greece

By the *nanobuilding block* approach, functionalized nanoscopic moieties react with oligomers or monomers to produce organic-inorganic hybrid polymers. This approach suppresses aggregation of nanoparticles and allows tailoring their location inside copolymer matrices.
The polyhedral oligomeric silsesquioxanes (POSS) are ideal nanobuilding blocks: They are based on a siliceous polyhedral core, with Si atoms on the vertices and O atoms on the edges. Organic ligands (*vertex groups*) are attached on each of the Si atoms. The number of the reactive vertex groups defines the topology of the material. POSS moieties with more than two reactive groups may act as rigid chemical crosslinks.

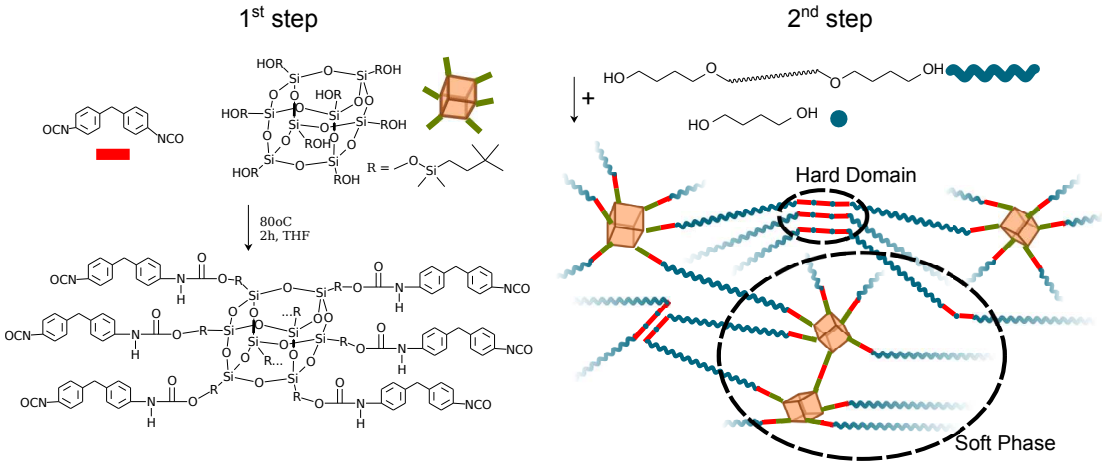

Figure 6.6:
Synthesis and anticipated topology of the organic inorganic hybrid polyurethane networks. Some links have been omitted for clarity.

In this work, POSS moieties with 8 OH-functional groups crosslink a linear polyurethane (PU) matrix prepared in a two step process (Fig. 6.6). Polyurethanes are essentially copolymers of a macrodiol (soft segments) and an alternating sequence of a diisocyanate and a short diol (hard segments). The segments are immiscible with each other, and thus, elastomeric PUs are typically microphase separated. Our aim is to examine how the siliceous POSS crosslinker affects the microphase separation and how this effect is reflected in the segmental dynamics.
Starting from the high q side of the combined WAXS and SAXS diffractogram (Fig. 6.7A), the narrow halo at 1 Å^{-1} is related to the internal structure of the hard domains [1,2]. It is virtually unaffected, indicating that POSS do not penetrate the hard microdomains and rather reside on the soft phase. One more halo emerges systematically on addition of the POSS at the position of a major POSS reflection (0.3 Å^{-1}). We may assign it to highly distorted crystals or to the internal structure of a highly crosslinked phase.
The halo on the small angle diffractogram below 10^{-1} Å^{-1} is related to the microphase separation. This one diminishes monotonically on addition of POSS indicating that the microphase separation is inhibited.
We quantified the characteristic sizes of the microphase separated domains by the *correlation triangle* approach [3]. While the hard microdomains become progressively thinner upon addition

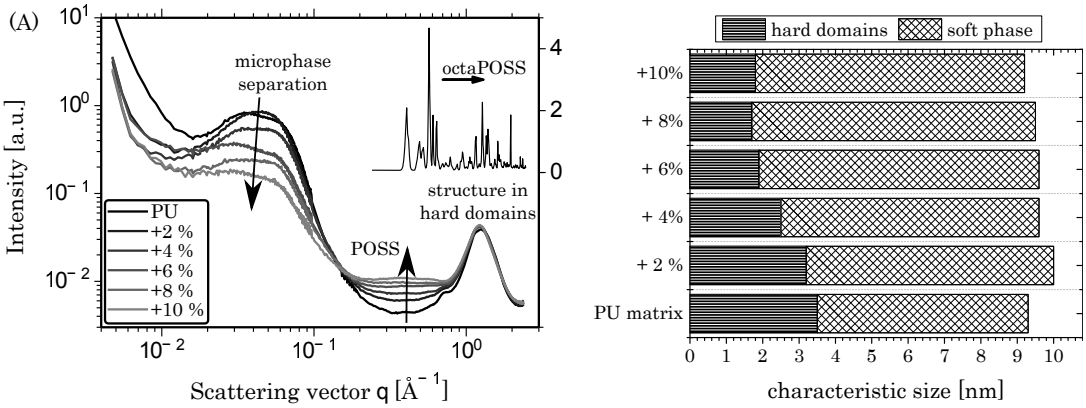

Figure 6.7:
(A) X-ray diffractograms of the PU matrix and the hybrids. The arrows show the evolution of the main features with increasing POSS content. (B) Characteristic sizes of hard domains and soft phase as calculated by the correlation triangle method.

of POSS, the soft phase becomes thicker (Fig. 6.7B). However, the sum of the two sizes (the *long period (LP)*), shows only a slight decrease. Apparently, the hard segments which are bound on the silsesquioxane units are sterically unavailable to form hard microdomains.
The α relaxation (dynamic glass transition) peak, as observed in the dielectric loss function, moves to lower frequencies (longer relaxation times) upon crosslinking (Fig. 6.8). Two mechanisms cause this deceleration: i) The crosslinking particles restrict mobility of the chains, and ii) more relatively rigid hard segments, and bulky POSS moieties participate in the segmental dynamics of the soft phase.

Summing up, the siliceous chemical crosslinks reside in the soft phase of the polyurethane and suppress the formation of hard microdomains. As a result, the soft phase dynamic glass transition is significantly decelerated.

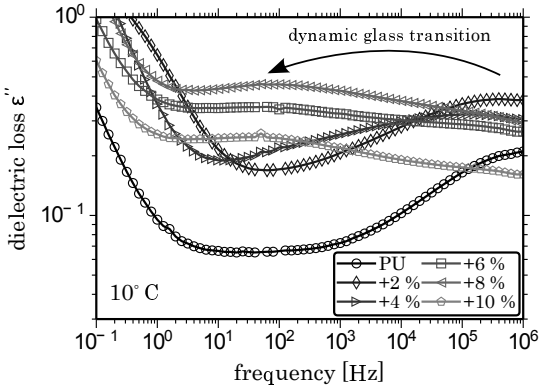

Figure 6.8:
Dielectric loss spectra of the PU matrix and the hybrids at 10 °C. The peaks correspond to the α relaxation (dynamic glass transition) of the soft phase. The arrow marks the evolution of the relaxation with increasing POSS content.

This research has been co-funded by the the National Science Center in Poland (contr. DEC-2011/02/A/ST8/00409), and the European Social Fund ESF and Greek national funds (Programs Aristeia and Thales).

[1] J. T. Koberstein, A. F. Galambos, L. M. Leung, *Macromolecules* **25**, 6195 (1992)

[2] K. N. Raftopoulos, S. Koutsoumpis, M. Jancia, J. P. Lewicki, K. Kyriakos, H. E. Mason, S. J. Harley, E. Hebda, C. M. Papadakis, K. Pielichowski, P. Pissis, DOI: 10.1021/ma5023132 (2015)

[3] B. Goderis, H. Reynaers, M. H. J. Koch, V. B. F. Mathot, *J. Polym. Sci.: B. Polym. Phys.* **37**, 1715-1738 (1999)

7 Methodological and instrumental developments

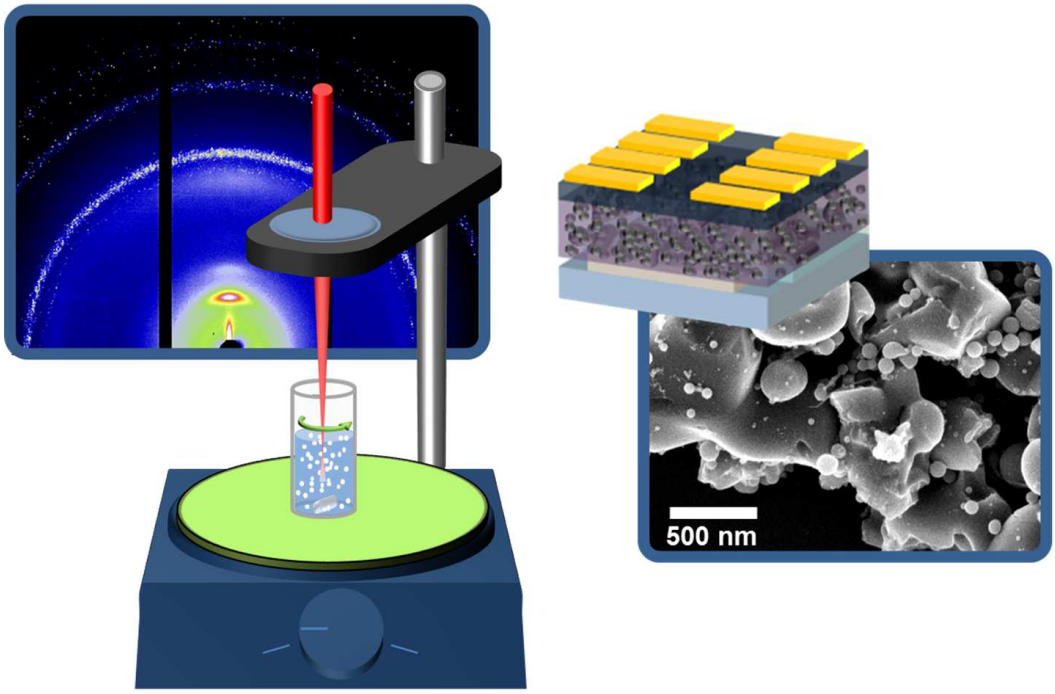

7.1 Implementing an OPV slot die coating device for printed organic solar cells and determining the ramifications on morphology and device efficiency

S. Günther, C. J. Schaffer, P. Müller-Buschbaum

A continuously increasing energy demand, combined with aggravating environmental problems, fuels the need for new, innovative and sustainable energy sources. Organic photovoltaics is a highly investigated research area, which has the potential of solving the problems of material costs, which most of the currently used PV technologies are faced with. However, for the feasibility of large scale fabrication it is still necessary to understand the processes, which are involved in the applied fabrication methods, in more detail in order to understand the ramifications on the obtained printing results. That regards especially the analysis of the morphology, which is a key parameter to efficient devices and also affects degradation as well as device lifetime. Therefore, particularly the processing method is of interest as it has an extensive influence on the morphology and structure of the created photoactive layers. In the scope of this investigation, slot die coating, a technique which is viable for the use in large scale fabrication and combines high production output with desired film quality and morphology, has been focused. A new printing device has been developed, based on the principle of *meniscus guided slot die coating*. This coating method allows for the use of dilute, low viscosity solutions and offers the advantages of comparatively high film quality and a wide range of morphology affecting parameters [1]. An investigation on the structural characteristics has been conducted on the basis of samples and organic solar cells, produced by meniscus guided slot die coating. In Fig. 7.1 the developed printing device is shown.

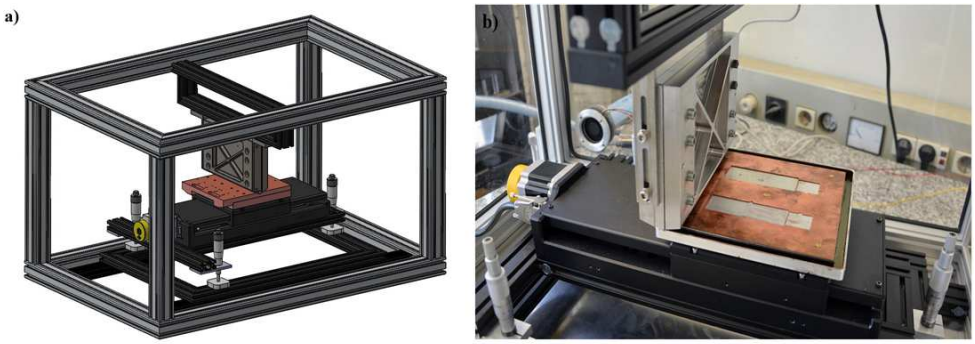

Figure 7.1:
Illustration of the complete assembly. a) SolidWorks® rendering of the complete machine (without external functional devices). b) Close up picture of the (real) printhead-substrate holder arrangement.

The printing machine enables the user a solution based application of thin layers for the use in organic solar cell devices. With printing speeds ranging from 0-24 mm/s, exchangeable shim mask and meniscus guide mask, volume flow control, substrate heating and (to a certain degree) atmospheric controls the printer offers a large variety of control parameters in order to achieve the desired film characteristics. The key aim for the machine is the uniform deposition of the photoactive layer material for polymer based solar cells. The initial focus is on the use of rigid substrates based on a non-inverted cell architecture. The principle of meniscus guided slot die coating has the special characteristic of an (almost) indirect proportionality between printing speed and deployed layer thickness, as this technique resembles more the meniscus coating method than the standard pre-metered slot die process. The layer application is realized simply by translation of the coating substrate along the perpendicular direction of the print head. Due to the fact that the meniscus size and shape determine the printing results and a very close

distance between substrate and shim mask have to be maintained throughout the printing process, a very planar movement of the substrate holder has to be guaranteed. The decision for the movement of the substrate is based on the idea of being able to compare the printed layers of this device to very large scale manufacturing, as it is done by roll-2-roll-coating (R2R). Regardless of difficult technical requirements, due to the need of a very narrow spacing between translating parts and a rather low printing speed, the technique of meniscus guided slot die coating allows for application of very thin films, homogeneous layer surfaces and an overall higher film quality [2]. This is due to a lower viscosity of the printed solution and thus also a lower pressure in the printhead, which allows for the solution to wet the substrate surface in a more uniform manner.

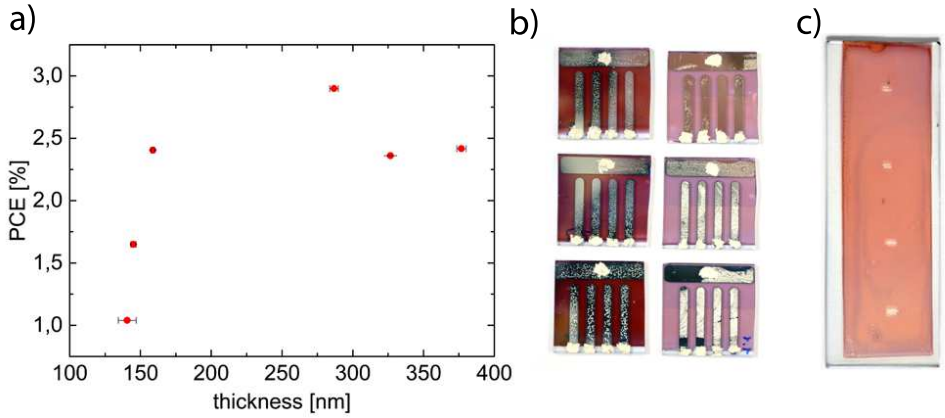

Figure 7.2:
a) Photon conversion efficiency of (P3HT:PCBM based) solar cells with printed active layer. A active layer thickness of about 300 nm lead to the best device efficiency. b) Solar cell samples on glass substrates. Thickness difference was achieved by using two different solution concentrations for the printing of the active layer. c) P3HT:PCBM film on glass substrate.

P3HT:PCBM based films have been printed on glass substrates covered with PEDOT:PSS from a 12-24 mg/ml solution in chlorobenzene. The thereby created films have been analyzed using X-ray reflectivity (XRR), UV/Visible light spectroscopy (UV/Vis), microscopy and tactile profilometrie as characterization methods. The morphology of these films on a nanometer scale has been probed with grazing incidence small angle X-ray scattering (GISAXS). In addition solar cells with printed active layer have been fabricated and device efficiencies up to 3,14% have been found. Important device characteristics for a highly efficient organic solar cells are especially the active layer morphology. A good intermixing of donor and acceptor material, resulting in a large heterojunction interface, combined with highly ordered (crystalline) domains, leads to an enhanced device performance. Printed active layer films offer these characteristics, due to a longer drying time, as has been shown by UV/Visible light spectroscopy and GISAXS data.

[1] S. Hong, J. Lee, H. Kang, K. Lee, *Solar Energy Materials and Solar Cells* **27-35**, 112 (2013)

[2] F. C. Krebs, *Solar Energy Materials and Solar Cells* **93**, 394-412 (2009)

[3] F. C. Krebs, *Solar Energy Materials and Solar Cells* **93**, 465-475 (2009)

[4] F. Jakubka, *Solar Energy Materials and Solar Cells* **109**, 120-125 (2013)

7.2 Design and application of a temperature controlled UV/Vis sample holder

C. Mayr, V. Körstgens, P. Müller-Buschbaum

There are several ways to improve the efficiency of organic or hybrid solar cells. One important factor is the crystallinity of the hole conducting polymer in the active layer. It has been shown that crystallinity of the polymer as well as the efficiency of the corresponding device increases with so called thermal annealing [1]. In practice, the solar cell is heated up for some minutes to a particular polymer-specific temperature. In order to ascertain the ideal annealing temperature and to investigate the annealing process in situ, we developed a temperature controlled sample holder for an UV/Vis spectrometer (see Fig. 7.3). The sample holder is custom built for a Lambda 650S spectrometer from Perkin Elmer, but can easily adapted to other systems. The device is connected to an external heat bath, a Julabo F12-MA, which heats the bottom copper block (1). The actual sample holder (2,3) contains the sample (4) and is screwed on the base block (1). A study about the temperature distribution was done with Solid Works, in order to simulate the heat flow inside the sample holder and to see temperature gradients inside the sample. The simulation showed, that without the two thin cover slips (5), the sample has no homogeneous temperature. The reason is the low heat conductivity of glass and the loss of heat via convection. The two glass slips, with a thickness of 0.13-0.16 mm, prevent heat convection from the inside of the sample holder to the environment and assures a homogeneous sample temperature. In order to prove the results from the simulation, we calibrated the sample temperature in dependence of the bath temperature with a Pt 100 thermometer in two steps. First, we measured the temperature inside the cell-environment (i.e. 1 mm over the sample) and second, we used a thermal glue to fixate the Pt 100 thermometer on the sample. The results show, that the temperature of the bath and the sample temperature have a linear dependence over a wide range. This allows to control the temperature of the sample very well in the range from 20 °C up to 150 °C, being in the range for the thermal annealing of many polymers.

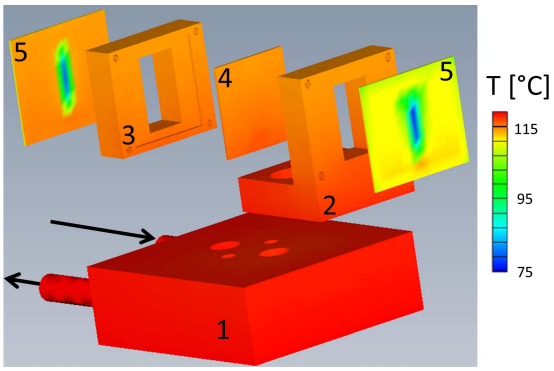

Figure 7.3:
Solid works temperature simulation of the sample holder designed for in situ UV/Vis measurements with the spectrometer Lambda 650S. The investigated sample (4) is mounted in between two copper blocks (2,3) and indirectly heated with a thermal liquid. The liquid is heated externally and circulates through the base plate (1), which is indicated with the two arrows. The cover slips (5) prevent convection between sample and environment.

In order to show the possibilities of our new device, we investigate a thermochromic film. Such materials change their color, by changing the temperature. One of the prominent examples of thermochromic materials is based on crystal violet lactone (CVL) [2]. The color change in the system is enabled by addition of a proton donor (in our case camphersulfonic acid (CSA)), which induces the ring opening of the lacton. Whereas this reversible effect in principle is halochrom (color change in dependence of pH), it also can be controlled by temperature if a solvent is added witch has a melting point in the suitable region. We chose a system of 1-octadecanol, which has a melting point of 58-60 °C, CSA and CVL in a weight ratio of 40:7:1. The reversible thermochromic effect of this composition is demonstrated by a candle we produced (Fig. 7.4 d). Whereas at room temperature the candle appears white to light yellow, in the lighted state near the flame, the material is blue. After putting the flame out, with cooling and solidification the color turns from blue to green into white again.

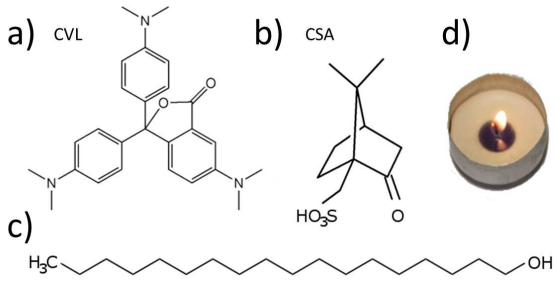

Figure 7.4:
Chemical structures of the materials used for the thermochromic samples. a) crystal violet lactone ($C_{26}H_{29}N_3O_2$) , b) camphorsulfonic acid ($C_{10}H_{16}O_4S$) and c) 1-octadecanol ($C_{18}H_{38}O$) are mixed together in the ratio 1:7:40. d) Candle based on these materials shows a reversible change of color.

The thermochromic properties of the material were investigated in situ with an UV/Vis spectrometer 650 S from Perkin Elmer. For sealing, we used a frame of adhesive transfer tape (467MP from 3M) and cover slips as top and bottom surface. This results in a film thickness of 60 μm. The bath temperature was raised from 70.0 °C to 110.0 °C in 10.0 °C steps, resulting in a sample temperature from 59.9 °C to 93.3 °C. Between each step, the system had ten minutes time to reach thermal equilibrium, then the transmission spectrum was measured. The transmission curves have a range from 320 nm to 800 nm, and are depicted in Fig. 7.5. The arrows in the two graphs indicate the change in temperature over time for heating in a), and for cooling in b), respectively. It can be seen, that the transmission of the film decreases upon heating, especially in the range from 320 to 400 nm and around 610 nm. In the latter region, there also is a small shift of the transmission minimum to lower wavelengths. If the sample is cooled again, which is depicted in b), one can see that the change in transmission is in the opposite direction, which means that the thermochromic effect is reversible.

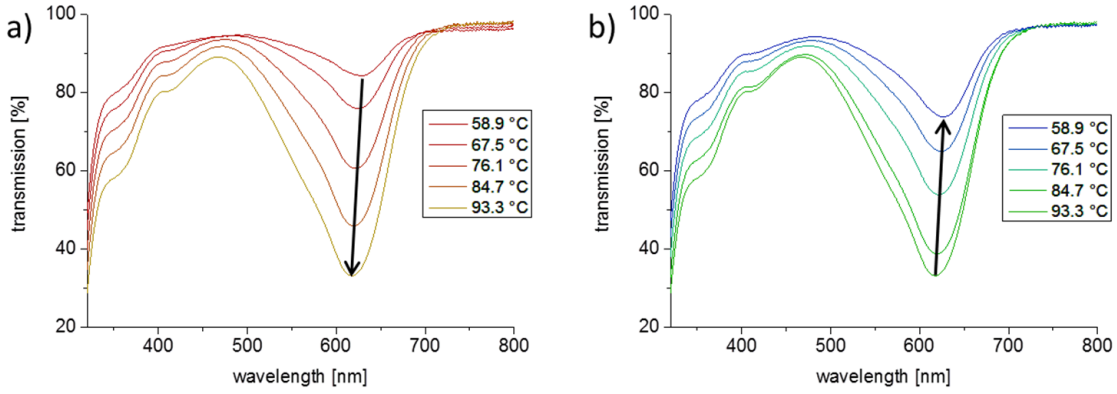

Figure 7.5:
UV/Vis spectrum of the thermochromic film during heating (a) and cooling (b). The arrows highlight the course of transmission with temperature.

It has to be noted, that the measurements were made in the liquid state of the system. The transmission between solid and liquid state changes the optical transmission, but covering this effect would go beyond the scope of this discussion.
The newly constructed sample holder is suitable to investigate temperature dependent changes of optical properties of films. Therefore it is now possible to study the change in light absorption of a polymer during annealing and to find the optimal temperature and time for this fabrication step. This knowledge helps to improve the overall light absorption and the crystallinity of a solar cell's active layer, both key factors towards higher efficiencies.

[1] M. A. Ruderer, S. M. Prams, M. Rawolle, Q. Zhong, J. Perlich, S. V. Roth, and P. Müller-Buschbaum, *J. Phys. Chem.* **114**, 15451-15458 (2010)

[2] D. C. MacLarena and M. A. White, *J. Mater. Chem.* **13**, 1701-1704 (2003)

7.3 C-SPEC: The cold time-of-flight spectrometer for the ESS

W. Lohstroh[1], L. Silvi[1], J. Neuhaus[1], W. Petry[1], S. Longeville[2], J. M. Zanotti[2], Chr. Alba-Simionesco[2]

[1] E13 and MLZ, Garching, Germany
[2] LLB, Saclay, France

In 2019, the European Spallation Source (ESS), a joint project of 17 European countries, will start operations. Construction of the facility has just started with the ground-breaking and the cornerstone ceremony in autumn 2014. Alongside, the selection process for the scientific instrumentation is ongoing and the first instruments have been chosen and endorsed by the ESS steering committee. Among the endorsed instruments foreseen for day one instrumentation at the ESS, is the cold time-of-flight spectrometer C-SPEC. C-SPEC is a joint proposal of the Technische Universiät München and the Laboratoire Léon Brillouin, Saclay, France.

Many research fields and scientific questions will benefit from a high performance direct geometry time-of-flight spectrometer. For instance, dynamic properties govern the response of stimuli responsive polymers, hydrogels, or of molecular liquids and the understanding and development of the materials properties will have significant impact on technological applications. Studies of the complex interplay of structural form, dynamic properties and functionality of e.g. proteins will improve our understanding of diseases and will assist in the drug development. In the field of hard condensed matter, measurements of the excitation spectrum of novel magnetic materials are crucial for the understanding of the interaction potentials and to benchmark experiments with theory. While current experiments mainly probe the static state of a sample, neutron spectroscopy experiments that probe the dynamic response e.g. of electrolytes in an electric field, or laser excited light harvesting proteins, are still in an exploration stage mainly due to the lack of intensity at the instruments available today.

All these questions require a spectrometer that explores relaxation times in the range from pico- to nanoseconds. Therefore, the instrument is designed to cover an energy resolution of $\Delta E/E$ = 6 - 1% and it will utilize cold neutrons in the range from λ = 1.5 - 15 Å with the focus on the cold part of the spectrum. The unique pulse structure of the ESS with its long pulse duration (2.86 ms) and a repetition rate of 14 Hz requires new concepts for the instrumentation to make optimum use of the available source time frame. The concept for C-SPEC is illustrated in Fig. 7.6, where the time-distance diagram is shown.

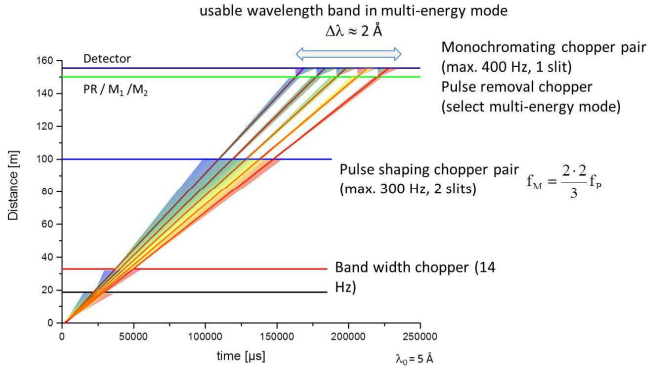

Figure 7.6:
Time-distance-diagramm of C-SPEC. The P- and M-chopper sets utilized wavelength and the energy resolution. The PR-chopper enables the choice between multi- and single energy mode. With an instrument length of 155.4m, the usable wavelength band is $\Delta\lambda \leq 2$Å.

The neutron pulse coming from the source first passed to band width choppers that both shape the pulse and prevent overlap of successive source pulses. These two choppers rotate with the source frequency. The instrument length of 155.4 m permits a wavelength band of $\leq$ 2 Å at

the detector position. The source pulse is then divided by a cascade of fast rotating chopper discs into a series of monochromatic sub-pulses, i.e. the pulsing chopper pair (P-chopper) at 100 m and the monochromatizing chopper pair at 150m (M-chopper). The phase and rotation frequency defines the utilized wavelength λ and the chosen energy resolution. A pulse removal chopper (PR-chopper) just in front of the monochromatizing chopper pair enables to chose the number of sub-pulses (all with a different λ and thus different incoming neutron energy E_i) and their separation in time which then impinge on the sample. Figure 7.7 illustrates the energy resolution function as obtained from McStas simulations (scattering on a vanadium sample) for 3 subsequent impinging wavelength, centred around $\lambda = 5$Å. During one source time frame, the number of data sets is thus multiplicated (Rate repetition multiplication, RRM or multi-energy mode)

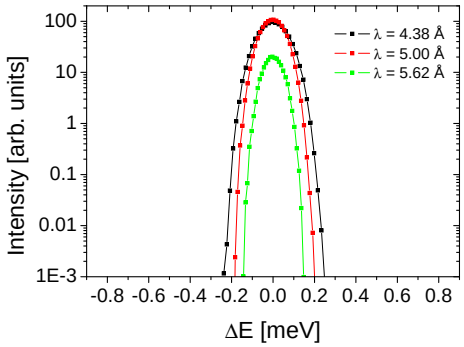

Figure 7.7:
Energy resolution (obtained from McStas simulations (vanadium scatterer). The chopper settings are for medium energy resolution, i.e. 100 μeV at 5 Å.

The neutron guide system is illustrated in Fig. 7.8. A ballistic guide will minimizes the number of neutron reflections and the s-shaped bender section moves the instrument out of the line-of-sight from the moderator, and thus the fast neutron background at the sample position is minimized. The ballistic section will be followed by an elliptic compression towards the PR/M-chopper system. After the last chopper, an exchange guide system is planned to switch between two beam configurations: (i) a large homogeneous beam spot and a focussing option.

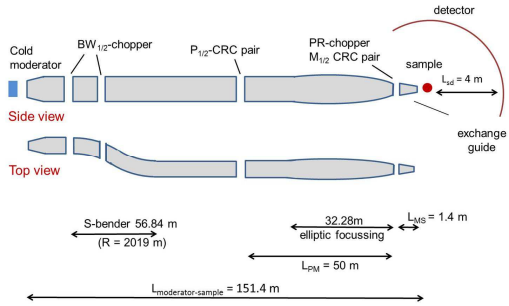

Figure 7.8:
Schematic represenation of the instrument layout.

The dynamic range of the spectrometer will cover the relevant length scales required by the science drivers. I.e. the Q-range should extend to low values ($Q \leq 0.05$ Å^{-1}) for soft matter and biological applications whose characteristic length scales are often in the range of 10 - 1000 Å while on the other hand, large accessible momentum transfer values ($q \leq 10$ Å^{-1}) are required for materials science questions with length scales on the order of Ångströms. C-SPEC will serve a broad user community and significant advances in the field of biology, soft condensed matter, materials science and magnetic phenomena can be expected from day one of instrument operation. With the high flux and the multi energy mode, the special strength of the proposed instrument C-SPEC will be the possibility for driven experiments, pump-probe type experiments and time-resolved kinetic measurements.

7.4 Progress in UMo fuel development

H. Breitkreutz, F. Alder, B. Baumeister, T. Chemnitz, H.-Y. Chiang, A. Egle, L. Fiedler, R. Großmann, T. Hollmer, T. K. Huber, M. Kraut, C. Reiter, R. Schauer, R. Schenk, C. Steyer, A. Wolf, T. Zweifel, A. Röhrmoser, W. Petry

The main tasks of the working group "Hochdichte Brennstoffe" are settled around the development of the new UMo fuel which will serve as replacement for the current U_3Si_2 HEU fuel. This comprises reactor physics calculations to specify fuel conditions during the full reactor cycle to guarantee safety and performance of the reactor; fabrication technology to pave the way for industrialisation; irradiation testing, in-pile and with heavy ions as well as physical-properties measurements to study fuel behaviour and determine operation parameters.

Reactor physics: A draft for a fuel element with 25% enrichment based on monolithic UMo has been published at RRFM 2014. This draft utilizes Molybdenum depleted in ^{95}Mo to mitigate the strong parasitic absorption and is similar to the 27% draft that was presented last year [7].

To quantify the transient reactor behaviour with a possible new fuel element, calculations that take the full reactor system into account are under development to assess the reactor behaviour in these time dependent processes. First thermal-hydraulic simulations with an ATHLET model of FRM II have been performed and a core model is being adapted for the neutronic code TORT-TD.

Fuel production: TUM contributes to the development of monolithic as well as dispersion UMo fuel.

Monolithic fuel: A dedicated chemistry glove box has been constructed and tested in the Uranium lab of the group for the chemical cleaning of UMo foils prior to coating with thin diffusion barriers using PVD. To obtain a thorough understanding of the optimum process parameters, a prototype mini-plate device has been tested and further improved using surrogate material. These surrogate plates will later be tested with the C2TWP process at CERCA to pave the way for the usage of uranium in the fabrication process.

Based on the experience with the mini device, a dedicated glove box and vacuum chamber are currently under construction to house an optimized full-size PVD device. Such a device is necessary to produce coated full-size fuel foils equivalent to the current fuel geometry for future irradiation tests and manufacturing industrialization.

Dispersion fuel: FRM II and CERCA have succeeded in designing and implementing an industrial prototype U-8Mo fuel-powder production facility. After hot commissioning of the production facility in 2014 and first feasibility tests with uraniferous material, atomizer parametrization tests using depleted U-8Mo were carried out showing results that are consistent with industrial standards including safety, repeatability and reliable performance. Notably, powder fuel requirements with respect to particle size, shape, satellites, porosity, voids, surface, homogeneity and oxidation are met [6].

Irradiations: The HERACLES group has begun preparations for two in-pile irradiations tests, EMPIrE and SEMPER FIDELIS. Besides fundamental fuel behaviour aspects like the high burn-up swelling, the irradiations also target the quantification of the influence of production technology on the fuel performance.

Heavy ion irradiation was used to further test transition metal (X = Ti, Zr, Nb, Mo) diffusion barriers to prevent IDL formation. No UMo-Al compounds were found, only slight atomic mixing at interfaces. Each formed intermetallic compounds with Al that can act as additional barriers at the X/Al interface. However, Ti and Zr might lead to γ-UMo decomposition by forming orthorhombic U-Ti compounds or segregation of Mo from UMo, respectively. Nb is stable at both interfaces; however the crystallinity of the Nb-Al compound is poor. Altogether, Mo is the best performing candidate for diffusion barriers in UMo/X/Al systems with its high strength Mo-Al compound to protect the interface [1]. As consequent continuation of the Iodine irradiation, Kr was implanted into the irradiated UMo/Al layer system to study inert gas behaviour. SEM and SIMS revealed that Kr accumulates inside the IDL in μm-sized bubbles with a 1000 times higher quantity than in IDL free regions. This result is in full agreement with in-reactor irradiation experiments, extending the out-of-reactor irradiations' ability to predict in-pile results [8].

Physical properties: Measurement of thermo-physical properties of spent dispersion UMo fuel were performed at PNNL together with INL (US) using fuel segments from the AFIP-1 irradiation test (atomized U-7 wt.% Mo in an Al/2.1 wt.% Si matrix, max. burn-up $6.0 \cdot 10^{21}\mathrm{fiss/cc}$. The specific heat capacity hardly depends neither on temperature nor burn-up. Density decreases by 21% with burn-up due to fission gas bubbles. The thermal diffusivity increases with temperature but decreases significantly with burn-up. The calculated thermal conductivity therefore slightly increases with temperature but decreases from originally $50\,\mathrm{W/m \cdot K}$ down to $7\mathrm{W/m \cdot K}$ for the highest burn-up [5]. Parallel measurements of alloyed fresh matrix material have been performed at FRM II to allow for effects separation [2].

The last missing crystal structure for the α''-phase of UMo has been determined as P1121/n using X-ray diffraction [4]. Attempts to reproduce the Si-rich layer found around UMo grains during irradiation by out-of-pile alloying showed differences to the crystal structure found in-pile [3].

Uranium laboratory: All requirements for the Uranium laboratory associated with §9 AtG license were fulfilled and the laboratory has entered into trial operation. Further licensing processes for additional glove boxes were initiated.

[1] H.-Y. Chiang, *Material Selection of UMo Fuel: Swift Heavy Ion Irradiation Studies*, PhD Thesis

[2] A. Wolf, *Einfluss des Si-Anteils im Matrix-Material hinsichtlich der Wärmeleitfähigkeit von dispersen UMo-Brennstoffen*, Bachelor Thesis

[3] L. Fiedler, *SEM- and XRD-Studies on Arc-casted U-Mo-Si compounds*, Master Thesis (FH)

[4] M. Kraut, *Untersuchungen zur a"-Phase in Uran-Molybdän-Legierungen*, Bachelor Thesis

[5] T. K. Huber et. al., *Thermal Conductivity of In-pile Irradiated AFIP-1 Dispersion U-Mo Fuel*, RERTR 2014

[6] R. Schenk et. al., *FRM II / CERCA UMo atomizer project status*, RRFM 2014

[7] H. Breitkreutz et. al., *Influence of depleted Molybdenum on monolithic UMo fuel plate designs for FRM II*, RRFM 2014

[8] T. Zweifel, *Fission Gas Behaviour and Interdiffusion Layer Growth in in-pile and out-of-pile Irradiated U-Mo/Al Nuclear Fuels*, PhD Thesis

7.5 Development of a cylindrical PVD-reactor for the manufacturing of LEU-targets for ^{99}Mo production

T. Hollmer[1]

[1] MLZ, Garching, Germany

The decay product of molybdenum-99 (^{99}Mo), technetium-99m (^{99m}Tc), is the most widely used diagnostic medical isotope. It is used for a variety of medical investigations such as the detection of diseases or the study of organ structures and functions. The metastable ^{99m}Tc decays to ^{99}Tc by emission of a 140keV photon. This photon can be detected by scintillator devices and, in this way, be used to localize ^{99m}Tc-labled pharmaceuticals inside the human body. The main production route of ^{99}Mo is the nuclear fission of uranium-235 (^{235}U). Approximately 6% of the fission products result in ^{99}Mo. Current production mainly uses irradiation targets with highly-enriched uranium (HEU) embedded in an aluminum matrix.

Due to proliferation concerns, a great deal of effort has been made in recent years to convert the production from HEU to low-enriched uranium (LEU, enrichment below 20%). Decreasing the enrichment of uranium, not only decreases the amount of fissile ^{235}U but also increases the neutron absorbance due to a higher ^{238}U amount. One approach to compensate these two effects is to increase the total uranium mass in the irradiation targets. This can be achieved by using metallic uranium foils instead of dispersed uranium in an aluminum matrix, as it is used in current targets.

Figure 7.9: Irradiation target for ^{99}Mo production

A promising target design is the cylindrical foil target, which was developed by Argonne National Laboratory (ANL) together with other institutes. This target consists of a thin metallic LEU foil (approx. 125 μm - 150 μm thick) wrapped in an interlayer material (e.g. nickel), which is then encapsulated between two concentric aluminum cylinders. Figure 7.9 shows a schematic of the target (all dimensions in inch). The cylindrical design guarantees a good structural integrity and heat transfer. The interlayer material prevents bonding of the uranium

and the aluminum cladding during irradiation and, therefore, allows an easy disassembly of the target afterwards. In this way, just the uranium foil needs to be chemically processed in order to isolate the produced ^{99}Mo. This reduces the amount of highly-radioactive liquid waste significantly and, therefore, lowers processing costs.

Currently, the foils used in these targets are either produced by hot and cold rolling (Argonne National Laboratory) or by a direct casting method (Korea Atomic Energy Research Institute). Both methods have their specific assets and drawbacks. The rolling process is labor intensive but is able to produce foils of high and homogenous quality. The direct casting method, on the other hand, is economical but the foils produced show surface irregularities and an uneven thickness [1, 2]. To overcome these problems, a novel manufacturing method was developed. The interlayer material and the uranium are directly coated on the inside of the outer aluminum cylinder. The material is deposited by a PVD process, where the target material is eroded by the bombardment of argon ions. This way of production allows the application of a large variety of interface materials. Compared to pre-produced foils, it also gives the possibility to easily adjust the target geometry and the foil thickness.

A dc magnetron sputtering device was build at the uranium laboratory at the MLZ. This reactor features a movable sputter target, which allows a deposition of layers with a homogenous thickness. The necessary sputter target has a simple geometry and can be produced by casting. This facilitates a recycling of used sputter targets and, in this way, significantly reduces the scrap material. By a substrate heating and cooling system, the adhesion and the layer properties of the deposited foil can be adjusted. To guarantee a safe handling of uranium and a reliable operation, the PVD-reactor was integrated in an inert-gas glove-box and equipped with a programmable logic controller.

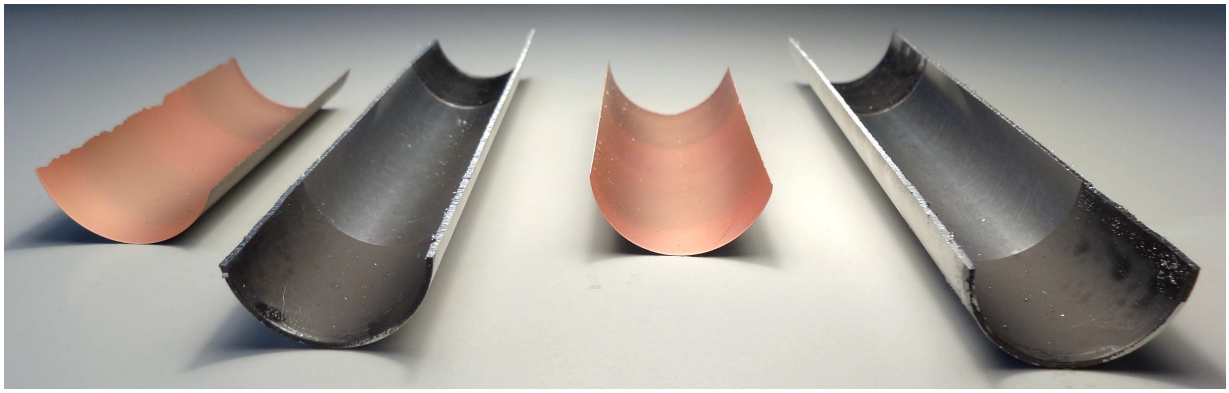

Figure 7.10: Copper foils produced by PVD coating

The sputtering device was extensively characterized using copper as a non-radioactive surrogate of uranium. Figure 7.10 shows a sliced outer cylinder and the deposited self-sustaining foil. So far, coatings of several different non-radioactive materials were produced. Also, the casting of new sputter targets was demonstrated. In a further step, complete targets using uranium will be manufactured.

[1] T. C. Wiencek, *Status and Progress of foil and target fabrication activities for the production of 99Mo from LEU*, ANL, Proceedings of the RERTR International Meeting (2008)

[2] A. Bakel, *Overview of progress related to implementation of the LEU-modified Cintichem process*, ANL, Proceedings of the RERTR International Meeting (2008)

7.6 Investigation of Li precipitation in Al-Cu-Li alloys by Atom Probe Tomography

P. Neibecker, M. Leitner, M. Kushaim[1], T. Boll[2], T. Al-Kassab[1], F. Haider[3]

[1] King Abdullah University of Science and Technology, Thuwal, Saudi Arabia
[2] Chalmers University, Gothenburg, Sweden
[3] University of Augsburg, Augsburg, Germany

Al-Cu-Li alloys are an alloy family of great technical importance and interest, especially due to their suitability for aerospace applications [1]. Their combination of desirable properties such as high Young's modulus and high yield strength at low mass density thereby results from complex precipitation sequences including but not limited to the precipitation sequences found in binary Al-Li and Al-Cu alloys. These precipitation sequences as well as the mechanisms and kinetics of the mentioned precipitation processes are in this respect under ongoing discussion and many aspects have not been resolved yet. For obtaining a complete picture, investigating these precipitation processes requires the combination of various experimental methods.

An experimental method well suited for real space observations of precipitation processes in metallic materials is Atom Probe Tomography (APT) [2]. In this technique, an atomically sharp tip with a tip radius of a few nm is prepared from the sample material. At low temperatures of approximately 30 K and under ultra high vacuum, high voltage pulses are applied between the tip and a position sensitive detector, resulting in an ionization of the surface atoms and their acceleration towards the detector. Finally, the mass to charge ratio and the position of the detected ions is analyzed and the 3D-sample volume is reconstructed in real space. In modern Atom Probes, analysis volumes of 10 to 100 Million atoms are obtainable with a detection efficiency of 30- 50 % per ionized atom.

Technical Al-Cu-Li alloys nowadays consist of a number of additional alloying elements such as e.g. Mg, Ag and Zr. This large number of elements makes it difficult to study the underlying mechanisms of Li and Cu precipitation due to the increased interactions and interdepedencies between the elements. As a consequence, for a basic understanding of the complex precipitation processes, it is useful to reduce the complexity of the alloy systems by preparing pure Al-Cu-Li model alloys. This approach was followed in the presented work via preparing an Al-Cu-Li model alloy from high purity elements with a composition of 1.0 at. % Cu and 5.8 at. % Li. The precipitation process was then studied by APT in different aging conditions. Thereby, especially the clustering and precipitation of Li is of interest and was analyzed using a cluster finding algorithm. This algorithm first identifies the e.g. 99 nearest neighbours of any reconstructed atom in the analysis volume and, in a second step, determines the composition of each 100-atom cluster. To investigate shape, size and volume of precipitates, the spatial distribution of 100-atom clusters that fulfil certain analysis criteria can then be presented in the original sample volume. Figure 7.11 gives an example for such a cluster finding procedure in the stated Al-Cu-Li alloy aged for 1 h at 160 °C. While in a) the complete analysis volume with all reconstructed atoms is shown, in b) only the center atoms of 100-atom clusters having a composition of $\geq$ 15 at. % Li are depicted. Figure 7.11 b) shows spherical precipitates with a precipitate radius of 5.7 ± 0.6 nm after an annealing treatment of 1 h at 160 °C. The composition of these precipitates as well as their shape can be associated with and are characteristic for the δ' phase (Al_3Li). This δ' phase is the major hardening phase in binary Al-Li alloys and one of the important hardening phases in ternary Al-Cu-Li alloys [1].

Besides visualizing precipitates, APT is well suited for the quantitative, statistical analyis of precipitation and demixing processes. While a random Li distribution in the matrix would

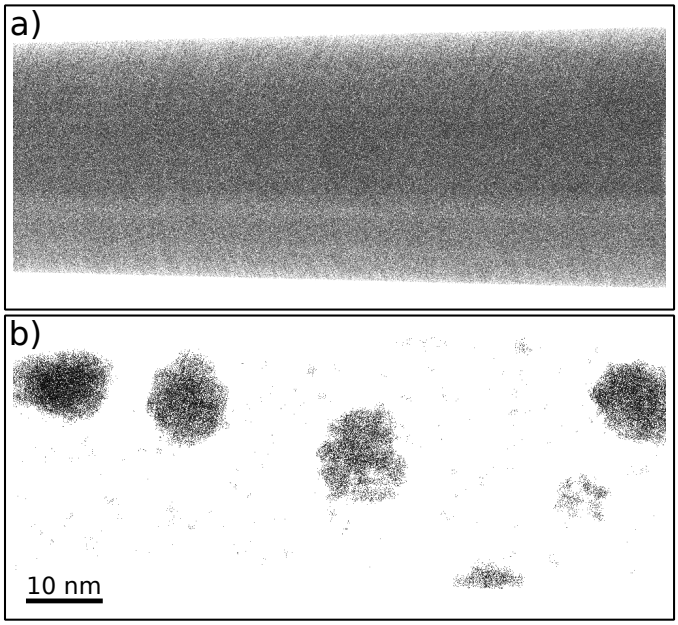

Figure 7.11:
APT reconstruction of an Al-Cu-Li alloy annealed for 1 hour at 160 °C; a) depicting all reconstructed atoms, b) depicting Li clusters with a local Li concentration of $\geq$ 15 at. %

in this respect correspond to a binomial distribution of Li atoms in the 100-atom clusters analyzed with the cluster finding algorithm, deviations from this binomial distribution indicate precipitation and clustering processes. Figure 7.12 shows the measured distribution of Li atoms in the 100-atom clusters as well as the ideal binomial distribution of a sample having the reconstructed overall Li composition. As can be seen, after an annealing treatment of 1 h at 160 °C, the demixing of the matrix is evident, statistically describing the already observed decomposition depicted in Figure 7.11. As can be seen, the precipitation of the δ' phase with a nominal composition of 25 at. % Li is visible in an icreased number of clusters around this composition and also, as a consequence, a decreased Li composition in the matrix.

In summary, the presented results demonstrate the analysis of precipitation processes in an Al-Cu-Li alloy by APT and more specific, its microstructure after an annealing treatment for 1 hour at 160 °C, clearly showing the presence of δ' precipitates with an average radius of 5.7 nm.

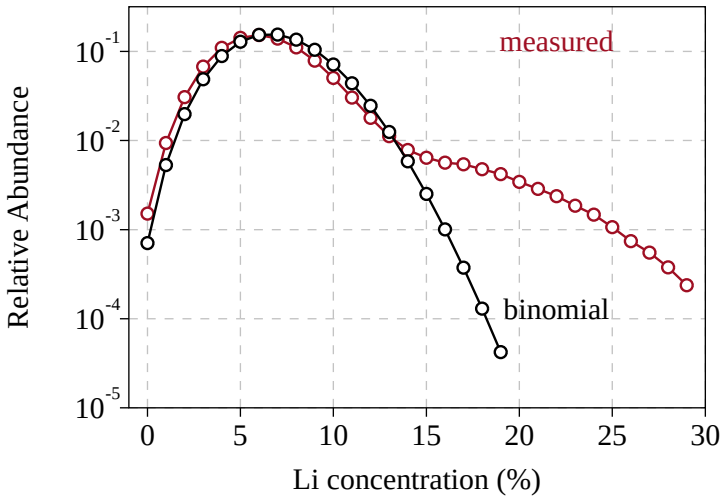

Figure 7.12:
Distribution of the Li concentration in 100-atom clusters for an ideal binomial distribution (black) and for the measured data obtained by APT (red) in the 1 h at 160 °C annealed condition; the results indicate a clear demixing/ decomposition of the matrix giving statistical insights into the qualitative observations shown in Figure 7.11

[1] S.C. Wang, M. Starink, *Int. Mater. Rev.* **50**, 193-215 (2005)

[2] T. Al-Kassab, H. Wollenberger, G. Schmitz, R. Kirchheim, *High Resolution Imaging and Spectrometry of Materials, Springer Verlag, Berlin* (2003)

7.7 Probing short-range order by differential scanning calorimetry in magnetic materials

M. Leitner, P. Neibecker, G. Benka[1], W. Petry
[1] E51, TUM, Garching, Germany

Intermetallic compounds are essential for today's engineering. Ever since the bronze age, their superior properties compared to pure elements, e.g. large creep resistance at low mass densities, have been recognized and utilized. These desired structural features are due to their ordered arrangement of atoms, which impedes dislocation movement. In addition to the long-range order corresponding to the structure being made up of sublattices with distinct elemental compositions, which is the defining property of intermetallic compounds, also short-range order, i.e. correlations between the occupations of nearby lattice sites that decay with distance, defines the state of a system. This short-range order can arise in a solid solution or in addition to the division of the lattice into sublattices. In contrast to long-range order, which is conveniently and regularly accessed for instance by powder diffraction, short-range order is a more elusive quantity. However, as the electronic structure of a material depends on the local arrangement of atoms, it is nonetheless of high relevance for the resulting macroscopic properties.

Magnetism in a multicomponent system is a case in point. In the picture of local-moment magnetism, the local moments interact with each other depending on the overlap of the respective electron wave-functions. Therefore, these interaction parameters vary characteristically as a function of distance, and can specifically take both positive and negative values as evidenced by the Bethe-Slater curve, which explains the occurrence of ferromagnetism or antiferromagnetism over the periodic system via the overlap of d-states between nearest neighbours.

The Heusler alloys of the Ni_2MnZ group, with Z either Al or Ga, are classified as magnetic shape-memory alloys, that is, samples of these materials have the potential to show macroscopic shape changes under an applied magnetic field. This is due to, first, a twinned structure on the microscopic scale with low twin boundary movement stresses, and second, a pronounced magnetic anisotropy, so that an external field leads to a growth of favourably oriented domains. In Ni_2MnGa, strains of up to 10% have been reported [1], while in Ni_2MnAl the low degree of $L2_1$-order limits both the achievable strain and suppresses ferromagnetism [2]. This can be understood by the fact that in B2-order, with a common disordered Mn/Al-sublattice, distances between the localized Manganese moments corresponding to both positive and negative interactions occur, leading to magnetic frustration.

We used differential scanning calorimetry (DSC) for investigating the behaviour of the critical temperature corresponding to the magnetical transition in a $Ni_{50}Mn_{28}Al_{22}$ polycrystalline sample. As evidenced by Fig. 7.13, the transition leads to a clear signal in the specific heat. We define the transition temperature as the cross-over between polynomials fitted to either side of the transition. Using an automated fitting procedure, the position of the transition temperature can be determined in independent measurements of the same state of a sample with a reproducibility of about $0.1\,\mathrm{K}$. Fig. 7.13 demonstrates that by an appropriate heat treatment the transition temperature of the sample can be changed by significant amounts. While after quenching from $1273\,\mathrm{K}$ into ice water the transition temperature is at $304\,\mathrm{K}$, it rises to $328\,\mathrm{K}$ after heat-treating the sample for $48\,\mathrm{h}$ at $673\,\mathrm{K}$.

A major advantage of using differential scanning calorimetry for determining the transition temperatures in our case is the experimental convenience in following their kinetic evolution thanks to the inherent ability of a DSC to apply well-defined heat-treatments. An example for this procedure is given in Fig. 7.14. It displays the evolution of the magnetic transition temperature during consecutive heat-treating steps.

We interpret the observed changes in the transition temperature as being due to different states of order in the sample. For Ni_2MnAl it is known that while the separation of Ni on the one hand

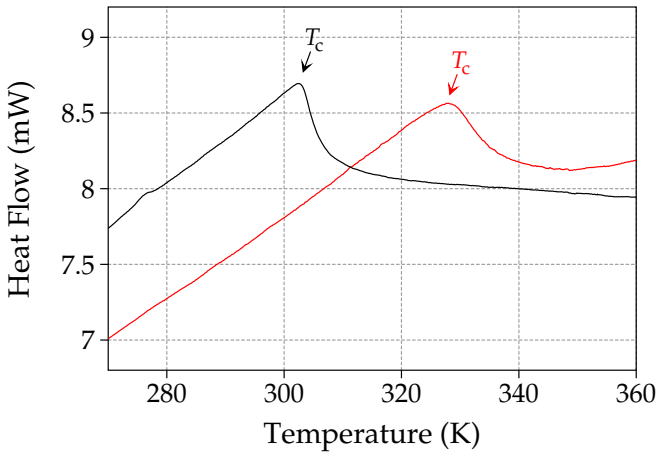

Figure 7.13:
DSC curves of a sample of $Ni_{50}Mn_{28}Al_{22}$ after quenching from 1273 K (black) and after heat-treating for 48 h at 673 K (red), measured upon heating with 10 K/min. Positive heat flow corresponds to endothermic behaviour.

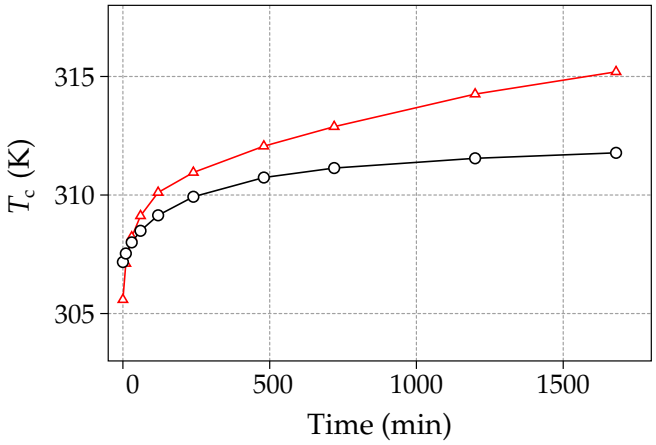

Figure 7.14:
Evolution of magnetic transition temperature starting from disordered state during heat-treating at 623 K (circles connected by black line) and 673 K (triangles connected by red line).

and Mn and Al on the other hand onto distinct sublattices leading to B2-order happens at high temperatures, the tendency for further separation of Mn and Al to achieve $L2_1$-order is much weaker and happens at lower temperatures, if at all. For our sample $L2_1$-order is not observed in any prepared state. Therefore, the order parameter that changes during the heat treatment applied here is short-range order corresponding to the arrangement of Mn and Al atoms, where a regular arrangement allows non-frustrated ferromagnetism and therefore leads to a higher transition temperature.

DSC measurements have been performed at the Materials Science Lab of the Heinz Maier-Leibnitz Zentrum (MLZ), Technische Universität München (TUM) in collaboration with A. Kriele.

[1] A. Sozinov, A. A. Likhachev, N. Lanska, K. Ullakko, *Appl. Phys. Lett.* **80**, 1746 (2002)

[2] M. Acet, E. Duman, E. F. Wassermann, L. Mañosa, A. Planes, *J. Appl. Phys.* **92**, 3867 (2002)

8 Teaching and outreach

8.1 Lectures, seminars and lab courses

Spring semester 2014

Prof. Dr. Peter Müller-Buschbaum, *Experimentalphysik 2 für MSE*
Prof. Dr. Peter Müller-Buschbaum, *Angewandte Physik: Polymerphysik 2*
Prof. Dr. Christine M. Papadakis, *Nanostructured Soft Materials II*
Prof. Dr. Peter Müller-Buschbaum, Prof. Dr. Christine M. Papadakis,
Seminar über Struktur und Dynamik kondensierter Materie
Prof. Dr. Peter Müller-Buschbaum, Prof. Dr. Christine M. Papadakis, *Seminar: Polymere*
Prof. Dr. Peter Müller-Buschbaum, Prof. Dr. Christine M. Papadakis,
Studentenseminar: Grundlegende Phänomene der Physik der weichen Materie
Prof. Dr. Peter Müller-Buschbaum, *Seminar: Aktuelle Probleme der organischen Photovoltaik*
Prof. Dr. Peter Müller-Buschbaum, Prof. Dr. Christine M. Papadakis,
Bachelor-Seminar: Funktionelle weiche Materialien
Prof. Dr. Winfried Petry, Prof. Dr. Peter Böni, Prof. Dr. Wolfgang Häußler,
Seminar über Neutronen in Forschung und Industrie
Prof. Dr. Winfried Petry, *Blockseminar Erasmus Mundus MaMaSELF Summerschool*

Fall semester 2014/2015

Prof. Dr. Peter Müller-Buschbaum, *Experimentalphysik 1 für MSE*
Prof. Dr. Peter Müller-Buschbaum, Dr. Ezzeldin Metwalli Ali, *Nanostructured Soft Materials 1*
Prof. Dr. Christine M. Papadakis: *Angewandte Physik: Polymerphysik 1*
Prof. Dr. Christine M. Papadakis: *Höhere Physik 1*
Prof. Dr. Peter Müller-Buschbaum, Prof. Dr. Christine M. Papadakis,
Seminar über Struktur und Dynamik kondensierter Materie
Prof. Dr. Peter Müller-Buschbaum, Prof. Dr. Christine M. Papadakis, *Seminar: Polymere*
Prof. Dr. Peter Müller-Buschbaum, Prof. Dr. Christine M. Papadakis,
Studentenseminar: Grundlegende Phänomene der Physik der weichen Materie
Prof. Dr. Peter Müller-Buschbaum, *Seminar: Aktuelle Probleme der organischen Photovoltaik*
Prof. Dr. Winfried Petry, Prof. Dr. Peter Böni, Prof. Dr. Wolfgang Häußler,
Seminar über Neutronen in Forschung und Industrie

Lab courses 2014

Theoretische und praktische Einführung in AFM (Fortgeschrittenenpraktikum)
Thermische Analyse (Fortgeschrittenenpraktikum)
Neutronenstreuung am FRM II (Fortgeschrittenenpraktikum)
JCNS Laboratory Course - Neutron Scattering (Forschungspraktikum)

8.2 Conferences and public outreach

W. Petry, A. Kastenmüller
Jubiläumsfeier: 10 Jahre Forschungs-Neutronenquelle Heinz Maier-Leibnitz (FRM II)
Technische Universität München
Garching, 12 March 2014

Sehr geehrte Damen und Herren, liebe Kolleginnen und Kollegen,

am 2. März 2014 begehen wir den 10. Jahrestag der Inbetriebnahme der Forschungs-Neutronenquelle Heinz Maier-Leibnitz (FRM II).

Sie sind mit dieser Forschungseinrichtung der Technischen Universität München auf verschiedene Weise und schon seit langen Jahren verbunden. Ihrem kontinuierlichen Engagement und Einsatz, Ihrer täglichen Arbeit ist der große Erfolg dieser Anlage bei Wissenschaftlern und industriellen Anwendern zu verdanken.

Aus diesem Anlass möchten wir Sie ganz herzlich zu unserer Festveranstaltung einladen.

Diese findet am Mittwoch, 12. März 2014 im Physik Department der Technischen Universität München in Garching statt.

Die Direktoren der

Forschungs-Neutronenquelle Heinz Maier-Leibnitz (FRM II)

Mittwoch, 12. März 2014 - Physik Department der TUM, Garching

15:00 – 16:30 Uhr **Begrüßungskaffee mit Kunstausstellung der 10. Jahrgangsstufe des Gymnasiums Garching**

16:30 – 17:30 Uhr **Begrüßungsansprachen**

Dr. Ludwig Spaenle, MdL
Bayerischer Staatsminister für Bildung und Kultus, Wissenschaft und Kunst

Dr. Edmund Stoiber
Bayerischer Ministerpräsident a.D.

Prof. Dr. Dr. h.c. mult. Wolfgang A. Herrmann
Präsident der TUM

Bundesministerium für Bildung und Forschung

Dr. Anton Kastenmüller
Technischer Direktor FRM II

17:30 – 18:30 Uhr **Wissenschaftliche Vorträge**

Prof. Dr. Jörg Kotzerke
Präsident der Deutschen Gesellschaft für Nuklearmedizin und Direktor der Klinik und Poliklinik für Nuklearmedizin des Universitätsklinikums Dresden *Carl Gustav Carus*

Aktuelle Forschung am MLZ
PD Dr. Christoph Hugenschmidt
Dr. Sebastian Mühlbauer
Dr. Tobias Schrader

18:30 Uhr **Ausklang der Veranstaltung mit Imbiss im Foyer des Physik Departments**

Um das Gelände der Technischen Universität München in Garching zu erreichen, nehmen Sie auf der Autobahn A9 die Abfahrt Garching Nord oder fahren mit der Linie U6 Richtung Garching Forschungszentrum bis zur Endstation.

Veranstaltungsort:

Physik Department der Technischen Universität München

James-Franck-Straße 1
85748 Garching

weitere Infos unter:

www.frm2.tum.de
www.mlz-garching.de

Kontakt:

Prof. Dr. Winfried Petry
Technische Universität München
Forschungs-Neutronenquelle
Heinz Maier-Leibnitz (FRM II)

E-Mail: frm2@frm2.tum.de
Telefon: 0049.(0)89.289.14688
0049.(0)89.289.13862

From left to right: Hannelore Gabor, the then-mayor of Garching; Dr. Karl-Eugen Huthmacher, Federal Ministry of Education and Research, Johanna Rumschöttl, head of the district of Munich, Dr. Hans Zehetmair, former Bavarian Minister for Science and Arts, Prof. Dr. Dr. h.c. mult. Wolfgang A. Herrmann, President of TUM, Dr. Ludwig Spaenle, Bavarian Minister for Education, Research and Arts, Dr. Anton Kastenmüller and Prof. Winfried Petry, the Technical respectively Scientific Director of FRM II, Dr. Wolfgang Heubisch, Bavarian Minister for Science and Arts from 2008 to 2013.

P. Müller-Buschbaum, W. Petry
Lehrerfortbildung 'Umwelt- und Geophysik'
38. Edgar-Lüscher-Seminar
Zwiesel, 28 – 30 March 2014

Programm

Freitag, 28. März 2014

13.00 - 14.30	Studienberatung der TUM	
15.00 - 15.30	Begrüßung	
15.30 - 16.45	**Klimawandel und Klimasimulationen**	*Dr. Ingo Kirchner, FU Berlin Institut für Meteorologie*
16.45 - 17.30	Diskussion und Kaffeepause	
17.30 - 18.15	**Regionale Klimasimulationen**	*Dr. Kai Radtke, BTU Cottbus LS Umweltmeteorologie*
18.45 - 19.00	Diskussion	

Samstag, 29. März 2014

09.00 - 10.15	**Naturkatastrophen und Klimawandel**	*Dipl.-Geophys. Ernst Rauch, Munich Re*
10.15 - 11.00	Diskussion und Kaffeepause	
11.00 - 12.15	**Ein Planet am Zittern – was uns seismisches Rauschen über das Erdinnere erzählt**	*Prof. Dr. Heiner Igel, LMU Erdbebendienst Bayern*
12.15 -12.30	Diskussion	
14.30 - 15.45	**Hochdruckforschung / Struktur des Erdinnern**	*Prof. Dr. Dan Frost, Bayerisches Geoinstitut, Universität Bayreuth*
15.45 - 16.30	Diskussion und Kaffeepause	
16.30 - 17.45	**Energiekonzepte der Zukunft**	*Prof. Dr. Hardo Bruhns, Arbeitskreis Energie der DPG*
17.45 - 18.00	Diskussion	

Sonntag, 30. März 2014

09.00 - 10.15	**Geologische Speicherung von CO_2 - Ein Beitrag zur Minderung der Treibhausgasemissionen?**	*Dr. habil. Axel Liebscher, Helmholtz-Zentrum Potsdam - Deutsches GeoForschungsZentrum GFZ*
10.15 - 11.00	Diskussion und Kaffeepause	
11.00 - 12.15	**Physik der Tsunami**	*Prof. Dr. Leo van Hemmen, TUM Physik*
12.15 - 13.00	Diskussion, Themenfindung für das 39. Seminar	

Organisation

Prof. Dr. Peter Müller-Buschbaum
TUM

Prof. Müller-Buschbaum ist Sprecher für das Netzwerk „Regenerative Energien (NRG)" in der Munich School of Engineering (MSE) der TU München, Leiter des KeyLabs „TUM.solar" im Forschungsnetzwerk „Solar Technologies Go Hybrid", Deutscher Vertreter bei der European Polymer Federation (EPF) für den Bereich Polymerphysik und Associate Editor der Zeitschrift „ACS Applied Materials & Interfaces" der „American Chemical Society" (ACS). Er befasst sich in seiner Forschungsarbeit mit der Entwicklung polymerbasierter Materialien mit neuartigen Struktur-Eigenschaftsbeziehungen.

Prof. Dr. Winfried Petry
TUM

Prof. Petry ist Ordinarius am Lehrstuhl für Funktionelle Materialien (E13) des Physik Departments der TU München, Betreuungsprofessor für die Bayerische Eliteakademie und Wissenschaftlicher Direktor der Forschungsneutronenquelle Heinz Maier-Leibnitz (FRM II). Er forscht auf dem Gebiet der Materialwissenschaften mit Neutronen.

Organisatorische Hinweise

Organisation vor Ort:

OStD Heribert Strunz,	*Gymnasium Zwiesel*
StD Wolfgang Achatz,	*Gymnasium Zwiesel*
OStR Christian Stoiber,	*Gymnasium Zwiesel*
StR Claus Starke,	*Gymnasium Zwiesel*

E-Mail:
luescherseminar@gymnasium-zwiesel.de

Hinweise:

- Alle Veranstaltungen finden in der Aula des Gymnasiums Zwiesel statt. Die Teilnehmer erhalten am Ende des Seminars für 5,- € eine CD mit sämtlichen Vorträgen.
- In den ausgewiesenen Kaffeepausen wird in der Mensa des Gymnasiums Kaffee und Kuchen gegen eine freiwillige Spende angeboten.
- Am Rande der Aula findet eine Ausstellung verschiedener Lehrmittelausstatter und Verlage statt.

Titelfoto: ©

38. Edgar-Lüscher-Seminar

Umwelt- und Geophysik

am Gymnasium Zwiesel

Freitag, 28. März 2014, bis Sonntag, 30. März 2014

Schirmherr:
Prof. Dr. Dr. h.c. mult. Wolfgang Herrmann, *Präsident der TUM*

Veranstalter:
Ltd. OStD, Anselm Räde
Ministerialbeauftragter für die Gymnasien in Niederbayern

Wissenschaftliche Leitung:
Prof. Dr. Peter Müller-Buschbaum, *TUM*
Prof. Dr. Winfried Petry, *TUM*

GYMNASIEN NIEDERBAYERN

C. M. Papadakis, A. Kyritsis
German-Greek Workshop: Structural methods for the investigation of responsive soft matter 2014
Garching, 12 – 16 May 2014

	Monday May 12, 2014	**Tuesday** May 13, 2014	**Wednesday** May 14, 2014	**Thursday** May 15, 2014	**Friday** May 16, 2014
	Faculty Club, IAS	Glass palace, FRM II		Glass palace, FRM II	Faculty Club, IAS
09.00-10:00	**A. Laschewsky:** Synthesis of thermoresponsive polymers	**A. Schulte:** Vibrational spectroscopy	***Lab course: FCS, DLS, SAXS, FTIR, computer simulations***	**V. Pipich:** Time-resolved small-angle neutron scattering	**P. Müller-Buschbaum:** Time-resolved neutron reflectometry
10:00-11.00	**C.M. Papadakis:** Phase behavior of thermoresponsive polymers	**A. Bausch:** Rheology on biopolymers		**S. Maccarrone:** Neutron spin-echo spectroscopy	**M. Zacharias:** Computer simulations on atomistic level
11.00-11.30	Coffee break	Coffee break		Coffee break	Coffee break
11.30-12.30	**A. Kyritsis:** Hydration of polymers and biomolecules	**S. Förster**: Small-angle X-ray scattering		**D. Aravopoulou:** Differential scanning calorimetry and modulated techniques **S. Koutsoumpis:** Dielectric relaxation spectrocopy	**A. Berezkin:** Computer simulations on mesoscopic level
12.30-13.30	Lunch break	Lunch break	Lunch break	Lunch break	Lunch
13.30-14.30	**D. Wöll:** Fluorescence correlation spectroscopy	***Lab course: FCS, DLS, SAXS, FTIR, computer simulations***	**Visit of Residenz in Munich, Conference Dinner**	**W. Petry:** Materials science with neutrons (Glaspalast at FRM II)	
14.30-15.30	**S. Filippov:** Dynamic light scattering			***Visit of FRM II***	
15.30-16.30	**M. Philipp:** Quasi-elastic neutron scattering				
16.30-18.00	***Poster session***				

D. Richter, W. Petry
MLZ review
Garching, 19 – 20 May 2014

The excellent results of the first MLZ review in May 2014 make smile both the reviewers - scientists from national and international universities and research institutes - and the directors of MLZ.

P. Müller-Buschbaum, C. M. Papadakis
Summer School Polymer Physics
Obertauern, Austria, 24 – 27 June 2014

E13 Summer School
Bergheim, Obertauern
24.-27.06.2014

	Tuesday, 24.06.2014	Wednesday, 25.06.2014	Thursday, 26.06.2014	Friday, 27.06.2014
09:00 - 10:30	Journey from Garching	XRR / NR	GISAXS / GISANS Conducting polymers	Computer simulation Thermo responsive polymers
10:30-11:00		Excursion and scientific discussions	Coffee break	Coffee break
11:00 - 12:30			Polymer based solar cells Hybrid solar cells	Polyelectrolytes
12:30-14:00	Lunch		Lunch	Lunch
14:00 - 15:30	SAXS / SANS Polymer crystallization		Discussion I	Presentation of Discussion II
15:30-16:00	Coffee break		Coffee break	Coffee break
16:00 - 17:30	Polymer blend films Block copolymer films		Discussion II	Journey to Garching
17:30-20:00	Dinner		Dinner	
20:00 - 22:00	GIWAXS	Poster	Presentation of Discussion I	

W. A. Herrmann, T. Hamacher, N. Adams, H. Gasteiger, W. Lang, M. Lienkamp, P. Müller-Buschbaum, H. Spliethoff, W. Wall
4th Colloquium of the Munich School of Engineering: Energy in motion
Garching, 3 July 2014

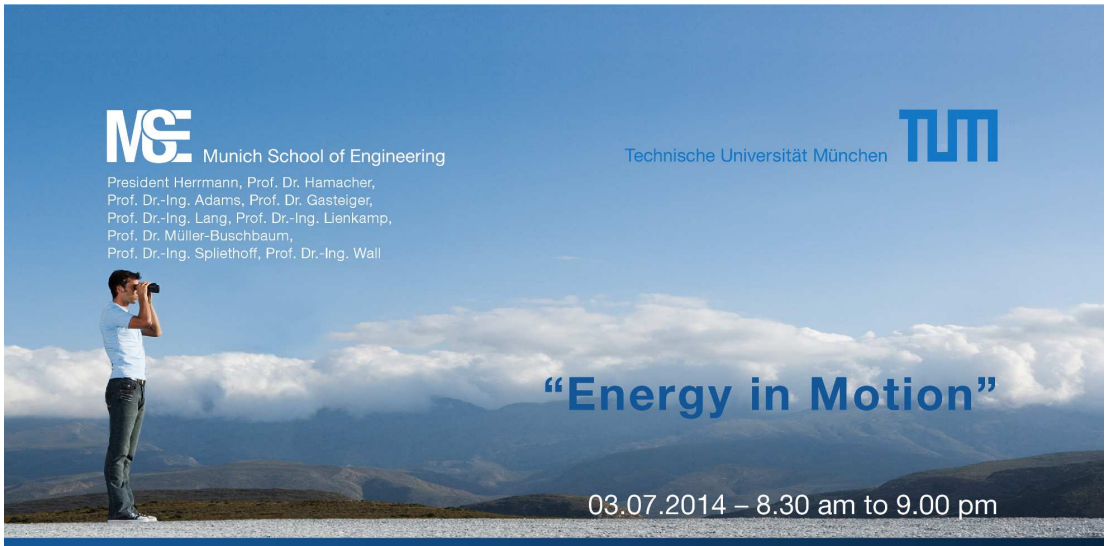

8.30 - 9.00 am
Registration

9.00 - 9.15 am
Opening
Hans Pongratz, TUM Senior Vice President
Thomas Hamacher, Director Munich School of Engineering

9.15 - 9.45 am
Keynote: Hydrogen Fuel Cell – Future-Oriented Technology for Long-Distance Electromobility
Tobias Brunner, BMW Group

9.45 - 11 .00 am
Session Chair: Markus Lienkamp, WZE MSE

Incentives for Energy-Efficient Behavior of Professional Drivers – An Empirical Investigation Using a Natural Field Experiment
Dominik Schall, Chair of Corporate Management, School of Management

e-MOBILie – From Concept Development to HiL Test Bench
Christian Kandler, Chair of Energy Economics and Application Technology

Bringing Limited Energy Resources to Market
Christoph Goebel, Chair for Application and Middleware Systems

11.00 - 11.45 am
Poster Presentation, Coffee Break

11.45 - 1.00 pm
Session Chair: Werner Lang, ZNB MSE

Integrating Requirement Analysis and Multi-Objective Optimization for Office Building Energy Retrofit Strategies
Yunming Shao, Institute for Energy Efficient Building and Design

Unified Device-Level Modeling Framework for Demand Scheduling
Andreas Veit, Chair for Application and Middleware Systems

Analysis of Potential Biomimetic Applications of Skin Analogies on the Building Shell
Leopoldo Saavedra, Institute for Energy Efficient Building and Design

1.00 - 2.30 pm
Poster Presentation, Lunch Break

2.30 - 3.45 pm
Session Chair: Peter Müller-Buschbaum, NRG MSE

Watching a Solar Cell Die – Structural Degradation in Polymer Solar Cells
Christoph Schaffer, Chair E13 for Experimental Physics

Hydrogen Oxidation Reaction in Alkaline Electrolytes on Pt/C Electrocatalysts: Mechanistic Aspects and Application in Fuel Cell Devices
Julien Durst, Chair of Technical Electrochemistry

Improved Knowledge of Wind Conditions for Wind Turbine and Wind Farm Control
Stefano Cacciola, Wind Energy Institute

3.45 - 4.30 pm
Poster Presentation, Coffee Break

4.30 - 5.45 pm
Session Chair: Hartmut Spliethoff, CPG MSE

Chemical Storage of Excess Electricity - Interdisciplinary Collaboration at TUM
Sebastian Fendt, Institute for Energy Systems

Analysis of a Sailwing Concept for Wind Turbine
Julie Piquee, Institute of Aerodynamics and Fluid Mechanics

Combined Heat and Power – Utilization of Geothermal Heat in ORC Processes
Dominik Meinel, Institute for Energy Systems

5.45 - 6.15 pm
Keynote: Coming Full Circle: Energy Research at a Synchrotron and Beyond
Alexander Hexemer, Lawrence Berkeley National Laboratory

6.15 - 6.30 pm
Summary of the Day

6.30 - 9.00 pm
Poster and Presentation Award, Colloquium Dinner

Location:
TUM – Institute for Advanced Study, Garching

Registration:
http://www.mse.tum.de

CEA, TUM
CEA TUM Kick-Off Meeting
Garching, 18 July 2014

The first CEA-TUM Meeting initiated by Jean-Claude Perraudin and Daniel Iracane, Ambassador respectively Director of International Affairs at the French Alternative Energies and Atomic Energy Commission (CEA) and by President Wolfgang A. Herrmann and Hannemor Keidel, TUM. Scientists from CEA-LITEN und the Munich School of Engineering (TUM) discuss the opportunities of a collaboration in the field of renewable energies.

P. Müller-Buschbaum (TUM), A. Hexemer (ALS Berkeley, USA)
Grazing Incidence Surface Techniques
Microsymposium held at the 23rd Congress and General Assembly of the International Union of Crystallography
Montreal, Canada, 9 August 2014

Program

MS56 9 August 2014
Intro by Co-chair(s) (5') **9:40** 9:45 **68526** Grazing Incidence Surface Techniques 520def

1 (Invited - 30') **9:45** 10:15 **ROTH Stephan** DESY, Hamburg, Germany
In-situ grazing incidence scattering in information and communication technology

2 (Invited - 30') **10:15** 10:45 **YAGER Kevin** Brookhaven National Laboratory, NY, USA
Grazing-Transmission Scattering for Measuring Nano-structured Thin Films

3 (Submitter - 20') **10:45** 11:05 **PAPADAKIS Christine** TUM, Munich, Germany
Vapor Treatment of Block Copolymer Thin Films: GISAXS and Simulations

4 (Submitter - 20') **11:05** 11:25 **SAKURAI Kenji** National Inst. Mat. Sci., Tsukuba, Japan
Realtime X-ray reflectometry to see changes at buried interfaces

5 (Submitter - 20') **11:25** 11:45 **MATRINGE Caroline** Centre Céramique, Limoges, France
Self-ordering on vicinal surfaces studied by 3D GISAXS measurements

6 (Invited - 30') **11:45** 12:15 **TORIKAI Naoya** Mie University, Tsu, Japan
In-Situ Neutron Reflectometry on Polymer Thin Films in Different Environments

V. K. Peterson (ANSTO, Australia), C. M. Papadakis (TUM)
In Operando and Structure Evolution - from Atomic to Micron
Microsymposium held at the 23rd Congress and General Assembly of the International Union of Crystallography
Montreal, Canada, 10 August 2014

Program

1.50 pm: Andrew J. Allen, National Institute of Standards, U.S.A. (invited)
Towards in operando material process characterization
over many length scales

2.20 pm: Toru Ishigaki, Ibaraki University, Japan (invited)
In operando and wide-*d* neutron diffraction measurements at J-Parc

2.50 pm: Kamila Wiaderek, Argonne National Laboratory, U.S.A.
From atoms to electrodes:
Mesoscale effects in electrochemical conversion

3.10 pm: Peter Müller-Buschbaum, TU München, Germany
In-operando study of swelling and switching
of thermo-responsive polymer films

3.30 pm: Eric Dooryhee, Brookhaven National Laboratory, U.S.A.
Tracking cation migration in catalysts by
modulated enhanced powder diffraction

3.50 pm: Ezzeldin Metwalli, TU München, Germany (invited)
Growth kinetics of metal nanoparticles on solid surfaces

A. P. Eggert (VDI Materials Engineering), W. Petry (TUM), R. Gilles (TUM)
VDI-TUM Expertenforum: Zerstörungsfreie Prüfung für die Mobilität und Energie der Zukunft
Garching, 11 September 2014

Since 2004 the VDI-TUM experts' meeting jointly organized by Verein Deutscher Ingenieure (VDI) and TUM has been addressing different aspects of the use of neutrons for industrial applications. In 2014 the 5th meeting focussed on nondestructive tests for the future mobility and energy.

P. Müller-Buschbaum
Lehrerfortbildung 'Die Energiewende'
Edgar-Lüscher-Lectures
Dillingen, 29 September – 1 October 2014

EDGAR–LÜSCHER–LECTURES DILLINGEN/DONAU 2014
Thema: Die Energiewende
Datum: Montag, 29. September bis Mittwoch, 01. Oktober 2014
Tagungsort: Akademie für Lehrerfortbildung Dillingen
Veranstalter: Akademie für Lehrerfortbildung Dillingen und TU München
wissenschaftliche Leitung: Prof. Dr. Peter Müller-Buschbaum,
Technische Universität München.

Programm

Montag, 29. 09. 2014
15:00 – 15:30 Begrüßung
StD Werner Ettinger / Prof. Dr. Peter Müller-Buschbaum (Physik-Department TUM)

15:30 – 17:00 Prof. Dr. Thomas Hamacher, TUM MSE
Die Energiewende in Bayern

18:30 – 20:00 Prof. Dr. Jürgen H. Werner, Universität Stuttgart, Institut für Photovoltaik
Silizium-basierte Photovoltaik

Dienstag, 30. 09. 2014
8:30 – 10:00 Prof. Dr. Vladimir Dyakonov, University of Würzburg
Organische Photovoltaik

10:00 – 10.30 Kaffeepause

10:30 – 12:00 Jennifer Strunk, Nachwuchsgruppenleiterin Ruhr-Universität Bochum
Photokatalyse für die Energieumwandlung

15:30 – 17:00 Dr. Gerhard Luther, Universität des Saarlandes, Experimentalphysik
Das Zusammenwirken von PSKW - artigen und P2G - artigen Energiespeichern und die mögliche Rolle von Tiefschachtspeichern bei der Energiewende

18:30 – 20:00 Dr. Christoph Hackl, TUM MSE
Windenergie

Mittwoch, 01. 10. 2014
8:30 – 10:00 Dipl.-Ing. Steffen Kahlert, TUM Fakultät für Maschinenwesen
Flexible Kraftwerke

10:00 – 10.30 Kaffeepause

10:30 – 12:00 Prof. Dr. Hartmut Zohm, Max-Planck-Institut für Plasmaphysik, Garching
Status und Perspektive von Fusionsreaktoren

Ab 12:00 Lehrgangsabschluss
Prof. Dr. Peter Müller-Buschbaum / StD Werner Ettinger

8.3 Service to the community

Prof. Dr. Peter Müller-Buschbaum:

- since 11/2012 member of „Peer Review Panel 3 – Surfaces & Interfaces“ of „Diamond Light Source Ltd“
- since 9/2012 Associate Editor of journal 'ACS Applied Materials & Interfaces' of the American Chemical Society
- since 1/2012 member of the Scientific Selection Panel of the Helmholtz-Zentrum Berlin für Materialien und Energie (HZB)
- since 2011 member of European Spallation Source (ESS) Scientific Advisory Panel (Reflecfivity)
- since 2011 German representative at the European Polymer Federation (EPF) for polymer physics
- since 2011 elected member of '9th Committee Research with Synchrotron Radiation (KFS)', section user matters
- since 2010 spokesman of the regenerative engergies section (NRG) at the Munich School of Engineering (MSE) of TU Munich
- since 2010 member of TUM Energie at TU Munich
- since 2010 spokesman of the energy section at the Physics Department/TU Munich
- since 2010 German representative at the ESUO European Synchrotron User Organization
- since 2008 chairman of 'HASYLAB User Committee (HUC)' at the synchrotron radiation laboratory HASYLAB in Hamburg

Prof. Dr. Christine Papadakis:

- since 9/2014 Regional Editor Europe for Colloid & Polymer Science, Springer
- member of the Project Review Panel 5: 'Soft Condensed Matter/Scattering' at DESY Photon Science, Hamburg
- member of the subcommittee 'College 9: Structure And Dynamics Of Soft-Condensed Matter' at Laue-Langevin Institute (ILL), Grenoble, France
- deputy women's representative of the Physics Department at TU München

Prof. Dr. Winfried Petry:

- since 1999 liaison professor of Bayerische Eliteakademie (Bavarian Leadership Academy) and since May 2011 member of the curatorium
- since 2005 Board member of the 'Deutsches Atomforum e.V.' (DAtF e.V.), since May 2014 Vice President of DAtF
- since 2007 member of the Steering Comittee of the Laue Langevin Institute and chairman of the instrumentation review panel of the CEA Leon Brillouin Laboratory

9 Publications, talks and funding

9.1 Publications

- R. Aleksandrova, M. Philipp, U. Müller, R. Jiménez Riobóo, M. Ostermeyer, R. Sanctuary, P. Müller-Buschbaum, J. K. Krüger
Phase instability and molecular kinetics provoked by repeated crossing of the demixing transition of PNIPAM solutions
Langmuir **30**, 11792-11801 (2014)

- G. Benecke, W. Wagermaier, C. Li, M. Schwartzkopf, G. Flucke, R. Hoerth, I. Zizak, M. Burghammer, E. Metwalli, P. Müller-Buschbaum, M. Trebbin, S. Förster, O. Paris, S. V. Roth, P. Fratzl
A customizable software for fast reduction and analysis of large X-ray scattering data sets: applications of the new DPDAK package to small-angle X-ray scattering and grazing-incidence small-angle X-ray scattering
J. Appl. Cryst. **47**, 1797-1803 (2014)

- H. Breitkreutz, A. Röhrmoser, W. Petry
Influence of depleted Molybdenum on monolithic UMo fuel plate designs for FRM II
Transactions of RRFM 2014, Ljubljana, Slovenia (2014)

- H. Ceeh, J.-A. Weber, C. Hugenschmidt, M. Leitner, P. Böni
Positron beam optics for the 2D-ACAR spectrometer at the NEPOMUC beamline
J. Phys. Conf. Ser. **505**, 012041 (2014)

- H.-Y. Chiang, M. Döblinger, S.-H. Park, L. Beck, W. Petry
Ion beam induced spinodal decomposition and amorphization in the immiscible bilayer system UMo/Mg
J. Nucl. Mater. **453**, 41-47 (2014)

- M. A. Dyakonova, N. Stavrouli, M.-T. Popescu, K. Kyriakos, I. Grillo, M. Philipp, S. Jaksch, C. Tsitsilianis, C. M. Papadakis
Physical hydrogels via charge driven self-organization of a triblock polyampholyte - rheological and structural investigations
Macromolecules **47**, 7561-7572 (2014)

- B. Elgh, N. Yuan, H. Sung Cho, D. Magerl, M. Philipp, S. V. Roth, K. Byung Yoon, P. Müller-Buschbaum, O. Terasaki, A. E. C. Palmqvist
Controlling morphology, mesoporosity, crystallinity, and photocatalytic activity of ordered mesoporous TiO_2 films prepared at low temperature
APL Materials **2**, 113313 (2014)

- V. S. Gevaerts, E. M. Herzig, M. Kirkus, K. H. Hendriks, M. M. Wienk, J. Perlich, P. Müller-Buschbaum, R. A. J. Janssen
Influence of the position of the side chain on crystallization and solar cell performance of DPP-based small molecules
Chem. Mat. **26**, 916-926 (2014)

- S. Guo, C. Brandt, T. Andreev, E. Metwalli, W. Wang, J. Perlich, P. Müller-Buschbaum
First step into space: performance and morphological evolution of P3HT:PCBM bulk heterojunction solar cells under AM0 illumination
ACS Appl. Mater. Interfaces **6**, 17902-17910 (2014)

- S. Guo, E. M. Herzig, A. Naumann, G. Tainter, J. Perlich, P. Müller-Buschbaum
Influence of solvent and solvent additive on the morphology of PTB7 films probed via x-ray scattering
J. Phys. Chem. B **118**, 344-350 (2014)

- S. Guo, J. Ning, V. Körstgens, Y. Yao, E. M. Herzig, S. V. Roth, P. Müller-Buschbaum
The effect of fluorination in manipulating the nanomorphology in PTB7:$PC_{71}BM$ bulk heterojunction systems
Adv. Energy. Mater. **5**, 1401315 (2014)

- S. Jaksch, A. Schulz, K. Kyriakos, J. Zhang, I. Grillo, V. Pipich, R. Jordan, C. M. Papadakis
The collapse and aggregation of thermoresponsive poly(2-oxazoline) gradient copolymers: A time-resolved SANS study
Colloid Polym. Sci. **292**, 2413-2425 (2014)

- M. Koenig, D. Magerl, M. Philipp, K.-J. Eichhorn, M. Müller, P. Müller-Buschbaum, M. Stamm, P. Uhlmann
Nanocomposite coatings with stimuli-responsive catalytic activity
RSC Advances **4**, 17579-17586 (2014)

- V. Körstgens, M. Philipp, D. Magerl, M. A. Niedermeier, G. Santoro, S. V. Roth, P. Müller-Buschbaum
Following initial changes in nanoparticle films under laminar flow conditions with in-situ GISAXS microfluidics
RSC Advances **4**, 1476-1479 (2014)

- K. Kyriakos, D. Aravopoulou, L. Augsbach, J. Sapper, S. Ottinger, C. Psylla, A. Aghebat Rafat, C. A. Benitez-Montoya, A. Miasnikova, Z. Di, A. Laschewsky, P. Müller-Buschbaum, A. Kyritsis, C. M. Papadakis
Novel thermoresponsive block copolymers having different architectures – structural, rheological, thermal, and dielectric investigations
Colloid Polym. Sci. **292**, 1757-1774 (2014)

- K. Kyriakos, M. Philipp, J. Adelsberger, S. Jaksch, A. V. Berezkin, D. M. Lugo, W. Richtering, I. Grillo, A. Miasnikova, A. Laschewsky, P. Müller-Buschbaum, C. M. Papadakis
Cononsolvency of water/methanol mixtures for PNIPAM and PS-b-PNIPAM: Pathway of aggregate formation investigated using time-resolved SANS
Macromolecules **47**, 6867-6879 (2014)

- M. Leitner, A. Mikikits-Leitner
Nonlinear differential identities for cnoidal waves
Math. Nachr. **287**, 2040–2056 (2014)

- E. Metwalli, I. Krisch, I. Markovits, M. Rawolle, M. A. Ruderer, S. Guo, S. Wyrzgol, A. Jentys, J. Perlich, J. A. Lercher, P. Müller-Buschbaum
Polymer coated PtCo nanoparticles deposited on diblock copolymer templates: Chemical selectivity versus topographical effects
Chem. Phys. Chem. **15**, 2236-2239 (2014)

- P. Müller-Buschbaum
The active layer morphology of organic solar cells probed with grazing incidence scattering techniques (invited progress report)
Adv. Mater. **26**, 7692-7709 (2014)

- P. Müller-Buschbaum, G. Kaune, M. Haese-Seiler, J.-F. Moulin
Morphology determination of defect-rich diblock copolymer films with time-of flight grazing incidence small angle neutron scattering
J. Appl. Cryst. **47**, 1228-1237 (2014)

- P. Neibecker, M. Leitner, G. Benka, W. Petry
Increasing the achievable state of order in Ni-based Heusler alloys via quenched-in vacancies
Appl. Phys. Lett. **105**, 261904 (2014)

- J. Neuhaus, M. Leitner, K. Nicolaus, W. Petry, B. Hennion, A. Hiess
Role of vibrational entropy in the stabilization of the high-temperature phases of iron
Phys. Rev. B **89**, 184302 (2014)

- P. Nugent, T. Pham, K. McLaughlin, P.-A. Georgiev, W. Lohstroh, J.-P. Embs, M.-J. Zaworotko, B. Space, J. Eckert
Dramatic effect of pore size reduction on the dynamics of hydrogen adsorbed in metal-organic materials
J. Mater. Chem. A **2**, 13884-13891 (2014)

- C. M. Palumbiny, C. Heller, C. J. Schaffer, V. Körstgens, G. Santoro, S. V. Roth, P. Müller-Buschbaum
Molecular reorientation and structural changes in cosolvent-treated highly conductive PEDOT:PSS electrodes for flexible indium tin oxide-free organic electronics
J. Phys. Chem. C. **181**, 13598-13606 (2014)

- C. M. Papadakis, P. Košovan, W. Richtering, D. Wöll
Polymers in focus: Fluorescence correlation spectroscopy
Colloid Polym. Sci. **292**, 2399-2411 (2014)

- A. Paul, N. Paul, P. Müller-Buschbaum, A. Bauer, P. Böni
Superparamagnetic regular nanopillar-like structures studied by grazing incidence X-ray scattering: effect of vertical correlation
J. Appl. Cryst. **47**, 1056-1076 (2014)

- T. Pfadler, M. Coric, C. M. Palumbiny, A. C. Jakowetz, K.-P. Strunk, J. A. Dorman, P. Ehrenreich, C. Wang, A. Hexemer, R. Q. Png, P. K. H. Ho, P. Müller-Buschbaum, J. Weickert, L. Schmidt-Mende
Influence of interfacial area on exciton separation and polaron recombination in nanostructured bilayer all-polymer solar cells
ACS Nano **8**, 12397-12409 (2014)

- T. Pham, K.-A. Forrest, J. Eckert, P.-A. Georgiev, A. Mullen, R. Luebke, A.-J. Cairns, Y. Belmabkhout, J.-F. Eubank, K. McLaughlin, W. Lohstroh, M. Eddaoudi, B. Space
Investigating the gas sorption mechanism in an rht-metal-organic framework through computational studies
J. Phys. Chem. C **118**, 439-456 (2014)

- T. Pham, K.-A. Forrest, P.-A. Georgiev, W. Lohstroh, D.-X. Xue, A. Hogan, M. Eddaoudi, B. Space, J. Eckert
A high rotational barrier for physisorbed hydrogen in an fcu-metal-organic framework
Chem. Commun. **50**, 14109-14112 (2014)

- M. Philipp, R. Aleksandrova, U. Müller, M. Ostermeyer, R. Sanctuary, P. Müller-Buschbaum, J. K. Krüger
Molecular versus macroscopic perspective on the demixing transition of aqueous PNIPAM solutions by studying the dual character of the refractive index
Soft Matter **10**, 7297-7305 (2014)

- M. Philipp, K. Kyriakos, L. Silvi, W. Lohstroh, W. Petry, J. K. Krüger, C. M. Papadakis, P. Müller-Buschbaum
From molecular dehydration to excess volumes of phase-separating PNIPAM solutions
J. Phys. Chem. B **118**, 4253-4260 (2014)

- C. Pistidda, D. Pottmaier, F. Karimi, S. Garroni, A. Rzeszutek, M. Tolkiehn, M. Fichtner, W. Lohstroh, M. Baricco, T. Klassen, M. Dornheim
Effect of NaH/MgB_2 - ratio on the hydrogen absorption kinetics of the system $NaH+ MgB_2$
Int. J. Hydrogen Energy **39**, 5030-5036 (2014)

- N. V. Pogodina, T. Amann, C. Dold, E. Metwalli, P. Müller-Buschbaum, A. Kailer, C. Friedrich
Triborheology and orientational dynamics of ionic liquid crystals
J. Mol. Liq. **192**, 118-126 (2014)

- M. Reihle, M. Hofmann, U. Wasmuth, W. Volk, H. Hoffmann, W. Petry
In situ strain measurements during casting using neutron diffraction
Materials Science Forum **768-769**, 484-491 (2014)

- M. Ross, M. Stana, M. Leitner, B. Sepiol
Direct observation of atomic network migration in glass
New J. Phys. **16**, 093042 (2014)

- G. Santoro, A. Buffet, R. Döhrmann, S. Yu, V. Körstgens, P. Müller-Buschbaum, U. Gedde, M. Hedenqvist, S. V. Roth
Use of intermediate focus for grazing incidence small and wide angle x-ray scattering experiments at the beamline P03 of PETRA III, DESY
Rev. Sci. Instrum. **85**, 043901 (2014)

- S. Säubert, R. Jungwirth, T. Zweifel, H.-Y. Chiang, H. Breitkreutz, W. Petry *Isothermal transformation kinetics in uranium molybdenum alloysIsothermal transformation kinetics in uranium molybdenum alloys*
Transactions of RRFM 2014, Ljubljana, Slovenia (2014)

- K. Sarkar, E. V. Braden, T. Fröschl, N. Hüsing, P. Müller-Buschbaum
Spray-deposited zinc titanate films obtained via sol-gel synthesis for application in dye-sensitized solar cells
J. Mater. Chem. A **2**, 15008-15014 (2014)

- K. Sarkar, E. V. Braden, S. Pogorzalek, S. Yu, S. V. Roth, P. Müller-Buschbaum
Monitoring structural dynamics of in-situ spray-deposited zinc oxide films for application in dye-sensitized solar cells
Chem. Sus. Chem. **7**, 2140-2147 (2014)

- K. Sarkar, M. Rawolle, M. A. Niedermeier, W. Wang, E. M. Herzig, V. Körstgens, A. Buffet, S. V. Roth, P. Müller-Buschbaum
  A quantitative approach to tune metal oxide network morphology based on grazing incidence small angle x-ray scattering investigations
  J. Appl. Cryst. **47**, 76-83 (2014)

- K. Sarkar, C. J. Schaffer, D. Moseguí González, A. Naumann, J. Perlich, P. Müller-Buschbaum
  Tuning pore size of ZnO nano-grids via time-dependent solvent annealing
  J. Mater. Chem. A **2**, 6946-6951 (2014)

- R. Schenk, W. Petry, B. Stepnik, M. Grasse, G. Bourdat, C. Moyroud, C. Coullomb, C. Jarousse
  FRM II/CERCA UMo-atomizer project progress
  Transactions of RRFM 2014, Ljubljana, Slovenia (2014)

- W. Schmid, S. Dirndorfer, H. Juranowitsch, M. Kress, W. Petry *Adhesion strength of sputter desposited diffusion barrier layer coatings fort he use of U-Mo nuclear fuels* Nuclear Engineering and Design **276**, 115-12 (2014)

- A. Schönhals, C. M. Papadakis
  Special issue in honor of Friedrich Kremer
  Colloid Polym. Sci. **292**, 1735-1736 (2014)

- A. Schulz, S. Jaksch, R. Schubel, E. Wegener, Z. Di, Y. Han. A. Meister, J. Kressler, A. Kabanov, R. Luxenhofer, C. M. Papadakis, R. Jordan
  Drug-induced morphology switch in drug delivery systems based on poly(2-oxazoline)s
  ACS Nano **8**, 2686-2696 (2014)

- A. Sepe, Z. Rong, M. Sommer, Y. Vaynzof, X. Sheng, P. Müller-Buschbaum, D.-M. Smilgies, Z.-K. Tan, L. Yang, R. H. Friend, U. Steiner, S. Hüttner
  Structure formation in P3HT/F8TBT blends
  Energy Environ. Sci. **7**, 1725-1736 (2014)

- B. Stepnik, M. Grasse, C. Coullomb, C. Jarousse, D. Geslin, W. Petry, R. Jungwirth, H. Breitkreutz, A. Röhrmoser, T. Huber, D. Wachs
  UMo monolithic fuel development progress in CERCA-AREVA
  Transactions of RRFM 2014, Ljubljana, Slovenia (2014)

- J. Swenson, K. Elamin, G. Chen, W. Lohstroh, V. Garcia Sakai
  Anomalous dynamics of aqueous solutions of di-propylene glycol methylether confined in MCM-41 by quasielastic neutron scattering
  J. Chem. Phys. **141**, 214501 (2014)

- R. Tietze, H. Unterweger, B. Weigl, S. Lyer, N. Taccardi, P. Kudejova, L. Canella, F. M. Wagner, W. Petry, C. Alexiou
  Boron containing magnetic nanoparticles for neutron capture therapy: An innovative approach for specifically targeting tumors
  Proceedings of International Congress on Neutron Capture Therapy, Helsinki, Finland (2014)

- J. Wang, W. H. de Jeu, U. Ziener, M. S. Polinskaya, S. A. Ponomarenko, U. Rücker, M. A. Ruderer, E. M. Herzig, P. Müller-Buschbaum, M. Möller, A. Mourran
Monolayer properties of asymmetrically substituted sexithiophene
Langmuir **30**, 2752-2760 (2014)

- J.-A. Weber, P. Böni, H. Ceeh, M. Leitner, C. Hugenschmidt
The effect of regularization on the reconstruction of ACAR data
J. Phys. Conf. Ser. **505**, 012047 (2014)

- S. Wellert, Y. Hertle, M. Richter, M. Medebach, D. Magerl, W. Wang, B. Deme, A. Radulescu, P. Müller-Buschbaum, T. Hellweg, R. von Klitzing
Inner structure of adsorbed ionic microgel particles
Langmuir **30**, 7168-7176 (2014)

- Y. Yao, E. Metwalli, J.-F. Moulin, B. Su, M. Opel, P. Müller-Buschbaum
Self-assembly of diblock copolymer-maghemite nanoparticle hybrid thin films
ACS Appl. Mater. Interfaces **6**, 18152 (2014)

- Y. Yao, E. Metwalli, M. A. Niedermeier, M. Opel, C. Lin, J. Ning, J. Perlich, S. V. Roth, P. Müller-Buschbaum
Nano- and microstructures of magnetic field guided maghemite nanoparticles in diblock copolymer films
ACS Appl. Mater. Interfaces **6**, 5244-5254 (2014)

- Y. Xiao, X. Wang, Y. Xia, Y. Yao, E. Metwalli, Q. Zhang, R. Liu, B. Qiu, M. Rasool, Z. Liu, J. Meng, L.-D. Sun, C.-H. Yan, P. Müller-Buschbaum, Y.-J.Cheng
Green facile scalable synthesis of titania/carbon nanocomposites: New use of old dental resins
ACS Appl. Mater. Interfaces **6**, 18461 (2014)

- J. Zhang, D. Posselt, D.-M. Smilgies, J. Perlich, K. Kyriakos, S. Jaksch, C. M. Papadakis
Lamellar diblock copolymer thin films during solvent vapor annealing studied by GISAXS: Different behavior of parallel and perpendicular lamellae
Macromolecules **47**, 5711-5718 (2014)

- J. Zhang, D. Posselt, D.-M. Smilgies, J. Perlich, K. Kyriakos, S. Jaksch, C. M. Papadakis
Complex macrophase-separated nanostructure induced by microphase separation in binary blends of lamellar diblock copolymer thin films
Macromol. Rapid Commun. **35**, 1622-1629 (2014)

- P. Ziegler, N. Paul, P. Müller-Buschbaum, B. Wiedemann, W. Kreuzpaintner, J. Jutimoosik, R. Yimnirun, A. Setzer, P. Esquinazi, P. Böni, A. Paul
Self-organization of Fe clusters on mesoporous TiO_2 templates
J. Appl. Cryst. **47**, 1921-1930 (2014)

- T. Zweifel, C. Valot, Y. Pontillon, J. Lamontagne, A. Vermersch, L. Barallier, T. Blay, H. Palancher, W. Petry
Annealing test of in-pile irradiated oxide coated U-Mo/Al-Si dispersed nuclear fuel J. Nuclear Materials **452**, 533-547 (2014)

- T. Zweifel, C. Valot, Y. Pontillon, J. Lamontagne, T. Blay, W. Petry, H. Palancher *In-pile irradiated U-Mo/Al(Si) dispersed nuclear fuel behaviour under thermal annealing: fission gas release and microstructure evolutions*
Transactions of RRFM 2014, Ljubljana, Slovenia (2014)

9.2 Talks

- A. Berezkin
  Computer simulations on mesoscopic level
  German-Greek Workshop 'Structural methods for the investigation of soft responsive matter 2014', Garching, 12-16 May 2014

- A. Berezkin
  Computer simulations on mesoscopic level
  Polymer Physics Summer School, Obertauern, Austria, 24 – 27 Jun 2014

- L. Biessmann, M. Dyakonova
  Polyelectrolytes
  Polymer Physics Summer School, Obertauern, Austria, 24 – 27 Jun 2014

- A. Campanella, H. Frielinghaus
  Telechelic polymers and magnetic nanoparticles nanocomposites thin dry film and hydrogels
  DPG Frühjahrstagung, Dresden, 30 Mar – 4 Apr 2014

- A. Campanella, H. Frielinghaus
  HEUR polymers and magnetic nanoparticles nanocomposites: thin dry films and hydrogels
  SoftComp Annual Meeting 2014, Heraklion, Greece, 26 – 29 May 2014

- A. Campanella, H. Frielinghaus
  HEUR polymers and magnetic nanoparticles nanocomposites:thin dry films and hydrogels
  XXV Annual Meeting Italian Society for Neutron Spectroscopy (SISN), Naples, Italy, 3 – 4 Jul 2014

- R. Hengstler-Eger, P. B. Hoffmann, M. A. Krik, W. Petry
  The effect of external stress on ion irradiation-induced c-loop
  TMS2014 Annual Meeting, San Diego, USA, 16 – 20 Feb 2014

- V. Körstgens, S. V. Roth, P. Müller-Buschbaum
  Following structural changes in nanoparticle films with in-situ GISAXS microfluidics
  DESY Photon Science Users' Meeting, satellite meeting: Status and Perspectives of Small Angle X-ray Scattering at DESY, Hamburg, 29 – 31 Jan 2014

- V. Körstgens, M. Philipp, D. Magerl, M. A. Niedermeier, J. Schlipf, L. Song, G. Santoro, V. Haramus, S. V. Roth, P. Müller-Buschbaum
  Following structural changes in nanoparticle films under laminar flow conditions with in-situ SAXS microfluidics
  DPG Frühjahrstagung, Dresden, 30 Mar – 4 Apr 2014

- V. Körstgens
  MicroGISAXS and microfluidics
  Seminar Physical Chemistry Lund University, Lund, Sweden, 10 Apr 2014

- V. Körstgens
  X-ray and neutron reflectivity
  Polymer Physics Summer School, Obertauern, Austria, 24 – 27 Jun 2014

- V. Körstgens, M. Philipp, D. Magerl, S. V. Roth, P. Müller-Buschbaum
  Microfluidics and microGISAXS - in situ characterization at the solid-liquid interface
  SNI Tagung, Bonn, 21 – 23 Sep 2014

- J. K. Krüger, M. Philipp, U. Müller
  Dynamical volume expansion coefficients studied during isothermal polymerization of epoxies using Temperature Modulated Optical Refractometry
  Polydays 2014, Berlin, 30 Sep – 2 Oct 2014

- K. Kyriakos, N. Vishnevetskaya
  Thermoresponsive polymers
  Polymer Physics Summer School, Obertauern, Austria, 24 – 27 Jun 2014

- K. Kyriakos, M. Philipp, J. Adelsberger, S. Jaksch, I. Grillo, A. Miasnikova, A. Laschewsky, P. Müller-Buschbaum, C. M. Papadakis
  Cononsolvency in P(S-b-NIPAM) diblock copolymers - a time-resolved SANS study
  Third International Workshop Studying Kinetics with Neutrons, Grenoble, France, 24 – 27 Mar 2014

- K. Kyriakos, M. Philipp, J. Adelsberger, S. Jaksch, I. Grillo, A. Miasnikova, A. Laschewsky, P. Müller-Buschbaum, C. M. Papadakis
  Cononsolvency in P(S-b-NIPAM) diblock copolymers - a time-resolved SANS study of the aggregation process
  DPG Frühjahrstagung, Dresden, 30 Mar – 4 Apr 2014

- K. Kyriakos, M. Philipp, M. Dyakonova, N. Vishnevetskaya, C. H. Lin, A. Miasnikova, A. Laschewsky, I. Grillo, P. Müller-Buschbaum, C. M. Papadakis
  Cononsolvency in P(S-b-NIPAM) in different solvent mixtures – a time-resolved SANS investigation
  Molecular Order and Mobility in Polymer Systems, St. Petersburg, 2 – 6 June 2014

- M. Leitner
  Measuring atomic dynamics by coherent X-ray scattering
  DESY, Hamburg, 20 Feb 2014

- M. Leitner
  Electronic structure and martensitic phase transformations
  TRR-80 Retreat Meeting, Freising, 24 – 25 Feb 2014

- W. Lohstroh, L. Silvi, E. Röhm, Zh. Zhao-Karger, M. Fichtner
  Hydrogen Dynamics in the alkaline and alkaline earth borohydrides $LiBH_4$, $Mg(BH_4)_2$ and the mixture $LiBH_4$-$Mg(BH_4)_2$
  QENS WINS 2014, Autrans, France, 11 – 16 May 2014

- W. Lohstroh, G. G. Simeoni, J. Neuhaus, W. Petry
  The time-of-flight spectrometer TOFTOF
  Trends and Perspectives in Neutron Scattering - From spallation to continuous neutron sources - a positive feedback on neutron instrumentation, Tutzing, 20 – 23 Oct 2014

- W. Lohstroh
  WP I1: C-SPEC
  ESS-DU Annual Project meeting, Düsseldorf, 24 Nov 2014

- W. Lohstroh
  WP K1: Chopper development
  ESS-DU Annual Project meeting, Düsseldorf, 24 Nov 2014

- E. Metwalli
  Growth kinetics of metal nanoparticles on polymer surfaces
  DPG Frühjahrstagung, Dresden, 30 Mar – 4 Apr 2014

- E. Metwalli
  GISAXS/GISANS
  Polymer Physics Summer School, Obertauern, Austria, 24 – 27 Jun 2014

- E. Metwalli
  Growth kinetics of metal nanoparticles on solid surfaces
  Congress and General Assembly of the International Union of Crystallography, Montreal, Canada, 5 - 12 Aug 2014

- D. Moseguí González, W. Wang
  Polymer based solar cells
  Polymer Physics Summer School, Obertauern, Austria, 24 – 27 Jun 2014

- P. Müller-Buschbaum
  Report of the Users Committee (DPS-UC) - report 2013
  DESY User Meeting, Hamburg, 30 Jan – 1 Feb 2014

- P. Müller-Buschbaum, M. A. Niedermeier, B. Su, L. Song, S. V. Roth
  Tailoring titania nanostructures for solar cell applications
  247th American Chemical Society National Meeting, Dallas, USA, 16 – 20 Mar 2014

- P. Müller-Buschbaum, M. A. Niedermeier, M. Rawolle, E. V. Braden, K. Sarkar, E. M. Herzig, V. Körstgens
  Towards low-temperature synthesis of polymer/titania hybrid films for application in photovoltaics
  DPG Frühjahrstagung, Dresden, 30 Mar - 4 April 2014

- P. Müller-Buschbaum
  Organic photovoltaics
  ERIAN/MSE Meeting, Munich, 11 Apr 2014

- P. Müller-Buschbaum
  Towards low-temperature synthesis of polymer/titania hybrid films for application in photovoltaics
  3rd International SolTech Conference, Wildbad Kreuth, 28 – 30 Apr 2014

- P. Müller-Buschbaum
  Time-resolved neutron reflectometry
  German-Greek Workshop 'Structural methods for the investigation of soft responsive matter 2014', Garching, 12 – 16 May 2014

- P. Müller-Buschbaum
  Future generation solar cells
  NIM Area 3 Workshop 2014, Munich, 11 Jul 2014

- P. Müller-Buschbaum
  Photovoltaics and Wind Energy
  CEA-TUM Kick-off meeting: Research Cooperation in the Field of Renewable Energies, Garching, 18 Jul 2014

- P. Müller-Buschbaum, Q. Zhong, W. Wang, A. M. Bivigou-Koumba, A. Laschewsky, C. M. Papadakis, R. Cubitt
  In-operando study of swelling and switching of thermo-responsive polymer films
  Congress and General Assembly of the International Union of Crystallography, Montreal, Canada, 5 - 12 Aug 2014

- P. Müller-Buschbaum
  Grazing Incidence Small Angle Neutron Scattering: Challenges and Possibilities
  ESS Science Symposium 2014 - Surface and Interface Reconstruction: A Challenge for Neutron Reflectometry, Bernried, 25 – 26 Sep 2014

- P. Müller-Buschbaum
  Polymer and hybrid nanostructures for applications in organic electronics
  Colloquium at Leibniz-Institut für Polymerforschung Dresden e.V. (IPF), Dresden, 6 – 7 Nov 2014

- P. Müller-Buschbaum
  Materials for batteries
  2nd meeting on opportunities of relation development in the field of sustainable energy supply, CEA, Grenoble, France, 1 - 2 Dec 2014

- P. Müller-Buschbaum
  Organic solar cells
  2nd meeting on opportunities of relation development in the field of sustainable energy supply 2014, Liten, Chambery, France, 1 – 2 Dec 2014

- C. M. Palumbiny, C. Heller, C. J. Schaffer, V. Körstgens, G. Santoro, S. V. Roth, P. Müller-Buschbaum
  Polymeric electrode by co-solvent treatment: Molecular reorientation, structural changes and artificial structuring
  EuroTech Meeting Neuchâtel, Switzerland, 23 – 24 Jan 2014

- C. M. Palumbiny, F. Liu, T. P. Russell, A. Hexemer, C. Wang, P. Müller-Buschbaum
  In-situ GIWAXS on slot die coated highly conductive PEDOT:PSS as electrode for ITO-free organic electronics: Crystallinity and molecular orientation
  DPG Frühjahrstagung, Dresden, 30 Mar – 4 Apr 2014

- C. M. Palumbiny, J. Lebert
  Conducting polymers
  Polymer Physics Summer School, Obertauern, Austria, 24 – 27 Jun 2014

- C. M. Palumbiny, F. Liu, C. Wang, A. Hexemer, E. Schaible, T. P. Russell, P. Müller-Buschbaum
  Following the evolution of nanomorphology: In-situ GIWAXS on slot die coated PEDOT:PSS polymeric electrodes
  EuroTech Meeting Brussels, Belgium, 27 – 28 Oct 2014

- C. M. Papadakis
  Phase behavior of thermoresponsive polymers
  German-Greek Workshop 'Structural methods for the investigation of soft responsive matter 2014', Garching, 12 – 16 May 2014

- C. M. Papadakis, J. Adelsberger, I. Grillo, A. M. Bivigou-Koumba, A. Laschewsky, P. Müller-Buschbaum
  Kinetics of collapse and aggregation in thermoresponsive micellar block copolymer solutions
  Molecular Order and Mobility in Polymer Systems, St. Petersburg, 2 – 6 June 2014

- C. M. Papadakis
  Thermoresponsive hydrogels - what can neutron scattering tell us?
  Fakultät für Pharmazie, Ludwig-Maximilians-Universität, München, Germany, 16 Oct 2014

- C. M. Papadakis
  Thermoresponsive hydrogels - what can neutron scattering tell us?
  Fakultät für Physik und Geowissenschaften, Universität Leipzig, Germany, 6 Nov 2014

- W. Petry
  Building the instrument suite at FRM II with universities
  European Spallation Source (ESS)- workshop, Kopenhagen, Denmark, 25 Feb 2014

- W. Petry
  Auf der Suche nach dem Wissen von morgen: Mit Neutronen die Welt entdecken
  Deutsche Tagung für Forschung mit Synchrotronstrahlung, Neutronen und Ionenstrahlen an Grossgeräten 2014, Bonn, 21 – 23 Sep 2014

- W. Petry
  From Phonons to Functionality
  Festveranstaltung zum 50-jährigen Bestehen der Arbeitsgemeinschaft und des Fachverbandes Metall- und Materialphysik - DPG Frühjahrstagung, Dresden, 30 Mar – 4 Apr 2014

- W. Petry
  Neutrons for Nano and Materials Science
  MiFuN - Workshop Microstructural Functionality, Dynamics, Adaption, and Self Healing at the Nanocale (MiFuN), University of Duisburg-Essen, 28 – 30 Apr 2014

- W. Petry
  Innovation designed to deal with major society's challenges
  Jahrestagung Kerntechnik, Frankfurt, 6 May 2014

- W. Petry
  Materials science with neutrons
  German-Greek Workshop 'Structural methods for the investigation of soft responsive matter 2014', Garching, 12 – 16 May 2014

- W. Petry
  Evaluation of MLZ
  Evaluation of the Heinz Maier-Leibnitz Zentrum, 19 May 2014

- W. Petry
  Auf der Suche nach dem Wissen von morgen - mit Neutronen die Welt entdecken
  Wirtschaftsbeirat der Union e.V., 28 Nov 2014

- M. Philipp, J. K. Krüger, P. Müller-Buschbaum
  Mechanical and structural instabilities of phase-separating PNIPAM solutions
  Polymer and Soft Matter Seminar, SFB TRR 102, Martin-Luther-Universität Halle-Wittenberg, 7 Jan 2014

- M. Philipp, K. Kyriakos, L. Silvi, W. Lohstroh, W. Petry, J. K. Krüger, C. M. Papadakis, P. Müller-Buschbaum
  Dehydration behavior of phase separating PNIPAM solutions
  DPG Frühjahrstagung, Dresden, 30 Mar – 4 Apr 2014

- M. Philipp
  Quasi-elastic neutron scattering
  German-Greek Workshop 'Structural Methods for the Investigation of Soft Responsive Matter', Garching, 12 – 16 May 2014

- M. Philipp
  Structure, dynamics and order parameter susceptibilities at demixing transitions of thermoresponsive polymer solutions
  Emmy Noether projects selection meeting of the Deutsche Forschungsgemeinschaft, Frankfurt, 23 May 2014

- M. Philipp
  Small angle scattering - SAXS, SANS
  Polymer Physics Summer School, Obertauern, Austria, 24 – 27 Jun 2014

- M. Philipp, J. K. Krüger, P. Müller-Buschbaum
  Nonlinear and kinetic processes within phase-separating model thermo-responsive solutions
  Hydrogels in applied science workshop, Lübbenau, 9 – 11 Jul 2014

- M. Philipp, J. K. Krüger, P. Müller-Buschbaum
  Nonlinear and kinetic processes at demixing transitions
  5th Workshop of Young European Scientists (European Polymer Federation), Cracow, Poland, 7 – 11 Sep 2014

- M. Philipp, K. Kyriakos, R. Aleksandrova, W. Lohstroh, W. Petry, C. M. Papadakis, J. K. Krüger, P. Müller-Buschbaum
  Molecular perspective on the phase separation mechanisms of thermo-responsive solutions
  Polydays 2014, Berlin, 30 Sep – 2 Oct 2014

- C. Psylla
  Bottlebrush copolymers with poly(ethylene oxide)-b-poly(propylene oxide) side chains
  Faculty of Physics, National Technical University of Athens, Greece, 8 Jun 2014

- N. Saxena, M. Coric
  Polymer blend films
  Polymer Physics Summer School, Obertauern, Austria, 24 – 27 Jun 2014

- C. J. Schaffer, C. M. Palumbiny, M. A. Niedermeier, C. Jendrzejewski, G. Santoro, S. V. Roth, P. Müller-Buschbaum
  Watching a solar cell die - morphological degradation in organic photovoltaics
  EuroTech Meeting Neuchâtel, Switzerland, 23 – 24 Jan 2014

- C. J. Schaffer, C. M. Palumbiny, M. A. Niedermeier, C. Jendrzejewski, G. Santoro, S. V. Roth, P. Müller-Buschbaum
  Structural degradation of polymer solar cells
  DPG Frühjahrstagung, Dresden, 30 Mar – 4 Apr 2014

- C. J. Schaffer, S. Pröller
  Polymer crystallization
  Polymer Physics Summer School, Obertauern, Austria, 24 – 27 Jun 2014

- C. J. Schaffer, C. M. Palumbiny, M. A. Niedermeier, C. Jendrzejewski, G. Santoro, S. V. Roth, P. Müller-Buschbaum
  Watching a solar cell die - morphological degradation in organic photovoltaics
  4th Colloquium of the Munich School of Engineering, Garching, 3 Jul 2014

- C. J. Schaffer, P. Müller-Buschbaum
  On the morphology of PCPDTBT;$PC_{71}BM$ thin films for organic photovoltaics
  EuroTech Meeting Brussels, Belgium, 27 – 28 Oct 2014

- J. Schlipf, P. Müller-Buschbaum
  Hybrid perovskites for application in solar cells - a morphological study
  2nd meeting on opportunities of relation development in the field of sustainable energy, Grenoble/Chambéry, France, 1 – 2 Dec 2014

- A. F. Schulte
  Micro-spectroscopy of single cells at ambient and high pressure
  Soft matter seminar, Physics department, FAU Erlangen, 14 Apr 2014

- A. F. Schulte
  Vibrational Spectroscopy
  German-Greek Workshop 'Structural Methods for the Investigation of Soft Responsive Matter', Garching, 12 – 16 May 2014

- A. Sepe, D. Posselt, J. Zhang, J. Perlich, D.-M.Smilgies, A. A. Rudov, I. I. Potemkin, C. M. Papadakis
  Guiding reorganization in block copolymer thin films on the nanoscale by judicious control of solvent vapor exposure
  DPG Frühjahrstagung, Dresden, 30 Mar - 4 Apr 2014

- L. Silvi, W. Lohstroh
  Hydrogen dynamics in $LiBH_4$ across structural phase transition
  DPG Frühjahrstagung, Dresden, 30 Mar – 4 Apr 2014

- L. Silvi, W. Lohstroh
  Quasielastic neutron scattering on $Mg(BH_4)_2$
  14th International Symposium on Metal-Hydrogen Systems: Fundamentals and applications – Manchester UK, 20 – 25 July 2014

- L. Song
  Hybrid solar cells TiO_2/conducting polymer system
  Polymer Physics Summer School, Obertauern, Austria, 24 – 27 Jun 2014

- H. Sternschulte, I. Staudinger, S. Simeth, A. Sepe, C. M. Papadakis, J. Perlich, S. V. Roth, J.-F. Moulin, S. Ghodbane, S. Steinmüller-Nethl
  Ultrananocrystalline diamond films studied using GISAXS/GISANS
  DPG Frühjahrstagung, Dresden, 30 Mar - 4 Apr 2014

- N. Vishnevetskaya, V. Hoang, A. Laschewsky, C. M. Papadakis
  Aggregation behavior of doubly responsive poly(sulfobetaine-b-(N-isopropylmethacrylamide) diblock copolymers
  Polydays 2014, Berlin, Germany, 30 Sept - 2 Oct 2014

- N. Vishnevetskaya, V. Hoang, A. Laschewsky, C. M. Papadakis
  Orthogonally switchable diblock copolymers
  12th European Summer School on Scattering Methods Applied to Soft Condensed Matter, Bombannes, France, 16 - 23 May 2014

- R. Wang, Z. Di, H. Frielinghaus, P. Müller-Buschbaum
  Morphology investigation on copolymer based organic solar cells
  SoftComp & ESMI Annual Meeting 2014, Greece, 26 – 30 May 2014

- R. Wang, Z. Di, H. Frielinghaus, P. Müller-Buschbaum
  Grazing incidence small angle neutron scattering applied on organic solar cell investigation
  Fourth Annual Niels Bohr International Academy Workshop on ESS Science, Denmark, 10 – 14 Nov 2014

- Y. Yao, R. Wang
  Block copolymer films
  Polymer Physics Summer School, Obertauern, Austria, 24 – 27 Jun 2014

- J. Zhang, D. Posselt, A. Sepe, X. Shen, J. Perlich, D.-M. Smilgies, C. M. Papadakis
  Structural evolution of perpendicular lamellae in diblock diblock copolymer thin films during solvent vapor treatment investigated by GISAXS
  DPG Frühjahrstagung, Dresden, 30 Mar - 4 Apr 2014

- J. Zhang, D. Posselt, A. Sepe, J. Perlich, D.-M. Smilgies, A. A. Rudov, E. S. Patyukova, I. I. Potemkin, C. M. Papadakis
  Vapor treatment of block copolymer thin films: GISAXS and computer simulations
  23rd Congress and General Assembly of the International Union of Crystallography, Montreal, Canada, 5 – 12 Aug 2014

9.3 Posters

- A. Abdelsamie, L. Song, P. Müller-Buschbaum
  Low-temperature synthesis of nano-patterned TiO_2 thin film by combining sol-gel method and nano-imprinting
  MaMaSELF status meeting, Rigi Kulm, Switzerland, 21 – 24 May 2014

- A. Abdelsamie, L. Song, P. Müller-Buschbaum
  Low-temperature synthesis of nano-patterned TiO_2 thin film by combining sol-gel method and nano-imprinting
  Polymer Physics Summer School, Obertauern, Austria, 24 – 27 Jun 2014

- D. Aravopoulou, K. Bika, K. Kyriakos, L. Augsbach, Z. Di, A. Miasnikova, A. Laschewsky, C. M. Papadakis, A. Kyritsis
  Novel thermoresponsive systems based on poly(methoxy diethylene glycol acrylate) copolymers
  8th International Conference on Broadband Dielectric Spectroscopy and its Applications, Wisla, Poland, 14 – 19 Sep 2014

- D. Aravopoulou, K. Bika, K. Kyriakos, L. Augsbach, A. Miasnikova, A. Laschewsky, C. M. Papadakis, A. Kyritsis
  Structural, thermal and dielectric studies on novel thermoresponsive systems based on poly(methoxy diethylene glycol acrylate) copolymers
  10th Hellenic Polymer Society Conference, Rio-Patras, Greece, 4 – 6 Dec 2014

- L. Augsbach, K. Kyriakos, A. Miasnikova, A. Laschewsky, Z. Di, P. Müller-Buschbaum, C. M. Papadakis
  Micellar solutions of novel thermoresponsive diblock copolymers
  DPG Frühjahrstagung, Dresden, 30 Mar - 4 Apr 2014

- M. Bahr, E. Metwalli, P. Müller-Buschbaum
  Metal salt doped diblock copolymers
  Polymer Physics Summer School, Obertauern, Austria, 24 – 27 Jun 2014

- E. Barabino, W. Wang, P. Müller-Buschbaum
  Measurements of I-V characteristics of P3HT:PCBM bulk heterojunction solar cells
  Polymer Physics Summer School, Obertauern, Austria, 24 – 27 Jun 2014

- K. Bika, S. Kripotou, P. Pissis, A. Miasnikova, A. Laschewsky, C. M. Papadakis, A. Kyritsis
  Study of the thermoresponsive symmetrical triblock copolymer poly(styrene-block-methoxy diethylene glycol acrylate-block styrene) using differential scanning calorimetry and dielectric relaxation spectroscopy
  German-Greek Workshop 'Structural Methods for the Investigation of Soft Responsive Matter', Garching, 12 – 16 May 2014

- H. Caller
  In-situ growth of titania films by spray deposition for solid-state dye-sensitized solar cells
  MaMaSELF status meeting, Rigi Kulm, Switzerland, 21 – 24 May 2014

- M. Darweesh
  Choice of solvents for inducing complex structures in thin films for binary blends of diblock copolymers
  6th Mamaself Status Meeting, Rigi Kulm, Switzerland, 21 – 24 May 2014

- M. Darweesh, J. Zhang, D. Posselt, D.-M. Smilgies, J. Perlich, K. Kyriakos, S. Jaksch, C.M. Papadakis
  Effect of different solvents on thin films of polystyrene-block-polybutadiene diblock copolymers
  Polymer Physics Summer School, Obertauern, Austria, 24 – 27 Jun 2014

- M. A. Dyakonova, N. Stavrouli, M.-T. Popescu, K. Kyriakos, I. Grillo, M. Philipp, S. Jaksch, C. Tsitsilianis, C. M. Papadakis
  Stimuli-responsive reversible hydrogels from triblock polyelectrolytes and polyampholytes
  Molecular Order and Mobility in Polymer Systems, St. Petersburg, 2 – 6 Jun 2014

- M. A. Dyakonova, N. Stavrouli, M.-T. Popescu, K. Kyriakos, I. Grillo, M. Philipp, S. Jaksch, C. Tsitsilianis, C.M. Papadakis
  Stimuli-responsive reversible hydrogels from triblock polyelectrolytes and polyampholytes
  German-Greek Workshop 'Structural Methods for the Investigation of Soft Responsive Matter', Garching, 12 - 16 May 2014

- M. A. Dyakonova, N. Stavrouli, M.-T. Popescu, K. Kyriakos, I. Grillo, M. Philipp, S. Jaksch, C. Tsitsilianis, C. M. Papadakis
  Stimuli-responsive reversible hydrogels from triblock polyelectrolytes and polyampholytes
  DPG Frühjahrstagung, Dresden, 30 March - 4 April 2014

- A. Eisele, K. Kyriakos, M. Dyakonova, C. M. Papadakis, B. Rieger
  Structure and conductivity of liquid crystals having carbonate segments
  DPG Frühjahrstagung, Dresden, 30 Mar – 4 Apr 2014

- G. Goracci, A. Arbe, J. Colmenero, A. Alegria, F. Jurani, V. Garcia-Sakai, G. Schneider, W. Lohstroh
  Neutron scattering and dielectric spectroscopy study on localized motions of PDMAEMA in concentrated solution of THF
  QENS WINS 2014, Autrans, France, 11 – 16 May 2014

- S. Günther, C. Schaffer, P. Müller-Buschbaum
  Implementing a OPV slot dye coating device and determining the ramifications on morphology and device lifetimes
  DPG Frühjahrstagung, Dresden, 30 Mar – 4 Apr 2014

- S. Günther, C. Schaffer, P. Müller-Buschbaum
  Implementing a OPV slot dye coating device and determining the ramifications on morphology and device lifetimes
  Polymer Physics Summer School, Obertauern, Austria, 24 – 27 Jun 2014

- S. Guo, B. Cao, W. Wang, J.-F. Moulin, P. Müller-Buschbaum
  Efficiency enhancement of polymer solar cells introduced by alcohol solvent treatment
  DPG Frühjahrstagung, Dresden, 30 Mar – 4 Apr 2014

- S. Guo, B. Cao, W. Wang, J.-F. Moulin, P. Müller-Buschbaum
  Enhanced efficiency by solvent treatment for PTB7:PC71BM bulk heterojunction system
  4th Colloquium of the Munich School of Engineering, Garching, 3 Jul 2014

- A. Hassan, V. Körstgens, P. Müller-Buschbaum
  Hierarchically structuring of hybrid materials with the breath figure method
  DPG Frühjahrstagung, Dresden, 30 Mar - 4 Apr 2014

- A. Hassan, V. Körstgens, P. Müller-Buschbaum
  Functional layers for organic photovoltaics
  Polymer Physics Summer School, Obertauern, Austria, 24 – 27 Jun 2014

- N. Hohn, D. Moseguí González, P. Müller-Buschbaum
  Structure and performance of water soluble solar cells functionalized with non-magnetic nanoparticles
  DPG Frühjahrstagung, Dresden, 30 Mar – 4 Apr 2014

- N. Hohn, D. Moseguí González, P. Müller-Buschbaum
  Structure and performance of aqueous processed solar cells based on a P3P6T/C60 active layer
  Polymer Physics Summer School, Obertauern, Austria, 24 – 27 Jun 2014

- N. Hohn, D. Moseguí González, P. Müller-Buschbaum
  Structure and performance of aqueous processed solar cells based on a P3P6T/C60 active layer
  4th Colloquium of the Munich School of Engineering, Garching, 3 Jul 2014

- E. D. Indari, C. J. Schaffer, S. Bernstorff, P. Müller-Buschbaum
  Morphology Changes of Organic Solar Cells Introduced via Aging
  MaMaSELF status meeting, Rigi Kulm, Switzerland, 21 – 24 May 2014

- E. D. Indari, C. J. Schaffer, S. Bernstorff, P. Müller-Buschbaum
  Morphology changes of organic solar cells introduced via aging
  Polymer Physics Summer School, Obertauern, Austria, 24 – 27 Jun 2014

- D. Jehnichen, D. Pospiech, G. He, P. Friedel, J. Zhang, C. M. Papadakis, J. Perlich
  PPMA-PMMA block copolymer thin films with modified gold nanoparticles
  DPG Frühjahrstagung, Dresden, 30 Mar - 4 Apr 2014

- V. Körstgens, S. V. Roth, P. Müller-Buschbaum
  In-situ GISAXS microfluidics: following the attachment, detachment and growth of nanoparticles at the solid-liquid interface
  DESY Photon Science Users' Meeting, Hamburg, 29 – 31 Jan 2014

- V. Körstgens, V. Haramus, P. Müller-Buschbaum
  Following structural changes in nanoparticle films under laminar flow conditions with in-situ SAXS microfluidics
  DESY Photon Science Users' Meeting, Hamburg, 29 – 31 Jan 2014

- A. Kupijai, C. M. Palumbiny, C. J. Schaffer, W. Aigner, M. Brandt, M. Stutzmann, P. Müller-Buschbaum
  Strom aus Kunststoffen - Neue Möglichkeiten durch organische Photovoltaik
  Tag der offenen Tür, Garching, 11 Oct 2014

- K. Kyriakos, C. Psylla, S. Ottinger, A. Miasnikova, A. Laschewsky, P. Müller-Buschbaum, C. M. Papadakis
  Novel thermoresponsive block copolymers of various architectures - a fluorescence correlation spectroscopy investigation of the micelle formation
  DPG Frühjahrstagung, Dresden, 30 Mar - 4 Apr 2014

- K. Kyriakos, C. Psylla, S. Ottinger, A. Miasnikova, A. Laschewsky, P. Müller-Buschbaum, C. M. Papadakis
  Novel thermoresponsive block copolymers of various architectures - a fluorescence correlation spectroscopy investigation of the micelle formation
  German-Greek Workshop 'Structural Methods for the Investigation of Soft Responsive Matter', Garching, 12 - 16 May 2014

- K. Kyriakos, M. Philipp, J. Adelsberger, S. Jaksch, A. V. Berezkin, I. Grillo, A. Miasnikova, A. Laschewsky, P. Müller-Buschbaum, C. M. Papadakis
  Cononsolvency in P(S-b-NIPAM) diblock copolymers - a time-resolved SANS study of the aggregation process
  German-Greek Workshop 'Structural Methods for the Investigation of Soft Responsive Matter', Garching, 12 - 16 May 2014

- M. Leitner, H Ceeh, J.-A. Weber, W. Petry
  Quantitative Fermi surface reconstruction by positron annihilation
  TRR 80 continuation on-site assessment, Augsburg, 15 – 17 Jul 2014

- W. Liu
  In-situ growth study of gold nano domains on P_3HT films for hybrid solar cells
  MaMaSELF status meeting, Rigi Kulm, Switzerland, 21 – 24 May 2014

- W. Liu, B. Su, P. Müller-Buschbaum
  In-situ growth study of gold nano domains on P3HT films for hybrid solar cells
  Polymer Physics Summer School, Obertauern, Austria, 24 – 27 Jun 2014

- D. Magerl, X.-P. Qiu, F.M. Winnik, P. Müller-Buschbaum
  Thermoresponsive switching behavior in thin films of cyclic and linear PNIPAM
  DPG Frühjahrstagung, Dresden, 30 Mar – 4 Apr 2014

- J. F. Martínez Grisales, E. M. Herzig, P. Müller-Buschbaum
  Aggregation control in organic photovoltaic blends
  DPG Frühjahrstagung, Dresden, 30 Mar – 4 Apr 2014

- J. F. Martínez Grisales, E. M. Herzig, P. Müller-Buschbaum
  Influence of solvent additives on performance of organic photovoltaics
  Polymer Physics Summer School, Obertauern, Austria, 24 – 27 Jun 2014

- J. F. Martínez Grisales, E. M. Herzig, P. Müller-Buschbaum
  Influence of solvent additives on performance of organic photovoltaics
  4th Colloquium of the Munich School of Engineering, Garching, 3 Jul 2014

- C. Mayr, S. Pröller, V. Körstgens, H. Iglev, P. Müller-Buschbaum
  Hybrid solar cells based on aqueous processed titania nanoparticles
  DPG Frühjahrstagung, Dresden, 30 Mar – 4 Apr 2014

- C. Mayr, S. Pröller, V. Körstgens, H. Iglev, C. J. Schaffer, L. Song, H. Caller, G. Santoro, S. V. Roth, P. Müller-Buschbaum
  Hybrid solar cells based on aqueous processed titania nanoparticles
  Polymer Physics Summer School, Obertauern, Austria, 24 – 27 Jun 2014

- C. Mayr, S. Pröller, V. Körstgens, H. Iglev, C. J. Schaffer, L. Song, H. Caller, G. Santoro, S. V. Roth, P. Müller-Buschbaum
  Hybrid solar cells based on aqueous processed titania nanoparticles
  4th Colloquium of the Munich School of Engineering, Garching, 3 Jul 2014

- P. Müller-Buschbaum
  Nanostrukturierte Polymergrenzflächen
  NIM Nanoday, Munich, 22 Nov 2014

- D. Moseguí González, V. Körstgens, Y. Yao, L. Song, G. Santoro, S. V. Roth, P. Müller-Buschbaum
  Performance of P3HT:PCBM solar cells modified with iron oxide nanoparticles
  DPG Frühjahrstagung, Dresden, 30 Mar - 4 Apr 2014

- D. Moseguí González, V. Körstgens, Y. Yao, L. Song, G. Santoro, S. V. Roth, P. Müller-Buschbaum
  Performance of P3HT:PCBM solar cells modified with iron oxide nanoparticles
  Third 'Solar Technologies Go Hybrid' Workshop, Wildbad Kreuth, 27 Apr - 30 Apr 2014

- D. Moseguí González, V. Körstgens, Y. Yao, L. Song, G. Santoro, S. V. Roth, P. Müller-Buschbaum
  Performance of P3HT:PCBM solar cells modified with iron oxide nanoparticles
  MSE Colloquium, Munich, 2 Jul 2014

- C. M. Palumbiny, T. Pfadler, F. Liu, C. Heller, J. Schlipf , C. J. Schaffer, S. V. Roth, T. P. Russell, A. Hexemer, C. Wang, L. Schmidt-Mende, P. Müller-Buschbaum
  A glance into the inner life of thin films for organic PVs: In-situ and ex-situ advanced scattering investigations
  Third 'Solar Technologies Go Hybrid' Workshop, Wildbad Kreuth, 27 – 30 Apr 2014

- C. M. Palumbiny, F. Liu, T. P. Russell, A. Hexemer, C. Wang, P. Müller-Buschbaum
  Polymeric electrode for all-printed organic electronics: Following film formation and crystallization in-situ
  4th Colloquium of the Munich School of Engineering, Garching, 3 Jul 2014

- C. M. Palumbiny, C. Heller, C. J. Schaffer, V. Körstgens, G. Santoro, F. Liu, C. Wang, A. Hexemer, T. P. Russell, S. V. Roth, P. Müller-Buschbaum
  Conductivity in Polymeric Electrode for Roll-to-Roll Printed Organic Electronics: Evolution of Nanostructure and Molecular Orientation in PEDOT:PSS
  CeNS Workshop "Walk and talk at the nanoscale", Venice, Italy, 22 – 26 Sep 2014

- C.M. Papadakis, J. Adelsberger, I. Grillo, A.M. Bivigou-Koumba, A. Laschewsky, P. Müller-Buschbaum
  Kinetics of collapse and aggregation in thermoresponsive micellar block copolymer solutions
  German-Greek Workshop 'Structural Methods for the Investigation of Soft Responsive Matter', Garching, 12 - 16 May 2014

- M. Philipp, U. Müller, R. Aleksandrova, R. Sanctuary, P. Müller-Buschbaum, J. K. Krüger
  About the elastic nature of the demixing transition of aqueous PNIPAM solutions
  German-Greek Workshop 'Structural Methods for the Investigation of Soft Responsive Matter', Garching, 12 – 16 May 2014

- M. Philipp, K. Kyriakos, L. Silvi, W. Lohstroh, W. Petry, J. K. Krüger, C. M. Papadakis, P. Müller-Buschbaum
  From molecular dehydration to volume expansion of phase-separating PNIPAM solutions
  Deutsche Tagung für Forschung mit Synchrotronstrahlung, Neutronen und Ionenstrahlen an Grossgeräten 2014, Bonn, 21 – 23 Sep 2014

- C. Psylla, K. Kyriakos, J. Zhao, S. Pispas, C. M. Papadakis
  Core-shell brush copolymers with poly(propylene oxide)-b-poly(ethylene oxide) side chains
  DPG Frühjahrstagung, Dresden, 30 Mar – 4 Apr 2014

- C. Psylla, K. Kyriakos, J. Zhao, S. Pispas, C. M. Papadakis
  Core-shell brush copolymers with poly((propylene oxide)-b-poly(ethylene oxide)) side chains
  German-Greek Workshop 'Structural Methods for the Investigation of Soft Responsive Matter', Garching, 12 – 16 May 2014

- M. Rasool, E. Metwalli, A. Eberle, H. A. Gasteiger, P. Müller-Buschbaum
  Block copolymer based membrane for lithium ion microbatteries
  DPG Frühjahrstagung, Dresden, 30 Mar – 4 Apr 2014

- M. Rasool, E. Metwalli, A. Eberle, H. A. Gasteiger, P. Müller-Buschbaum
  Block copolymer based membrane for lithium ion microbatteries
  Polymer Physics Summer School, Obertauern, Austria, 24 – 27 Jun 2014

- N. Saxena, A. Greppmair, M. S. Brandt, P. Müller-Buschbaum
  Novel nanostructured thermoelectric hybrid materials
  MSE Colloquium 2014, Garching, 4 Jul 2014

- N. Saxena, A. Greppmair, M. Coric, J. Wernecke, S. Marggraf, E. M. Herzig, M. S. Brandt, P. Müller-Buschbaum
  Novel thermoelectric films based on a polymer-nanoparticle composite
  CeNS Workshop „Walk and talk on the nanoscale", Venice, Italy, 22 – 26 Sep 2014

- N. Saxena, A. Greppmair, M. S. Brandt, P. Müller-Buschbaum
  Thermoelektrika: Strom aus Wärme
  NIM Nanoday, Munich, 22 Nov 2014

- C. J. Schaffer, C. M. Palumbiny, M. A. Niedermeier, C. Jendrzejewski, G. Santoro, S. V. Roth, P. Müller-Buschbaum
  Structural Degradation of Polymer Solar Cells
  Third 'Solar Technologies Go Hybrid' Workshop, Wildbad Kreuth, 27 – 28 Apr 2014

- C. J. Schaffer, C. M. Palumbiny, M. A. Niedermeier, C. Jendrzejewski, G. Santoro, S. V. Roth, P. Müller-Buschbaum
  Watching aging in organic solar cells with in-situ GISAXS
  Deutsche Tagung für Forschung mit Synchrotronstrahlung, Neutronen und Ionenstrahlen an Großgeräten, Bonn, 21 – 22 Sep 2014

- J. Schlipf, C. M. Palumbiny, M. Algasinger, K. Sarkar, A. Kriele, M. S. Brandt, P. Müller-Buschbaum
  Novel structuring of organic thin films for improved absorption and performance in organic solar cells
  DPG Frühjahrstagung, Dresden, 30 Mar – 4 Apr 2014

- J. Schlipf, C. M. Palumbiny, P. Müller-Buschbaum
  Reduced sheet resistance in PEDOT:PSS with surfactant additive and multilayers
  Polymer Physics Summer School, Obertauern, Austria, 24 – 27 Jun 2014

- A. Schulte, M. Philipp, C. J. Schaffer, P. Müller-Buschbaum
  Hydration and molecular interactions in PNIPAM films probed with FTIR spectroscopy
  DPG Frühjahrstagung, Dresden, 30 Mar – 4 Apr 2014

- A. Schulte, S. H. Park, S. Arora, A. Antoine, D. Chakrabarti
  Volume and morphological changes in single erythrocytes at high hydrostatic pressure
  DPG Frühjahrstagung, Dresden, 30 Mar – 4 Apr 2014

- L. Silvi, E. Röhm, Z. Zaho-Karger, W. Lohstroh
  Hydrogen dynamics in $LiBH_4$ across structural phase transition
  MLZ Evaluation Meeting, Garching, 17 – 18 May 2014

- L. Song, M. A. Niedermeier, V. Körstgens, D. Magerl, B. Su, S. Bernstorff, P. Müller-Buschbaum
  Synthesis of porous TiO_2 nanostructures by the sol-gel method
  DPG Frühjahrstagung, Dresden, 30 Mar – 4 Apr 2014

- L. Song, M. A. Niedermeier, V. Körstgens, D. Magerl, B. Su, S. Bernstorff, P. Müller-Buschbaum
  Synthesis of porous TiO_2 nanostructures by the sol-gel method
  3rd Colloquium of the Munich School of Engineering, Garching, 3 Jul 2014

- B. Su, Y. C. Rui, A. Niedermeier, V. Körstgens, S. Bernstorff , P. Müller-Buschbaum
  Hierarchically structured titania films for efficient light harvesting in dye-sensitized solar cells
  DPG Frühjahrstagung, Dresden, 30 Mar – 4 Apr 2014

- R. M. Torrademé, S. Guo, B. Cao, W. Wang, P. Müller-Buschbaum
  Investigation of a third component addition on high efficiency organic solar cells
  DPG Frühjahrstagung, Dresden, 30 Mar – 4 Apr 2014

- R. M. Torrademé, S. Guo, B. Cao, W. Wang, P. Müller-Buschbaum
  Investigation of a third component addition on organic solar cells
  Polymer Physics Summer School, Obertauern, Austria, 24 – 27 Jun 2014

- N. Vishnevetskaya, V. Hoang, A. Laschewsky, C. M. Papadakis
  Aggregation behavior of doubly thermo-responsive poly(sulfobetaine-b-(N-isopropylmethacrylamide) diblock copolymers
  Deutsche Tagung für Forschung mit Synchrotronstrahlung, Neutronen und Ionenstrahlen an Großgeräten 2014, 21 – 23 Sep 2014

- N. Vishnevetskaya, V. Hoang, A. Laschewsky, C. M. Papadakis
  Aggregation behaviour of doubly thermo-responsive poly(sulfobetaine-b-(N-isopropylmethacrylamide) diblock copolymers
  DPG Frühjahrstagung, Dresden, 30 Mar – 4 Apr 2014

- N. Vishnevetskaya, M. Dyakonova, A. Bogomolova, S. K. Filippov, A. Miasnikova, C.M. Papadakis
  Polymeric nanoparticles for drug delivery, stability and pH response
  DPG Frühjahrstagung, Dresden, 30 Mar – 4 Apr 2014

- N. Vishnevetskaya, V. Hoang, A. Laschewsky, C. M. Papadakis
  Orthogonally switchable blockcopolymers
  German-Greek Workshop, Garching, Germany, 12 – 16 May 2014

- R. Wang, H. Frielinghaus, P. Müller-Buschbaum
  Conjugated diblock copolymer/fullerene bulk heterojunction system in organic photovoltaic application
  Fourth Annual Niels Bohr International Academy Workshop on ESS Science, Denmark, 10 – 14 Nov 2014

- T. Wang, L. Song, P. Müller-Buschbaum
  Low temperature synthesis of TiO_2 thin films with micrometer-sized channels via wet imprinting
  MaMaSELF status meeting, Rigi Kulm, Switzerland, 21 – 24 May 2014

- T. Wang, L. Song, P. Müller-Buschbaum
  Low temperature synthesis of TiO_2 thin films with micrometer-sized channels via wet imprinting
  Polymer Physics Summer School, Obertauern, Austria, 24 – 27 Jun 2014

- W. Wang, S. Guo, K. Sarkar, M. Schindler, D. Magerl, M. Philipp, J. Perlich, P. Müller-Buschbaum
  The influence of solvent atmosphere on bulk heterojunction solar cells
  DPG Frühjahrstagung, Dresden, 30 Mar – 4 Apr 2014

- T. Widmann, W. Wang, L. Song, P. Müller-Buschbaum
  Flexibility investigations on low temperature processed nanostructured hybrid films
  DPG Frühjahrstagung, Dresden, 30 Mar – 4 Apr 2014

- T. Widmann, W. Wang, L. Song, P. Müller-Buschbaum
  Mechanical investigations on low-temperature processed nanostructured hybrid films
  Polymer Physics Summer School, Obertauern, Austria, 24 – 27 Jun 2014

- T. Widmann, W. Wang, L. Song, P. Müller-Buschbaum
  Mechanical investigations on low-temperature processed nanostructured hybrid films
  4th Colloquium of the Munich School of Engineering, Garching, 3 Jul 2014

- Y. Yao, E. Metwalli, B. Su, V. Körstgens, D. M. Gonzalez, G. Santoro, S. V. Roth, M. Opel, P. Müller-Buschbaum
  Nano- and microstructures of magnetic field-guided maghemite nanoparticles in diblock copolymer films
  DPG Frühjahrstagung, Dresden, 30 Mar – 4 Apr 2014

- J. Zhang, D. Posselt, K. Kyriakos, S. Jaksch, J. Perlich, D.-M. Smilgies, C.M. Papadakis
  Complex macrophase separated nanostructure induced by microphase separation in lamellar diblock copolymer thin films
  DPG Frühjahrstagung, Dresden, 30 Mar – 4 Apr 2014

- X. Zhang, K. Kyriakos, M. Rikkou-Kalourkoti, E. N. Kitiri, C. Patrickios, C. M. Papadakis
  Networks from amphiphilic star block copolymers
  Polymer Physics Summer School, Obertauern, Austria, 24 - 27 Jun 2014

9.4 Invited talks at the chair

- Dr. Frederik Lipfert, JCNS, Jülich
  Surface effects of microemulsions
  16 Jan 2014

- Dr. Aristeidis Papagiannopoulos, Theoretical and Physical Chemistry Institute, National Hellenic Research Foundation, Greece
  Small angle neutron scattering on self-assembled nanoparticles
  22 Jan 2014

- Nitin Saxena, Ludwig-Maximilians-Universität München
  Exploring gold nanorod self-assembly through a ligand-phase-separation approach
  5 Feb 2014

- Dr. Stephan V. Roth, DESY, Hamburg
  Recent developments at MiNaXS (P03)
  10 Mar 2014

- Lorenz Bießmann, Universität Würzburg
  Fast prediction of electronic band gaps using machine learning
  13 Mar2014

- Christian Reiter, MLZ, TU München
  Methodenentwicklung, Kalorimetrie und Messen der Dichte von hochdichten Kernbrennstoffen
  26 Mar 2014

- Dr. Heide Götz, European Patent Office, München
  Introduction into patent law
  8 Apr 2014

- Dr. Madlen Hubert, Ludwig-Maximilians-Universität München
  Development of new carrier systems for the delivery of immunomodulators
  17 Jun 2014

- Franziska Löhrer, Ludwig-Maximilians-Universität München
  Synthesis and characterization of Cd- and Cu-telluride nanocrystals
  23 Jun 2014

- Alina Lyuleeva, Walter-Schottky-Institut, TU München
  Functionalization of graphene for bioelectronic application
  24 Jun 2014

- Prof. Dr. Jiping Wang, Zhejiang Sci-Tech University, PR China
  Smart textiles with thermo-responsive polymers
  22 Jul 2014

- Prof. Dr. Jianzhong Shao, Zhejiang Sci-Tech University, PR China
  Structural coloration of textiles
  17 Sep 2014

- Prof. Dr. Alessio Zaccone, TU München
  Towards a theoretical framework for controlling self-assembly, large-scale structure, rheology, and electrical properties with functional polymers
  5 Nov 2014

- Stephan Pröller, MSE, TU München
  Morphology development in printed active layers for OPV
  12 Nov 2014

- Mihael Čorić, MSE, TU München
  Tender GISAXS of conducting polymers
  19 Nov 2014

- Kai Müller, WMI, TU München
  Manipulation of phosphorus donor spins in silicon at low temperatures
  17 Dec 2014

9.5 Funding

Deutsche Forschungsgemeinschaft:

- Within DFG priority programm SPP 1355:
  Controlled morphologies by molecular design and nano-embossing
  Grant Number: MU 1487/13-3
  Project Leader: Prof. Dr. Peter Müller-Buschbaum

- *Zweifach und orthogonal schaltbare Blockcopolymere aus zwitterionischen und thermoresponsiven Blöcken: Synthese und Strukturen in Lösung und im dünnen Film*
  Grant Number: MU 1487/17-1
  Project Leader: Prof. Dr. Peter Müller-Buschbaum

- *In-situ Untersuchungen zu Kondensation, Nukleation und Wachstum von Metallfilmen und Nanostrukturen auf organischen Oberflächen während Sputterbeschichtung*
  Grant Number: MU 1487/18-1
  Project Leader: Prof. Dr. Peter Müller-Buschbaum

- *In-situ-Messung deformationsinduzierter Martensitbildung in ausferritischem Gusseisen (ADI)*
  Grant Number: PE 580/14-1
  Project Leader: Prof. Dr. Winfried Petry

- Within DFG Collaborative Research Centre SFB TRR 80/2:
  Elektronische Struktur und martensitische Phasenumwandlungen
  Teilprojekt: G04
  Project Leader: Prof. Dr. Winfried Petry

- *Structural changes in block copolymer thin films during solvent vapor treatment*
  Grant Number: PA 771/10-1
  Project Leader: Prof. Dr. Christine Papadakis

- *Zweifach und orthogonal schaltbare Blockcopolymere aus zwitterionischen und thermoresponsiven Blöcken: Synthese und Strukturen in Lösung und im dünnen Film*
  Grant Number: PA 771/14-1
  Project Leader: Prof. Dr. Christine Papadakis

Bayerisches Staatsministerium für Bildung und Kultus, Wissenschaft und Kunst:

- Im Rahmen der Munich School of Engineering (MSE):
  Solar Technologies Go Hybrid (SolTech) - Forschungsnetzwerk TUM.solar
  Project Leader: Prof. Dr. Peter Müller-Buschbaum

- Im Rahmen der Munich School of Engineering (MSE): Netzwerk Regenerative Energien
  Aufbau eines interdisziplinären Netzwerks aus Lehrstühlen der Technischen Universität München und anderen Forschungseinrichtungen zur Förderung der Forschungsaktivitäten im Bereich der regenerativen Energien
  Project Leader: Prof. Dr. Peter Müller-Buschbaum

- Seedfunding im Rahmen der Energy Valley Bavaria (Munich School of Engineering, MSE)
  Tailored TCO nanostructures for PV applications (Tailor TCO)
  Project Leader: Prof. Dr. Peter Müller-Buschbaum

- Seedfunding im Rahmen der Energy Valley Bavaria (Munich School of Engineering, MSE)
  Novel Nanostructured Thermoelectric Hybrid Materials (NovelNTHM)
  Project Leader: Prof. Dr. Peter Müller-Buschbaum

- Nachwuchsgruppe im Rahmen des Energy Valley Bavaria (Munich School of Engineering, MSE)
  Organische Photovoltaik
  Project Leader: Dr. Eva M. Herzig

Others:

- Im Rahmen des Exzellenzclusters Nanosystems Initiative Munich (NIM)
  Nanosystems for Energy Conversion
  Principal Investigator: Prof. Dr. Peter Müller-Buschbaum

- Im Rahmen von Bund der Freunde der TUM
  Autark durch gedruckte Energieversorgung
  Project Leader: Dr. Eva M. Herzig; Collaboration Partner: Prof. Dr. Peter Müller-Buschbaum

- Im Rahmen des Programms Projektbezogener Personenaustausch mit Tschechien (Deutscher Akademischer Austausch Dienst, DAAD)
  Klinisch relevante makromolekulare Nanopartikel mit Cholesterin
  Project Leader: Prof. Dr. Christine Papadakis; Co-Project Leader: Dr. Sergey Filippov (Institute of Macromolecular Chemistry of Academy of Sciences of the Czech Republic, Prague).

- Im Rahmen des Programms Hochschulpartnerschaften mit Griechenland (Deutscher Akademischer Austausch Dienst, DAAD)
  Thermoresponsive polymers of copmlex architecture (ResComp)
  Project Leader: Prof. Dr. Christine Papadakis; Co-Project Leader: Prof. Dr. Apostolos Kyritsis (National Technical University of Athens, NTUA).

Technische Universität München:

- Im Rahmen der International Graduate School of Science and Engineering (IGSSE)
  Interface Science for Photovoltaics - a EuroTech GreenTech Initiative
  Project Leader: Prof. Dr. Peter Müller-Buschbaum

10 The chair

10.1 Staff

Chair: Prof. Dr. Winfried Petry

Head: Prof. Dr. Peter Müller-Buschbaum

Professor: Prof. Dr. Christine M. Papadakis

Fellows:

Dr. Anatoly V. Berezkin
Dr. Volker Körstgens
Dr. Michael Leitner
Dr. Wiebke Lohstroh
Dr. Ezzeldin Metwalli Ali
Dr. Jürgen Neuhaus
Dr. Neelima Paul
Dr. Martine Philipp
Dr. Konstantinos Raftopoulos
Dr. Giovana Giulia Simeoni
Dr. Jianqi Zhang

PhD students:

Bruno Baumeister
Lorenz Bießmann
Antonella Campanella
Hsin-Yin Chiang
Margarita A. Dyakonova
Shuai Guo
Tobias Hollmer
Stefan Huber
Tanja Huber
Konstaninos Kyriakos
Xiaohu Li
Franziska Löhrer
David Magerl
Juan-Francisco Mora
Humphrey Morhenn
Daniel Moseguí González
Pascal Neibecker
Claudia Palumbiny
Christian Reiter
Yichuan Rui
Kuhu Sarkar
Nitin Saxena
Christoph Schaffer
Rupert Schauer
Markus Schindler
Johannes Schlipf
Martin Schmiele
Luca Silvi
Lin Song
Christian Steyer
Bo Su
Natalya Vishnevetskaya
Rui Wang
Weijia Wang
Stephan Wlokka
Senlin Xia
Yuan Yao
Tobias Zweifel

Master students:

Amr Abdelsamie
Lukas Augsbach
Edoardo Barabino
Michael Bahr
Erik Braden
Herbert A. Caller-Guzman
Biye Cao
Mohamed Darweesh
Rajesh Dutta
Luise Fiedler
Moritz Futscher
Sebastian Günther
Ali Hassan
Nuri Hohn
Efi Dwi Indari
Wei Liu
Maria Freiria Lopez
Avishek Maity
Sumit Maity
Juan Felipe Martinez Grisales
Christoph Mayr
Bart-Jan Niebuur
Lukas Oesinghaus
Christina Psylla
Majid Rasool
Johannes Schlipf
Richard Stockhausen
Lorenz Sykora
Rosa Maria Torrademé
Tianyi Wang
Tobias Widmann
Xiaohan Zhang

Bachelor students:

Melis Aça
Simon Barth
Jessica Böhm
Ruben Burkhardt
Tobias Chemnitz
Kora-Lee Claude
Lisa-Marie Fellinger
Peter Haslauer
Alexander Hollering
Manuela Alexandra Huber
Ferdinand Jarisch
Florian Jung
Max Kraut
Thomas Maier
Philipp Marzak
Merlin Mitschek
Justus Oberhausen
Stefan Oswald
Josef Sapper
Stefan Schmalzl
Dominik Schullerer
Susanne Schwarzwälder
Julian Seyfried
Peter Spieler
Stephan Umkehrer
Alexander Wolf

Student assistants:

Ali Aghebat Rafat
Kora-Lee Claude
Moritz Futscher
Abishek Khanna
Evangelos Makrygiannis
Kilian Rückschloß

Technical/administrative staff:

Susanna Fink
Reinhold Funer
Josef Huber
Raffael Jahrstorfer
Josef Kaplonski
Matthias Maier
Dieter Müller
Patrick Schreiber
Nick Schröder
Marion Waletzki

10.2 Graduations

- **Accomplished PhD theses**

  Hsin-Yin Chiang
  Material selection of UMo fuel for research reactors: Swift heavy ion irradiation studies

  Shuai Guo
  Nanostructures for polymer-based organic photovoltaic

  Humphrey Morhenn
  Dynamics at the onset of self-diffusion in molecular liquids

  Kuhu Sarkar
  Nanostructured zinc oxide films for application in photovoltaics

  Markus Schindler
  Pressure sensitive adhesives - inner structure and adhesive performance

  Tobias Zweifel
  Fission gas behaviour and interdiffusion layer growth in in-pile and out-of-pile irradiated U-Mo/Al nuclear fuels

- **Accomplished master theses**

  Amr Abdelsamie
  Low temperature synthesis of nano-patterned TiO_2 thin films by combining sol-gel synthesis and nano-imprinting

  Lukas Augsbach
  Temperature-resolved mesoscopic structures of a novel thermoresponsive diblock copolymer

  Erik Valentin Braden
  Sol-gel templated films of different zinc oxide and titania ratios for application in photovoltaics

  Biye Cao
  High-performance organic solar cells based on PTB7:PC71BM bulk heterojunction system

  Mohamed Darweesh
  Effect of temperature and different solvents on bulk and thin films of diblock copolymers

  Rajesh Dutta
  Tuning magnetic properties of SrCoO2.5+d/CaFeO2.5 hetero-structures

  Luise Fiedler
  SEM and XRD studies on Arc-casted U-Mo-Si compounds

  Efi Dwi Indari
  Morphology changes of organic solar cells introduced via aging

  Wei Liu
  In-situ growth study of gold nano domains on P3HT films for hybrid solar cells

  Maria Freiria Lopez
  Options for the conversion of the FRM II outside the core

  Avishek Maity
  Structure, magnetic and chemical reactivity of SrFeO2.5-x explored by single crystal neutron and synchrotron diffraction studies

  Christina Psylla
  Thermoresponsive core-shell brush copolymers with poly(propylene oxide)-b-poly(ethylene oxide) side chains

Majid Rasool
Block copolymer electrolyte based membrane for lithium ion micro batteries

Johannes Schlipf
Novel structuring of organic thin films for improved absorption and performance in organic solar cells

Lorenz Sykora
Towards attenuated total reflectance infrared spectroscopy using micro- and nanostructured silicon crystals

Tianyi Wang
Low temperature synthesis of TiO_2 thin films with superstructures via wet imprinting

Xiaohan Zhang
Networks from amphiphilic star bloccopolymers

- **Accomplished bachelor theses**

Melis Aça
Nanoparticles via laser ablation for solar cells

Simon Barth
Implementierung von Honigwaben-Goldstrukturen als transparente Elektrode in organischen Solarzellen

Jessica Böhm
Aggregationsverhalten von Pfropfcopolymeren in wässriger Lösung

Ruben Burkhardt
Metal-decorated colloidal films for application in organic photovoltaic

Tobias Chemnitz
Inbetriebnahme und Parametrisierung einer Sputteranlage in der Kernbrennstoffentwicklung

Kora-Lee Claude
Phasenübergang thermoresponsiver Polymere unter Einfluss von Temperatur und Druck

Lisa-Marie Fellinger
Temperaturabhängige Messungen des Brechungsindex von thermoresponsiven Polymerlösungen

Peter Haslauer
Aufbau einer Heizzelle für die Fluoreszenz-Korrelationsspektroskopie

Alexander Hollering
Aufbau eines Neutronen Speicherexperiments zur Charakterisierung von Neutronenleitern für ultrakalte Neutronen

Manuela Alexandra Huber
Optimierung und Herstellung von Neutronenleitern für die zukünftige Quelle ultrakalter Neutronen am FRMII

Ferdinand Jarisch
Controlling adhesion via relative humidity

Florian Jung
Hexagonal structures in thin films from block copolymers

Max Kraut
Untersuchungen zur a″-Phase in Uran-Molybdän-Legierungen

Merlin Mitschek
pH schaltbare polymere Hydrogele

Thomas Lorenz Maier
Aging in active layers of organic solar cells - an infrared spectroscopic analysis

Philipp Marzak
Establishment of thermoresponsive polymers for the use in switchable thin films - investigation into the LCST demixing phase transition of a novel homopolymer

Stefan Oswald
Herstellung und Untersuchung eines Spaltproduktsurrogats zur Erprobung eines 99Mo-Extraktionsverfahrens

Josef Sapper
Viskositätsmessungen an temperatur-responsiven Polymeren verschiedener Architektur

Stefan Schmalzl
Sensors based on metal-polymer nanocomposites

Dominik Schullerer
Verhalten von Blockcopolymeren bei gleichzeitiger Bedampfung mit zwei verschiedenen Lösungsmitteln

Susanne Schwarzwälder
Block copolymer electrolytic membranes for lithium ion batteries

Julian Seyfried
Double thermo-responsive diblock copolymers: A dynamic light scattering investigation

Peter Spieler
Die Rolle der molekularen Wechselwirkungen in thermo-responsiven Polymer-Nanoschaltern am LCST-Entmischungsübergang

Stephan Umkehrer
Nanoparticles via laser ablation for solar cells

Alexander Wolf
Einfluss des Si-Anteils im Matrix-Material hinsichtlich der Wärmeleitfähigkeit von dispersen U-Mo Brennstoffen

10.3 Guests

- Prof. Dr. Alfons Schulte, University of Central Florida, USA
  16 Aug 2013 – 31 May 2014
- Prof. Dr. Igor I. Potemkin, Andrey Rudov, Lomonosov Moscow State University, Russia
  9/10 Jan 2014
- Dr. Aristeidis Papagiannopoulos, Theoretical and Physical Chemistry Institute, National Hellenic Research Foundation, Athens, Greece
  20 Jan – 3 Feb 2014
- Dr. Sergey Filippov, Institute of Macromolecular Chemistry, Prague, Czech Republic
  6 – 9 Feb 2014, 11 – 13 May 2014, 23 – 27 Nov 2014
- Dr. Stephan V. Roth, DESY, Hamburg
  10 Mar 2014
- Katerina Bikas, National Technical University of Athens, Greece
  10 Apr – 10 Jun 2014
- Lorenz Sykora, Technical University of Denmark
  14 – 16 Apr 2014
- Prof. Dr. André Laschewsky, Universität Postdam
  11 – 13 May 2014
- Prof. Dr. Dominik Wöll, Universität Konstanz
  11 – 14 May 2014
- Prof. Dr. Apostolos Kyritsis, National Technical University of Athens, Greece
  11 – 16 May 2014
- Dimitra Apostolidou, National Technical University of Athens, Greece
  11 - 17 May 2014
- Stefanos Koutsoumpis, National Technical University of Athens, Greece
  11 – 17 May 2014
- Dionysia Aravopoulou, National Technical University of Athens, Greece
  11 - 17 May 2014, 6 Oct – 21 Dec 2014
- Alexandros Manochis, National Technical University of Athens, Greece
  11 - 17 May 2014
- Prof. Dr. Stephan Förster, Universität Bayreuth
  13 May 2014
- Prof. Pedro William Pérez Orozco with group of students, Universidad Central, Bogotá, Colombia
  15 May 2014
- Dr. Madlen Hubert, Ludwig-Maximilians-Universität München
  17 Jun 2014

- Dr. Qi Zhong, Zhejiang Sci-Tech University, PR China
  12 Jul - 2 Aug 2014, 13 - 28 Nov 2014
- Prof. Dr. Jiping Wang, Zhejiang Sci-Tech University, PR China
  22 Jul 2014
- Prof. Dr. Jianzhong Shao, Zhejiang Sci-Tech University, PR China
  17 Sep 2014
- Dr. Petr Chytil, Dr. Sergey Filippov, Institute of Macromolecular Chemistry, Prague, Czech Republic
  23 – 27 Nov 2014